ISAS - INTERNATIONAL SCHOOL
FOR ADVANCED STUDIES

Large Scale Clustering in the Universe

Thesis submitted for the degree of

"Doctor Philosophiae"

Astrophysics Sector

Candidate:

Yi-peng Jing

Supervisor:

Professor Dennis Sciama

Academic year 1991-92

TRIESTE

SISSA - SCUOLA
INTERNAZIONALE
SUPERIORE
STUDI AVANZATI
TRIESTE
Strada Costiera 11

Large Scale Clustering in the Universe

Thesis presented by

Yi-peng Jing

for the degree of Doctor Philosophiae

Supervisor: Professor Dennis Sciama

S.I.S.S.A. - I.S.A.S.

Astrophysics Sector

Academic year 1991-92

Acknowledgements

I am very grateful to Professor Dennis Sciama, my thesis supervisor, for his invaluable advice and continuous encouragement of my research work. I am also very grateful to him for his various supports, scientific and non-scientific, during my two-year graduate study course.

I deeply thank my collaborators: Drs. Stefano Borgani, Gerhard Börner, Yu Gao, Hou-jun Mo, Manolis Plionis, Riccardo Valdarnini, and You-yuan Zhou for their fruitful collaboration and insightful discussions on which the thesis is based. From them I indeed learned a lot about the large scale structures of the Universe. In particular, I am very grateful to Gerhard, Hou-jun and Riccardo for their continuous collaboration and for their friendship.

Dr. Paul Haines has spent a lot of time carefully reading through this thick thesis, which improved its readability. I thank him so much for his patience and especially for his friendship.

Most of the work presented here was done during my graduate study at the International School for Advanced Studies (SISSA), Trieste. The school is greatly acknowledged for providing financial aid and research facilities during the course.

My graduate study started at the Center for Astrophysics, University of Science and Technology of China, Hefei. I am very grateful to Professor Li-zhi Fang and Professor Jia-lü Zhang (my supervisor in Hefei), for their effective guidance and various kinds of aid in my career.

Contents

An Overview

One major task of modern cosmology is to understand the Large Scale Structures (LSS) of the Universe. To complete this task, we have to proceed in three steps. The first step is to accumulate the observational data, such as catalogues of galaxies. The second step is to analyse the data, usually introducing certain statistical quantities, in order to give an objective description of the structures existing in the Universe. And the final step is to propose and test theoretical models of the LSS formation. These three steps are interactive: the observations and the statistical analyses often are motivated and guided by the proposed theories; and the theories are often proposed or/and improved to explain and understand the observations.

A contribution to understanding the LSS of the Universe is given in this thesis. The first part of the thesis will summarize the recent developments in the theories, the observations, and the statistics, which will be given in the first three chapters. The following chapters contain our original contributions to the subject, which are mostly concentrated on the second step — the statistical measures. More precisely, the thesis is arranged as follows:

In Chapter 1, I will give an outline of the theories of galaxy formation. I will only describe the gravitational instability theory and the conventional Gaussian fluctuation models dominated by certain types of particles. The description is rather qualitative; it is only intended to supply a frame for understanding the statistical results given in the following chapters.

In Chapter 2, I will list the main catalogues and samples of extragalactic objects which are often used in the LSS studies. The information relevant to the LSS studies will be outlined. I will emphasize the size of each sample (such as the number of objects, volume covered), so that we can judge the quality and universality of statistical results based on these samples.

Chapter 3 will describe the commonly used statistical measures of clustering. These are: the correlation function analysis, the void probability function, the minimal-spanning trees, the topological analysis and the percolation method. The results, obtained both by us and by other people, will be summarized, together with the constraints that they impose on the theoretical models (if known). An evaluation of our research work can be made from this chapter.

Afterwards, I will present the details of our research work. Chapter 4 extensively studies the error estimates in the correlation function analysis. Analytical formulae are given for the ensemble and the bootstrap resampling errors in the two- and three-point correlation functions. The relations between the above two types of errors and the Poissonian errors are clarified. The results provide a convenient way of estimating errors in the correlation analysis; in particular, one does not need a lot of computational time to obtain the bootstrap resampling errors.

In Chapter 5, I present the angular two- and three-point correlation functions of galaxies in the ESO-Uppsala catalog, using angular-diameter-limited samples. Based on the analysis, the questions regarding the scaling-depth relation, the volume effect on the correlation length, the morphology segregation, etc., are addressed.

Chapter 6 presents our work on the superposition effect on the cluster-cluster correlation ξ_{cc}. By a *consistency* check of the redshift correlation function between three redshift samples of Abell clusters and by running numerical simulations, we found that there is *no evidence* that the contamination effect has seriously enhanced the ξ_{cc}, thus the result of ξ_{cc} initially obtained by Bahcall & Soneira (1983) still challenges most of the current models of LSS formation.

In Chapter 7, I present our original statistical analyses on the three-point correlation function ζ_{ccc} of rich clusters. We found that the ζ_{ccc} can be approximated by the hierarchical form, just like galaxies. The richness dependence of ζ_{ccc} is also studied with the help of the samples of poorer clusters. At the end, theoretical implications are outlined.

The explosive models of galaxy formation were proposed to explain the two-point correlation of Abell clusters (Weinberg et al. 1989; Bahcall et al. 1989). Chapter 8 explores the three-point correlation function of rich clusters in this type of models. It is found that the hierarchical form emerges in this scenario, with weak dependence on model details.

It appears impossible to extract the higher-order ($N \geq 4$) correlation functions of rich clusters by the correlation analysis. In Chapter 9, we study the problem using the void probability function $P_0(V)$, which is known to be connected with all N-point correlation functions (White 1979). The results show that the spatial distribution of Abell clusters is scale-invariant and this property is independent of cluster richness. Furthermore, comparing with the CfA sample, we tentatively conclude that there is a universal scaling in the distributions of galaxies and of clusters.

In Chapter 10, we analyse subsamples of the Abell and ACO cluster catalogues, which are nearly redshift complete, in order to study the large-scale structure traced by rich clusters. We use a variety of statistical techniques: minimal spanning trees, percolation, void probability functions and cluster alignments; then we compare our findings with those expected from an ensemble of simulated cluster catalogues having the same selection functions and low-order clustering as the real data. In this way we test the reproducibility of the real data statistics in our simulations. We find that the minimal spanning tree distribution reveals features which are not reproduced in our simulations at a $\geq 3\sigma$ level. Similarly, not reproduced are the shapes of many superclusters, found by a friends-of-friends algorithm. We suggest that the real cluster distribution might be described by a statistic more complicated than a simple Gaussian or/and the formation process of clusters might be more complicated than that we have simulated.

In the last chapter [Chapter 11], we attempt to explore the clustering in the linear regime. First assuming that the structures are amplified by the gravitational instability and the primordial fluctuation is Gaussian-distributed, we give a self-contained framework which links a variety of observational quantities (the correlation function, the peculiar velocities, the flux- and gravity-dipoles, the Sachs-Wolfe effect, etc.) to the density power spectrum. Then we apply Fourier analysis to measuring the power spectrum in the 2-Jy IRAS galaxy sample and the Abell cluster samples. The measurement method is examined in great detail there. Finally we compare the observed power spectrum with the APM angular correlation function, the two-point correlation function of Abell clusters, the local peculiar velocity fields, the acceleration dipoles, the IRAS count-in-cell analysis, the recent COBE experiment, etc. All these observations are consistent, giving clear guidance to the study of galaxy formation theories.

1

An outline of the theories of galaxy formation

In this chapter, I shall give an outline of current galaxy formation theories. To prove or disprove these theories is one of the major tasks of LSS studies. The statistics of galaxy clustering are often guided and motivated by these theories. An accurate description of the models usually needs to solve a set of differential equations in the linear regime and to run N-body simulations in the nonlinear regime, to follow the evolution of density perturbations. It is beyond the scope of this thesis to give much detail. Instead here I give a qualitative description of the main features of the models which are mostly relevant to the statistics used in the thesis. I hope the material presented here is helpful for understanding the following chapters. Rigorous treatment of the models can be found in several excellent textbooks.

In §1.1, I will summarize the parameters upon which current models of galaxy formation depend, and classify the models according to these parameters. Then a qualitative description of the gravitational instability theory follows in §1.2. The biasing mechanisms are illustrated, in §1.4, by choosing 'peaks' in the Gaussian fields. The transfer functions and the main features of the conventional models will be given in §1.3 and §1.5 respectively. Here we shall not discuss the cosmic string (or texture) scenario and the explosion theory, though they may also be plausible.

1.1 The model parameters

The current theories of galaxy formation generally are based on the hot big-bang cosmology. Therefore the parameters of the big-bang model are also the parameters of the galaxy formation theories. These are:

a). The density parameter Ω_o: $0.1 \leq \Omega_o \leq 1$;

b). The Hubble constant H_o: $H_o = 100\,h\,\mathrm{km\ sec^{-1}\ Mpc^{-1}}$ and $0.4 \leq h \leq 1$;

c). The temperature of the cosmic background radiation T_o: $T_o \approx 2.7\,\mathrm{K}$;

d). The cosmological constant Λ, which is usually set to zero.

Besides these, there are further parameters which are relevant to galaxy formation theories. They are:

e). The contents of the Universe: Is there dark matter? If it exists, is it baryonic matter, Cold Dark Matter (CDM), Hot Dark Matter (HDM), unstable dark matter? And how much of it is there? (Ω_i?)

f). The primordial fluctuations: How did these fluctuations originate? Are they Gaussian or non-Gaussian? What spectrum $P(k)$ do they have? If $P(k)$ is a power law, how large is the amplitude and what is the slope?

g). Biasing: does light trace mass in the spatial distribution? If not, how is it biased? Which physical process leads to the biasing?

h). The effects of non-gravitational processes: Are these effects, like explosions, important in forming LSS?

According to the distinctive features of the resulting structures, I group the models into the following categories:

i). Gaussian fluctuation models dominated by
  - ♣ Baryonic matter
  - ♣ Cold dark matter (CDM)
  - ♣ Hot dark matter (HDM)

ii). Non-Gaussian fluctuation models
  - ♣ Cosmic strings
  - ♣ Cosmic textures

iii). Explosions

In each set of the models, the 'biasing' mechanism can be further introduced. In this chapter, I will concentrate on the first set of models.

1.2 The basics of the gravitational instability theory

It's generally thought that the structures we see today, such as galaxies, clusters and superclusters, originate from the small density inhomogeneities in the early Universe. The amplification mechanism of the perturbations is thought to be the gravitational instability. In this section, I shall give the fundamentals of this mechanism.

1.2.1 Three different eras

According to the different behaviours of perturbation growth, we divide the entire history of the Universe into three eras. This division will help us to describe the evolution of density inhomogeneities (see §1.3).

a. The first era is the radiation dominated phase at $1+z \geq 1+z_{eq} = 2.5 \times 10^4(\Omega_o h^2)$. During this phase, radiation density exceeds that of the non-relativistic matter. The comoving horizon size at $1+z_{eq}$ is: $\lambda_{eq} = 13(\Omega_o h^2)^{-1}\mathrm{Mpc}$;

b. The second era is between $1+z_{eq}$ and $1+z_{dec} \sim 1100$. During this stage, non-relativistic matter begins to dominate over the radiation. The radiation is strongly coupled with the baryons at the initial stage of the era, and begins to decouple from the baryons at the final stage, therefore the baryon-radiation can be approximated as an perfect fluid in this era;

c. The last era is after $1+z_{dec}$, when ions and free electrons recombine. Eventually the free electron density becomes so low that radiation and matter become decoupled. Because of the decoupling, the pressure in matter drops immensely. If there is no reionization, photons behave like collisionless particles of $m = 0$ afterwards.

1.2.2 Three important length scales

There are three length scales which are relevant to the size of the resulting structures. These are:

a. The Jeans length of a fluid: As we know, the time scale of gravitational growth is: $t_g \sim (G\rho)^{-1/2}$; and the time scale of diffusion on scale l due to pressure is: $t_d = l/v_s$ (where v_s is the sound speed). If $t_g < t_d$, the fluctuation on scale l can gravitationally grow; otherwise the fluctuation behaves like a sound wave. For the critical case,

$t_g \sim t_d$, we have a length $\lambda_J = v_s(G\rho)^{-1/2}$ which we call the Jeans length. Clearly, only fluctuations larger than λ_J can grow under gravitational instability. Because the baryonic matter and the radiation are strongly coupled before z_{dec}, the Jeans length is $\sim$ the horizon size; afterwards λ_J drops dramatically.

b. Perturbations in collisionless components suffer Landau damping. Until the perturbation becomes unstable and begins to grow at t_{eq}, the collisionless particles can stream out from the overdense regions into the underdense regions, thus erasing the inhomogeneities. The length scale of the damping is obtained by solving the collisionless Boltzmann equation. Its approximate value can be estimated by calculating the path traveled by a particle from the beginning to t_{eq}. The comoving length traveled by a particle is

$$\lambda_{FS} \equiv r(t_{eq}) - r(t_i) = \int_{t_i}^{t_{eq}} \frac{v(t)}{R(t)} dt$$

Assuming the particle becomes non-relativistic at t_{NR}, then

$$\lambda_{FS} = \int_0^{t_{NR}} \frac{1}{R(t)} dt + \int_{t_{NR}}^{t_{eq}} \frac{R_{NR}}{R^2(t)} dt$$

In the radiation dominated era, $R(t) \propto t^{1/2}$, so

$$\lambda_{FS} = (\frac{t_{NR}}{R_{NR}})[2 + \ln(\frac{t_{eq}}{t_{NR}})]$$

For the light neutrinos, $\lambda_{FS} = 20(30\text{ev}/m_\nu)$Mpc.

c. The perturbations in the baryon-photon fluid are subjected to the Silk damping around the recombination era, because the perfect fluid approximation breaks down. A rigorous treatment of the problem needs to solve the collisional Boltzmann equation. The length scale of the damping is approximately the diffusion length of a photon. It can be estimated as follows. The photon mean free path : $\lambda_\gamma = (\chi_e n_e \sigma_T)^{-1}$ (where χ_e is the ionization rate; n_e is the density of electrons; and σ_T is the Thomson cross-section). In a time interval Δt, a photon suffers $\Delta t/\lambda_\gamma$ collisions and makes a random walk whose size squared is

$$\Delta r^2 = \frac{\Delta t}{\lambda_\gamma(t)} \frac{\lambda_\gamma^2(t)}{R^2(t)} = \frac{\Delta t \lambda_\gamma(t)}{R^2(t)}$$

So the Silk damping scale is

$$\lambda_S = \sqrt{\int_0^{t_{dec}} dt \frac{\lambda_\gamma(t)}{R^2(t)}}$$

If we take suitable values for each parameter, we get λ_S:

$$\lambda_S \approx 3.5(\Omega_0/\Omega_b)^{1/2}(\Omega_0 h^2)^{-3/4} \text{ Mpc}.$$

Note that isocurvature perturbations do not suffer from this effect, since the spatial distribution of photons is homogeneous.

1.2.3 Linear perturbation theories

If the fluctuations are well within the horizon and the characteristic velocity $\ll$ the light speed c, the Newtonian approximation suffices. If δ is the density contrast on scales much larger than the Jeans length for the fluid, the linear perturbation equation is:

$$\frac{d^2\delta}{dt^2} + 2\frac{\dot{R}}{R}\frac{d\delta}{dt} = 4\pi\rho_b G\delta$$

For a flat model which is matter dominated, we have

$$\delta_1 = D_1(t)\delta_i \qquad D_1(t) \propto R(t) \propto t^{2/3} \qquad \text{growing mode;}$$

and

$$\delta_2 = D_2(t)\delta_i \qquad D_2(t) \propto R(t)^{-3/2} \propto t^{-1} \qquad \text{decaying mode.}$$

Since the second mode decays very rapidly, we are mostly interested in the growing mode. The explicit expressions of $D(t)$ can be obtained separately for the closed and open Universes, but here we only give some qualitative, approximate properties of such solutions.

In an open model of $\Omega_o < 1$, $\delta_1 = D_1(t)\delta_i$. When $z > \Omega^{-1}$, $D_1(t) \propto t^{2/3}$; however for $z < \Omega^{-1}$, the growth is suppressed.

In a closed model of $\Omega_o > 1$, $\delta_1 = D_1(t)\delta_i$. Its growth is more rapid than in the flat model.

Since the physical length $l_{ph} \propto R(t) l_{co}$, and the horizon length is $\sim t$ (which is proportional to R^2 in the radiation-dominated era and to $R^{3/2}$ in the matter dominated era), the fluctuations which give rise to galaxies or other structures, must be larger than the size of the horizon (i.e., $l_{ph} > t$) at sufficiently early times. In order to treat such super-horizon-sized fluctuations, one needs a full general-relativistic analysis. In this case, the universe can always be regarded as a flat one. In the synchronous metric, there are two physical modes: a decaying mode and a growing mode; and two pure gauge modes. The growing mode evolves as $\delta \propto R^2$ in the radiation dominated era and $\delta \propto R$ in the matter dominated era.

1.3 The transfer functions and the processed power spectrum in the baryon, CDM and HDM models

Let the density fluctuation spectrum be $P_i(k)$ at the initial time. As the perturbation evolves, we would observe at the present the processed density spectrum $P(k) = T^2(k,t_0)D_1^2(t_0)P_i(k)$. The function $T(k,t_0)$ is called the transfer function. Its importance to the LSS studies is obvious and it can be strictly solved in the linear regime. Here I qualitatively discuss $T(k,t_0)$ in the baryon, CDM and HDM dominated models.

At the first stage $t < t_{eq}$, the fluctuations of size greater than the horizon grow as D_1 (*i.e.*, $T(k) = 1$). The sub-horizon fluctuations in WIMP (Weak Interacting Massive Particles) components can not grow (or at best logarithmically grow with R) due to the radiation domination (also called the Meszaros effect). This effect leads to $T(k) \propto R_h^2(k)$, i.e., $T(k) \propto k^{-2}$ [$R_h(k)$ is the scale factor when fluctuations of k enter the horizon]. Furthermore, the perturbations of size less than λ_{FS} are erased in this stage due to the Landau damping. This effect can be modeled as $T(k) = 0$. Baryon-Radiation (B-R) fluctuations within the horizon behave like sound waves due to the large Jeans length. This effect can be written as $T(k) = k^{-2}f(\text{oscillating})$.

During the next stage ($t_{eq} < t < t_{dec}$), fluctuations in WIMP grow $\propto D_1(t)$. B-R perturbations inside the horizon behave like sound waves, but the super-horizon perturbations grow also $\propto D_1(t)$. How to model these effects is obvious (see above).

At and after the recombination ($t \geq t_{dec}$), fluctuations in WIMP grow $\propto D_1(t)$ [until $z = \Omega_0^{-1} - 1$ if the universe is open]. At recombination, baryons and radiation are decoupled, and the Jeans mass of the baryons is reduced to the (sub-)galactic scale. In the meantime,

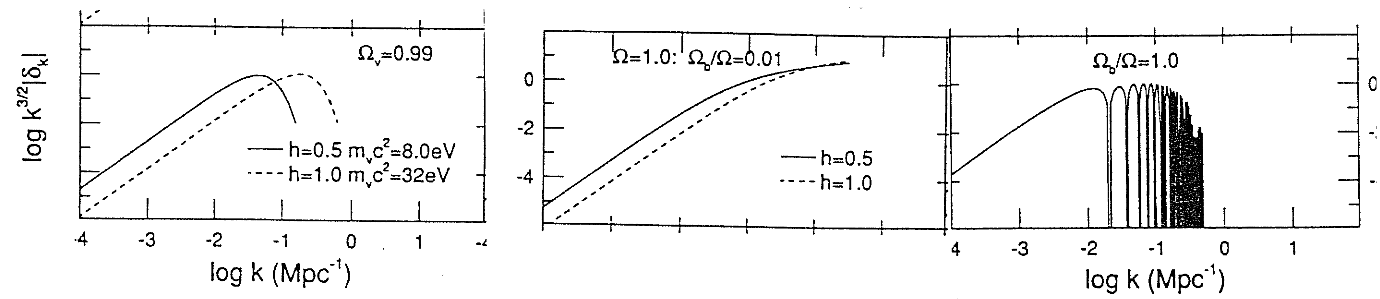

Figure 1.1 — The processed spectrums for baryon ($\Omega_b = 0.2$), CDM (flat) and neutrinos (flat) dominated universes with scale-invariant adiabatic initial conditions (from right to left). Note $k^{3/2} \mid \delta_k \mid$ in the vertical coordinate corresponds to $k^{3/2}P^{1/2}(k)$ in the text.

Silk damping erases all baryonic perturbations of $\lambda < \lambda_S$. Afterwards in the baryon dominated universe, the fluctuations grow $\propto D_1(t)$; in the WIMP dominated universes, baryons will soon catch up to the fluctuations of WIMP after the recombination (taking several expansion factors). The Silk damping is modelled as $T(k) = 0$ for $k < k_S$, and other processes are apparent.

Finally we can write the $T(k, t_0)$ approximately as:

$$T_{baryon}(k, t_0) = \begin{cases} 0, & \text{if } k > k_S; \\ \propto k^{-2}\ f(\text{oscillating}), & \text{if } k_S > k > k_{dec}; \\ 1, & \text{if } k < k_{dec}, \end{cases}$$

for the baryon universe;

$$T_{CDM}(k, t_0) = \begin{cases} \propto k^{-2} & \text{if } k > k_{eq}; \\ 1, & \text{if } k < k_{eq}, \end{cases}$$

for the CDM universe; and

$$T_{HDM}(k, t_0) = \begin{cases} 0, & \text{if } k > k_{FS} \sim k_{eq}; \\ 1, & \text{if } k < k_{FS} \sim k_{eq}, \end{cases}$$

for the neutrinos dominated universe. With these transfer functions, we can easily get the processed spectrum. Figure 1.1 shows the processed spectrums $P(k) = \mid \delta^2(k) \mid$ for baryon (open), CDM (flat) and HDM (flat) universes with the initial Zel'dovich spectrum $P_i(k) \propto k$, taken from the numerical calculation of Holtzman (1989). The various effects emphasized above are obvious in the figure. We can also see the qualitative features of $T(k)$ given above.

1.4 A simple 'biasing' scheme — An example

1.4.1 Why do we need 'biasing'?

Up to now, we have only discussed the matter distribution. It is unclear to us whether galaxies (or clusters) trace the mass distribution in space. It is not a trivial problem. The strong clustering exhibited by rich clusters at least shows that clusters and galaxies are not equivalent tracers in the spatial distribution. This is one motivation for the proposal of biased galaxy formation (Kaiser 1984).

The dynamical studies of galaxy distributions, such as the 'infall' argument, the Virial theorem, etc., always give an Ω about 0.2, while the inflation theories require $\Omega = 1$. In these studies, $\Omega \propto \delta_m^{-2}$, and assume $\delta_m = \delta_g$ (i.e., galaxies trace mass). However, if galaxies are a biased tracer, e.g., $\delta_g = 2 \sim 3\delta_m$, we can have $\Omega = 1$ in such studies, i.e., a flat universe.

The huge voids, such as Böotes, are rather difficult to produce in the Gaussian models, if light traces mass. However, if galaxies do not trace mass, the void regions could be less empty in mass distribution than in galaxy distribution, and the problem could be solved.

N-body simulations of both hot and cold dark matter models need anti-biasing and biasing respectively, otherwise they can't produce the right amplitude and right slope of the galaxy-galaxy correlation function ξ_{gg}.

There are other theoretical arguments, though not as strong or clear as those listed above, that galaxies could be a biased tracer of the mass (see Dekel & Rees 1987)

1.4.2 One simple biasing scheme as an example

If fluctuations are Gaussian, the rare high peaks are more clustered than the background. This can be understood from Figure 1.2. In the figure, the small-wavelength perturbation is modulated on the long-wavelength one. If we choose only rare peaks with $\delta > \nu\sigma = 2$, such peaks must be more clustered than the background, as clearly shown in the figure. A rigorous treatment of peak properties in a Gaussian fluctuation field is given in Bardeen et al. (1986).

1.5 Main features of the conventional models

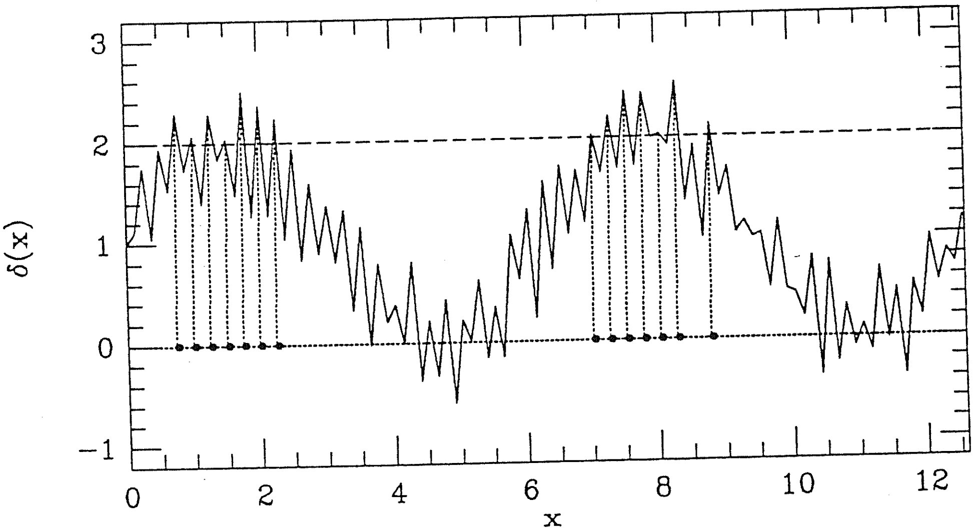

Figure 1.2 — A sketch map of the biasing scheme. Taken from Borgani (1990).

1.5.1 The baryon dominated Universe

The most attractive feature of this model is "what we see is what we get": we do not need any exotic particles. The model is always open, since the big-bang nucleosysthesis theory puts the upper limit on the baryonic density $\Omega_b < 0.2$. The galaxies and mass are the equal tracers of the spatial structures.

If the initial fluctuation is adiabatic, the fluctuations in baryonic matter are erased during the decoupling on scales smaller than the Silk damping length (see §1.2 & §1.3). The first forming objects are of mass $10^{13} \sim 10^{14} M_\odot$, i.e., the mass scale of rich clusters and superclusters. So the model is of the nature of the 'top-down' scenario.

In the adiabatic model, the gravitational growth becomes effective only from the decoupling $z = 1100$ to $z \approx \Omega_b^{-1} \sim 5$, giving a growth factor ~ 200 (see §1.2). In order to produce structures observed, we have to require a large fluctuation amplitude at decoupling which would lead to anisotropy $\Delta T/T \sim 10^{-3}$ in the Cosmic Background Radiation (CBR) at arcminutes scale, in severe conflict with the available experiments (Uson & Wilkinson 1984; Readhead et al. 1989). Because of this difficulty, the model has lost its initial popularity.

If the initial fluctuation is isothermal, there is no Silk damping effect, so the structures form as in the 'bottom-up' picture. The attractive feature is that it can produce coherent clustering on the large scale, such as large scale bulk motion of Dressler et al. (1987). The anisotropy $\Delta T/T$ on arcminutes is much smaller than in the adiabatic case, however the observations of Readhead et al. (1989) have already ruled out this model if there are no reionizations after the decoupling (Efstathiou 1988). But if the universe is reionized, the model can be consistent with all the observations of $\Delta T/T$, although the constraint is quite stringent (Efstathiou 1988).

The studies of the isocurvature model, up to date, have been limited within the linear perturbation theories. The model is consistent with the observations of $\Delta T/T$, the galaxy clustering on tens h^{-1}Mpc, the large scale peculiar velocity fields and the flux dipoles. However, there is no simulation study in the non-linear regime, and many properties regarding the clustering statistics given below are not yet clear.

1.5.2 The standard HDM model

The standard HDM model is attractive because the neutrinos, as the missing mass, is a known particle. Especially, it was declared that the mass of neutrinos had been detected to be several tens eV, which is just large enough to close the Universe.

The distinctive feature of the HDM model is the large streaming length $\sim$ tens Mpc, so the first objects formed are of the size of superclusters. Galaxies and clusters of galaxies are the results of fragmentation of the first forming objects ('top-down' scenario). So this model can easily produce filamentary structures.

The most severe problem of the scenario is that galaxies have formed very recently $z \sim 1$, in contrast with the observations of quasars at $z > 4$. The problem is inevitable, since galaxies form when superclusters collapse and the observations show that superclusters are reaching or have reached very recently nonlinearity.

The model has been studied in much detail, both by linear perturbation theories and by N-body simulations. As a result, the model has been convincingly ruled out by the recent observation of $\Delta T/T$ at a one degree scale (Bond et al. 1991; Vittorio et al. 1991). If there is no biasing, the detailed N-simulations show that the model is unable to produce the right amplitude A_{gg} of ξ_{gg}, the hierarchical form of the three-point correlation function of galaxies, the cluster-cluster correlation function, the scaling behaviour of voids, etc. (e.g., Batuski et al. 1987; Fry et al. 1989). Introducing biasing or anti-biasing may resolve some of the problems, but at the expense of making other problems more severe. The theory seems out of repair.

1.5.3 The standard CDM model

The standard CDM model has dominated galaxy formation theories for many years. This is the most successful model, though it is facing challenges from recent observations. The most attractive feature of the model is that it is just the one that the inflation theories predicted. There are only three parameters: h, the amplitude of $P(k)$ and the biasing prescription, to be adjusted. But there are several sets of observations against which the model can be tested.

One distinctive feature of the model is that smaller objects form earlier than larger ones, i.e., the 'bottom-up' scenario (see §1.3).

Another feature is 'biasing'. In the standard CDM model, the galaxies must be a biased tracer of the mass distribution, as discussed in §1.4. White et al. (1987a) proposed that galaxies preferentially form at halos with large circular velocities v_c. Their simulations show that the objects of large v_c are clustered more than those of smaller v_c. Because of the Faber-Jackson and the Tully-Fisher relations, the model predicts that faint galaxies are distributed more randomly than bright ones. The prescription, however, may still be too simple. But as hinted by their studies, galaxies of different types (e.g., luminosity, morphology, rotation velocity) are likely to have different clustering properties.

The model has been studied in great detail. It can reproduce all the clustering features observed on scales from tens h^{-1}Kpc to 10 h^{-1}Mpc: e.g., the correlation functions of galaxies, the Faber-Jackson and the Tully-Fisher relations, the scaling behaviours of voids, the relative pair-velocities, ... etc. However, because of the lack of clustering power on large scales, the model is unable to explain the features observed recently on several tens h^{-1}Mpc: the cluster-cluster correlation function, the angular two-point correlation function from the APM survey, the variance of the IRAS survey, the large-scale peculiar velocity fields, the acceleration dipoles, the power spectra of radio galaxies and rich clusters, etc. Similarly, the model is consistent with the current observational upper limits of $\Delta T/T$ on angle scales up to 1 degree, but can hardly account for the recent detection of the $\Delta T/T$

quadrupole in the COBE DMR experiment. As shown in Chapter 11, all these observations are consistent, indicating that the standard model has to be revised. The revisions might be able to improve the comparisons of the model with the observations, but some attractive properties of the 'standard' model would be lost.

1.5.4 The CDM models revisited

As described in the last subsection, the standard CDM model is facing a series of severe challenges from the recent observations on large scales greater than $\sim 10\,h^{-1}$Mpc. However, the model is quite successful in producing smaller structures. These facts imply that a model with a similar shape to the standard CDM model of the power spectrum but with relatively more power on large scales would be in better fit to the observations (e.g., Vittorio, Matarrese, & Lucchin 1988). Although the density parameter and the primordial power spectrum used in the standard CDM model are the very likely ones predicted by current inflation theories, a lower Ω_0 and a flatter $P(k)$ are not impossible to predict even in these theories (e.g., Lucchin & Matarrese 1985). Raising the baryon content, adding a small fraction of neutrinos to the cold dark matter, lowering the density parameter and introducing a cosmological constant, anti-biasing the spatial galaxy clustering on less than ten h^{-1}Mpc, and/or altering the initial Zel'dovich spectrum $P(k) \propto k$ to the $P(k) \propto k^n$ with $n < 1$, all may improve the confrontations with the observations. Detailed and quantitative studies are still needed in these directions before we can say yes or no to these models.

2

Major observational samples

Our understanding of the matter distribution in the Universe mainly comes from the distributions of galaxies, of galaxy groups and of galaxy clusters, since telescopes can only directly detect these objects. Although presently we are still unclear which (if any) of these objects fairly traces the matter distribution in the universe (see §1.4), it is of no doubt that these distributions are closely related. Moreover, the ultimate goal of the galaxy formation theories is to understand the distribution of these objects. Thus it is very important to study their spatial distributions.

As in any branch of astronomy, meaningful statistics regarding their distribution need samples (or catalogues) whose selection procedures are well defined and as free as possible of systematic biases and effects. Here I list the major observational samples and catalogues in the LSS studies, together with their defining criteria. There certainly exist, in some (perhaps all) of these samples, systematic biases which must be corrected in the LSS studies, otherwise spurious clustering could result. However the procedures for correcting such effects are usually very complicated, and their description is beyond the scope of this thesis but could be found in the literature.

♣ The Lick catalogue

This catalogue contains $\sim$ one million galaxies with $m_b \leq 18.9$ in the sky $\delta > -22.5°$ (Shane & Wirtanen 1967; Seldner et al. 1977). Galaxies are counted in each 10×10 arcmin^2 cell. The characteristic sample depth is about 210 h^{-1}Mpc. The reduction and correction procedures of the catalogue can be found in Seldner et al. (1977) and Plionis (1988).

♣ The Zwicky Catalogue

The Zwicky catalog contains 28,000 galaxies in the northern sky $\delta > -3°$. Galaxies are listed down to $m_{pg} = 15.7$, and the catalog is reasonably complete to $m_{pg} = 15.5$. This catalog is the important database for the LSS study in the northern sky (Zwicky et al. 1961-68).

♣ The Uppsala Catalogue

This catalogue lists angular positions of $\sim$ 13,000 galaxies in the sky area $\delta > -2.5°$. The sample is complete to major (apparent) axis $D_1 \simeq 1'$. Morphological types, diameters, and magnitudes (if observed) are also given. The characteristic sample depth is about 70 h^{-1}Mpc (Nilson 1973).

♣ The ESO/Uppsala catalogue

This catalogue lists angular positions of $\sim$ 15,000 galaxies in the southern sky with $\delta < -17.5°$. It's also claimed to be complete to major (apparent) axis $D_1 \simeq 1'$. Morphological types and diameters are presented for all galaxies. The sample depth is slightly deeper than that of the Uppsala catalogue (Lauberts 1982).

♣ The APM galaxy survey

This is a uniform sample of $\sim$ 2 million galaxies to a magnitude limit of $b_J = 20.5$, covering the 4300 square degrees area of $b \leq -40°$ and $\delta < -20°$. The survey is based on 185 UKSTU J survey plates which are scanned and digitized by the APM facility in Cambridge (Maddox et al. 1990b).

♣ The COSMOS galaxy survey

This is a uniform sample of $\sim$ 1.5 million galaxies to a magnitude limit of $b_J = 20.5$, covering the 1400 square degrees area centered at the South Galactic Pole. The survey is based on 60 UKSTU J survey plates which are scanned and digitized by the COSMOS facility (Collins et al. 1989).

♣ The IRAS galaxy samples

A new type of galaxy samples, IRAS galaxy samples, come from IRAS database (*IRAS Point Source Catalog*, Version 2 1988; e.g., Saunders et al. 1990; Strauss et al. 1990). These samples are usually flux limited (mostly at 60μm), and are selected on the flux quality at 60μm and far-infrared colours, in order to discriminate against cirrus, stars and planetary nebulae. The advantages of the large sky coverage ($\sim$ 80%), no Galactic extinction in the far-infrared, well-calibrated flux densities, and $\sim 120h^{-1}$Mpc characteristic sample depth, make such samples very useful in the LSS studies. If the limiting flux is 0.5 Jy at 60μm, there are roughly 17,000 galaxies.

♣ CfA Redshift Survey

The sample presents the radial velocities for the *all* 2401 galaxies in the merged Zwicky-Nilson catalogue brighter than 14.5 m_Z with $b^{II} \geq 40^\circ$ and $\delta \geq 0^\circ$, or $b^{II} \leq -30^\circ$ and $\delta \geq 0^\circ$. Its typical sample depth is ~40 h^{-1}Mpc (Huchra et al. 1983).

♣ Southern Sky Redshift Survey

This is a diameter-limited redshift survey in the southern sky with comparable depth and sky area to the CfA survey. The galaxies are selected from the ESO/Uppsala catalogue. The survey contains all 1957 galaxies with face-on diameter greater than 1.23′, on the sky with $\delta < -17.5^\circ$ and $b^{II} < -30^\circ$. A total of 1735 galaxies have available redshift. Redshift incompleteness is a strong function of morphology types; dwarfs are especially incomplete (da Costa et al. 1991).

♣ CfA2 Redshift Survey of Galaxies

This survey, intended to extend the original CfA redshift survey (1983) to the magnitude limit $m_{pg} = 15.5$ over a similar sky area, is still emerging. Eleven strips of 6° in declination are reported to be complete in redshift. Only the data of the first slice of $8^h \leq \alpha \leq 17^\circ$ and $26.5^\circ \leq \delta \leq 32.5^\circ$, which consists of 1057 galaxies, have been published (Huchra et al. 1990a).

♣ Northern Redshift Survey of Dwarf and LSB galaxies

As shown by Thuan & Seitzer (1979), the UGC was fairly complete for all dwarf and low surface brightness (LSB) galaxies larger than 1′ (the UGC diameter lower limit), so the UGC could become a good database for selecting a sample of Dwarf and LSB galaxies. The sample of Thuan et al. (1991) contains *all* galaxies classified in the UGC with a Hubble type of Dwarf, Dwarf Irregular, Dwarf Spiral, Ir, Sc-Irr, or S-Irr; a de Vaucouleurs type of Sd-dm, Sdm, Sm, or Im; or in the absence of these classifications, a van den Bergh luminosity class of IV-V or V. These selection criteria result in a sample of 1845 galaxies. The observation were made at Arecibo and Green Bank telescopes at 21 cm. The detection rate of 84% gives a total sample of 1557 galaxies with 21 cm redshift.

♣ A Redshift Survey of IRAS Galaxies with $f_{60} > 1.936$ Jy

This is a redshift complete sample of IRAS galaxies with the flux limit $f_{60\mu m} > 1.936$ Jy. It contains 2649 galaxies, covers 87.6% of the sky, and has sample depth $\sim 50h^{-1}$Mpc (Strauss et al. 1992b).

♣ The QDOT Redshift Survey of IRAS Galaxies

This is a sparsely-sampled redshift survey of IRAS galaxies, at sampling rate of one in six, complete to the flux limit $f_{60} = 0.6$Jy at $\mid b \mid \geq 10°$. It consists of 2163 galaxies, of which 2093 have available redshift. It is about 2 times deeper than the sample of Strauss et al. (1992b), at the expense of sparse-sampling.

♣ ACO Catalogue of Clusters of Galaxies

This is an all-sky catalogue of rich clusters of galaxies, complete nominally to $z = 0.2$ for clusters with populations (N_A) of 30 or more galaxies within Abell radius $r_A = 1.5h^{-1}$Mpc and in the magnitude range m_3 to $m_3 + 2.0$, where m_3 is the magnitude of the third brightest cluster member. There are a total of 4073 clusters. Their positions in the sky are listed, together with the distance class D, the richness class R, m_{10} (the magnitude of the tenth brightest cluster member), Bautz-Morgan types, redshift if available, etc. (Abell et al. 1989).

♣ Shectman Catalogue of Clusters of Galaxies

The Shectman catalogue, consisting of 646 clusters, has been constructed from the Shane-Wirtanen counts in $10'$ bins by identifying local density maxima above a threshold value (about 3.6 times the mean density) relative to eight surrounding cells, after slightly smoothing the data to reduce the effect of the sampling grid. It covers the sky region of $\delta \geq -22.5°$ and $\mid b \mid \geq 40°$. About 70% of $D \leq 4$ and 10% of $D \leq 5$ Abell clusters have been identified in the catalogue. It also includes much poorer clusters, which consist of 60% the sample. The characteristic sample depth is similar to the $D \leq 4$ sample of Abell clusters (Shectman 1985).

♣ The APM Catalogue of Clusters of Galaxies

The catalogue is constructed by applying an objective selection algorithm to the APM galaxy survey (Dalton et al. 1992). The algorithm is complicated and is not described here. There are 240 clusters, with similar richness to the $R \geq 0$ Abell clusters.

♣ The COSMOS Catalogue of Clusters of Galaxies

The COSMOS catalogue consists of 737 clusters, selected from the COSMOS galaxy survey. The clusters are selected using an objective peak-finding algorithm, similar to that of Shectman (1985). The clusters, on average, are poorer in richness than the $R \geq 0$ Abell clusters. One set of ~ 90 richest clusters is almost redshift complete (Lumsden et al. 1992).

♣ Plionis et al. Catalogue of Clusters of Galaxies

This catalogue, also based on the Shane-Wirtanen counts in $10'$ bins, has been compiled by identifying overdensity regions above certain threshold values: $\sigma/\langle\sigma\rangle$ =3.6, 3.0, 2.5, 1.8. It contains $\sim$ 6000 clusters, covering the sky of $\delta \geq -22.5^\circ$ and $\mid b \mid \geq 40^\circ$. At the highest overdensity threshold all clusters found are either Abell or Zwicky clusters (Plionis et al. 1991).

♣ Redshift samples of Abell clusters

Two subsamples, extracted from the original Abell catalogue (1958), now have complete redshift information. One is the sample of 103 clusters of richness $R \geq 1$ and distance $D \leq 4$ at the high galactic latitude $\mid b \mid \geq 30^\circ$ (Hoessel et al. 1980). The other, completed recently, covers 561 square degrees in the region of $10^h \leq \alpha \leq 15^\circ$ and $58^\circ \leq \delta \leq 78^\circ$, and includes 145 clusters with $R \geq 0$ and $D \leq 6$ (Huchra et al. 1990b).

The nearby sample of $D \leq 4$ and $R \geq 0$ at $\mid b \mid \geq 30^\circ$, is also near to redshift completion ($\sim$ 95%). An update compilation by Struble & Rood (1991a) lists $\sim$ 650 redshifts for Abell clusters.

♣ CfA Catalogue of Groups of Galaxies

Catalogues of groups of galaxies are usually produced by the friends-friends finding algorithm (Huchra & Geller 1982). The CfA catalogue, based on the 14.5 m_B CfA redshift survey, identifies groups as density enhancements in redshift space of a factor greater than 20. It consists of 176 groups with more than two members. It covers the same sky area and has a similar sample depth as the 14.5 m_B CfA redshift survey (Geller & Huchra 1983).

♣ SSRS Catalogue of Groups of Galaxies

This catalogue, based on the SSRS redshift survey, is produced by the same techniques used in the CfA catalogue. It contains 87 groups with more than two members (Maia et al. 1989).

♣ CfA2 Catalogue of Groups of Galaxies

The groups of the catalogue are identified, in the two CfA redshift slices of $8^h \leq \alpha \leq 17^h$ and $26.5^\circ \leq \delta \leq 38.5^\circ$, as density enhancements in redshift space of a factor greater than 80. It contains 128 groups with three or more members (Ramella et al. 1989).

3

Statistical measures of clustering

Even from two-dimensional maps (or catalogs) of galaxies and clusters, we can easily find that their spatial distribution is quite clumpy. An example, Figure 3.1 shows the positions of all the galaxies from the Zwicky et al. catalog which satisfy $m_B \leq 15.5$, $8^h \leq \alpha \leq 17^h$ and $8.5° \leq \delta \leq 50.5°$. The grid is Cartesian in R.A. and decl., and the deficiency of galaxies west of 9^h and east of 16^h is caused by the galactic obscuration. The Coma cluster and the Virgo cluster are the dense regions at ($\alpha = 13^h$, $\delta \approx +29°$) and at ($\alpha = 12.5^h$, $\delta \approx +12°$). Several other well known clusters, e.g., Abell 1367 (11.7^h, $+21°$), Abell 2197/2199 complex (16.3^h, $+38°$), are also obvious. These dense regions appear to be connected by "galaxy chains/surfaces". Between these structures, prominent "voids" (i.e., the regions which are devoid of galaxies) can be seen, for example, at ($\alpha \approx 15.5^h$, $\delta \approx +35°$), ($\alpha \approx 12.8^h$, $\delta \approx +21°$), ($\alpha \approx 10^h$, $\delta \approx +26°$), etc.

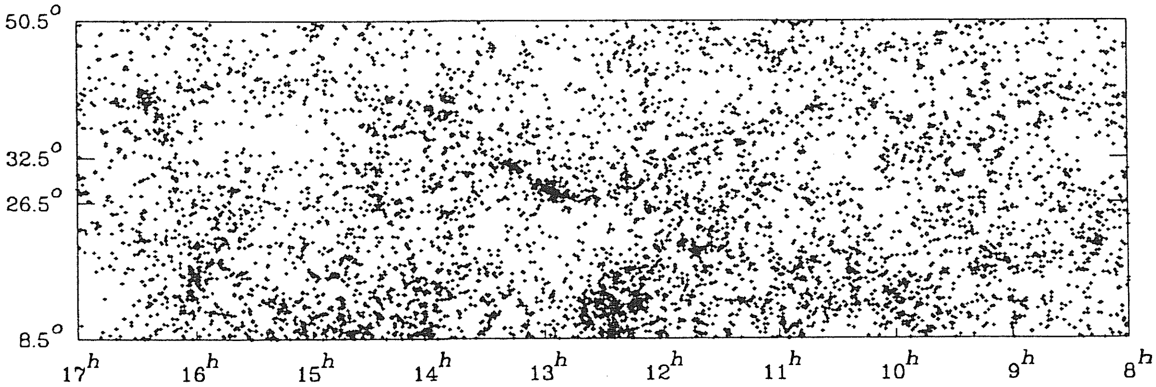

Figure 3.1 — The map of the 7031 objects with $m_B \leq 15.5$, listed by Zwicky et al. in the region bounded by $8^h \leq \alpha \leq 17^h$ and $8.5° \leq \delta \leq 50.5°$. Taken from de Lapparent et al. (1986).

Though the 2-D maps have already clearly shown prominent structures, the projection on 2-D must have smeared a lot of 3-D structures. An example is that a cell-like structure, which is of course very inhomogeneous, would have a quite smooth 2-D projection. 3-D

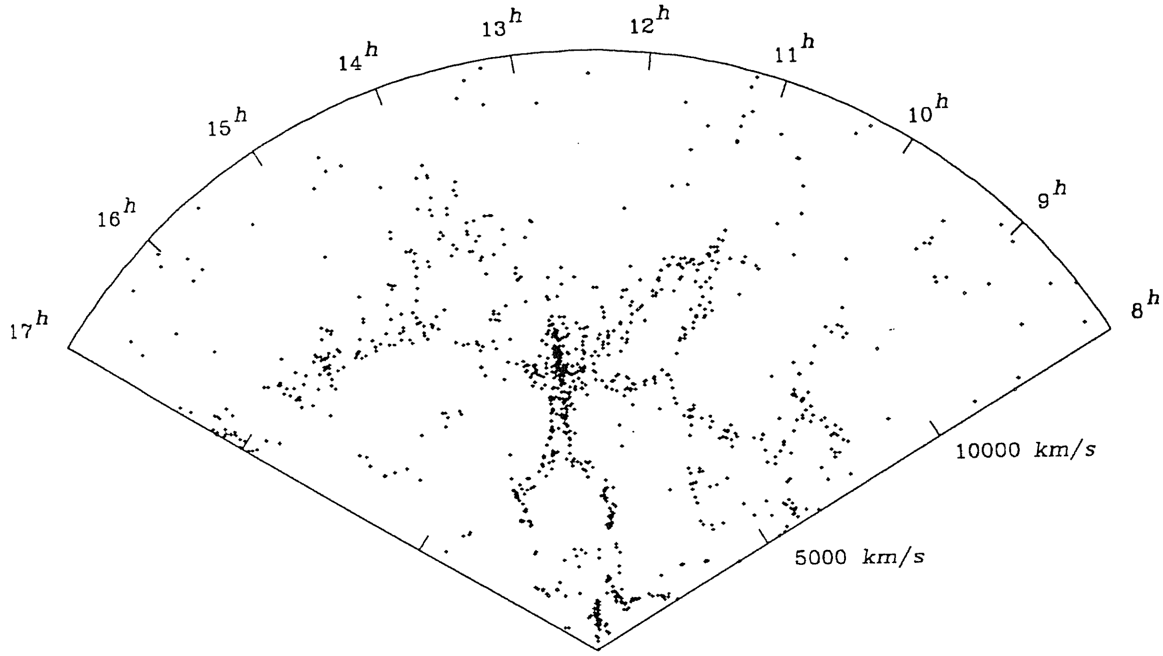

Figure 3.2 — Map of the observed velocity plotted vs. right ascension in the declination wedge $26.5^\circ \leq \delta \leq 32.5^\circ$. The 1061 objects plotted have $m_B \leq 15.5$ and $V \leq 15,000$ km s^{-1}. Taken from de Lapparent et al. (1986).

maps with complete redshift information, therefore, should contain much richer information on the structures. In the Figure 3.2, we show the famous plot of the observed velocity versus right ascension for the 1061 galaxies which are brighter than $m_B = 15.5$ and with velocities less than 15,000 km s^{-1} in the full 6° thick slice (from de Lapparent et al. 1986). The most striking features of the figure are several large regions almost devoid of galaxies and the sharpness of the boundaries of the high density regions which surround the voids. Combining the other two neighboring slices and comparing these surveys with the 2-D plot (Figure 3.1), Geller & Huchra (1988) strongly argue for a bubble-like structure, i.e., the galaxies are distributed on the surfaces of shells tightly packed next to each other (see also Joeveer & Einasto 1978). However, other studies show that galaxies are distributed as a hierarchy of clusters (e.g., Soneira & Peebles 1978; Bhavsar 1978 & 1980), a network of filaments (Einasto et al. 1984; Haynes & Giovanelli 1986; Bhavsar & Ling 1988a & 1988b), or a sponge like topology (e.g., Gott et al. 1986 & 1989).

To quantify these clustering features and to test theoretical models, we need objective and free-of-bias statistical measures. An *ideal* statistic of clustering should have the following features:

1.) On the observational side, the statistic should be able to quantify the clustering strength and coherence length, as well as the geometry and topology;

2.) On the theoretical side, it should be a good discriminant between different theories of galaxy formation;

3.) From the practical point of view, the statistic should be well defined and should be easily applied.

Several statistical measures have been frequently used in the studies of the large scale structure of the Universe. They are:

1.) N-body correlation functions;

2.) Power spectrum analysis;

3.) Void probability functions;

4.) Minimal-spanning trees;

5.) Percolation analysis;

6.) Topological analysis.

Each method has its pros and cons, and they are often used complementarily. In the following sections, I shall present the basic features of these methods, their main results (observational and theoretical), their main successes and failures, etc. Since the power spectrum analysis is being used more and more frequently but the method itself has not been examined very carefully in literature, a rather detailed account of the method is given in §11.2.

3.1 Correlation function analysis

Correlation function analysis is still the most important statistical tool in the LSS studies. A full account of N-body correlation functions can be found in the excellent book by Peebles (1980). Here we shall only summarize up the basic points, which will be referred to in the following chapters. Main results regarding galaxy clustering will be presented in the next section.

3.1.1 Two-point spatial correlation function

The two-point correlation function is defined by writing the joint probability, d^2P, of finding each object in two volume elements dV_1 at $\vec{r_1}$ and dV_2 at $\vec{r_2}$ as:

$$d^2P = n(\vec{r_1})n(\vec{r_2})[1+\xi(\vec{r_1},\vec{r_2})]dV_1dV_2, \tag{3.1.1}$$

where $\xi(\vec{r_1},\vec{r_2})$ is the two-point correlation function, and $n(\vec{r})$ is the *expected* number density at position $\vec{r}$. In the LSS studies, the cosmological principle tells us that $\xi(\vec{r_1},\vec{r_2})$ is only a function of the pair separation $r_{12} = \mid \vec{r_1} - \vec{r_2} \mid$, i.e., $\xi(\vec{r_1},\vec{r_2}) = \xi(r_{12})$ (however, cf. Pietronero 1987).

Now let $DD(r)$ be the pairs of objects within the separation range $r \sim r + \Delta r$ in the observed sample, and $RR(r)$ the corresponding pairs in a random sample which has the same boundaries and selection effects as the real sample. By integrating Eq.(3.1.1), we can easily find

$$\xi(r) = \frac{DD(r)}{RR(r)} - 1. \tag{3.1.2}$$

The meaning of $\xi(r)$, clearly shown by Eq.(3.1.2), is the excess of pairs of objects, relative to the random distribution, therefore its value reflects the degree of clustering at scale r.

Eq.(3.1.2) also provides us with the base of estimating $\xi(r)$. We construct a large set of random samples, or equivalently one random sample of much higher density. The random sample should have the same boundaries and the same observational selection effects (e.g., magnitude- or diameter-limited; galactic extinction; variations in plate sensitivity, etc.) as the observed sample. Then we count pairs in a given separation range in both the observed sample and the random sample, and finally we can obtain $\xi(r)$ through Eq.(3.1.2).

3.1.2 Three-point spatial correlation function

In the same way as for $\xi(r)$, we can define the three-point correlation function. The joint probability, d^3P, of finding three objects concentrated in each of the three volume elements dV_1, dV_2 and dV_3, separated by r_{12}, r_{23} and r_{31} can be written as:

$$d^3P = n(\vec{r_1})n(\vec{r_2})n(\vec{r_3})[1+\xi(r_{12})+\xi(r_{23})+\xi(r_{31})+\zeta(r_{12},r_{23},r_{31})]dV_1dV_2dV_3, \tag{3.1.3}$$

where $\zeta(r_{12}, r_{23}, r_{31})$ is the three-point correlation function, and $n(\vec{r_i})$ the *expected* number density at position $\vec{r_i}$ of dV_i

Integrating equation (3.1.3), we can easily find,

$$\zeta(r_{12}, r_{23}, r_{31}) = \frac{DDD(r_{12}, r_{23}, r_{31})}{RRR(r_{12}, r_{23}, r_{31})} - 1 - \xi(r_{12}) - \xi(r_{23}) - \xi(r_{31}), \tag{3.1.4a}$$

or equivalently,

$$\zeta(r_{12}, r_{23}, r_{31}) = \frac{DDD(r_{12}, r_{23}, r_{31}) - DDR(r_{12}, r_{23}, r_{31})}{RRR(r_{12}, r_{23}, r_{31})} + 2, \tag{3.1.4b}$$

where $DDD(r_{12}, r_{23}, r_{31})$ is the count of triplets with shapes (r_{12}, r_{23}, r_{31}) in the observed sample, $RRR(r_{12}, r_{23}, r_{31})$ the *expected* count in a random sample, and $DDR(r_{12}, r_{23}, r_{31})$ the *expected* count of triplets formed by two real objects and one random point.

The direct estimations of ζ usually are based on the equations (3.1.4), through counting triplets DDD, DDR and RRR. If the two-point function can be determined quite accurately, it is wise to use Eq.(3.1.4a), since we can save a lot of computational time needed to obtain DDR. Otherwise Eq.(3.1.4b) should be used.

In analogy with the procedure of defining ζ, we can also define other higher-order (e.g., 4-body, 5-body, ...) correlation functions. Since the direct determination for extragalactic objects of the four-point or higher-point functions is rather uncertain at the present (see, e.g., Groth & Peebles 1977; Sharp et al. 1984), we will not go further. Instead we will discuss the transformation equation between angular and spatial correlation functions.

3.1.3 Limber's equation

Since most of the extragalactic-object catalogues give only positions on the sky and the completion of large redshift surveys (a few thousand for galaxies; a few hundred for clusters) usually takes several years even today, most of our knowledge about correlation functions is still based on two-dimensional samples. In this case, angular correlation functions are defined in exactly the same way as the spatial ones, and we shall not repeat them. One of the most remarkable features of the correlation analysis is that the spatial and angular correlation functions are related by the so-called 'Limber's equation'. From Limber's equation, we are able to extract information on the spatial functions, which reflect the real clustering properties, from the angular ones.

Usually the two-point and three-point angular functions are denoted by $\omega(\theta)$ and $z(\theta_{12},\theta_{23},\theta_{31})$. Assuming that the radial selection function is $\phi(r)$ and using the small angle approximation, the relation between $\omega(\theta)$ and $\xi(r)$ reads (Peebles 1980):

$$\omega(\theta)=\frac{\int_0^\infty \phi^2(r)r^4\,dr\int_{-\infty}^{\infty}\xi(\sqrt{u^2+r^2\theta^2})du}{[\int_0^\infty \phi^2(r)r^2\,dr]^2}. \tag{3.1.5}$$

For a special case where $\xi(r)$ is a power law, $\xi(r)=Br^{-\gamma}$, then Eq.(3.1.5) shows that $\omega(\theta)$ must also be a power law $\omega(\theta)=A\theta^{-\beta}$. Furthermore their slopes and amplitudes are connected by

$$\gamma=\beta+1, \tag{3.1.6a}$$

and

$$A=B\frac{\int_0^\infty \phi^2(r)r^{5-\gamma}dr}{[\int_0^\infty \phi^2(r)r^2\,dr]^2}\frac{\Gamma(1/2)\Gamma(\beta/2)}{\Gamma(1+\beta/2)}. \tag{3.1.6b}$$

The observational studies have shown that the two-point correlation functions of galaxies, groups and clusters closely obey the power law with $\gamma\approx 1.8$ (e.g., Davis & Peebles 1983, Groth & Peebles 1977 for galaxies; Jing & Zhang 1988 for groups; Bahcall & Soneira 1983 for rich clusters; more details in §3.2), therefore the simple relations (3.1.6) are very relevant to the LSS studies.

A general relation between $z(\theta_{12},\theta_{23},\theta_{31})$ and $\zeta(r_{12},r_{23},r_{31})$ can also be easily derived. Instead of presenting this general relation, we now consider a special case where $\zeta(r_{12},r_{23},r_{31})$ is of the hierarchical form, i.e.,

$$\zeta(r_{12},r_{23},r_{31})=Q[\xi(r_{12})\xi(r_{23})+\xi(r_{23})\xi(r_{31})+\xi(r_{31})\xi(r_{12})]. \tag{3.1.7}$$

In the power law model of ξ, the transformation predicts that $z(\theta_{12},\theta_{23},\theta_{31})$ must also be a hierarchical form

$$z(\theta_{12},\theta_{23},\theta_{31})=q[\omega(\theta_{12})\omega(\theta_{23})+\omega(\theta_{23})\omega(\theta_{31})+\omega(\theta_{31})\omega(\theta_{12})]. \tag{3.1.8}$$

Furthermore, Q and q are simply related by

$$\frac{q}{Q}=\frac{(\int_0^\infty r^{8-2\gamma}\phi(r)^3dr)(\int_0^\infty r^2\phi(r)dr)}{(\int_0^\infty r^{5-\gamma}\phi(r)^2dr)^2}. \tag{3.1.9}$$

Interestingly, this model agrees well with the observations of galaxies and clusters in great detail (e.g., Groth & Peebles 1977, Efstathiou & Jedrzejewski 1984 for galaxies; Jing & Zhang 1989, Tóth et al. 1989 for clusters; more details in §3.2)

Several important points must be pointed out here. 1). The Limber equations are the projection of the spatial functions to the angular ones. To acquire the spatial functions, some specific models [e.g., Eq.(3.1.6) & Eq.(3.1.7)] have to be assumed in advance and be tested later by two- and three-dimensional data. The inversions of the Limber equations, of course, can overcome this limitation. However, as shown by Fall & Tremaine (1977) and Parry (1977) for the two-point correlation function, such an inversion is complicated and is unstable against statistical fluctuations. For higher order correlations, the inversions would become even more complicated and unstable, unless some specific forms, such as power laws, are assumed (Tóth et al. 1989). 2). All the above discussions assume a Euclidean space, which is valid for samples of redshift much less than 0.1. For deep samples, the effects of space curvature must be considered in the Limber equations. A full treatment of the relativistic effects has been given in Peebles (1980). 3). The value B is quite sensitive to the sample depth, to the shape of the selection function, and to the relativistic corrections, while the ratio q/Q is independent of the sample depth and insensitive to the selection function and the relativistic corrections. 4). The selection function is usually obtained from the luminosity or diameter functions of galaxies, or from the space density of objects.

3.1.4 The scaling relation

Another striking property of the correlation functions is the so-called 'scaling relation'. If the characteristic sample depth is D, in the small angle approximation, we have the following scaling (Peebles 1980):

$$\omega(\theta) = D^{-1} W(\theta D), \tag{3.1.10a}$$

The relation (3.1.10a) can be understood as follows. The correlation function $\omega(\theta)$ measures the ratio of the number of neighbors in excess of random to the number expected for a uniform distribution. If one counts neighbors in solid angle $\delta\Omega \propto D^{-2}$ at angular distance $\theta \propto D^{-1}$ from a galaxy at distance D from the observer, one is looking at a fixed projected area at the galaxy and a fixed projected distance from the galaxy, so the number of correlated neighbors seen is independent of D while the number of accidental neighbors from the foreground and background is proportional to D. Thus $\omega \propto D^{-1}$ at fixed θD.

The function $W(\theta D)$ depends both on the spatial correlation function and on the shape of the selection function. For each kind of catalogue (e.g., magnitude-limited catalogue, diameter-limited catalogue), the shape of the selection function is fixed. So for two samples of depths D_1 and D_2, their angular correlation functions $\omega_1(\theta)$ and $\omega_2(\theta)$ are related by

$$\omega_1(\theta) = \frac{D_2}{D_1}\omega_2(\theta\frac{D_1}{D_2}). \tag{3.1.10b}$$

If the two-point function $\omega(\theta)$ is a power law $\omega(\theta) = A\theta^{-\beta}$, as observed for galaxies and clusters, we can easily find:

$$A \propto D^{-(1+\beta)}. \tag{3.1.10c}$$

Equations (3.1.10) are frequently used to test the reality of detected ω signals (see, Peebles 1980; Bahcall 1988a) and to test the volume dependence or the fractal property (Einasto et al. 1986) of galaxy clustering (e.g., Peebles 1980; Jing et al. 1991).

3.1.5 A brief outline of estimation techniques and error analysis

The techniques, employed for estimating correlation functions, can be divided roughly into two types: the *direct counting method* and the *moment method*.

The direct counting methods for estimating two- and three-point correlation functions have already been given in §3.1.1 and §3.1.2. There the description for the two-point function is almost complete. However, since ζ (or z) is a function of three variables r_{12}, r_{23}, r_{31} (or $\theta_{12}, \theta_{23}, \theta_{31}$), its functional form has a less obvious interpretation than that for ξ (or ω). The general method to study the dependence of $\zeta(r_{12}, r_{23}, r_{31})$ on side length is described in Peebles & Groth (1975). However, if we want to test models of ζ or/and to find out some parameters, the least-square fitting to the triplets count is more suitable (e.g., Tóth et al. 1989; Jing et al. 1991). More details of these two methods will be presented along with our original work in the following chapters.

Since the $(n-1)$-moments of the neighbor counts are related to the integrals of correlation functions up to n-points (e.g., Peebles 1980; Appendix), we are certainly able to get correlation functions from the moments (see, e.g., Peebles 1975; Peebles 1980; Sharp et al. 1984). The main advantage of this method is that it can save a lot of computational time in estimating high-order correlation functions. The disadvantages are 1.) the functional forms for correlation functions have to be first assumed and then checked; 2.) unless only a single large shell is taken (but in this case, the assumed model can not be checked), it looses a lot of information on configurations, based on which correlation functions are extracted. The first point is rather obvious. To illustrate the second point, we take an example of the three-point function and of the second moments estimated in thin shells. The information of the three-point function is, of course, contained in *all possible triplets*, however the second moment only explores the *triplets with roughly two equal sides* (the shell radius).

Therefore, in my opinion, the direct counting method is favored to study samples of moderate size (without any requirement on *a priori* knowledge of correlations), while the moment method is suitable to study the samples of very large size (e.g., numerical simulations) with (or to test) *a priori* knowledge of correlations. If the functional form of the high-order correlation function is already known, the moment method would be effective to estimate the coefficients by taking large shells even for small samples.

The errors, in the correlation analysis, can be divided roughly into two types: systematic errors (e.g., systematic variations in plates sensitivity; a sample biased due to the dominance of a supercluster or a void) and statistical fluctuations. The former type of errors is rather difficult to estimate if we only have one sample. The error estimates mentioned in the literature are usually meant to estimate the later type of error. This was generally thought (but not proved) to be well estimated by the bootstrap resampling technique (hereafter, BRT) (Barrow et al. 1984; Ling et al. 1986). In the BRT approach, the error is given by the standard variation of a large set of pseudo-samples, each of which is produced by randomly choosing N points, with replacement, from the original sample of N points. In our recent paper (Mo, Jing, & Börner 1992), we have extensively studied the problem of how the BRT errors and the Poissonian errors are related to the ensemble errors in the correlation analysis. There we give analytical formulae for these errors in the two- and three-point correlation functions ξ and ζ. The ensemble errors of pair count $DD(r)$ and triplet count $DDD(r,u,v)$

are well approximated by $\sigma_{DD}(ens) = [\langle DD(r)\rangle + 4\langle DD(r)\rangle^2/N_g]^{1/2}$ and $\sigma_{DDD}(ens) = [\langle DDD(r,u,v)\rangle + 36\langle DDD(r,u,v)\rangle^2/N_g]^{1/2}$ (where N_g is the number of points in the sample; $\langle\cdots\rangle$ denotes ensemble mean), respectively. The bootstrap-resampling errors of $DD(r)$ and $DDD(r,u,v)$ can be approximated by $\sigma_{DD}(bo) = [3DD(r) + 4DD^2(r)/N_g]^{1/2}$ and $\sigma_{DDD}(bo) = [7DDD(r,u,v) + 36DDD^2(r,u,v)/N_g]^{1/2}$, respectively. These results are confirmed by our simulation test. We also discuss the fit errors of the parameters (i.e., the amplitude A of ξ and the Q-constant of ζ) in the regression models. The interdependence among the counts in different bins reduces the fit errors. If we adopt the ensemble errors [$\sigma_{DD}(ens)$ and $\sigma_{DDD}(ens)$] for the counts, the fit errors of A and Q in each sample are about half of the standard errors obtained from the ensemble of simulation samples. The underestimation of the fit errors due to the bin-bin interdependence is compensated by the overestimation of σ_{DD} and σ_{DDD} given by the BRT method. The fit errors of the parameters, given by the bootstrap-resampling errors for the counts, give the correct answers. A detailed account of the work will be presented in Chapter 4.

3.1.6 A summary of the main features of correlation functions

Correlation functions are still the most major measure of large-scale clustering in the Universe. In respect to other clustering measures, correlation analysis has its own advantages and disadvantages.

As has been seen above, the correlation functions can be easily defined, without any ambiguity. Their meaning, as clustering measures, is obvious, and the clustering strength and coherence length can be easily quantified. It is rather convenient to apply this measure to both 3-D samples as well as 2-D samples. The angular correlation functions can be related to the spatial ones through the Limber equations. And the scaling relations of angular functions at different depths are a convenient test of the clustering reality and universality. At least two- and three-point functions of galaxies and clusters obey the simple power-law and hierarchical forms. These functions, regarding different 2-D and 3-D samples, have good reproducibility.

The correlation functions are simple to analyze in theoretical studies, and are sensitive (at least in principle) to the model details. The two-point correlation function is the inverse

Fourier transformation of the *density power spectrum*. Different models of galaxy formation have different power spectra, which are even more distinguishable in the linear regime (i.e., $\xi(r) \ll 1$). Furthermore, the models with Gaussian fluctuations predict a vanishing three-point function in the linear regime. The particular form of three-point function is predicted at the high biasing level for the models of Gaussian and non-Gaussian fluctuations.

Though correlation functions only measure the spatial patterns of galaxy distributions, they can be easily related to the dynamics on the large scale through the BBGKY hierarchy. Very useful equations have been derived, such as the Cosmic Energy Equation and the Cosmic Virial Theorem, which are important in understanding the origins and evolution of LSS. These equations are also the important sources from which the density parameter Ω of the Universe can be estimated.

In comparison with the above advantages, the disadvantages are minimal but not negligible. Because the mean number densities of galaxies and clusters have not yet been determined accurately (e.g., de Lapparent et al. 1988), it is difficult to measure the $\xi(r)$ where $\xi(r) < 1$. The power spectrum analysis would be more powerful to probe the clustering in the linear regime (cf. §11.2). In principle, a full statistical description of a spatial point distribution needs the knowledge of *all* n-point correlation functions. In contrast, our present determination of even the 4-point function for galaxies and clusters is still rather uncertain. Furthermore, the low-order (2- and 3-point) correlation functions probably are not sensitive to the presence or absence of filamentary, bubble-like, sponge-like structures etc. Therefore, correlation analysis, in practice, may be unable to tell us anything about the topology and geometry of the distributions. With respect to high-order clustering, other measures (§3.3 – 3.4) may be more sensitive than the correlation functions.

3.2 The results of correlation analysis and confrontations with theories

In this section I shall summarize the results obtained from the correlation analysis, and outline how to use these results to constrain the current theories.

3.2.1 Two- and three-point correlation functions of galaxies

The two-point angular correlation function of galaxies at the small angular scale is well represented by a power law,

$$\omega(\theta) = A\theta^{-\beta}, \qquad \beta \approx 0.77. \tag{3.2.1}$$

The first reliable determinations of this relation were from the statistical studies of Peebles and his coworkers on the Lick and Zwicky catalogues (Groth & Peebles 1977; references therein). These two samples are magnitude limited and are in the northern hemisphere. Our recent study of the ESO/Uppsala catalogue confirms the result in the southern diameter-limited galaxy sample (Jing et al. 1991). The conversion of Eq.(3.2.1) to the spatial correlation function, through the Limber equation, yields,

$$\xi(r) = (r_0/r)^{\gamma}, \qquad \gamma = 1 + \beta \approx 1.77 \tag{3.2.2}$$

with $r_0 \approx 5\,h^{-1}$Mpc for $r \leq 10\,h^{-1}$Mpc (Groth & Peebles 1977; Jing et al. 1991). This estimate is roughly consistent with the results based on redshift surveys (Davis & Peebles 1983; Bean et al. 1983; Davis et al. 1988; cf. de Lapparent et al. 1988).

Now a new generation of large, uniform and machine-scanned catalogues of galaxies is emerging (Maddox et al. 1990b; Collins et al. 1989; Picard 1991). These catalogues are better defined and are less subject to artificial biases than the previous 'eye' selected catalogues. Maddox et al. (1990a) measured $\omega(\theta)$ for the APM catalogue, confirming the power-law (3.2.1) at the small scales as well as the break from the power-law at roughly the same physical separation as found previously. However, their $\omega(\theta)$ declines more gently from the power law on larger scales and they argue that Groth & Peebles (1977) may have removed some intrinsic clustering when correcting for large-scale gradients in the Lick counts (see also Plionis 1988; Brown & Groth 1989). Their results are plotted in Figure 3.3. The analyses of the COSMOS (Collins et al. 1992) and the POSS II (Picard 1991) surveys essentially confirm the large-scale power found in the APM survey, with a possible indication that there is even more large scale clustering than found by Maddox et al. (1990a).

To study $\xi(r)$ in theories at the range of $r \leq 10\,h^{-1}$Mpc, N-body simulations are needed in order to follow the nonlinear evolution of density perturbations. Though the

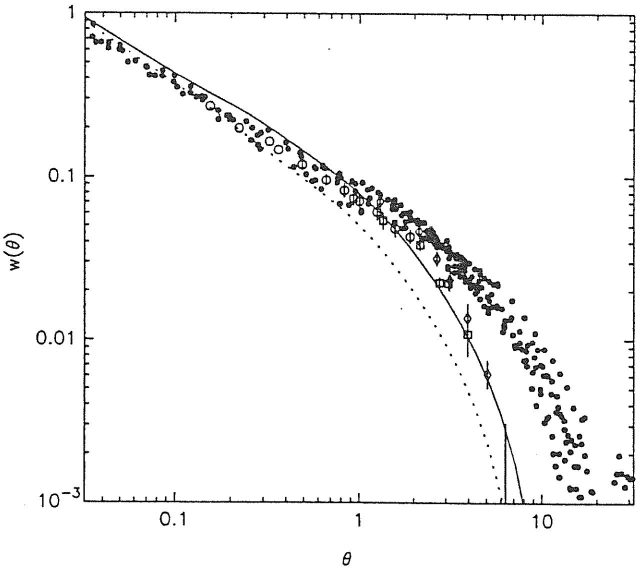

Figure 3.3 — The filled circles show the estimates of $\omega(\theta)$ of Maddox et al. (1990a) scaled to the Lick depth. The open symbols show $\omega(\theta)$ for the Lick catalogue from Groth & Peebles (1977). The dotted and solid lines show computations of $\omega(\theta)$ based on the CDM model with $h = 0.5$ and $h = 0.4$. Taken from Maddox et al. (1990a).

power law form of $\xi(r)$ with the observed slope and amplitude is not a trivial prediction in the theories of galaxy formation, most current attractive scenarios reproduce this form without difficulty at a certain epoch of evolution. So the power law is not a good discriminant between theories. Instead it is usually used to identify the present time in the simulations. The models could be further tested by other statistical measures.

The function $\xi(r)$ at large scales (i.e., where $\xi(r) \ll 1$) is related, by linear perturbation theory, to the primordial fluctuation power spectrum. The new features revealed by Maddox et al. (1990a) on large angular scales, are important for testing theories of the formation of large-scale structures. In particular, comparing with the $\omega(\theta)$ predicted by the N-body simulations of the 'standard' biased CDM models (White et al. 1987b), Maddox et al. (1990a) conclude that the CDM models have insufficient large scale power (Figure 3.3).

Efstathiou et al. (1990) performed estimates, for the QDQT redshift survey of IRAS galaxies, of the variance σ^2 which is related to $\xi(r)$ according to

$$\sigma^2(l) = 1/V^2 \int_{V=l^3} \xi(r_{12}) dV_1 dV_2.$$

Their results are plotted in Figure 3.4. The strong non-zero σ^2 at $l = 30, 40\, h^{-1}$Mpc provides us with further evidence for structures on these scales. They also estimated σ^2 in the CDM models of White et al. (1987b), which are given in Figure 3.4 too. Clearly, there is more large-scale power in the galaxy distribution than in the models. The variances obtained by the Gaussian window smoothing for the same catalogue give essentially the same results (Saunders et al. 1991).

Maddox et al. (1990a) and Efstathiou et al. (1990) tested the CDM models by comparing the observations with the N-body simulations. In fact, such tests can be done analytically, since linear perturbation theory is valid in these regimes. Using the same power spectrum as in White et al. (1987b), I calculated $\omega(\theta)$ and σ^2 in the CDM model, which are given in Figure 3.5 and Figure 3.4. The analytical results repeat the simulation results with high precision, indicating these observations are good probes to the primordial power spectrum.

Now we turn to the three-point function of galaxies. Based on the Lick and Zwicky catalogues, Groth & Peebles (1977) found that the galaxy angular three-point correlation function is well approximated by Eq.(3.1.8) with $q \approx 1.7$ at the physical scale $r \leq 10\ h^{-1}$Mpc. Thus the spatial three-point function must be represented by the Eq.(3.1.7), and $Q \approx 1.3$ from the Limber equation (3.1.9). The later studies based on redshift samples (Peebles 1981; Efstathiou & Jedrzejewski 1984) and on the ESO-Uppsala catalogue (Jing et al. 1991; see Chapter 5) result in a smaller $Q \approx 0.8$, probably due to the lack of prominent rich clusters in these samples.

The three-point correlation function is an independent probe to the origin of LSS. N-body simulations show a strongly scale-dependent Q in hot dark matter models (Fry & Melott 1985), a much weaker dependence in unbiased CDM models (Davis et al. 1985; Fry & Melott 1985), and an essentially constant $Q \approx 1$ in the biased CDM models (Davis et al. 1985; Melott & Fry 1986). The recent study of Valdarnini & Borgani (1991), using several typical power spectra, also shows that the Q-test is sensitive to both the power

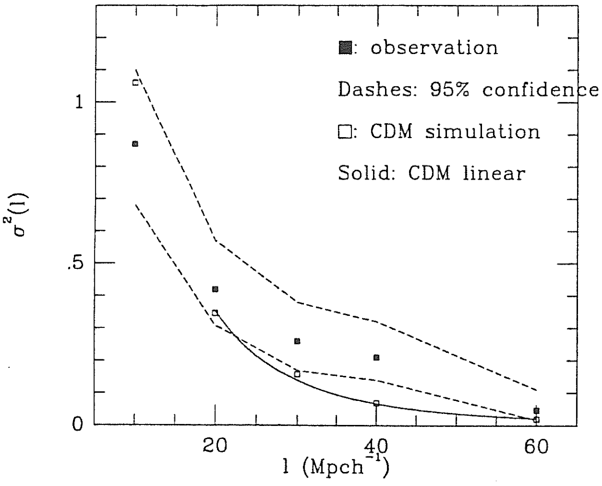

Figure 3.4 — The variances $\sigma^2(l)$ in the cubic volumes of size l. The filled squares are the results for the IRAS distribution, and the dashed lines represent the 95% confidence level. The empty squares are for the CDM simulations. All these data are taken from Efstathiou et al. (1990). The solid line represents the prediction by the author based on the linear perturbation theory.

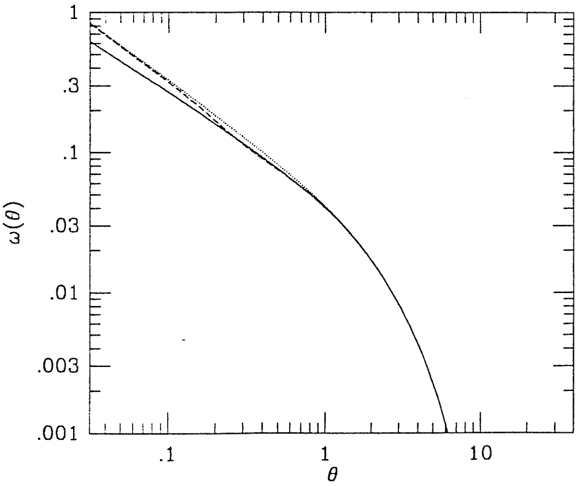

Figure 3.5 — The predicted $\omega(\theta)$ for the Lick catalogue in the CDM model with $h = 0.5$ based on the linear perturbation theory. The different lines correspond to different extrapolations of $\xi(r)$ at the small scales. The results are consistent with Maddox et al. (1990a) which used N-body simulations.

spectra and the biasing prescription. However, the apparent difference of Q between 3-D and 2-D observational samples reminds us to be cautious in such tests.

3.2.2 The scaling test and the volume dependence of the correlation length

The scaling (3.1.10) of $\omega(\theta)$ with the sample depth is important as a test for possible systematic errors in the data (which would lead to spurious clustering) and for the limited sample sizes. Groth & Peebles (1977) discussed the scaling relation for the Zwicky, Lick and Jagellonian catalogs, and found that the scaling is valid within a precision of 20% in amplitude. This uncertainty is expected because of the errors due to the luminosity function and sampling fluctuations. Recent estimates based on deep surveys, such as the APM and COSMOS surveys (e.g., Maddox et al. 1990a&b; Collins et al. 1992), support the validity of the scaling. All this indicates the conventional value $r_0 \approx 5\,h^{-1}$Mpc of the correlation length derived by Peebles and coworkers in the 1970s is reliable and samples with size such as that of the Zwicky and Jagellonian catalogs are fair for the two-point correlation analysis. Furthermore, systematic errors in the Zwicky, Lick and Jagellonian catalogs are not important for two-point correlation analysis at least on small scales (where $\xi(r) \geq 1$).

Einasto et al. (1986) claimed that the correlation length in the CfA redshift survey increases proportionally with the sample size, and that the effect is not a function of the intrinsic luminosity of galaxies (cf. §3.2.3). They argue rather that the available samples are far from being a fair sample of the universe. They estimate $r_0 = 10\,h^{-1}$Mpc for the true correlation length and a fair sample is reached if the CfA sample enlarges two times in the depth. Their results are an indication that galaxies are distributed in a fractal distribution possibly extending to $\sim 100\,h^{-1}$Mpc (Calzetti et al. 1988; Einasto et al. 1986; Pietronero 1987). However, the scaling tests of Groth & Peebles (1977) clearly oppose this idea.

The later detailed analyses of the nearby redshift samples (Davis et al. 1988; Börner & Mo 1990) point out that the effect found by Einasto et al. (1986) in fact is a combination of the sample-size dependence and the luminosity segregation (cf. §3.2.3). They estimate that in the skies surveyed by the CfA and SSRS, the increase of r_0 with the sample depth is significant only within the local region of depth less than $30\,h^{-1}$Mpc. Moreover, Davis et al. (1988) found no such effect in the all-sky survey of IRAS galaxies. Thus, these results argue against the existence of $\sim 100\,h^{-1}$Mpc fractal distributions in the Universe.

The effect on r_0 of the sample-size can also be studied by the scaling test of $\omega(\theta)$ in 2-D shallow catalogues. Since the samples of different depths are apparent diameter- or magnitude-limited, each sample has the same fraction of intrinsic bright and faint galaxies. Therefore, the luminosity segregation effect would not enter into such a study and the sample-size effect is isolated, in contrast with the analyses of 3-D samples. But the broad distribution of galaxies in the radial direction makes us able only to give a typical size where the sample-size effect could be effective.

Such a test has been done in our recent paper (Jing et al. 1991). We selected samples with different limiting diameters from the southern ESO/Uppsala catalog. Our scaling test gives $r_0 = 5\,h^{-1}$Mpc as the correlation length of galaxies, consistent with most previous analyses of the northern samples. Furthermore, we did find a smaller r_0 for samples with depth less than $30\,h^{-1}$Mpc, giving support to the results of Davis et al. (1988) and Börner & Mo (1990).

3.2.3 Luminosity and morphology segregation, and biasing

Some theories of biased galaxy formation (e.g., Dekel & Silk 1986; White et al. 1987) predicted that the more luminous the galaxies, the more clustered they are, and that dwarf galaxies are even more uniformly distributed than normal ones and that they fill the regions devoided of bright galaxies. Many authors have studied the problem observationally but with contradictory conclusions. Bothum et al. (1986), Thuan et al. (1987), Eder et al. (1989), Binggeli et al. (1990), and Thuan et al. (1991) found that there is no significant difference between the dwarf-LSB (Low Surface Brightness) and the bright galaxy distributions, while Davis & Djogovski (1985), Giovanelli et al. (1986), Xia et al. (1986), Börner, Mo & Zhou (1989), Börner & Mo (1989a), Salzer et al. (1990) and Santiago & da Costa (1990) found that dwarf-LSB galaxies are less clustered than the large HSB (High Surface Brightness) galaxies. Another set of studies based on the CfA and SSRS samples concluded that there is a tendency of increasing correlation length with luminosity in the subsamples of high brightness ($\geq$ the characteristic brightness L_*)

(Davis et al. 1988; Börner & Mo 1990), but this tendency is not significant in subsamples of lower brightness. The results are not conclusive because most of these studies suffer from various deficiencies. The sample used by Thuan et al. (1991) is the most complete, best-defined and largest one in these studies. If we make a judgement based on the quality of the samples, we would like to conclude that galaxies of different luminosities (including dwarfs) have the same degree of clustering except that very bright galaxies (brighter than L_*) are more clustered.

It has been known for a long time that early-type galaxies preferentially locate in rich dense regions and late-type ones in fields (i.e., the morphology segregation). The first statistical study of this effect was made by Davis & Geller (1976) based on the 2-D magnitude-limited ($14.5 m_B$) sample from the UGC. They found that early type galaxies are more clustered than late types. The two-point correlation function is well approximated by a power law for each type, but the slopes are steepened from late to early types. These results are confirmed by Giovanelli et al. (1986) in their study of the 2-D galaxy distribution in the Perseus-Pisces region. We made an independent test of this effect in the southern sky, using diameter-limited samples from the ESO/Uppsala catalogue (Jing et al. 1991). Our results support that late type galaxies are distributed more randomly, but show a weak dependence of the slope of $\xi(r)$ on morphology types. The studies of Börner & Mo 1990 and Santiago & da Costa (1990), using the CfA and SSRS redshift samples, reached the same conclusion as ours.

We are the first to study the morphology dependence of the three-point function (Jing et al. 1991). We found that the hierarchical form (3.1.8) is a good approximation for each morphology type. The constants Q of the early types (E/SO) and of the late types (Sbc and later) are roughly the same as that of the galaxies without morphology classification. However that of the early spirals (Sa, Sab, Sb) is much smaller. Redshift samples and larger 2-D samples are needed to clarify this effect.

All these observational results would be important inputs to the biasing mechanisms of galaxy formation. The results of Thuan et al. (1991) that the dwarfs/LSBs are good tracers of galaxy distribution, rule out a certain class of biased galaxy formation theories which predict a uniform spatial distribution of the dwarfs/LSBs. The observed morphology

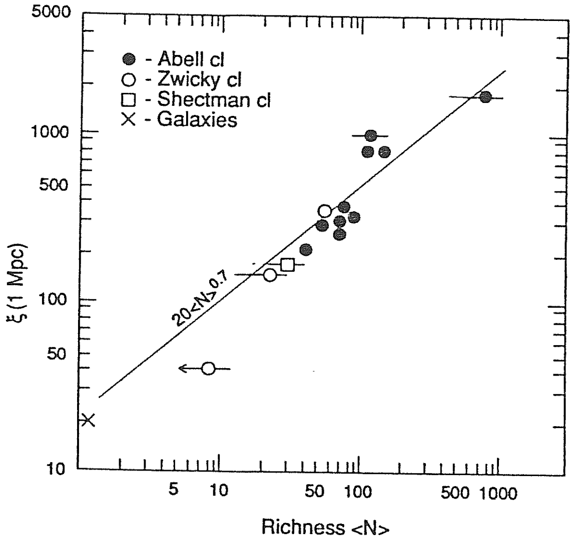

Figure 3.6 — The richness dependence of the amplitude. Taken from Bahcall (1988a).

segregation and luminosity segregation at high luminosity, both at the large scales $r \approx 5$ to $10\,h^{-1}$Mpc, provide valuable evidence for biased galaxy formation. Since only 'crude' theories of biasing mechanisms are available, it is premature to link these results to any specific theories.

3.2.4 Correlation functions of rich clusters and groups

Among the many others (see references in Bahcall 1988a), Bahcall & Soneira (1983) analysed both the angular and the spatial two-point correlation functions for the clusters of the Abell (1958) catalog. The $\xi(r)$ of the $R \geq 1$ clusters turned out to be $\xi_{R\geq 1} = (25/r)^{1.8}$ for $r \leq 100\,h^{-1}$Mpc. Moreover, the two-point function of clusters of different richness is of the power-law form $\xi(r) = (r_0/r)^\gamma$ with the same slope $\gamma = 1.8$ but with increasing amplitude r_0 with richness (Figure 3.6). These results have been confirmed by numerous other studies based on independent samples (e.g., Huchra et al. 1990b; Batuski & Burns 1985b; Kopylov et al. 1987; Postman et al. 1986; Shectman 1985; Gao & Jing, 1989; Batuski et al. 1989; Couchman et al. 1989; Plionis & Borgani 1992).

These statistical results have given important implications and constraints to theoretical models. The high amplitude of ξ_{cc} (relative to that of galaxies) and the richness dependence of r_0 indicate that the luminous systems in the Universe are not equivalent tracers of the structures. This feature, together with other observational facts (e.g., huge voids like Bootes; the density parameter Ω always ~ 0.2 found from the dynamical studies of galaxy distributions), led to the idea of biased galaxy formation (e.g., Kaiser 1984; Bardeen et al. 1986). The scale explored by ξ_{cc} is so large that ξ_{cc} is expected to reflect the primordial fluctuation spectrum. Its large amplitude as well as large coherence length are strong constraints on the flat models with primordial Gaussian fluctuations. In particular, the 'standard' CDM model fails to reproduce the observed ξ_{cc} (e.g., White et al. 1987b).

The crucial importance of the ξ_{cc} motivated people to check its reality carefully. Since the cluster catalogs, from which the above results are derived, are all compiled by 'eye' from the two-dimensional plates, some fraction of clusters could be the results of superposition of foreground and/or background galaxies. If the effect happens due to the chance superposition of 'field' galaxies (i.e., those not related with other rich clusters included), the resultant artificial clusters form a random component in the spatial distribution, which produces an unchanged or even a reduced ξ_{cc}. In contrast, if the effect is correlated with the positions of other rich clusters (i.e., the 'halo' galaxies of foreground or/and background clusters), an enhanced spurious clustering is produced with its manifestation in the line-of-sight direction. Since the observed ξ_{cc} is high, most of the present concern is on the later effect. It has been a matter of debate for several years whether the effect seriously enhances the ξ_{cc} (see §6.1 for a review). In our recent work (Jing, Plionis & Valdarnini 1992), we examined the effect very carefully in Abell cluster samples. We showed *no evidence* for significant enhancement of ξ_{cc} by the contamination effect, thus supporting that the ξ_{cc} detected by Bahcall & Soneira (1983) is due to the real clustering (see Chapter 6).

Cluster samples, identified by objective algorithms, have been recently constructed from the APM and COSMOS galaxy surveys (Dalton et al. 1992; Lumsden et al. 1992). The correlation analyses yield $\xi_{cc} = (r_0/r)^2$ with $r_0 = 12.9 \pm 1.4\,h^{-1}$Mpc in the APM sample (Dalton et al. 1992) and with $r_0 = 16 \pm 4\,h^{-1}$Mpc in the COSMOS sample (Nichol et al. 1992). The similar power-law form to that of Abell clusters is very encouraging. The derived correlation lengths seem a bit small. Since these clusters are much poorer than Abell clusters, these r_0 values in fact agree with the clustering-richness relation (Bahcall & West 1992).

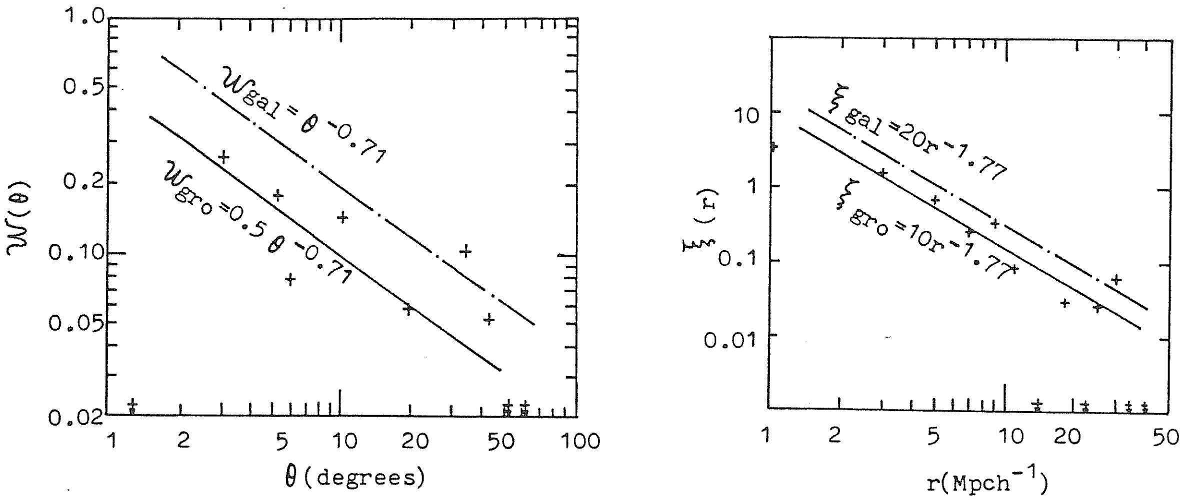

Figure 3.7 — The angular *a*) and spatial *b*) two-point correlation functions of CfA groups. The crosses are the statistical results, and the solid lines are the approximate fits to the data. The dot-dashed lines are the galaxy correlation functions: *a*) $\omega(\theta)$ of the $14.5m_B$ UGC catalogue; and *b*) $\xi(r)$ of the CfA survey (From Jing & Zhang 1988).

Several authors have studied the group-group correlation function ξ_{groups} for those available catalogs of groups. Jing & Zhang (1988) first analysed both the angular and the spatial two-point correlation functions for the CfA groups (Geller & Huchra 1983). We found that the ξ_{groups} can be approximated by $\xi_{groups} = Ar^{-1.8}$, with $A \approx 10(h^{-1}\mathrm{Mpc})^{1.8}$ about half of the amplitude of galaxies, thus groups are more uniformly distributed in space than galaxies. These results have been confirmed by Maia & da Costa (1990) based on an independent group catalog selected from the SSRS survey (Maia et al. 1989). The analysis by Ramella et al. (1990) of their independent group sample selected from the CfA slice survey (Ramella et al. 1989), however found a larger amplitude which is as large as that of galaxies within the errors. The discrepancy between the last and the former two studies has not been well understood. One possible cause is suspected to be the different density thresholds $\delta\rho/\rho$ used in forming these catalogues: in the first two catalogues, $\delta\rho/\rho = 20$; in the last catalog, $\delta\rho/\rho = 80$.

The ξ_{groups} could be a powerful test of the theories. In the hierarchical gravitational theory, Kashlinsky (1987) predicts that poor groups (with turnaround mass less than

$10^{14}M_\odot$) are less clustered than galaxies. The above results appear to support his model. However, I noted that the criteria of defining groups are different between the observations and the theory, so we must be cautious in such a detailed comparison. More important perhaps are that we have reached the capability of simulating a galaxy sample as large as the CfA and SSRS surveys using the N-body techniques and that exactly the same group-finding algorithms can be applied to both simulations and observations. Thus a proper evaluation of models can be made based on group properties. The recent simulation study of Gaussian and non-Gaussian CDM models by Matarrese et al. (1991), shows that the ξ_{groups} is a sensitive discriminant of the models. However their selection criteria of groups, although similar to, are not the same as the previous studies of the observations.

The angular three-point correlation function of Abell clusters was first analysed by Jing & Zhang (1989) and independently by Tóth et al. (1989). Both studies yield a consistent result that rich clusters of galaxies, just like galaxies, obey the hierarchical form (3.1.7) with $Q \approx 0.8$. Furthermore, after analysing clusters of richness $R \geq 2$, Jing & Zhang (1989) pointed out the hierarchical form is independent of cluster richness. These results have been further confirmed by the later analyses based on redshift complete, albeit small, samples of Abell clusters (Jing & Valdarnini 1991; Gott et al. 1991). A detailed presentation of our analyses will be given in Chapter 7.

A definite form has been predicted for ζ_{ccc} (e.g., Politzer & Wise 1984; Szalay 1988; Matarrese et al. 1986), if rich clusters form at high density peaks as guided by ξ_{cc} (Kaiser 1984). In the high peak approximation, Matarrese et al. (1986) showed

$$\begin{aligned}\zeta_{ccc}(1,2,3) = F(1,2,3) \times \{[\xi_{cc}(1,2)\xi_{cc}(2,3) + ...(3\text{ terms})] + \xi(1,2)\xi(2,3)\xi(3,1)\} \\ + [1 - F(1,2,3)] \times \{1 + [\xi(1,2) + ...(3\text{terms})]\},\end{aligned} \tag{3.2.3}$$

where $F(1,2,3)$ depends on the fluctuation type. If the fluctuation is Gaussian, $F(1,2,3)$ is 1. The same factor $F(1,2,3)$ before the quadratic and cubic terms of ξ seems contradictory with the observations (Tóth et al. 1989). The analytical modeling might be too simple. The recent N-body simulation of the 'standard' CDM model (Gott et al. 1991) showed a surprising result: the clusters (high peaks) in the simulations do obey the hierarchical form. The discrepancy has not been well understood, though Gott et al. (1991) tried to interpret the hierarchical form as the result of dynamical merges. Since their simulated sample of clusters is small and only one particular simulation (in fact they have done three) is analysed, in my opinion, further work both on analytical modeling and on simulations are needed to clarify this discrepancy.

In my recent papers (Jing 1990a & 1991), I explored the ξ_{ccc} in another distinct model of non-Gaussian fluctuation — the explosion scenario (e.g., Weinberg et al. 1989). In this model, clusters form at the intersections of the bubbles. I found that the hierarchical form holds for the simulated clusters with a similar Q to the observations, and the result is quite robust with respect to the model details (Chapter 8).

3.3 Void probability function

3.3.1 The general relation with N-point correlation functions

It was first shown by White (1979) that the probability that a given size and shaped volume V placed randomly in space be empty of objects is given by a sum over the correlation functions to all orders,

$$P_0 = \exp\big[\sum_{N=1}^{\infty} \frac{(-1)^N}{N} \overline{n}^N \int_V d^3\vec{x}_1 ... d^3\vec{x}_N \kappa_N(\vec{x}_1, ..., \vec{x}_N)\big], \tag{3.3.1}$$

where $\overline{n}$ is the average number density; $\kappa_N(\vec{x}_1, ..., \vec{x}_N)$ are the irreducible N-point correlations of the objects. The equation can also be applied to two dimensional samples, if we replace $\overline{n}$, $\kappa_N(\vec{x}_1, ..., \vec{x}_N)$ and V respectively by the surface number density, the N-point angular correlations and the surface area. Obviously, the measure is related to all N-point correlation functions.

3.3.2 A scaling property in the hierarchical distribution

In the hierarchical model, the irreducible N-point function $\kappa_N(\vec{x}_1, ..., \vec{x}_N)$ is given by a symmetrized sum of connected products of $N-1$ two-point functions ξ, conveniently associated with tree graphs of N points (e.g., Schaeffer 1984, Fry et al. 1989),

$$\kappa_N(\vec{x}_1, ..., \vec{x}_N) = \sum_{(i=\text{all trees})} Q_N(i)\xi(r_1)...\xi(r_{N-1}), \tag{3.3.2}$$

where the product runs over the $N-1$ limbs connecting the N-points of the tree and the sum over all N^{N-2} distinct labeled trees. The current available statistical studies of low order correlation functions of both galaxies and clusters (§3.2), support that the model works in the Universe. It was also expected that the model might be valid in some theories under certain approximations (for details, see, e.g., Fry et al. 1989).

As shown first by White (1979) and later by many others (e.g., Sharp 1981; Fry 1984; Schaeffer 1984), in the hierarchical distribution, the void probability obeys a scaling,

$$\Sigma \equiv \frac{\ln P_0}{\overline{n}V} = \Sigma(q), \tag{3.3.3}$$

where $q \equiv \overline{n}V\overline{\xi}$ and $\overline{\xi} \equiv 1/V^2 \int_V \xi(r_{12})dV_1dV_2$. This says that the function Σ depends on the $\overline{n}$, ξ and V only through the combination q (usually called the scaling variable). As in §3.1.3, it can be easily shown that the 2-D projection of a 3-D hierarchical distribution is still hierarchical, thus the scaling relation holds also for 2-D samples, though the functional form of $\Sigma(q)$ is different for 2-D and 3-D cases (depending on the radial selection function).

3.3.3 The scaling properties in galaxy distributions— a summary of observations

In the LSS studies, there are many ways to test the scaling relation, as indicated by Eq.(3.3.3) itself. For a 2-D sample, e.g., a magnitude-limited galaxy sample, we can study whether the scaling is established by using different shaped area (e.g., squares; circles), subsamples of different dilutions, and subsamples of different limiting magnitudes. The same method can also be applied to 3-D redshift samples. If the scaling does hold, Σ should only depend on the scaling variable q; otherwise Σ depends on the shape and the size of the volume (area) as well as on the number density.

The scaling property has now been examined for galaxies in great detail by a number of authors. Sharp (1981) first studied the scaling relation for the Zwicky catalogue of galaxies and found that the scaling is obeyed, so the data are consistent with a hierarchical distribution. The later analyses of the CfA redshift survey (Maurogordato & Lachiéze-Rey 1987; Mo & Börner 1990) and of the Giovanelli-Haynes redshift sample in the Pisces-Perseus region (Fry et al. 1989), using subsamples of different dilutions, confirmed the scaling found in 2-D studies. Furthermore, Maurogordato & Lachiéze-Rey (1987) and Fry

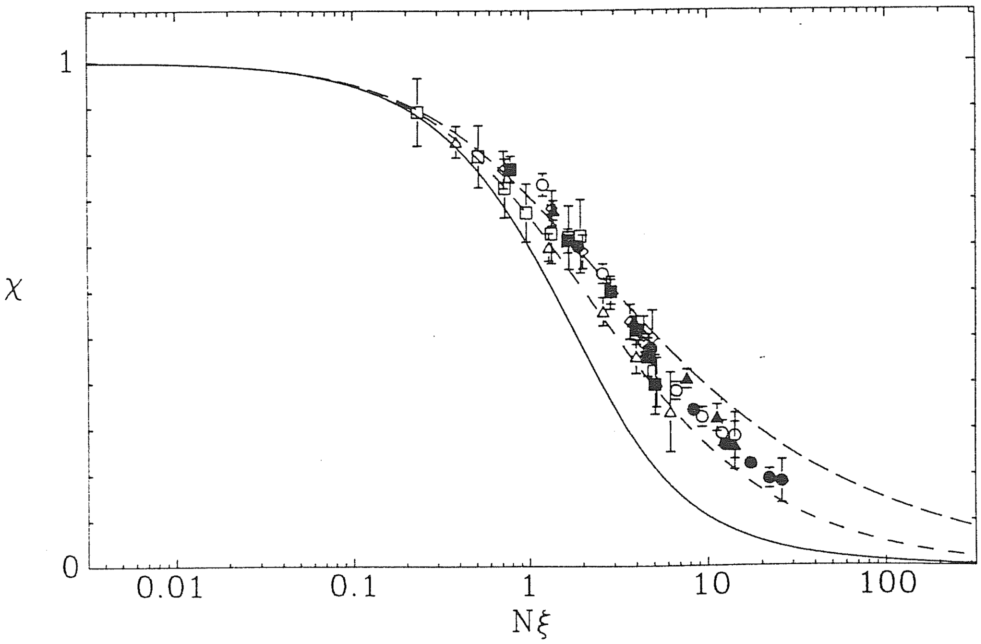

Figure 3.8 — The scaled void probability χ plotted against $\overline{N\xi}$ for the Perseus-Pisces catalog, showing the success of the scaling. The different symbols represent the subsamples of different luminosities and different dilutions. Taken from Fry et al. (1989).

et al. (1989) compared $\Sigma(q)$ for several samples of different luminosities, and found that $\Sigma(q)$ is independent of luminosity and is consistent with that of galaxies without luminosity division (see Figure 3.8). It was further found that the scaling relation is independent of galaxy morphology type (Mo & Börner 1990).

This universal scaling has two implications. First, for galaxies as a whole, their high-order correlation functions are consistent with the hierarchical model (3.3.2), though the values of $Q_N(i)$ (for $N \geq 4$) have not been fixed yet. Second, galaxies of different morphology types and luminosities obey the same hierarchical model (3.3.2). This further implies that $Q_N(i)$ (for $N \geq 3$) is independent of morphology type and of luminosity. Our direct analysis of the UGC and ESO/Uppsala catalogues (Jing et al. 1991) did show a weak dependence of $Q_N(i)$ ($N = 3$) on morphology type.

3.3.4 The scaling properties in cluster distributions— a summary of observations

The scaling properties for rich clusters were first studied by the author (Jing 1990b), a detailed account of the work will be presented in Chapter 9. As a summary, I examined

$\Sigma(q)$ for several cluster (2-D) samples of different depths and of different richness which were selected from the ACO catalog of rich clusters of galaxies. I found that the rich clusters also obey the scaling, and the scaling relation is independent of richness. So the distributions of rich clusters can be described by a hierarchical model, consistent with the statistics of the three-point correlation function (§3.2.4). All the scaling features have been further confirmed by a recent analysis on small 3-D samples (Cappi et al. 1991b), though the accuracy of their results is limited because of the small sample size.

As shown by Schaeffer (1987), the function $\Sigma(q)$ depends on the redshift selection function weakly, thus making possible a comparison of $\Sigma(q)$ with that of galaxies even in 2-D samples. The studies of Jing (1990b) and Cappi et al. (1991b) gave an indication that galaxies and clusters obey the same scaling, though more detailed studies with larger redshift samples are still needed.

3.3.5 Theoretical implications

As we saw above, the hierarchical scaling is established both in the galaxy and in the cluster distributions, and it depends weakly on the intrinsic properties of these objects (such as luminosity, morphology, richness). However, there is no *a priori* reason to expect the scaling necessarily to be followed, thus the observed scaling could become a strong constraint on the theories of galaxy formation.

Fry et al. (1989) have applied the statistics to numerical simulations of HDM and CDM inflationary models, initially Poisson models, and cosmic strings seeded models, in order to probe $\Sigma(q)$ of 'galaxies' in these models. They found that the simulation results obey the implied hierarchical scaling in many cases, but not in all. In particular, HDM models without biasing show the effect of a strong feature in the initial power spectrum. The cosmic string models exhibit scaling but do not agree well with the galaxy data. The rest of the models work well, implying that the initial fluctuation spectrum has a behavior closest to that in CDM models, or perhaps Poisson.

As discussed in §3.2.4, a hierarchical distribution, like Eq.(3.3.2), is not expected for rich clusters in the simple analytical models in which 'clusters' are formed at high density peaks. But these analytical prescriptions may be too simple, so large N-body simulations are needed to clarify this point.

3.4 The Other Measures of High-order Clustering

As stated in the beginning of this chapter, three other measures depending on high-order clustering are frequently used in the LSS study. Because of the limited space of the thesis, I shall only briefly discuss these measures. Despite its brevity, I try to keep the spirit of the previous sections: to summarize the basic features of each method and the main results obtained.

3.4.1 Minimal spanning trees

Any distribution of points in space is associated with a unique structure, the so-called 'Minimal Spanning Tree' (or MST) (Barrow et al. 1985). The MST picks out a dominant pattern of connectedness in a manner that emphasizes its intrinsic linear associations, so it is mostly useful in studying the properties related with 'filamentary' structure (Bhavsar & Ling 1988a&b). Since the MST depends on the high order clustering, some quantitative properties of the MST can be defined and then calculated for comparative purposes, so as to discriminate between theories which have similar low-order clustering (Barrow et al. 1985). Now we describe the definition and construction of the MST, following Barrow et al. (1985).

Our data set is termed a *graph* which will be composed of *nodes* (galaxies), *edges* (straight lines joining galaxies) and *edge-lengths* (distances between galaxies). A sequence of edges joining nodes is a *path*; a closed path is called a *circuit* and a graph will be called *connected* if there is a path between any pair of nodes. The number of edges emanating from a node is call its *degree.* A connected graph containing no circuit is a *spanning tree.* The length of a tree is defined to be the linear sum of the lengths of its component edges. The *minimal spanning tree* (MST) is the spanning tree of the minimum length. The MST will be unique, if no two edges have a equal length. A *k-branch* is a path of *k* edges connecting a node of degree 1 to a node of degree exceeding 2 with all intervening nodes of degree 2.

The simplest algorithm to construct explicitly the MST of a graph, Γ, first picks an arbitrary node of Γ and then adds the connected edge of smallest length. This edge and the two nodes at its ends form the first *partial tree*, Π_1. The kth partial tree, Π_k, is formed by adding to Π_{k-1} the shortest edge connecting Π_{k-1} to any nodes of Γ not already in Π_{k-1}. If Γ contains n nodes then Π_{n-1} is the required MST.

In order to distill the dominant features of the MST, two further reducing operations, *pruning* and *separating*, on the MST can be performed.

1). Pruning: An MST is pruned to level p when all k-branches with $k \leq p$ have been removed.

2). Separating: Remove from the MST any edges whose length exceeds some cut-off l_0.

Bhavsar and Ling (1988a&b) showed that the MST, combined with the data permuting technique, is a successful filament-finding algorithm which can identify the filaments and determine their statistical significance (physical associations or chance alignments of small clustered objects). Applying the technique to the CfA sample, they found the filaments of tens Mpc are *real*. This is the first objective, statistical evidence for the physical existence of filaments.

In the original paper of Barrow et al. (1985), they proposed two statistical quantities to quantify the structure of an MST: $F(l)$ and $R(l)$ distributions. The $F(l)$ is the frequency distribution of edge-lengths of the MST, and $R(l)$ is the ratio of $F(l)$ to the number of pairs with the separation l in the data set. In our recent work (Plionis, Valdarnini & Jing 1992; §10.2), besides the $F(l)$, we construct further statistical quantities in order to test whether the MST features of Abell clusters can be reproduced in simulation samples which are built by the Zel'dovich approximation from Gaussian density fluctuations and have the same *low-order* clustering and the same selection effects as the real data. They are: the mean edge-length, the ratio R_L of the start-to-end branch-length to the total length along the branch after l_0-separation, the frequency distribution $B(L)$ of the branch length after l_0-separation, the alignments of neighbouring clusters on the MST, etc. These estimates are sensitive to the existence of high order clustering, and therefore are expected to be good discriminants of theories (or hypotheses). Plionis et al. (1992) found that some features of the R_L and the $B(L)$ statistics cannot be reproduced in the simulated samples at $\geq 3\sigma$ levels, suggesting that density fluctuations might be more complicated than a simple Gaussian fluctuation.

3.4.2 Percolation analysis

Consider a system of N points in a cubic space of size l^3, its characteristic length is the mean separation $\bar{d} = l/N^{1/3}$. The *clusters* are identified by the *friends-of-friends* algorithm: two points are friends if their separation is less than a certain distance, say, d, and a cluster is the collection of points which are mutual friends (i.e., including the friends of friends). The percolation analysis is, in fact, used to study the geometrical properties of the clusters.

One commonly used analysis is to estimate the normalized length $l_m(b) = L_{max}(b)/l$, where $L_{max}(b)$ is the maximum length of the clusters, and b is the dimensionless separation parameter $b = d/\bar{d}$. When $l_m(b) = l_m(b_*) = 1$, the system is said to be percolated and b_* is called the percolation parameter. In a uniform distribution, b_* is 1; and in a Poissonian distribution, $b_* = 0.86$. If a sample contains large coherent structures such as filaments and sheets, the b_* is expected to be smaller than 0.86. On the contrary, if a sample contains a lot of small isolated clusters, the b_* is greater than 0.86.

There have been several studies on b_*, based on the CfA and SSRS redshift surveys. The results are between 0.6 to 0.8. As shown by Dekel & West (1985) and by Bhavsar & Barrow (1983), b_* is very sensitive to the sampling parameters (the mean density and the volume), so an interpretation of the results is not an easy task. They also argue that the parameter is not a very good discriminant between the current models.

However, this technique could still be useful if suitable quantities and suitable methods are chosen, because the clusters' properties depend on the high order clustering. One way, for example, is to estimate $l_m(b)$ for the purpose of comparison, that is, to estimate $l_m(b)$ in the observations as well as in the simulations and then to compare them so as to test the models. Another example is to compare $l_m(b)$ between a real sample and its random sample so as to exhibit the clustering (e.g., Börner & Mo 1989b; Mo & Börner 1990). Other physical properties of clusters, e.g., the multiplicity function, the fraction of isolated objects, shapes of clusters, and alignments within clusters may also be useful in testing models or hypotheses (e.g., Postman et al. 1989; Postman et al. 1992; Plionis et al. 1992; §10.3).

3.4.3 A topology measure — the genus-threshold density relation

Gott, Melott, Weinberg and their collaborators (Gott et al. 1989; and references therein) suggested that the genus of isodensity contours could be used as a quantitative measure of the topology of the large scale structure. The genus of the contour surface is defined by

$$G_s = (Number\ \ of\ \ holes) - (Number\ \ of\ \ isolated\ \ regions)$$

where "hole" means a hole like that in a doughnut, and an isolated region may be above or below the threshold density.

Gott et al. (1986) showed that G_s is related to the integral of Gaussian curvature K over the contour surface

$$G_s = -\frac{1}{4\pi}\int K dA.$$

The relation makes it possible to measure the genus of a contour surface in catalogs of extragalactic objects and in simulations. The computer program has already been published in Melott (1990) and Weinberg (1988).

In terms of density threshold ν (which is in units of the standard deviation from the mean), Hamilton et al. (1986) showed that for Gaussian random fields, the mean genus per unit volume is given by

$$g_s = N(1-\nu^2)\exp(-\nu^2/2),$$

where

$$N = \frac{1}{(2\pi)^2}\left(\int k^2 P(k) d^3k/3 \int P(k) d^3k\right)^{3/2}.$$

So while the amplitude N of the genus curve depends on the *shape* of the power spectrum, the shape of the genus curve depends only on the density threshold ν, $g_s \propto (1-\nu^2)\exp(-\nu^2/2)$. Any deviation from this genus shape indicates a deviation from

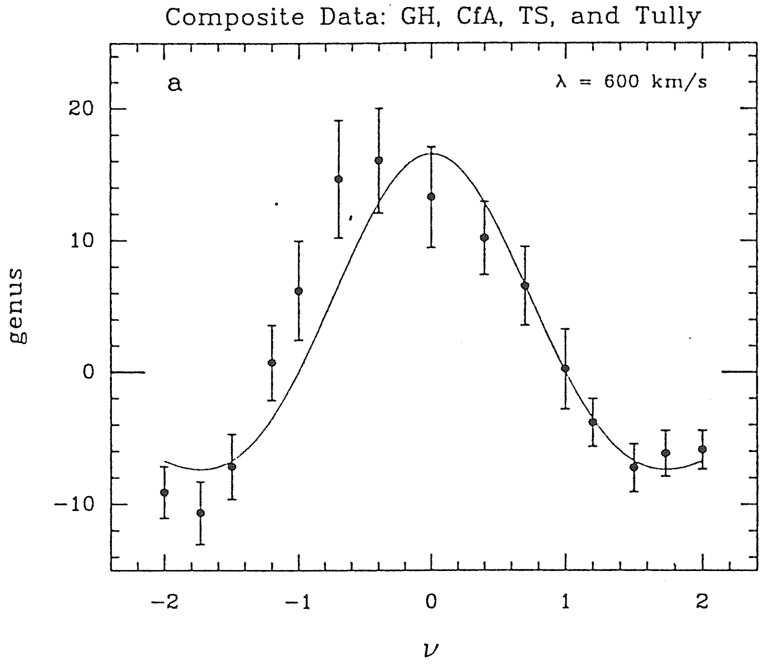

Figure 3.9 — The composite genus curve created by adding the (bootstrap average) curves from the Giovanelli and Haynes, CfA, dwarf and Tully samples, all smoothed at $\lambda \sim 600$ km s^{-1}. The best-fit random phase curve is shown for comparison. The curve shows a small shift to the left in the direction of a meatball topology. Taken from Gott et al. (1989).

the Gaussianity. For example, the meatball structures will shift the peak of g_s to negative ν but the bubbly structures will shift it in the opposite direction.

In gravitational instability theories, the primordial Gaussian or non-Gaussian features remain in the linear regime. So the analysis of galaxy samples or/and cluster samples in the linear regime (i.e., $r \geq r_0$), can in principle determine whether primordial fluctuations are of a Gaussian or a non-Gaussian nature. The shape of the primordial power spectrum, if Gaussian, can be further constrained by the observed amplitude N.

Gott et al. (1989) analysed most available redshift samples of galaxies and clusters and found that the distribution of these objects on linear scales is approximately Gaussian with slight meatball shifts (see Figure 3.7). Such similar shifts also show up in CDM simulations due to a combination of biasing and sampling effects. Notice that these shifts are in the opposite direction to what is expected in a bubble model, thus there is no evidence for the existence of bubbles from this quantitative study. The main results of their model tests are that, while the HDM model is consistent with the observational data, the standard CDM model seems the most successful one in explaining the observed genus-density relation.

Recently, Moore et al. (1992) have analysed the topology for the QDOT IRAS survey. While they confirm that the observed topology properties are consistent with an initially Gaussian fluctuation, they found, from the amplitude of the genus-density relation, that there is more power on scales $> 15\,h^{-1}$Mpc, in agreement with the count-in-cell analyses (Saunders et al. 1991; Efstathiou et al. 1990; §3.2).

A 2-D equivalent, the Euler-Poincáre characteristic (Adler 1981; Coles 1988) has also been applied to the study of the LSS (Coles & Plionis 1991), using the largest available galaxy catalogue, the Shane & Wirtanen catalogue. The results support that in the mildly non-linear regime the topology approaches that of a meatball, but in the linear regime the topology is indistinguishable from that of a Gaussian field, consistent with the 3-D study of Gott et al. (1989).

4

On the error estimates of correlation functions

The two- and three-point correlation functions have been widely used to measure the large-scale structure of the universe (e.g., Peebles 1980; §3.2). But how to estimate the statistical errors of these functions is unclear. The difficulty arises from the fact that there is no good ensemble of samples to represent the structure. Usually, the errors are given by assuming that the count of pairs $DD(r)$ [$DD(r)$ is the number of pairs of objects in the separation bin $r \pm dr/2$] in the two-point correlation function and the count of triplets $DDD(r,u,v)$ [$DDD(r,u,v)$ is the number of triplets of objects in the bin $(r \pm dr/2, u \pm du/2, v \pm dv/2)$ which determines the configuration of the triplet, see §3.1] in the three-point correlation function have Poissonian distributions (Peebles 1980, §48). The sampling errors are underestimated with this assumption, as will be demonstrated below. Another method, which was first proposed by Barrow, Bhavsar, & Sonoda (1984) and has been widely used in correlation analysis since then, is to use a bootstrap resampling technique to estimate the sampling errors. For example, Ling, Frenk, & Barrow (1986) made a detailed clustering study of galaxies and Abell clusters, and found a statistically significant difference in their clustering. But it is not clear whether or not and how the errors given by this technique are related with the sampling errors derived from an ensemble of independent samples.

In this chapter, we derive (in §4.1) formulae which relate the errors of correlation functions to those quantities which are easy to calculate. We test (in §4.2) the usefulness of these formulae using results of an ensemble given by numerical simulations. It is found that 1) the ensemble errors of the pair count DD and the triplet count DDD in given bins are well approximated by $\sigma_{DD}(ens) = [\langle DD(r)\rangle + 4\langle DD(r)\rangle^2/N_g]^{1/2}$ and $\sigma_{DDD}(ens) = [\langle DDD(r,u,v)\rangle + 36\langle DDD(r,u,v)\rangle^2/N_g]^{1/2}$ (where N_g is the number of points in the studied sample; $\langle\cdots\rangle$ denotes the ensemble mean), respectively; 2) the bootstrap errors of

$DD(r)$ and $DDD(r,u,v)$ can be approximated by $\sigma_{DD}(bo) = [3DD(r) + 4DD^2(r)/N_g]^{1/2}$ and $\sigma_{DDD}(bo) = [7DDD(r,u,v) + 36DDD^2(r,u,v)/N_g]^{1/2}$, respectively. The formulation in §4.1 provides a very fast and accurate algorithm to calculate the results of the bootstrap resamplings; 3) because of the inter-dependence of the counts in different bins, the regressions using the ensemble errors in different bins (to weight the data points) underestimate the errors in the parameters characterizing the regressions (e.g., the amplitude of the two-point correlation functions A and the reduced three-point correlation functions Q); the regressions using the bootstrap errors give good estimates of the errors in A and Q.

4.1 Formulae

4.1.1. Two-point correlation function

In one definition, the two-point correlation function is estimated by the following formula (Peebles 1980):

$$\xi(r) = \frac{DD(r)}{RR(r)}\frac{n_R^2}{n^2} - 1, \tag{4.1}$$

where $DD(r)$ is the number of object pairs with separation in the range $r \pm dr/2$ (dr: the bin size); $RR(r)$ is the corresponding pair count in a random sample constructed within the sample boundary and with the same selection function as the real sample; n and n_R are respectively the mean number densities of the data sample and of the random sample. In our discussion, we neglect the selection effect and the boundary effect and assume that the data sample is homogeneous and fair. In this case, the pair count $RR(r)$ can be estimated without error. The sampling error of $\xi(r)$ is then determined by that of $DD(r)$.

a). The ensemble error

To estimate the ensemble error of $DD(r)$, we write $DD(r)$ in another form (Peebles 1980, §48). We divide the sample volume (V) into a set of infinitesimal cells $\{\Delta V_i\}$ so that $\sum \Delta V_i = V$. The volume of each cell is assumed to be so small that the count $\mathcal{N}_i$ is either 1 or 0. The pair-count $DD(r)$ can then be written as

$$DD(r) = \frac{1}{2}\sum_{i,j} \mathcal{N}_i \mathcal{N}_j U_{ij}(r) \tag{4.2}$$

where $U_{ij}(r) = 1$ when the separation between cells i and j is within the bin $r \pm dr/2$ and $U_{ij}(r) = 0$ otherwise. The mean and mean square of $DD(r)$ can be written as ($\langle \cdots \rangle$ denotes ensemble average)

$$\langle DD \rangle = \frac{1}{2} \sum_{i,j} \langle \mathcal{N}_i \mathcal{N}_j \rangle U_{ij}; \tag{4.3a}$$

$$\langle DD^2 \rangle = \frac{1}{4} \sum_{i,j} \sum_{l,k} \langle \mathcal{N}_i \mathcal{N}_j \mathcal{N}_l \mathcal{N}_k \rangle U_{ij} U_{lk}. \tag{4.3b}$$

Since $i \neq j$, $l \neq k$, the sum in Eq.(4.3b) can be divided into three parts:

$$\langle DD^2 \rangle = \frac{1}{4} \sum_{i \neq l \neq j; i \neq k \neq j} \langle \mathcal{N}_i \mathcal{N}_j \mathcal{N}_l \mathcal{N}_k \rangle U_{ij} U_{lk}$$

$$+ \sum_{i; k \neq j} \langle \mathcal{N}_i \mathcal{N}_j \mathcal{N}_k \rangle U_{ij} U_{ik} + \frac{1}{2} \sum_{i,j} \langle \mathcal{N}_i \mathcal{N}_j \rangle U_{ij}^2 \tag{4.4}$$

where we have used that $\mathcal{N}_i = \mathcal{N}_i^2 = \cdots$. Using the definitions of the two-, three- and four-point correlation functions $\kappa_N(\vec{r}_1, ..., \vec{r}_i, ..., \vec{r}_N)$ ($N = 2, 3, 4$) and the integral constraints on $\kappa_N(\vec{r}_1, ..., \vec{r}_i, ..., \vec{r}_N)$: $\int_{\text{large } V} \kappa_N(\vec{r}_1, ..., \vec{r}_i, ..., \vec{r}_N) d\vec{r}_i = 0$ for $i = 1, ..., N$, we can write

$$\langle DD^2(r) \rangle = \frac{N_g^2}{4} (ndv)^2 [1 + 2\xi(r) + \xi^2(r)] + N_g (ndv)^2 [1 + 2\xi(r)$$

$$+ \frac{1}{(dv)^2} \int_{dv} \xi(r_{12}) d\vec{r}_1 d\vec{r}_2 + \frac{1}{(dv)^2} \int_{dv} \zeta(r, r, r_{12}) d\vec{r}_1 d\vec{r}_2] + \langle DD \rangle \tag{4.5}$$

where N_g is the number of objects in the sample, $dv = 4\pi r^2 dr$ and ζ is the three-point correlation function (see §3.1). The first term of Eq.(4.5) is $\langle DD \rangle^2$. So the variance of $DD(r)$, $\sigma_{DD}^2(ens)$ depends on two- and three-point correlation functions [cf. Peebles 1980 §48]. In weak clustering approximation [i.e., $\xi(r) < 1$], σ_{DD}^2 can be written as:

$$\sigma_{DD}^2(ens) \approx \langle DD(r) \rangle + \frac{4}{N_g} \langle DD(r) \rangle^2. \tag{4.6}$$

The first term is usually referred to as the Poissonian error. The second term, which was usually neglected, becomes important when $\langle DD(r) \rangle > N_g/4$. This condition can be approximately written as $dr/r > (\bar{d}/r)^3/8\pi$ ($\bar{d} \equiv n^{-1/3}$). In the real case, this condition is satisfied when r becomes so large that $\xi(r) < 1$. So Eq.(4.6) is a good approximation, as we will see in §4.2.

b). The bootstrap error

Barrow et al. (1984) suggested a bootstrap resampling technique to estimate the sampling error. In this technique, one constructs a set of bootstrap samples from the parent sample. Each bootstrap sample is constructed by selecting N_g times in the parent sample; each time each galaxy in the parent sample has a probability of $1/N_g$ to be selected into a bootstrap sample. The bootstrap resampling is equivalent to assigning to each object (object i) in the parent sample a weight w_i which is equal to the number of times that the galaxy is selected. The possible values of w_i are $0, 1, \cdots, N_g$; $w_i = 0$ means that the object i is not selected in the bootstrap procedure. Since in the N_g-time selections, an object in the parent sample is selected with a probability $1/N_g$ without depending on whether or not it has already been selected, the weight for each object has a Poissonian distribution with mean 1. In the following derivation, we will assume that the assignment of a weight to one object is independent of that to another. The bootstrap resampling process guarantees that the assumption is valid when a small fraction of objects is involved in counting pairs or triplets [in a given bin]. Otherwise, it is only approximately valid, since $\Sigma w_i \equiv N_g$ in each realization. More discussion on the assumption will be given in §4.2. Our task is now to calculate the deviation among realizations of the assignment of weights.

Here we give a general consideration. Suppose $\{w_i\}$ is a random observation from a distribution function $P(w)$ having mean $\bar{w}$ and variance σ_w^2. We define the weighted pair count:

$$DD_w(r) = \frac{1}{2}\sum_{i,j} w_i w_j U_{ij}(r) \tag{4.7}$$

where, unlike in Eq.(4.2), the indices i, j are for objects rather than for infinitesimal cells.

The mean of the weighted pair-counts is (here $\langle\cdots\rangle$ denotes the average over certain kind of weight assignments)

$$\langle DD_w(r)\rangle = \frac{1}{2}\sum_{i,j} U_{ij}(r)\int dw_i w_i P(w_i)\int dw_j w_j P(w_j) = \frac{\bar{w}^2}{2}\sum_{i,j} U_{ij}(r). \tag{4.8}$$

The mean square can be calculated as follows:

$$\langle [DD_w(r)]^2\rangle = \frac{1}{4}\sum_{i,j}\sum_{k,l}\langle w_i w_j w_k w_l\rangle U_{ij} U_{kl}$$

$$= \frac{1}{4} \sum_{i \neq k \neq j} \sum_{i \neq l \neq j} \langle w_i w_j w_k w_l \rangle U_{ij} U_{kl}$$

$$+ \sum_{i;k \neq j} \langle w_i^2 w_j w_k \rangle U_{ij} U_{ki} + \frac{1}{2} \sum_{i,j} \langle w_i^2 w_j^2 \rangle U_{ij}^2. \tag{4.9}$$

Assume the weights of different objects are independent, we have

$$\langle [DD_w(r)]^2 \rangle = \frac{\bar{w}^4}{4} \sum_{i,j} \sum_{k,l} U_{ij} U_{kl} + \bar{w}^2 \sigma_w^2 \sum_{i;k \neq j} U_{ij} U_{ki}$$

$$+ \frac{(\sigma_w^2 + 2\bar{w}^2)\sigma_w^2}{2} \sum_{i,j} U_{ij}^2. \tag{4.10}$$

The first term is equal to $\langle DD_w(r) \rangle^2$; the variance of $DD_w(r)$ is given by the second and the third terms. If $\sigma_w^2 = 0$, the variance of the pair counts is also zero, as expected. One can then proceed as we did in deriving Eq.(4.6), to obtain the variance of $DD_w(r)$

$$\sigma_{DD}^2(w) \approx \sigma_w^2(\sigma_w^2 + 2\bar{w}^2) DD(r) + \frac{4}{N_g} \sigma_w^2 \bar{w}^2 DD^2(r). \tag{4.11}$$

In the case of bootstrap resampling, $\bar{w} = 1$, $\sigma_w^2 = 1$ and

$$\sigma_{DD}^2(bo) \approx 3DD(r) + \frac{4DD^2(r)}{N_g}. \tag{4.12}$$

If $DD(r) \ll N_g$ we have $\sigma_{DD}^2(bo) = 3\sigma_{DD}^2(ens)$. In this case, the bootstrap resampling technique gives an estimate of σ_ξ which is about $\sqrt{3}$ times that given by the ensemble (or Poissonian) error. However, when $DD(r) \geq 4/3N_g$, the bootstrap error is comparable to the ensemble error.

A similar derivation can be done for the variance of sparse sampling. Sparse sampling is equivalent to assigning a weight 0 to each galaxy that is discarded by the sparse process and a weight 1 to other galaxies (which are selected into the sparse sample). Suppose the sparse rate is $\mathcal{P}_0$. Then a galaxy in the parent sample has a probability of $\mathcal{P}_0$ to be selected into one sparse sample, and has $1 - \mathcal{P}_0$ to be discarded. The mean and the mean square of the weight for each galaxy are respectively $\bar{w} = \mathcal{P}_0$, $\overline{w^2} = \mathcal{P}_0$, which gives $\sigma_w^2 = \mathcal{P}_0(1 - \mathcal{P}_0)$. Inserting these values into Eq.(4.11) and using $\sigma_\xi^2 \approx \sigma_{DD}/[DD(r)\mathcal{P}_0^2]^2$ (where $DD(r)$ is the count in the parent sample), we have

$$\sigma_\xi^2 \approx \frac{1}{DD(r)} \left[\frac{1}{\mathcal{P}_0^2} - 1 \right] + \frac{4}{N_g} \frac{1 - \mathcal{P}_0}{\mathcal{P}_0}. \tag{4.13}$$

One sees that $\sigma_\xi \to 0$ when $\mathcal{P}_0 \to 1$ and $\sigma_\xi \to \infty$ when $\mathcal{P}_0 \to 0$, as expected. Eq.(4.13) gives the deviation of the correlation function ξ of a sparse sample from that of its parent.

4.1.2. Three-point correlation function

The three-point correlation function ζ can be estimated by the formula (Peebles 1980):

$$\zeta(r_{12},r_{23},r_{31}) = \frac{DDD(r_{12},r_{23},r_{31})}{RRR(r_{12},r_{23},r_{31})}\frac{n_R^3}{n^3} - \xi(r_{12}) - \xi(r_{23}) - \xi(r_{31}) - 1 \tag{4.14}$$

where $DDD(r_{12},r_{23},r_{31})$ is the count of triplets with their three edge lengths in the range $(r_{12},r_{23},r_{31}) \pm 1/2(dr_{12},dr_{23},dr_{31})$ in the data sample; $RRR(r_{12},r_{23},r_{31})$ is the corresponding count in a set of points which are randomly distributed in the sample domain (see last subsection). Under the same assumption as in §4.1.1, we need to calculate the error in DDD in order to estimate the error in ζ.

The number of triplets with a given configuration (represented by r_{12}, r_{23}, r_{31}) can be written as

$$DDD(r_{12},r_{23},r_{31}) = \sum_{i,j,k} \mathcal{N}_i\mathcal{N}_j\mathcal{N}_k U_{ij}(r_{12})U_{ik}(r_{23})U_{ki}(r_{31}). \tag{4.15}$$

The mean and mean square of DDD can be calculated in the same way as those of DD. We divide $\langle DDD^2\rangle$ into terms which involve, respectively, counts of N-tuples ($N = 3$, 4, 5, 6). The $N = 3$ and $N = 6$ terms are equal to $\langle DDD\rangle$ and $\langle DDD\rangle^2$, respectively. Under the assumption of weak clustering ($\xi < 1$) and after tedious calculations, we obtain:

$$\sigma^2_{DDD} \approx \langle DDD\rangle + \frac{36}{N_g}\langle DDD\rangle^2. \tag{4.16}$$

The error in the weighting scheme can be discussed as we did for the two-point correlation function. It turns out that

$$\sigma^2_{DDD} \approx [(\bar{w}^2 + \sigma_w^2)^3 - \bar{w}^6]DDD + \frac{(DDD)^2}{N_g}\sigma_w^2\bar{w}^2(30\bar{w}^2 + 6\sigma_w^2). \tag{4.17}$$

For the bootstrap resampling

$$\sigma^2_{DDD} \approx 7DDD + 36\frac{(DDD)^2}{N_g}. \tag{4.18}$$

For the sparse sampling

$$\sigma_\zeta^2 \approx \left[\frac{1}{\mathcal{P}_0^3} - 1\right] \frac{1}{DDD}, \qquad \text{when } N_g \gg DDD. \tag{4.19}$$

4.2 Test by numerical simulations

4.2.1 Simulation samples

The simulation used here was originally designed to study the spatial distribution of Abell clusters by R. Valdarnini (see §10.1 for details). His algorithm is similar to that of Postman et al. (1989). The simulation was done in a box of $640^3\ h^{-3}\mathrm{Mpc}^3$ with 64^3 grid cells. The simulated objects are the peaks of a Gaussian random density field with height above $1.3\sigma_\rho$ (where σ_ρ is the *rms* density fluctuation within the grid cell). The Gaussian random field was so chosen that the simulated objects have a two-point correlation function $\xi(r) = (25/r)^{1.8}$ in the range of 10 to 60 h^{-1}Mpc, comparable to that of Abell clusters (Bahcall & Soneira 1983). The spatial peak distribution of a Gaussian field is non-Gaussian and the high-order reduced correlation functions are non-zero. As will be seen below, the constant Q of the three-point correlation function ζ is about 0.65, similar to the observed value 0.8 ± 0.3 of Abell clusters (Jing & Zhang 1989; Jing & Valdarnini 1991). The mean number density of simulated objects is fixed to be $6 \times 10^{-6}\ h^3\mathrm{Mpc}^{-3}$, again to match that of Abell clusters. Therefore the simulated samples resemble well the real ones. There are totally 50 simulated samples each of which contains 1572 objects.

4.2.2 Error definitions

In the following, we will discuss different kinds of errors. In order to avoid confusion, we give their definitions here. Some of them have already appeared in the previous section.

- The *ensemble errors* refer to the errors (in bins) given by Eq.(4.6) (for the pair count) and Eq.(4.16) (for the triplet count); in simulations, they refer to the errors given by the deviations of (pair and triplet) counts in bins among the 50 samples.
- The *bootstrap errors* refer to the errors (in bins) given by Eq.(4.12) (for the pair count) and Eq.(4.18) (for the triplet count); in (each of the) simulations, they refer to the

errors given by the deviations of (pair and triplet) counts in bins among 500 bootstrap resampling realizations.

- The *Poissonian errors* refer to the errors (in bins) given by $DD^{1/2}$ (for the pair count) and $DDD^{1/2}$ (for the triplet count) for individual samples.
- The *fit errors* refer to the errors of parameters A (in ξ) or Q (in ζ) given by a least-squares fit. They depend on the error model used to weight the data in bins.
- The *ensemble mean of fitted parameter* (AMFP) refers to the mean of the values A or Q of the 50 simulation samples; it is denoted by a bar over the corresponding parameter.
- The *ensemble error of fitted parameter* (AEFP) refers to the deviation among the values A or Q of the 50 simulation samples; it is denoted by a 'δ' before and a bar over the corresponding parameter.

4.2.3 Tests

a). Errors in individual bins

The pairs $DD(r)$ are counted in 10 equal logarithmic separation intervals with $\Delta \log r = 0.1$, starting from $r_{min} = 6.3\, h^{-1}$Mpc. In Figure 4.1a, the triangles represent the ensemble errors of DD calculated from the 50 simulated samples in each bin. The solid curve is the analytical prediction of Eq.(4.6). The analytical and the simulated results are in good agreement, indicating that Eq.(4.6) is a good formula for estimating the ensemble errors. The significant increase of $\sigma_{DD}/\sqrt{DD}$ at large r shows the importance of the second term on the right hand side (*rhs*) of Eq.(4.6).

In counting the triplets $DDD(r_{12}, r_{23}, r_{31})$, we use another set of variables: r, u, and v as usually chosen (see Peebles 1980). The same separation intervals are taken for r as in $DD(r)$. For the variables u and v, we start counting triplets at $u_{min} = 1$ and $v_{min} = 0$ and take 5 intervals for each variable with $\Delta \log u = 0.1$ and $\Delta v = 0.2$. The results of $\sigma_{DDD}/\sqrt{DDD}$ calculated from the simulation samples are shown in Figure 4.1b as a function of the mean triplet count $\langle DDD \rangle$. The analytical prediction of Eq.(4.16) is also plotted in the figure. Again the two results coincide very well, demonstrating that it is important to keep the second term on the *rhs* of Eq.(4.16), and that the equation gives a

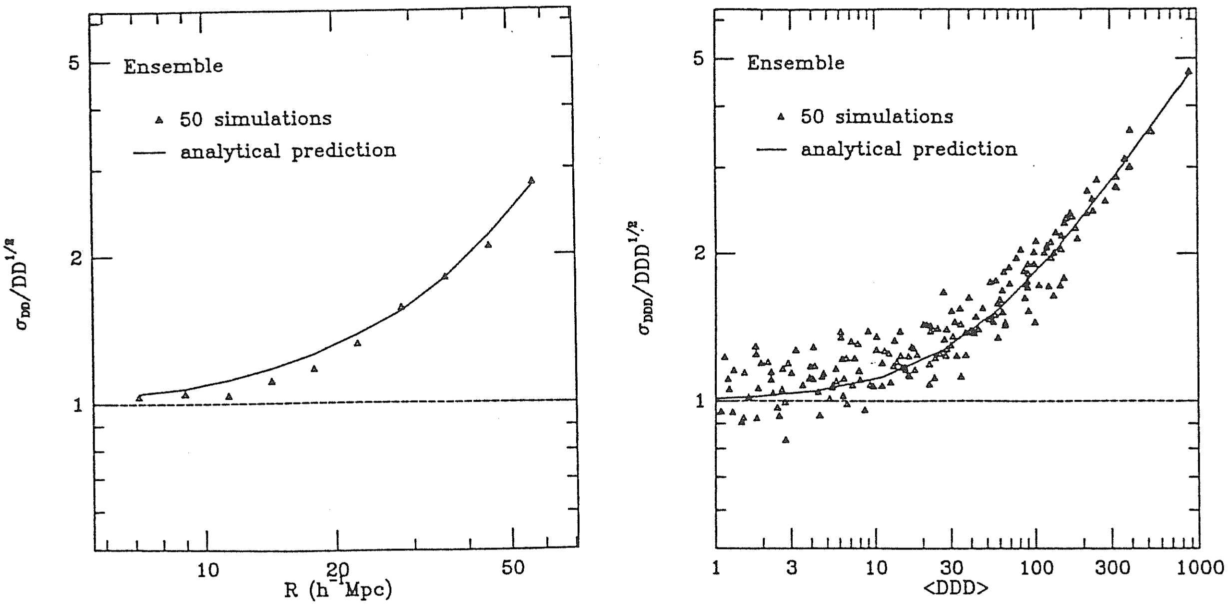

a) b)

Figure 4.1 — *a*). The ensemble error σ_{DD} of pair count $DD(r)$, normalized to $\sqrt{DD(r)}$, as a function of pair separation r. The triangles are the estimates from 50 simulation samples. The solid curve represents the analytical result Eq.(4.6). The dashed line is the Poissonian error. *b*). Similar to a), but for the triplet count DDD. The solid curve is the prediction of Eq.(4.16).

good estimate of the ensemble errors of DDD in different bins.

In Figures 4.2a and 4.2b, we plot respectively the bootstrap errors of DD and DDD for the first simulation sample [note: our conclusions here do not depend on our choice of the sample]. The errors are normalized to the Poissonian errors. The triangles represent the results calculated from 500 bootstrap resampling realizations. The analytical predictions [Eq.(4.12) and Eq.(4.18)] are drawn for comparison. For the triplet count, we find a very good agreement between the simulation results and the analytical formula. For the pair count, however, although Eq.(4.12) fits well the simulation results for the first 8 bins, it clearly gives a larger deviation in the last two bins. The discrepancy arises from the fact that the assumption of weight independence breaks down when a large part of objects in the sample contribute to the pair count in single bin [since $\sum w_i \equiv 1$], and that the correlation between weights reduces deviation in the count. In the first 8 bins, the counts

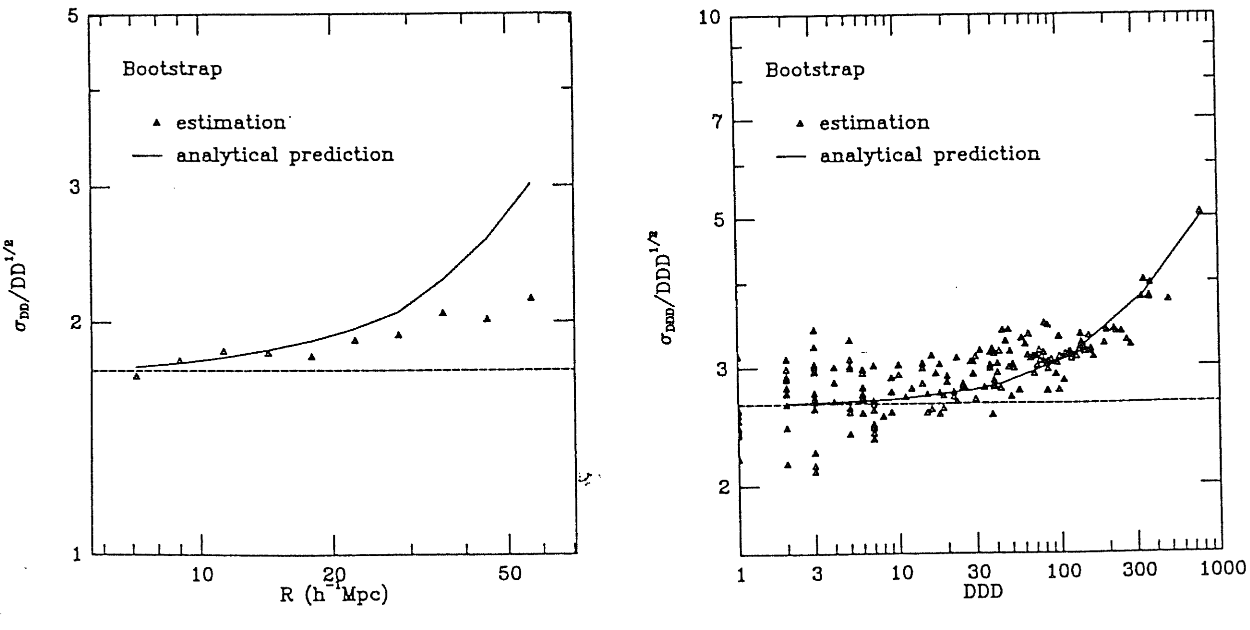

a)

b)

Figure 4.2 — *a*). The bootstrap resampling error σ_{DD} of pair count $DD(r)$, normalized to $\sqrt{DD(r)}$, as a function of pair separation r. The triangles are the estimates from 500 bootstrap resampling realization of the first simulation sample. The solid curve represents the analytical result Eq.(4.12). The dotted line is $\sqrt{3}$ times the Poissonian error. *b*). similar to a), but for the triplet count DDD. The solid curve is the prediction of Eq.(4.18) and the dotted line is $\sqrt{7}$ times the Poissonian error.

DD are less than 850, a small fraction of the objects contributing to the pair counts in single bins. In the last 2 bins, DD are 1394 and 2417 respectively, a considerable part of the objects will be involved for the single bins. In the case of triplets, the largest count is 781. Furthermore, it is easy to prove that for same value ($\gg 1$) of DD and DDD, the number of objects involved in the triplet count is much smaller than that in the pair count. This is why Eq.(4.18) fits the simulation result very nicely. At present, it is difficult to quantify when the assumption of weight independence breaks down for DD and DDD. From a check of our previous results of pair and triplet counts in galaxy and cluster catalogues, we found that, for a reasonable choice of bin sizes, both Eq.(4.18) and Eq.(4.12) give good approximations.

It is worthwhile to point out that our formulation for the bootstrap resampling process [e.g., Eq.(4.7)] provides a very convenient way to accurately estimate this type of errors. Before counting pairs and triplets, we assign to each object a weight given by a resampling process. The counts of pairs and triplets in each resampling realization can be obtained by assigning the weights of this realization to the pairs and triplets in the parent sample. The variances of the counts can easily be calculated. This algorithm needs only a small amount of computational time to get bootstrap errors. And the algorithm accurately simulates the bootstrap resampling process.

b). Fit errors

As well known, the two-point correlation functions of galaxies and clusters of galaxies obey the power law:

$$\xi = A r^{-\gamma} \;, \tag{4.20}$$

and the three-point functions can expressed well by the hierarchical form:

$$\zeta(r_{12}, r_{23}, r_{31}) = Q[\xi(r_{12})\xi(r_{23}) + \xi(r_{23})\xi(r_{31}) + \xi(r_{31})\xi(r_{12})]. \tag{4.21}$$

The parameters A, γ and Q together with their errors are often obtained by the least-square fit of the data in different bins. In doing the fit, it generally requires that the data at different bins are independent. But it may not be the case for the correlation functions. Here we show how the bin-bin interdependence affects the error estimates of the parameters and how the correct answers can be obtained.

We fit the two-point correlation function $\xi(r_i)$ $(i = 1, ..., 10)$ by the power law (4.20) with the slope γ chosen to be 1.8. To choose a fixed γ is only to simplify the discussion. The choice is reasonable as already shown by the simulations. Let $DD^E(r_i) \equiv DD(r_i) - \langle RR(r_i) \rangle$. The expected value $\langle RR(r_i) \rangle$ is estimated from a large random sample containing 10,000 points and is interpolated at small separations, so its error can be neglected. According to Eq.(4.20), we can get A by minimizing:

$$\chi^2 = \sum_i \left(\frac{DD^E(r_i) - \langle RR(r_i) \rangle r_i^{-\gamma} A}{\sigma_{DD}(r_i)} \right)^2 . \tag{4.22}$$

The values of A and its fit error δA depend on the error model for $\sigma_{DD}(r_i)$. Here we adopt three error models for $\sigma_{DD}(r_i)$: the ensemble error; the bootstrap error; and the Poissonian error.

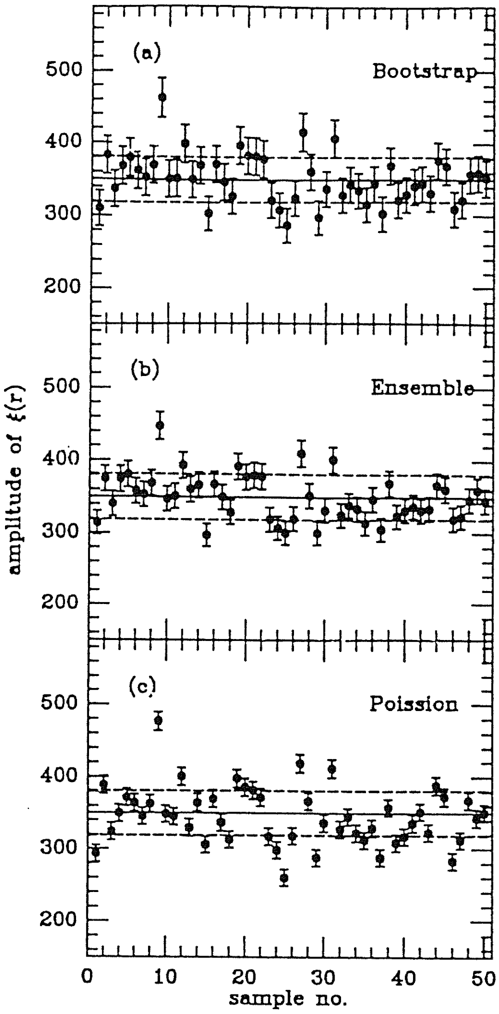

Figure 4.3

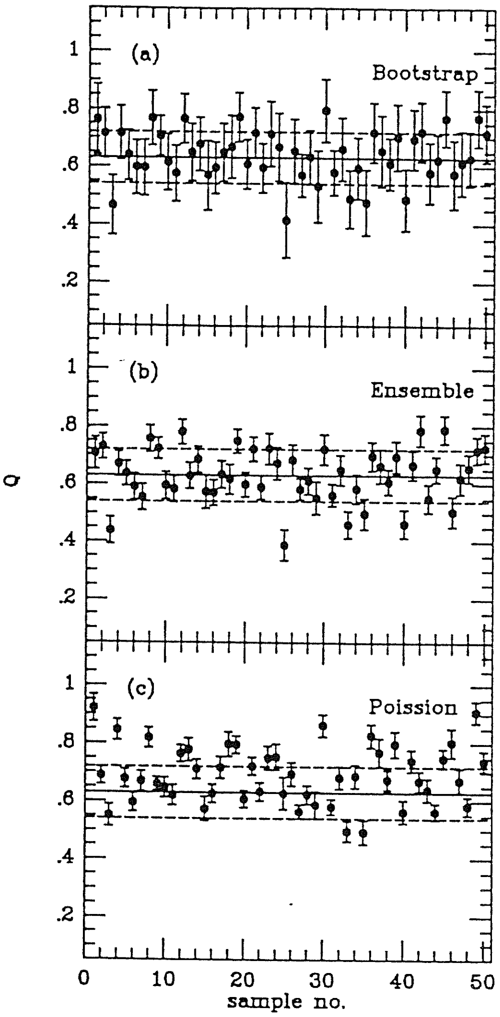

Figure 4.4

Figures 4.3&4 — **3**. The amplitude A of the two-point correlation function ξ and its fit error δA for 50 simulation samples, based on different error models (to weight the data in each bin) in the least-square fit: (a) the bootstrap error; (b) the ensemble error; (c) the Poissonian error. The solid line represents the mean value ($\bar{A}$) of the amplitudes A (based on the ensemble-error model) of the 50 simulation samples. The dashed lines represent the 1σ deviation among the 50 amplitudes. **4**. Similar to Figure 4.3, but for the amplitude Q of the three-point correlation function ζ.

The fit results for each sample are presented in Figure 4.3. The value A does not sensitively depend on the error model of σ_{DD}, but the fit error δA does. For each error model, the mean (i.e. AMFP) $\overline{A}$ of the 50 fit values of A (for the 50 samples) is about

350 $(h^{-1}\mathrm{Mpc})^{1.8}$, with the standard error (i.e. AEFP) $\delta\overline{A} \approx 31$ $(h^{-1}\mathrm{Mpc})^{1.8}$. Note that this error is what we want for A. For each individual sample, the fit error of A, δA, is typically 27 $(h^{-1}\mathrm{Mpc})^{1.8}$ for the bootstrap-error model, 16 $(h^{-1}\mathrm{Mpc})^{1.8}$ for the ensemble-error model, and 11 $(h^{-1}\mathrm{Mpc})^{1.8}$ for the Poissonian-error model. Such fit errors are what we can obtain in studying galaxy distribution, for usually we have only one observed sample. Clearly the bootstrap-error model gives the best and the correct result. The ensemble-error model underestimates the error of A by about 50%; the Poissonian-error model underestimates it by even a larger factor.

It is important to point out that the ensemble-error model gives correctly the error estimate of ξ in individual separation bins. Because of the interdependence of ξ among different bins, the least-squares fit, which requires that ξ in different bins are independent, results in an underestimated error of A. The overestimate of σ_{DD} in individual bins by the bootstrap method compensates for the underestimate due to the bin-bin dependence. The bootstrap resampling technique finally gives a correct estimate of the error of A. In the original paper of Barrow et al. (1984), they also found that the bootstrap method correctly estimates the error of A, consistent with our result.

Now we discuss the fit of the three-point correlation function. Here we assume that ζ obeys the form of Eq.(4.21) and use the least-square fit to find the constant Q. As in fitting ξ, three error models – the ensemble error, the bootstrap error, and the Poissonian error – are used to weight the data in each bin. The fitting procedure is similar to that for ξ, so we omit the details here. The fit results of Q are presented in Figure 4.4. For each weighting model, the mean (i.e. AMFP) $\overline{Q}$ of the 50 fit values is about 0.65 with the standard error (i.e. AEFP) $\delta\overline{Q} \approx 0.09$. The fit error δQ of each sample is typically 0.05 (Ensemble), 0.11 (Bootstrap) and 0.03 (Poisson). Again the bootstrap method gives the best and the correct estimate for the error of Q. The other two models underestimate the error for the same reasons as those in the fit of the two-point correlation function.

4.3 Conclusions

In this chapter, we have derived formulae which relate the widely-used error estimates of correlation functions to the quantities which can be easily obtained from real samples. We have used an ensemble of simulation samples to test these analytical results and found a good agreement. Because of the interdependence among the quantities in different bins, the errors of the parameters in the regressions (such as A in ξ and Q in ζ) are underestimated when we use the ensemble errors to weight the data. The bootstrap resampling technique overestimates the error in individual bins. This overestimation compensates for the underestimation due to the bin-bin interdependence. The fit using the bootstrap errors gives the best and correct results of the errors in the regression parameters. Our results provide a good and convenient way to estimate errors in the correlation functions.

‡The materials presented in this chapter are based on our paper: Mo, H.J., Jing, Y.P., & Börner, G. 1992, *The Astrophysical Journal*, **392**, 452.

5

Correlation functions of galaxies in the ESO-Uppsala catalogue

5.1 Introduction

Correlation functions have been widely used to measure the clustering in galaxy distribution (§3.1–3.2). During the last 15 years, several important results have been obtained. The two-point correlation function of galaxies is found to closely obey a power law

$$\xi(r) = (r_0/r)^{\alpha} \tag{5.1}$$

with $\alpha \approx 1.8$ and $r_0 \approx 5\,h^{-1}$Mpc (Groth & Peebles 1977, hereafter GP; Davis & Peebles 1983). A scaling relation is found between the spatial two- and three-point correlation functions (GP, see §3.1–3.2)

$$\zeta(r_1, r_2, r_3) = Q[\xi(r_1)\xi(r_2) + \xi(r_2)\xi(r_3) + \xi(r_3)\xi(r_1)] \tag{5.2}$$

with $Q \approx 1$. It is also found that galaxies with different morphological types have different correlation functions. In particular, Davis & Geller (1976) and Giovanelli et al. (1986), using respectively the two-dimensional magnitude-limited UGC samples (complete to $m = 14.5$) and the two-dimensional samples constructed in the Perseus-Pisces region, found that elliptical and lenticular galaxies have a two-point correlation function with larger amplitude and steeper shape. These statistical results are frequently used as important observational inputs to the theories of galaxy formation (see, e.g., Efstathiou & Silk 1983).

However, there are also questions concerning the universality of these results. First, the results are mainly derived from galaxy catalogs in the northern hemisphere, it is important to test whether or not galaxies in the southern hemisphere give the same results. Second, the previous results are mainly based on magnitude-selected samples. Since the diameter-function of galaxies (DF) is now available (Lahav et al. 1988, hereafter LRL), it is interesting to see whether or not the diameter-selected samples give similar results. Third, the morphological dependence found by Davis & Geller (1976) and Giovanelli et al. (1986) might apply only for galaxies in dense clusters, because their samples are dominated respectively by local superclusters and by Perseus-Pisces supercluster. It is important to test whether or not the same dependence holds for a statistically fairer sample.

To answer these questions, we estimate the two- and three-point correlation functions for galaxies in the ESO/Uppsala (hereafter ESO) catalog (Lauberts 1982), and analyze their dependence on the morphological type. This catalog is one of the largest catalogs in the southern hemisphere with a complete list of morphological type. It is also completely selected by a angular-diameter criterion. Furthermore, the catalog has a very similarly selected partner, the UGC catalog (Nilson 1973), in the northern hemisphere, which enables us to compare galaxy distributions in both hemispheres.

§5.2 summarizes data and samples. In §5.3 we present the results of the two- and three-point correlation functions for various samples, without dividing galaxies according to morphological type. The morphology dependence of the correlation functions is analysed in §5.4. §5.5 contains our conclusions.

5.2 Data and samples

We form samples from the ESO catalog (Lauberts 1982). Since we will also use the UGC catalog (Nilson 1973), it is also summarized below. The ESO catalog covers the sky south of $\delta = -17.5°$ and the UGC catalog covers the sky north of $\delta = -2.5°$. Both catalogs are claimed to be complete to a major-blue diameter (d_1) of 1 arcmin. We form samples in the region $b^{\mathrm{II}} \leq -25°$ (ESO) and $b^{\mathrm{II}} \geq 25°$ (UGC) with different angular-diameter limits $d_{1,\mathrm{lim}}$ [$\log d_{1,\mathrm{lim}}$ changes from 0.00 to 0.65 with increment 0.05; the samples are named as follows: E00 (U00) denotes the sample with $\log d_{1,\mathrm{lim}} = 0.00$, E05 (U05) denotes that with $\log d_{1,\mathrm{lim}} = 0.05$, and so on].

The selection effects due to the galactic obscuration are examined. The distribution of the galaxy density as a function of declination and galactic latitude is determined and compared with that expected from a random distribution over the same sample regions. The results are presented in Figure 5.1.

For the ESO catalog, the $b^{\rm II}$-dependence is negligible in the chosen region (Figure 5.1b) and there is a tendency for the galaxy density to decrease at high (negative) values of declination (Figure 5.1a). The dependence is represented by the smooth curve drawn in the figure. A similar dependence is found for the distribution of Abell clusters in the southern hemisphere (Batuski et al. 1989). For the UGC catalog, we found a negligible δ-dependence (Figure 5.1c) but a strong density excess around the Galactic pole ($b^{\rm II} > 60°$) (Figure 5.1d). The latter is obviously not due to the galactic obscuration, but due to the presence of the Coma and Virgo superclusters. So we will make no correction for the UGC samples.

A diameter function of galaxies (DF) is needed to transform the angular correlation function to the spatial correlation function. We use the DF given by LRL:

$$\phi(D)dD = \phi_\star t^{-\mu}[1+t/\nu]^{-\nu}\left[\mu/t + (1+t/\nu)^{-1}\right]dt, \tag{5.3}$$

where D is the metric diameter; $t \equiv (D/D_\star)^2$. For the ESO catalog $\mu = 0.25$; $\nu = 3.05$; $D_\star = 7103\,\mathrm{kms^{-1}arcmin}$; $\phi_\star = 0.0101(h^{-1}\mathrm{Mpc})^{-3}$. For the UGC catalog $\mu = 0.16$; $\nu = 3.78$; $D_\star = 6073\,\mathrm{kms^{-1}arcmin}$; $\phi_\star = 0.0139(h^{-1}\mathrm{Mpc})^{-3}$.

5.3 The two- and three-point correlation functions

5.3.1 The two-point correlation function

The two-point angular correlation function $\omega(\theta)$ is estimated by the definition (see §3.1)

$$\omega(\theta) = \frac{n_R^2}{n^2}\frac{DD(\theta)}{RR(\theta)} - 1 \tag{5.4}$$

where $DD(\theta)$ is the number of data pairs with separation in the range $\theta \pm \Delta\theta/2$; $RR(\theta)$ is the corresponding count in a set of points randomly distributed within the sample boundary; n and n_R are respectively the mean number densities of the data sample and of

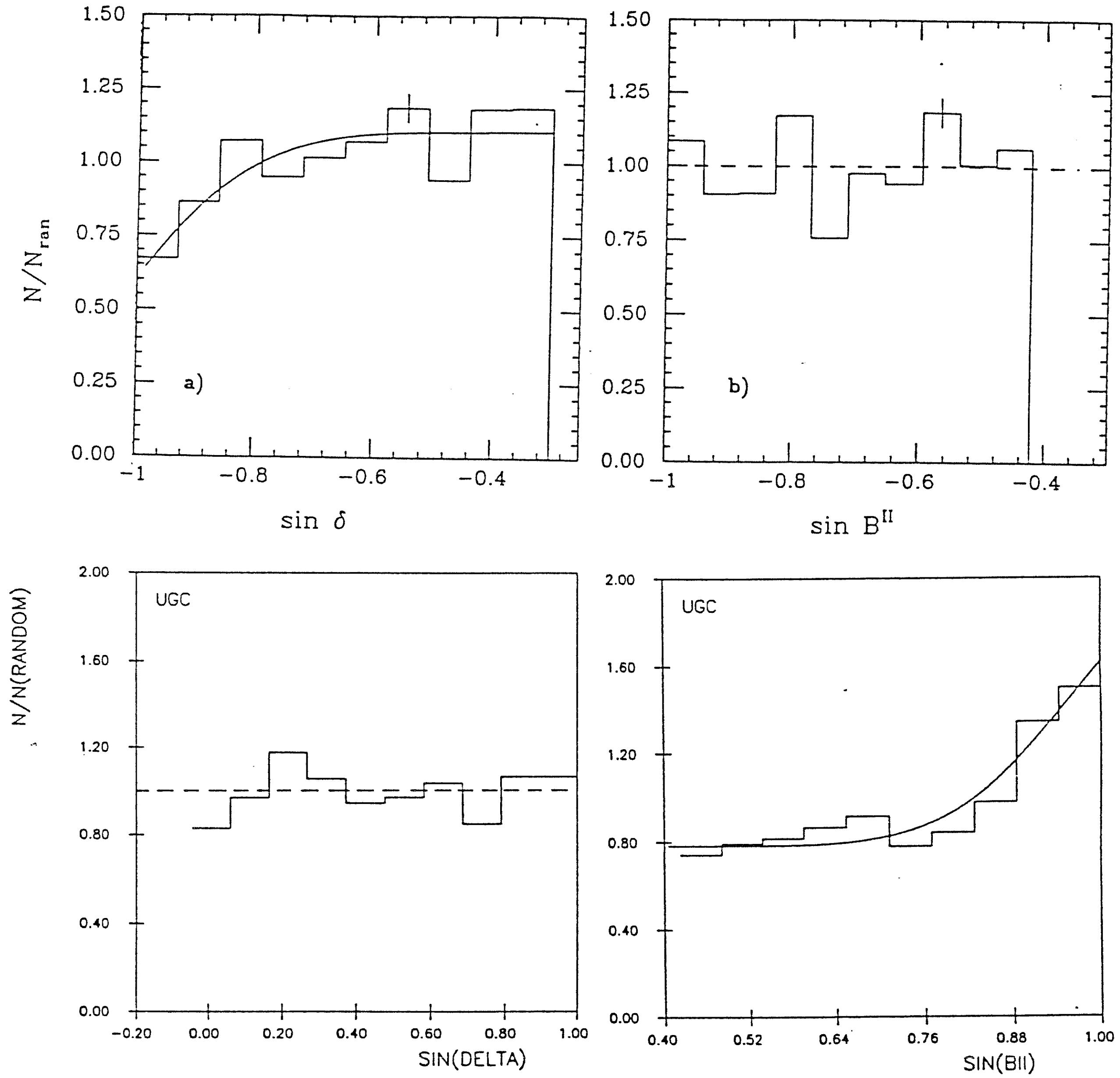

Figure 5.1 — *a*) The distribution of ESO galaxies (with $d_1 \geq 1.'0$) as a function of declination (as compared with a distribution of random points within the same boundary). The smooth curve represents the selection function used in our analysis. *b*) The same as a), but as a function of galactic latitude. *c*) and *d*) plot the corresponding curves for the UGC galaxies.

the random sample. For the ESO samples, the random sample is generated with the same declination dependence as is represented by the smooth curve in Figure 5.1a.

The pair counts *DD* and *RR* are estimated in 20 bins with the *i*th bin covering the

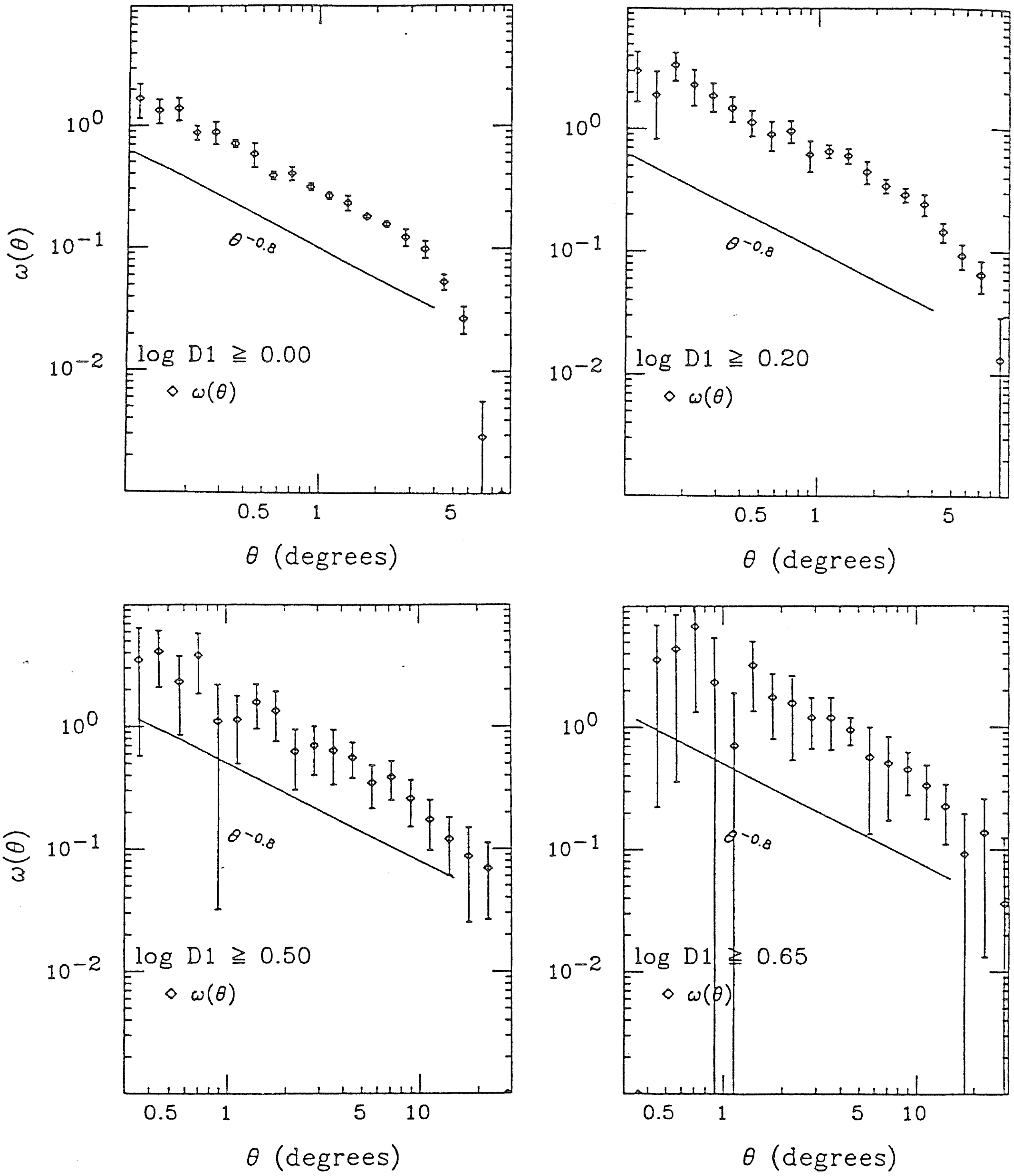

Figure 5.2 — Logarithmic plots of the two-point angular correlation functions for several typical samples (with their diameter limits indicated on the plots). The error bars represent 1σ variations among bootstrap resamplings.

Table 5.1

Fit of the two-point correlation functions

sample	N_g	θ°_{min}	θ°_{max}	β	B	P	$B_{0.8}$	$P_{0.8}$	r_0
E00	5477	0.10	4.00	0.79 ± 0.03	0.29 ± 0.01	0.91	0.29 ± 0.01	0.91	4.87 ± 0.07
E05	4523	0.10	4.00	0.79 ± 0.03	0.35 ± 0.01	0.97	0.35 ± 0.01	0.96	4.84 ± 0.08
E10	3574	0.13	5.01	0.86 ± 0.05	0.41 ± 0.02	0.98	0.42 ± 0.02	0.73	4.74 ± 0.11
E15	2371	0.13	5.01	0.84 ± 0.05	0.60 ± 0.03	0.74	0.57 ± 0.03	0.53	5.01 ± 0.12
E20	1889	0.16	6.31	0.89 ± 0.05	0.68 ± 0.04	0.70	0.61 ± 0.03	0.10	4.66 ± 0.12
E25	1362	0.16	6.31	0.87 ± 0.06	0.79 ± 0.05	0.88	0.71 ± 0.04	0.59	4.52 ± 0.13
E30	1051	0.20	7.94	0.92 ± 0.08	1.00 ± 0.07	0.99	0.88 ± 0.06	0.75	4.53 ± 0.16
E35	699	0.20	7.94	0.98 ± 0.08	1.31 ± 0.11	1.00	1.05 ± 0.08	0.71	4.47 ± 0.18
E40	487	0.25	10.00	1.03 ± 0.10	1.75 ± 0.16	0.99	1.39 ± 0.12	0.62	4.65 ± 0.22
E45	386	0.25	10.00	0.91 ± 0.10	1.81 ± 0.23	0.99	1.53 ± 0.15	0.99	4.37 ± 0.23
E50	303	0.32	12.59	0.90 ± 0.13	1.92 ± 0.37	1.00	1.51 ± 0.18	1.00	3.87 ± 0.25
E55	236	0.32	12.59	0.79 ± 0.13	1.99 ± 0.43	1.00	1.73 ± 0.19	0.98	3.72 ± 0.22
E60	199	0.40	15.85	1.00 ± 0.15	2.67 ± 0.62	1.00	1.73 ± 0.22	0.99	3.31 ± 0.23
E65	143	0.40	15.85	0.99 ± 0.20	3.79 ± 1.31	1.00	2.42 ± 0.33	1.00	3.55 ± 0.26

range $0.1 \cdot (i-1) - 1 < \log\theta \leq 0.1 \cdot i - 1$ for $\log d_{1,lim} \leq 0.45$ and $0.1 \cdot (i-1) - 0.6 < \log\theta \leq 0.1 \cdot i - 0.6$ for other samples. The bootstrap resampling technique (hereafter BRT, Barrow et al. 1984; Chapter 4) is used to estimate the error at each separation. In Figure 5.2 we plot $\omega(\theta)$ for several typical samples formed from the ESO catalog. The plots illustrate that the data points are guided well by a power-law

$$\omega(\theta) = B\theta^{-\beta} \tag{5.5}$$

at $\omega(\theta) > 0.1$. In Table 5.1, the results of the power-law fitting (which is given by minimizing χ^2 of the fit; the corresponding minimum is denoted by χ^2_{min}) of the estimates of the two-point angular correlation functions are presented for all the samples. The tail probability, $P = P(\chi^2 > \chi^2_{min})$, that the variable χ^2 of the chi-square-distribution for the given degrees of freedom exceeds χ^2_{min} is listed to represent the goodness-of-fit. $P(\chi^2 > \chi^2_{min})$ is calculated by assuming that the data points used for the fits (which are indicated by the range of θ, i.e., θ_{min} and θ_{max}, in Table 5.1) are independent. As we can see clearly from the table, for each sample, the power-law assumption [Eq.(5.5)] can be accepted at $\omega(\theta) > 0.1$, with the index β being about 0.8. We also try to fit the results by a single index $\beta = 0.8$ (which is approximately the weighted mean of the β values listed in Table 5.1). The results of the fit are also listed in Table 5.1 (with the amplitude B denoted by $B_{0.8}$ and the $\chi^2 > \chi^2_{min}$ probability P denoted by $P_{0.8}$). The χ^2-test shows that the universal power-law index ($\beta = 0.8$) can be accepted for all the samples. This result is remarkable, since the sample volume (given by the typical depth of the sample) varies from the shallowest ($\sim 25\,h^{-1}$Mpc) to the deepest ($\sim 120\,h^{-1}$Mpc) samples by a factor of ~ 100. The error estimated from the Poissonian variance of the pair counts is about half of that given by BRT. No universal power-law index can be accepted for all of the samples, if the Poissonian error estimate is used in the fitting.

The diameter function given by Eq.(5.3) is used in Limber's equation (§3.1.3) to compute the two-point spatial correlation functions with a power-law form represented by Eq.(5.1). We choose $\alpha \equiv 1 + \beta = 1.8$. The log$B$-log$d_{1,\mathrm{lim}}$ relation is drawn in Figure 5.3. For $\alpha = 1.8$ and a given r_0, the relation is a straight line with slope 1.8, for $B \propto (D_c^{-1} r_0)^\alpha \propto (d_{1,\mathrm{lim}} r_0)^\alpha$ where D_c is the characteristic depth of the sample. It is clear from Figure 5.3 that the data points can not be fitted (the fit in the following also refers to a weighted least chi-square) by a single value of r_0. We change r_0 to find a 'best fit' (i.e., to achieve a reasonable acceptance, e.g. $P > 5\%$, by removing the smallest number of data points), which gives $r_0 = 4.74\,h^{-1}$Mpc (the value of the variance among the used samples is about $0.20\,h^{-1}$Mpc which is compared to the largest internal error, $\approx 0.26\,h^{-1}$Mpc for the shallow samples) with $P \approx 15\%$. In this fit, we have to remove the data points for the four shallowest samples (E50, E55, E60, E65) and for the sample E15. Including E15 reduces $P(\chi^2 > \chi^2_{min})$ to $\sim 7\%$ which gives a marginally acceptable fit. The fit is not acceptable (with $P < 0.5\%$) if one or more data points of the four shallowest samples are used. We have also used other values of α. The results remain the same for all α values

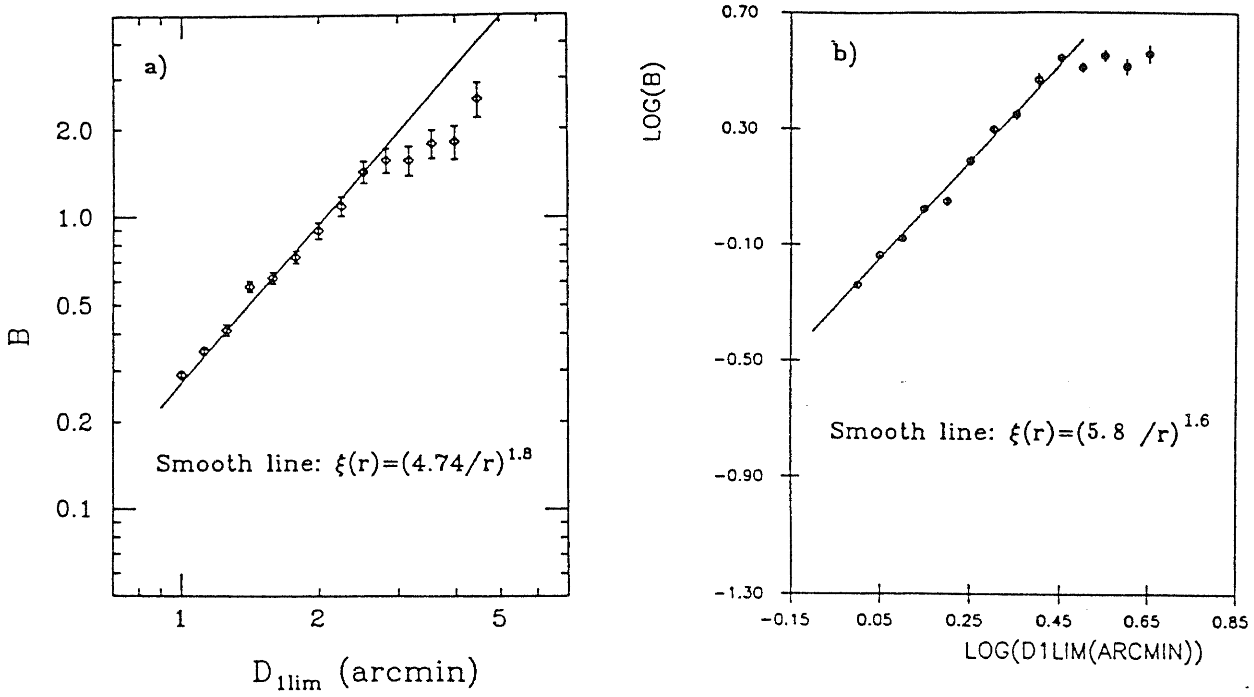

Figure 5.3 — *a*) The scaling of the angular correlation strength B with sample depth (represented by the diameter limit) for ESO samples. The straight line represents the power-law form of the two-point spatial correlation function indicated in the plot. The error bars represent variations in the power-law fits of the two-point angular correlation functions for the corresponding samples. *b*) The same as a), but for UGC samples.

that can be used in a power law fit [Eq.(5.5)] for each of the samples.

The deviations of the data points for the shallowest samples indicate a drop of the correlation function length of galaxies in the local region. For example, the correlation lengths for E60 and E65 are about $3.5\,h^{-1}$Mpc. A change of α in the acceptable range does not change the value significantly. A very similar behavior exists in the results of the similarly constructed UGC samples. Such a drop of correlation strength of galaxies in the local region is found by many other authors (e.g., Davis et al. 1978; Einasto et al. 1986; Börner & Mo 1990) and is interpreted as being due to a fractal structure in the galaxy distribution (e.g., Calzetti et al. 1988) or due to a density enhancement in the local region (Davis et al. 1988; Börner & Mo 1990). Our results show that the depth dependence of the galaxy correlation length is significant only in a region with depth $< 40\,h^{-1}$Mpc, giving support to the latter interpretation.

5.3.2 The three-point correlation function

The angular three-point correlation function $z(\theta_1, \theta_2, \theta_3)$ is defined by the joint probability of finding triplets in three surface elements $d\Omega_1$, $d\Omega_2$ and $d\Omega_3$ separated by θ_1, θ_2 and θ_3 on the celestial sphere:

$$dP = N^3[1 + \omega(\theta_1) + \omega(\theta_2) + \omega(\theta_3) + z(\theta_1, \theta_2, \theta_3)]d\Omega_1 d\Omega_2 d\Omega_3 \tag{5.6}$$

where n is the mean surface number density. Without loosing generality we can set $\theta_1 \leq \theta_2 \leq \theta_3$ and define another set of variables: $\theta = \theta_1$; $u = \theta_2/\theta_1$; $v = (\theta_3 - \theta_2)/\theta_1$. Here we use the following bins of θ, u, v:

$$\Theta_i < \theta \leq \Theta_{i+1} \qquad [\log(\Theta_{i+1}/\Theta_i) = 0.1, i = 1, \cdots, i_{max}, \Theta_1 = 0.1°];$$

$$U_i < u \leq U_{i+1} \qquad [\log(U_{i+1}/U_i) = 0.1, i = 1, \cdots, 10, U_1 = 1];$$

$$V_i < v \leq V_{i+1} \qquad [V_{i+1} - V_i = 0.1, i = 1, \cdots, 10, V_1 = 0].$$

We estimate the three-point correlation function for the sample E05. Since the power-law form of $\omega(\theta)$ holds only at $\theta \leq \theta_{max} = 4.0°$ for this sample, we limit our analysis to triangles with their longest sides smaller than θ_{max}. The value of i_{max} is determined by this condition. There are totally 922 bins.

Let DDD_{ijk} and RRR_{ijk} be respectively the counts of triplets in the bin $\Theta_i < \theta \leq \Theta_{i+1}$, $U_j < u \leq U_{j+1}$ and $V_k < v \leq V_{k+1}$ in the galaxy sample and in the random sample (the same random sample as in the estimate of the two-point correlation functions in §5.3.1). Integrating Eq.(5.6), we have:

$$Z_{ijk} = \frac{DDD_{ijk}}{RRR_{ijk}}(\frac{n_R}{n})^3 - 1 - W_{ijk}, \tag{5.7}$$

where

$$W_{ijk} = \frac{\int_{\Theta_i}^{\Theta_{i+1}} \int_{U_j}^{U_{j+1}} \int_{V_k}^{V_{k+1}} [\omega(\theta) + \omega(u\theta) + \omega((u+v)\theta)] \frac{1}{\Delta}\theta^3 (u+v) u d\theta du dv}{\int_{\Theta_i}^{\Theta_{i+1}} \int_{U_j}^{U_{j+1}} \int_{V_k}^{V_{k+1}} \frac{1}{\Delta}\theta^3 (u+v) u d\theta du dv}; \tag{5.7a}$$

$$Z_{ijk} = \frac{\int_{\Theta_i}^{\Theta_{i+1}} \int_{U_j}^{U_{j+1}} \int_{V_k}^{V_{k+1}} z(\theta_1, \theta_2, \theta_3) \frac{1}{\Delta}\theta^3 (u+v) u d\theta du dv}{\int_{\Theta_i}^{\Theta_{i+1}} \int_{U_j}^{U_{j+1}} \int_{V_k}^{V_{k+1}} \frac{1}{\Delta}\theta^3 (u+v) u d\theta du dv}; \tag{5.7b}$$

$$\Delta = \sqrt{4u^2 - ((u+v)^2 - 1 - u^2)^2}.$$

Knowing DDD_{ijk}, RRR_{ijk} and W_{ijk}, we obtain Z_{ijk} for each bin, using Eq.(5.7). The angular three-point correlation function can then be calculated from Eq.(5.7b). We fit the three-point spatial correlation function by two models (Q and Q_3 are constants):

$$\zeta(r_1, r_2, r_3) = Q[\xi(r_1)\xi(r_2) + \xi(r_2)\xi(r_3) + \xi(r_3)\xi(r_1)] + Q_3\xi(r_1)\xi(r_2)\xi(r_3) \qquad (5.8a)$$

with and without the cubic term. The corresponding models in the angular function can, by assuming the power-law form of $\xi(r)$ in Eq.(5.1), be written as (Tóth et al. 1989):

$$\begin{aligned} z(\theta_1, \theta_2, \theta_3) =& q[\omega(\theta_1)\omega(\theta_2) + \omega(\theta_2)\omega(\theta_3) + \omega(\theta_3)\omega(\theta_1)] \\ &+ q_3 \frac{180}{\pi} \frac{Y(\theta_1, \theta_2, \theta_3)}{H^3(\alpha)} \omega(\theta_1)\omega(\theta_2)\omega(\theta_3); \end{aligned} \qquad (5.8b)$$

where

$$H(\alpha) = \int_{-\infty}^{\infty} dx(1 + x^2)^{-\alpha/2};$$

$$Y(\theta_1, \theta_2, \theta_3) = \frac{1}{\theta_3} \int_{-\infty}^{\infty} dx[x^2 + 1]^{-\alpha/2} \int_{-\infty}^{\infty} dy[y^2 + 1]^{-\alpha/2}[(\frac{\theta_1}{\theta_3}x - \frac{\theta_2}{\theta_3}y)^2 + 1]^{-\alpha/2};$$

q/Q and q_3/Q_3 only depend on the DF and α (For the formulas, see Tóth et al. 1989). Actually we use the weighted least-chi-square to fit equation (5.7b) by expression (5.8b) to obtain q and q_3. The goodness-of-fit is represented by $P(\chi^2 > \chi^2_{min})$. The error in our fitting comes from two kinds of independent statistical uncertainties: that from DDD_{ijk} which is estimated by BRT and that from W_{ijk} which is given by the uncertainty in $\omega(\theta)$. We neglect the error from RRR_{ijk}, since we have constructed a large random sample (6,000 points) and used an interpolation formula for RRR_{ijk}.

For sample E05, there are 894 bins with counts ≥ 1. We only use these bins in our fitting, because BRT error of DDD_{ijk} in empty bins is zero. Had these small number (28) of empty bins been used, they would have overwhelming weight in χ^2- fitting and lead to incorrect results. In order to check sensitivity to the exclusion of these bins, we also fit the result by using bins with counts $\geq m\,(m = 2, \cdots, 20)$. All these bin choices give similar results, implying that excluding these empty bins does not influence our conclusions. The χ^2-test shows that the two models can all be accepted (with $P(\chi^2) \approx 1$) for all of the bin

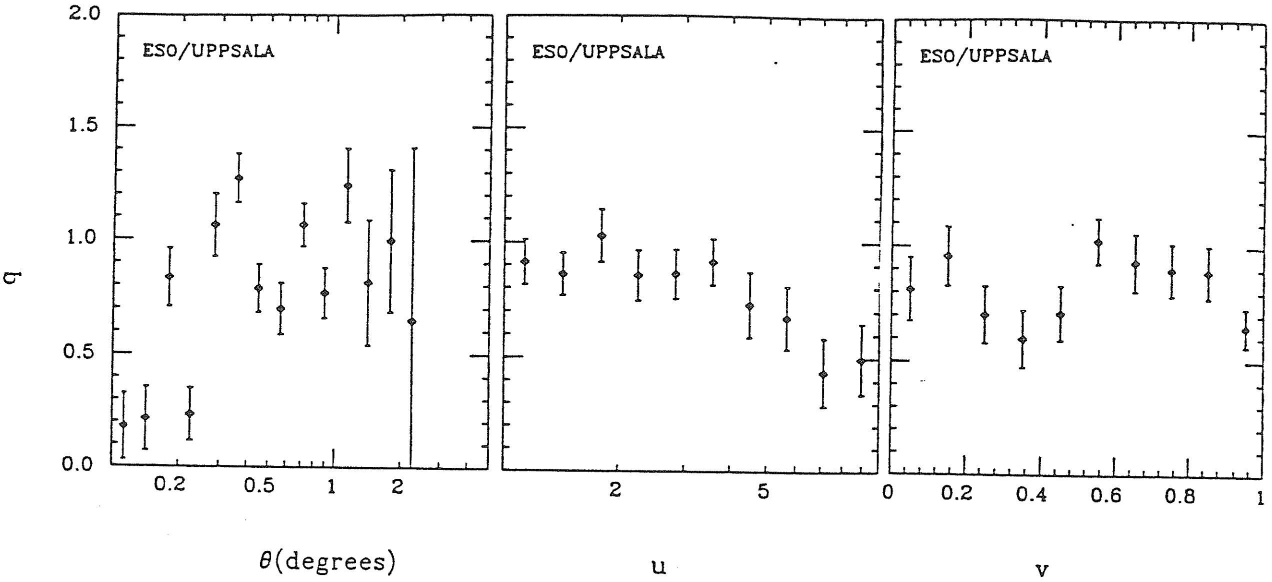

Figure 5.4 — The amplitude (q) of the three-point angular correlation function as a function of a) the size θ, b) the shape parameter u and c) the shape parameter v, obtained by using all bins with triplet-count ≥ 1. The error bars are 1σ variations among bootstrap resampling.

choices. This means that the cubic term is not important within the error of the results. The fitting without the cubic term gives a value of q in the range 0.79 — 0.92 for different bin choices, with $\bar{q} \approx 0.90$, $\sigma_q = 0.03$ (the internal error is about 0.04) and $q_3 < 0.16$. For illustration, we plot q with respect to θ, u, v for the fit with 894 bins in Figure 5.4.

Using the DF given in Eq.(5.3), we can find the conversion factors (see Tóth et al. 1989) $q/Q \approx 1.37$, $q_3/Q_3 \approx 8.09$. We then obtain $Q = 0.66 \pm 0.03$ and $|Q_3| < 0.02$. The value of Q obtained here is smaller than that given by GP. GP gave $Q = 1.29 \pm 0.21$. This discrepancy could be due to the fact that galaxy distribution in the southern hemisphere contains less prominent clusters than in the northern hemisphere. The result is in agreement with those given by Peebles (1981) ($Q = 0.68 \pm 0.05$) for the Rood sample and by Efstathiou & Jedrzejewski (1984) ($Q = 0.8 \pm 0.1$; see also Bean et al. 1983) for the CfA, AAT, KOS and KOSS redshift samples, all of which contain no prominent clusters.

We have carried out a similar analysis for sample U05, without removing the apparent galaxy concentration around the north pole of the Galaxy. We found $\bar{q} = 1.78 \pm 0.02$. Using the DF for UGC catalog (LRL), we obtained $q/Q \approx 1.32$; $q_3/Q_3 \approx 5.84$, which leads to

$Q = 1.35 \pm 0.02$, $|Q_3| < 0.02$.

It should be pointed out that, if we use error estimate given by a Poissonian distribution rather than by BRT, the result can not be fitted by the two models represented by Eq.(5.8) with reasonable degree of acceptance.

5.3.3 Discussion

It is interesting to compare our results with those obtained for other catalogs. The index of the two-point correlation function ($\beta = 0.8$) found here is in agreement with that found for many (northern) sky samples (see §3.2). The correlation length $r_0 = 4.74 \pm 0.20\,h^{-1}$Mpc is also in good agreement with the result ($r_0 = 4.7\,h^{-1}$Mpc) obtained in GP for the Lick catalog. The agreement is remarkable, considering that the Lick catalog is differently selected (magnitude selected), much deeper (about two times as deep) and covers a different sky region ($\delta > -23°$) than the ESO catalog. Our results show that samples selected by diameter give practically the same results for the two-point correlation function of galaxies. The results also demonstrate that $\omega(\theta)$ obeys a scaling relation represented by $\alpha \approx 1.8$ and $r_0 \approx 4.7\,h^{-1}$Mpc for all samples deeper than $\sim 40\,h^{-1}$Mpc.

Very recently Maddox et al. (1990a) have reported their results of the two-point correlation functions for samples constructed from the APM galaxy survey. They found a larger correlation length than that obtained here. A possible explanation could be that our correction for the declination dependence might erase some real clustering. If we calculate the two-point correlation function without correcting for the dependence, the correlation length becomes larger and the correlation index becomes smaller. It is unclear whether this declination dependence is due to clustering or it is due to a selection effect. For the UGC catalog, a strong excess of galaxy density was found only at $b^{\mathrm{II}} \geq 60°$. It is reasonable to assume that this dependence is due to galaxy clustering (around the galactic north pole) rather than galactic obscuration. In this case, we found a larger value of r_0 ($= 5.8 \pm 0.3\,h^{-1}$Mpc) and a smaller value of α ($= 1.6 \pm 0.1$).

The correlation length r_0 drops to $\sim 3.5\,h^{-1}$Mpc for the shallow samples (with depth $< 30\,h^{-1}$Mpc). This agrees with the result, $r_0 \approx 3.6\,h^{-1}$Mpc, for the bright galaxies (at $m \leq 13$) in the southern hemisphere (Davis et al. 1978). The analysis for UGC samples gives a very similar result. Our results demonstrate clearly that the depth-dependence is produced by the local region with a depth $\leq 40\,h^{-1}$Mpc.

The three-point correlation function has been demonstrated to obey the scaling relation given by Eq.(5.2) for galaxies (e.g., GP, Sharp et al. 1984) and for clusters of galaxies (Jing & Zhang 1989; Tóth et al. 1989). It is found that $Q \approx 1$. Our results show that galaxies in the ESO catalog also obey such a scaling relation, but with a smaller value of Q ($Q = 0.66 \pm 0.03$). This value is much smaller than that found by GP for the Lick catalog ($Q = 1.29 \pm 0.21$) and that obtained for the UGC catalog ($Q = 1.35$) by us. As pointed out by Peebles (1980), the existence of prominent clusters could enhance the value of Q. The low Q value we find for the ESO catalog could be due to the fact that the southern hemisphere contains less prominent clusters than northern hemisphere. It is interesting to note that redshift samples containing no prominent clusters also gave similar values: $Q \approx 0.7$ (Peebles 1981; Efstathiou & Jedrzejewski 1984).

The error estimates used for different quantities could be quite formal. The error at each bin in the two- and three-point correlation functions is estimated by BRT. The error is used only to weigh each point in the fitting. The errors quoted for the results (ΔB, $\Delta\beta$ for the two-point function; Δq, Δq_3 for the three-point function) for each sample are internal in the sense that they are estimated from the variance of the fit. The external errors based on the scatter of results among independent samples are larger. The universal scaling of $\omega(\theta)$ with depth can be accepted with higher confidence than that given by the χ^2 test. For the correlation length r_0, the standard deviation derived from the scatter of the results among the ten samples with $\log d_{1,\mathrm{lim}} < 0.5$ is about $0.2\,h^{-1}$Mpc which is comparable to the deviation ($0.26\,h^{-1}$Mpc) quoted by Peebles (1979) among galaxies of different fields. The deviation could be underestimated because the samples with different diameter limits are not completely independent. The error on Q quoted in our discussion represents only the internal error. The deviation among independent samples can be much larger (GP found $\Delta Q = 0.21$). A similar result might be obtained if we use the scattering among the results of different realizations of the bootstrap resampling.

5.4 Dependence on morphological type

The dependence of the two- and three-point correlation functions is analysed by using samples E05. The diameter limit ($\log_{10} d1 \geq 0.05$) is chosen for the sake of completeness. The sample is further divided into E (elliptical, lenticular and compact), S (Sa, Sab, Sb), and L (Sbc and later types) samples according to morphological types (see Table 5.2). The correction for the selection effects is made, and the two- and three-point correlation functions are estimated in the same way as in the last section.

5.4.1 The two-point correlation function

The two-point angular correlation function $\omega(\theta)$ is estimated by using Eq.(5.4). The pair counts DD and RR are estimated in 20 bins with the ith bin covering the range $0.1 \cdot (i-1) - 1 < \log\theta \leq 0.1 \cdot i - 1$ for each sample.

In Figure 5.5 we plot $\omega(\theta)$ for different morphological samples. The results clearly show that $\omega(\theta)$ of each sample can be fit by the power-law form [Eq.(5.5)] at $\omega(\theta) \geq 0.1$. In Table 5.2 we present the results of the power-law fitting for $\omega(\theta)$ by using the weighted least χ^2-techniques. The power law form [Eq.(5.5)] is acceptable for each sample. The early type galaxies have a slightly steeper slope than the other two types; the slopes of the S and L samples are comparable. Since $\alpha = \beta + 1$ without depending on the form of the diameter function, the dependence of the slope on the morphological type found here is much weaker than that found by Davis & Geller (1976, they found $\beta = 1.10 \pm 0.09$; 0.71 ± 0.05; 0.69 ± 0.06 for ellipticals, lenticulars and spirals, respectively) and Giovanelli et al. (1986, they found $\beta = 0.90 \pm 0.06$, 0.65 ± 0.07 and 0.37 ± 0.04 for the E, S and L types respectively). For the corresponding UGC samples (constructed from U05), we also found a weak morphology dependence: the slopes for the E, S and L samples are respectively 0.82 ± 0.06, 0.87 ± 0.12 and 0.54 ± 0.05.

Since there is no statistical results of the DFs for different morphological types, we assume that different morphological types obey the same form of the diameter function [Eq.(5.3)]. We should remember that the correlation length r_0 is sensitive to the form of the diameter function. From the Limber equation (Peebles 1980), we get the two-point spatial function $\xi(r) = (r_0/r)^{\beta+1}$, where r_0 is also listed in Table 5.2 for each sample. We see that the early type galaxies have a correlation strength about two times that of the

Table 5.2

Samples and their two-point correlation function

Sample	Morphology	N_g	θ°_{min}	θ°_{max}	$\beta \pm \Delta\beta$	$B \pm \Delta B$	$P(\chi^2)$	r_0
ESO-E	E-E0-S0a-Comp	861	0.1	4.0	0.96 ± 0.09	1.03 ± 0.10	1.00	8.35
ESO-S	Sa-Sab-Sb	1348	0.1	4.0	0.81 ± 0.09	0.49 ± 0.05	0.95	5.84
ESO-L	Sbc and Later	1719	0.13	4.0	0.83 ± 0.14	0.28 ± 0.03	1.00	4.29

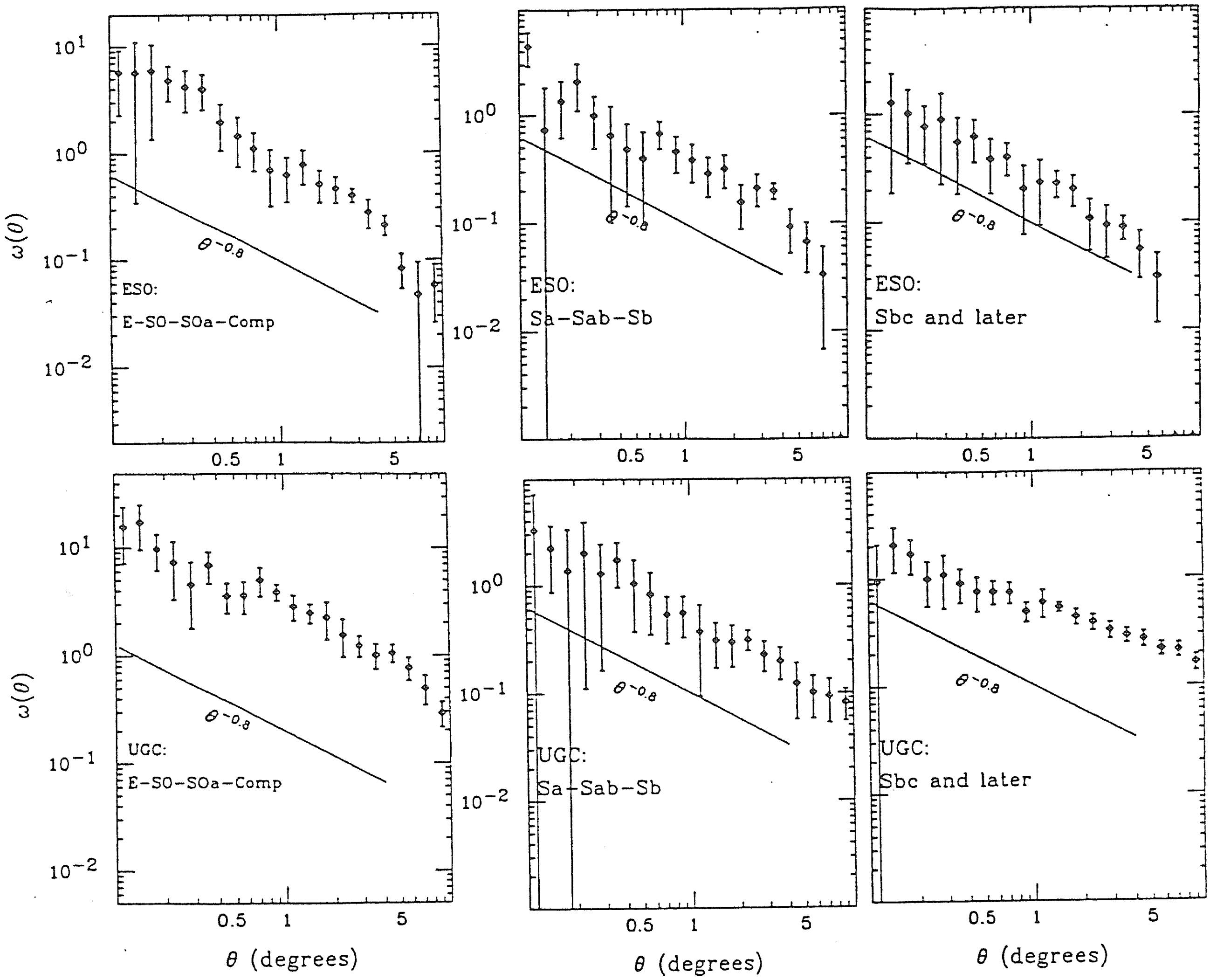

Figure 5.5 — Logarithmic plots of the two-point angular correlation functions for the morphology samples (with their morphological types indicated on the plots). The error bars represent 1σ variations among bootstrap resamplings.

S types and about four times that of the L types. The result is the same as that found by Davis & Geller (1976) and Giovanelli et al. (1986) for two-dimensional samples and by Börner et al. (1989) for redshift samples, indicating that the assumption of a universal diameter function for different types is reasonable for our purpose. The effective depth of the ESO catalog is about 70 h^{-1}Mpc. We see that the morphology dependence can exist on scales at least to $D_{eff}\theta_{max} \approx 5\,h^{-1}$Mpc.

5.4.2 The three-point correlation function

The three-point angular function for each morphology sample is calculated by using the following bins of θ, u, v:

$$\Theta_i < \theta \le \Theta_{i+1} \qquad [\log(\Theta_{i+1}/\Theta_i) = 0.2,\ i = 1, \cdots, i_{max},\ \Theta_1 = 0.1°];$$

$$U_i < u \le U_{i+1} \qquad [\log(U_{i+1}/U_i) = 0.2,\ i = 1, \cdots, 5,\ U_1 = 1];$$

$$V_i < v \le V_{i+1} \qquad [V_{i+1} - V_i = 0.2,\ i = 1, \cdots, 5,\ V_1 = 0].$$

We also limit our analysis to triangles with their longest sides less than $\theta_{max} \approx 5.0°$. There are totally 99 bins.

The results of the three-point functions for different morphological samples are presented in Table 5.3. The fitting is done in the same way as in §5.3.2. The upper limits of Q_3 for all of the bin choices are much smaller than Q (Table 5.3) for all the samples. Adding the cubic term reduces χ^2_{min} very little. So the cubic term is not important for galaxies of different morphological types, within the error of the statistics. The results of fitting without Q_3 for different bin choices are presented in Figure 5.6. We can easily see that, the E- and L- type samples have the same Q values within the statistical uncertainty; the mean value is about 0.6, which is in good agreement with the result for *all* galaxies without morphology division. However for the S sample, the Q value is much smaller and no meaningful signals are detected. A similar behaviour is seen in the results for the sample U05. In this case, the E and L types give a similar value $Q \approx 1.3$ which is in agreement with that found for the total sample; the S sample gives a much smaller value $Q \approx 0.7$. But the fits for bins with counts ≥ 7 give a similar Q value as the E and L samples.

Table 5.3

The three-point correlation functions

Sample	N_b	Q_3(upper limit)	Q(hierarchical)
ESO-E	92	0.03	0.55 ± 0.12
ESO-S	92	0.02	0.03 ± 0.12
ESO-L	90	0.05	0.48 ± 0.20
UGC-E	92	-0.05	1.08 ± 0.10
UGC-S	77	0.05	0.66 ± 0.20
UGC-L	93	-0.20	1.25 ± 0.10

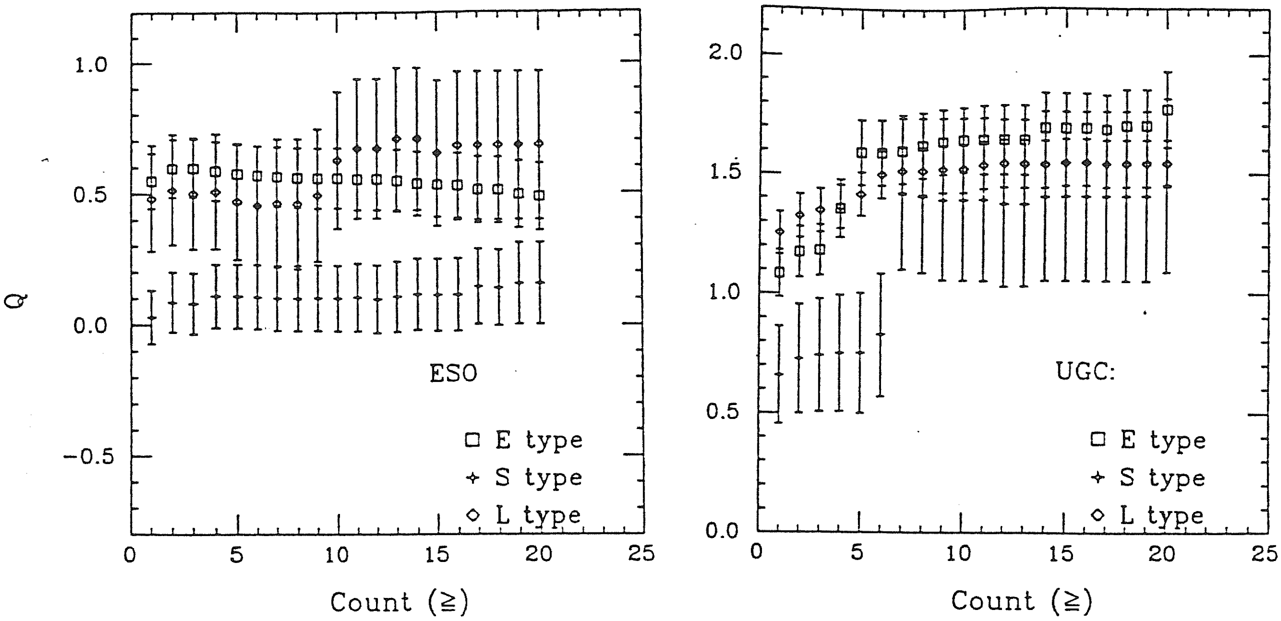

Figure 5.6 — The amplitudes (Q) of the three-point spatial correlation function for different bin choices (The morphological types are indicated on the figure). *a*) for the ESO samples; *b*) for the UGC samples. The error bars are 1σ variations among bootstrap resamplings.

5.4.3 Discussion

Since the slope of the two-point spatial correlation function is related to that of the angular function without depending on the form of the diameter function, our results suggest that the slopes of the two-point correlation functions for different morphological types are similar for a statistically fairer sample. The morphology dependence of the slope found before might be mainly due to galaxies in prominent clusters. The samples used by Davis & Geller (1976) and Giovanelli et al. (1986) are dominated respectively by the local superclusters and by the Perseus-Pisces supercluster. The fact that the northern sky contains several prominent clusters (Virgo, Coma and Perseus-Pisces) could account for some difference we found between the northern and the southern samples. It is interesting to note that the three dimensional analysis of CfA survey (Börner & Mo 1990) also gave a weak indication of morphology dependence.

If our assumption of a universal DF for different morphologies is not seriously in error, our results indicate that the clustering strength increases from late- to early- types. The trend is in good agreement with that given by previous studies for 2-D samples (Davis & Geller 1976; Giovanelli, et al. 1986) and for 3-D samples (Börner & Mo 1990). A more quantitative comparison between different morphological types needs more accurate knowledge of the DF. We should keep in mind that the uncertainty in DF can easily lead to a difference of a factor of 2 in the amplitude of ξ (Peebles 1980).

The results are interesting for the theories of galaxy formation. If the morphological segregation of galaxies is due to the fact that the galaxies of different types are formed on different peaks in a density field, as is predicted by the 'natural scheme' of the biased galaxy formation, galaxies with different types should have different two-point correlation strengths but approximately the same slope (Kaiser 1984; Bardeen et al. 1986). Environmental effects after galaxy formation can change such a relation in dense clusters (Whitmore 1989). The weak morphology dependence of the correlation slope for samples containing no prominent clusters may be due to biassing.

Previous studies have shown that the three-point correlation functions for galaxies (e.g., GP; Sharp et al. 1984) and clusters of galaxies (e.g., Jing & Zhang 1989; Toth et al. 1989) all obey the same hierarchical form with $Q \approx 1$. Using the void-probability function, Mo & Börner (1990) showed that the clustering of galaxies of different morphological types obey a similar hierarchical model. The results obtained here show that the three-point correlation functions for galaxies of different types also obey the hierarchical form

[Eq.(5.2)]. But the Q value for the ESO S sample is much smaller than those for the E and L samples. Such a difference could not be due to the difference in the DFs of different morphologies, since q/Q is insensitive to DFs. So it would be worthwhile to investigate such a difference by using a much larger sample.

5.5 Conclusions

In this paper, we analysed the angular two- and three-point correlation functions and their dependence on morphological types, using the diameter-limited samples constructed from the ESO-Uppsala catalog. We used the diameter function given by Lahav et al. (1988) to obtain the spatial functions. It is found that:

1. The two-point correlation functions for samples deeper than $\sim 40\,h^{-1}$Mpc can all be fitted by the power law $\xi(r) = (r_0/r)^{\alpha}$ with $\alpha = 1.8$, $r_0 = 4.74 \pm 0.20\,h^{-1}$Mpc. The result is in good agreement with that obtained for the magnitude-limited samples in the northern hemisphere, demonstrating that the diameter-limited samples can also be used to determine the two-point correlation, that the scalings for the two-point correlation function hold for galaxies in the southern sky.
2. The correlation length r_0 drops to about $3.5\,h^{-1}$Mpc for samples shallower than $40\,h^{-1}$Mpc. The result shows clearly that the depth-dependence of the two-point correlation function is produced by the local density enhancement with a depth smaller than $40\,h^{-1}$Mpc.
3. The early-type (elliptical, lenticular and compact) galaxies have a correlation strength about 2 times that for the early spirals (Sa, Sab, Sb) and about 4 times that for the late types (Sbc and later types). The result is in agreement with that for magnitude-limited samples.
4. The slope of the two-point correlation function does not depend strongly on morphological type. Our results suggest that the strong morphology dependence found before is mainly due to galaxies in some dominating clusters and that the morphological segregation outside clusters can be due to biassing.

5. The three-point correlation function for the ESO samples obey the hierarchical relation. The Q value is much smaller than that for the northern samples and in agreement with that for redshift samples containing no dominating clusters. The early spirals (Sa, Sab, Sb) give significantly smaller Q values than the other types. Whether the difference is real or it is due to that the early spirals have a different diameter function is not known.

‡The materials presented in this chapter are based on our paper: Jing, Y.P., Mo, H.J. & Börner, G. 1991, *Astronomy and Astrophysics*, **252**, 449.

6

Is the spatial cluster-cluster correlation function enhanced significantly by contaminations?

6.1 Introduction

In the past few years, both the angular and spatial cluster-cluster correlation functions have been studied in great detail (Hauser & Peebles 1973; Bahcall & Soneira 1983, hereafter BS83; Klypin & Kopylov 1983; Postman, Geller & Huchra 1986; Bahcall 1988a; see §3.2). Their results have consistently shown that Abell clusters (Abell 1958) of richness class $R \geq 1$ have positive correlations out to $70 \sim 100\ h^{-1}$ Mpc. The rich cluster-cluster correlation function, ξ_{cc}, is well represented by a power-law, $\xi_{cc} = (r_\circ/r)^\gamma$, with $\gamma \approx 1.8$ and $r_\circ \approx 25\ h^{-1}$ Mpc. Such a large correlation amplitude and coherence length strongly challenge the traditional galaxy formation theories which assume a Gaussian spectrum of the primordial density perturbations in an $\Omega = 1$ Universe. In particular, the standard biassed CDM model fails to reproduce the observed ξ_{cc} although it is consistent with many other features of galaxy clustering and with the microwave background radiation anisotropies (Davis et al. 1985, White et al. 1987a,b; Frenk et al. 1988).

Since the Abell clusters were selected by eye as surface galaxy-density peaks, some fraction of the clusters could result from the superposition of foreground and/or background galaxies or galaxy groups. If the 'artificial' clusters are the products of such chance superpositions then they would introduce a random component in the cluster catalogue, leaving ξ_{cc} mostly unaffected. If, however, the superposition effect is, as expected (Lucey 1983), correlated with the position of rich clusters (i.e., the high galaxy density around rich Abell clusters tends to increase the mean galaxy density around them and therefore nearby, in angular space, clusters could be revealed that otherwise would not have fulfilled the Abell selection criteria) then the 'artificial' clusters could spuriously enhance the spatial clustering of clusters, which would be manifested especially along the line-of-sight. In this work we are interested in this later type of cluster contamination which presently is in debate whether it can seriously enhance the amplitude of the cluster-cluster correlation function. Several tests like the scaling dependence of ξ_{cc}, the cross-correlation of different distance-class cluster samples and the *finger-of-God* effect (e.g., Bahcall 1988a; Szalay, Hollósi & Tóth 1989; Huchra et al. 1990b) show that contaminations have probably little effect on the estimation of ξ_{cc}. Furthermore, X-ray selected clusters and cD clusters, which should be less affected by contaminations, show as strong correlation functions as those of BS83 (Lahav et al. 1989; West & Van den Bergh 1991).

Two approaches have been used in an attempt to model the contamination effects and to correct the original ξ_{cc} and both have shown that ξ_{cc} could be seriously enhanced by such effects.

The first approach has been to correct the original galaxy count of each Abell cluster due to contaminations from neighbouring clusters, according to a model of the spatial and luminosity distribution of galaxies in clusters (Dekel et al. 1989; Olivier et al. 1990). These authors construct the galaxy distribution around each cluster centre using the observed cluster-galaxy cross-correlation function (Seldner & Peebles 1977; Lilje & Efstathiou 1988) while assuming spherical cluster halos and using the field galaxy luminosity function (Efstathiou, Ellis & Peterson 1988). Finally, after the above procedure has been applied and 'double' counted galaxies are eliminated, the clusters which have a corrected galaxy count < 50 are excluded from the catalogue. This results in a 10% to 15% decrease of the number of Abell clusters and a significantly weaker 2-point cluster correlation function. However, neither clusters are spherical [in fact they are highly flattened (Binggeli 1982; Plionis, Barrow & Frenk 1991)] and therefore the total projected area covered by each cluster is probably smaller than what expected in the spherical cluster model, nor do galaxies in clusters seem to follow a universal luminosity function (see discussion in Binggeli, Sandage & Tammann 1988). Furthermore, the high percentage of contamination found by the above model is in disagreement with a recent estimate of only a $\sim 3\%$ contamination based on redshift surveys of individual cluster regions (Struble & Rood 1991b). Note that such a small cluster contamination should have negligible effect on the statistics of ξ_{cc} (as compared with those of Olivier et al.).

The second approach (Sutherland 1988, hereafter S88 and Sutherland & Efstathiou

1991, hereafter SE91) has been to calculate the redshift correlation function within some fixed angle separation, $\xi_\theta(\Delta z)$, or within some projected separation, $\xi_{r_p}(R_z)$. These authors found that there is a significant excess of cluster pairs relative to random samples, i.e., a large positive $\xi_\theta(\Delta z)$ and/or $\xi_{r_p}(R_z)$ at large redshift separations ($\Delta z > 0.02$), and they attributed this effect to significant cluster contamination. Their method, can only indirectly test the superposition/contamination effect but is, however, independent of the contamination model details and so it could be a useful measure of the effect.

The potential importance of the results of Sutherland and Efstathiou prompted us to carefully check their reality. As well known, there are abundant large supercluster chains and voids in the spatial distribution of Abell clusters (e.g., Bahcall & Soneira 1984; Batuski & Burns 1985a,b; Tully 1987). Since the numbers of clusters involved in these studies are small, strong clustering of small number of clusters could produce certain specific patterns of superclustering and the resulting redshift correlation functions could be nonzero even on large redshift separations. In §6.2 we point out that the manifestation of real clustering and of the effects of contamination is rather different and we propose a *consistency* check between different cluster samples as means of discriminating between these two distinctive effects. Three observational data sets are used in our analysis, which are the redshift complete samples of Abell clusters used in S88 and SE91. Our results do not support the contaminations origin of the Sutherland effect but rather, they support real clustering as the origin of this effect.

To substantiate this indication we produced a set of simulated clusters, selected as peaks of a density field, the power spectrum of which is so chosen that the peaks have the same two-point correlation function as the Abell clusters (details in §6.3). The simulated catalogues are constructed in the same sky area and with the same selection functions as those of the real samples and they are analysed in an attempt to investigate *at what frequency can we observe the Sutherland effect in the simulated data which by construction have no contamination effects.*

6.2 Samples, redshift selection functions and analysis

6.2.1 Samples and definitions

Our first sample (hereafter DR41) includes all 100 clusters in the Abell catalogue with distance class $D \leq 4$, galactic latitudes $|b^{II}| \geq 30°$, richness $R \geq 1$ and redshift $z < 0.12$. This redshift limit is imposed in order to properly compare data and simulations (§6.3) since the simulation volume is a 640 h^{-1} Mpc ×640 h^{-1} Mpc ×640 h^{-1} Mpc box. Neglecting the 3 clusters with $z > 0.12$ is certainly unimportant to our analysis. Relaxing the richness constraint to include $R = 0$ clusters with measured redshifts $z \leq 0.12$, we obtain our second sample (hereafter DR40) which contains 210 clusters. The third sample (hereafter 'Deep') is from the complete deep survey of Huchra et al. (1990b), which contains 132 Abell clusters in the region $58° \leq \delta \leq 78°$ and $10^h \leq \alpha \leq 15^h$ with $z \leq 0.24$. All cluster redshifts used are from the updated compilation of Struble & Rood (1991a) and Huchra et al. (1990b). Comoving distances to clusters are estimated from redshifts using the standard relation (Mattig 1958):

$$R = \frac{c}{H_\circ q_\circ^2(1+z)} \left[q_\circ z + (1-q_\circ)(1-\sqrt{2q_\circ z+1})\right] \tag{6.1}$$

with $H_\circ = 100\ h$ km sec^{-1} Mpc^{-1} and $q_\circ = 0.5$ (as used by BS83). We now define the redshift correlation function within a fixed angular or projected spatial separation range:

$$\xi_{\mathcal{A}}(\mu) = \frac{N_{\mathcal{A}}^{cc}}{\langle N_{\mathcal{A}}^{rr}\rangle} - 1 \tag{6.2}$$

where $(\mathcal{A},\mu) = (\theta,\Delta z)$ for the angular separation case and $(\mathcal{A},\mu) = (r_p,R_z)$ for the projected spatial separation case. These correlation functions measure the excess, over random, number of clusters with redshift separation Δz (or R_z) at a certain angular or projected spatial separation range, $\mathcal{A}_1 \leq \mathcal{A} \leq \mathcal{A}_2$. $N_{\mathcal{A}}^{cc}$ is the number of sample cluster pairs and $\langle N_{\mathcal{A}}^{rr}\rangle$ is the expected number of random pairs at the same angular or projected separation range. The random catalogues are, of course, constructed using the same boundaries and selection functions as the real data. In all of the following analysis we adopt the BS83 galactic selection function:

$$P(|\,b\,|) = \text{dex}\ [0.3(1-\text{cosec}\ |\,b\,|)] \tag{6.3}$$

6.2.2 Dependence of $\xi_{\mathcal{A}}(\mu)$ on the redshift selection function

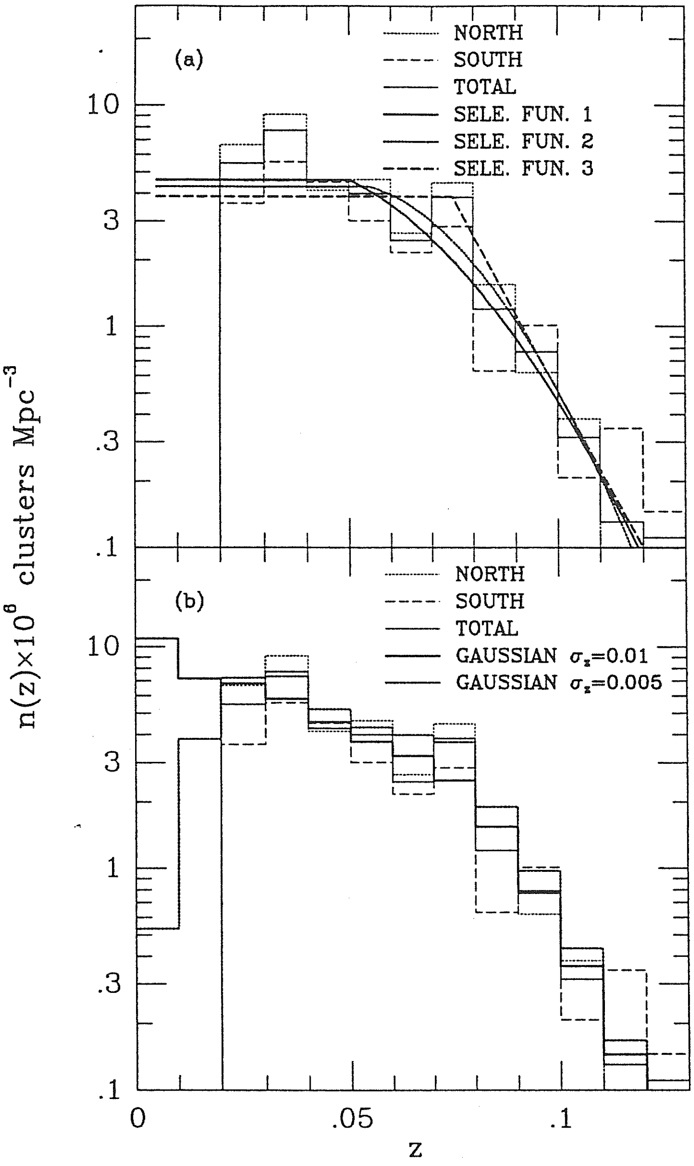

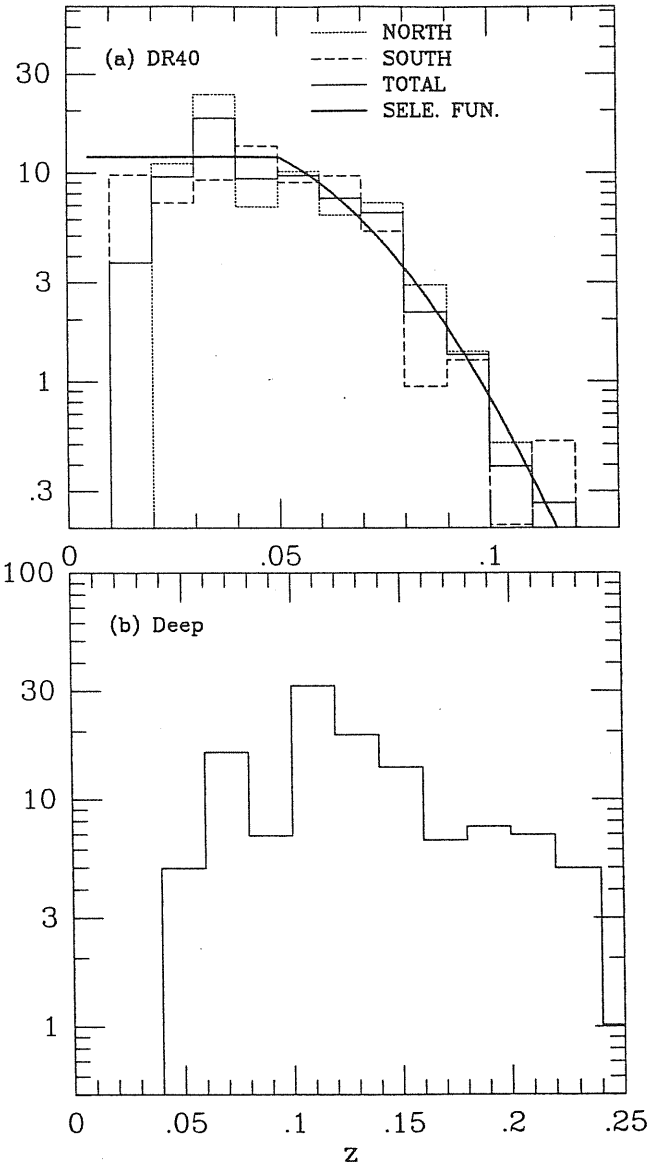

Figure 6.1

Figure 6.3

Figure 6.1 — The spatial density distribution of DR41 clusters as a function of redshift, plotted respectively for the north and south Galactic hemispheres as well as for the whole sky (details in the text). *a*). The three smooth redshift selection functions; *b*). The two selection functions based on a Gaussian convolution of the observed cluster redshifts with a dispersion σ_z (indicated in the plot).

Figure 6.3 — The spatial density distributions of: *a*). DR40 cluster sample (together with the RSF); *b*). 'Deep' cluster sample.

If one carefully examines the excess number of DR41 cluster pairs, $\Delta F_\theta(\Delta z)$, given by BS83 (their Figure 8) and $\xi_\theta(\Delta z)$ given by S88 (his Figure 2), she/he can easily find some discrepancies. For the angular separation $10^\circ \leq \theta \leq 25^\circ$ and redshift separation $\Delta z = 0.055 \sim 0.06$, $\Delta F_\theta(\Delta z)$ is negative while $\xi_\theta(\Delta z)$ is positive. Furthermore $\xi_\theta(\Delta z)$ remains almost at a constant value of ~ 0.3 in several redshift bins around $\Delta z = 0.05$, while there are large fluctuations in $\Delta F_\theta(\Delta z)$. These differences cannot be explained even by normalizing $\Delta F_\theta(\Delta z)$ by random pairs to obtain $\xi_\theta(\Delta z)$. Such discrepancies, however, could arise from different choices of the redshift selection function (RSF) used to construct the random samples.

We choose the $\xi_\theta(\Delta z)$ measure and the DR41 sample to illustrate the sensitivity of the redshift correlation analysis to the choice of the RSF. Since the spatial distribution of clusters is rather clumpy and we have no *a priori* knowledge of the intrinsic RSF, we use six different RSF models. In Figure 6.1 we plot the DR41 cluster density distribution and the different RSF models. The first three RSFs are smooth fits to the density distribution, giving different weight to the peak at $z = 0.075$. The other three RSFs are given by random assignments of the observed redshifts perturbed with a Gaussian dispersion in z of $\sigma_z = 0.0$, 0.005 and 0.01 (if $\sigma_z = 0$ then the RSF is identical to the sample density distribution). The RSFs with $\sigma_z = 0.005$ and 0.01, shown in Figure 6.1b, are estimated by constructing 1000 random samples. Since the peak around $z \approx 0.075$ is the result of strong clustering of several superclusters (Bahcall & Soneira 1984), we think that the solid line in Figure 6.1a probably represents better the sample redshift selection effects than the dotted or dashed lines.

The dependance of $\xi_\theta(\Delta z)$ [for the DR41 sample] on the different RSFs is shown in Figure 6.2. Different histograms correspond to the different RSFs. It is evident that $\xi_\theta(\Delta z)$ is quite sensitive to different RSFs, especially at small and large Δz. Some distinctive peaks at $\Delta z > 0.05$ in S88 vanish or are compressed significantly by choosing certain RSFs (e.g., the first RSF and the one based on random redshift assignments with a Gaussian dispersion). However, some high peaks around $\Delta z \sim 0.04$ do not disappear under any reasonable choice of the RSF, confirming the S88 effect. It is valuable to keep in mind that our inaccurate knowledge of the RSF can quite easily lead to a $\sim 25\%$ - 30% uncertainty in $\xi_\theta(\Delta z)$ although the dependence of the spatial correlation function $\xi(r)$ on the different

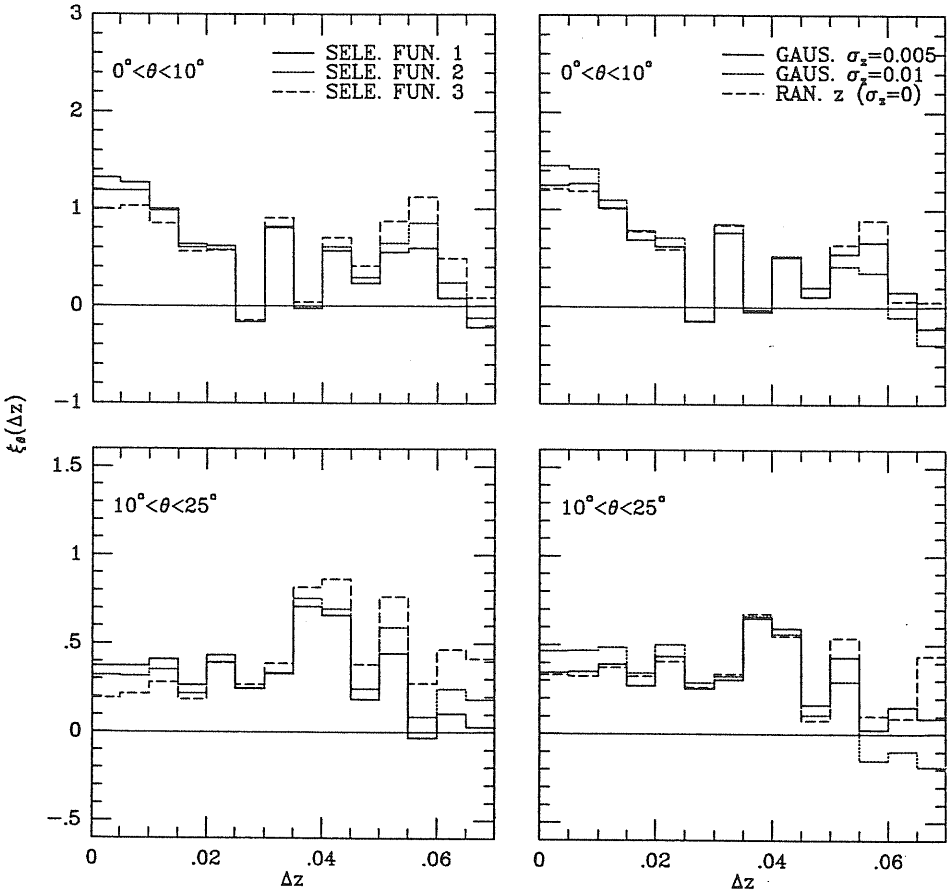

Figure 6.2 — The DR41 redshift correlation functions $\xi_\theta(\Delta z)$ estimated from the six different selection functions, shown in Figure 6.1.

RSFs is much weaker than that of $\xi_\theta(\Delta z)$ (less than 5% difference for the different RSFs models at $r < 50\ h^{-1}$ Mpc).

In the following analysis we use the RSF represented by the solid line of Figure 6.1 (RSF No 1) for the DR41 sample but note that our final results are mostly independent of this choice. The cluster density distribution of the DR40 sample with its smooth fit and the 'Deep' samples are plotted in Figure 6.3. A smooth function does not fit nicely the density distribution of the 'Deep' sample and we therefore use the RSF based on random assignments of the observed redshifts perturbed with a Gaussian dispersion of $\sigma_z = 0.01$.

6.2.3 Consistent comparison between three samples

S88 examined the redshift correlation functions $\xi_\theta(\Delta z)$ for the DR41 sample at angular separations $0^\circ \leq \theta \leq 10^\circ$ and $10^\circ \leq \theta \leq 25^\circ$, and for the DR40 sample at separations

$0^\circ \leq \theta \leq 6^\circ$ and $6^\circ \leq \theta \leq 12^\circ$. SE91 analysed the 'Deep' sample using the redshift correlation function $\xi_{r_p}(R_z)$ at projected separations $0 \leq r_p \leq 10\ h^{-1}$Mpc and $10 \leq r_p \leq 20\ h^{-1}$Mpc. Both studies have shown the same tendency; $\xi_\theta(\Delta z)$ and $\xi_{r_p}(R_z)$ do not vanish at large line-of-sight separations, which S88 and SE91 ascribed as evidences of strong cluster contaminations.

We should point out that the projected separations used in these two studies are quite different; angular separations of 10° correspond for the DR41 and DR40 samples to projected separations of $\sim 30\ h^{-1}$Mpc. In order to properly study the contamination effect using different samples, it is important to use the same physical projected separation. If the contamination effects are due to a unique physical process, they should show up at similar projected separations in the different samples. Furthermore, we should expect more contamination in samples including $R = 0$ clusters because of the higher cluster density and the possible incompleteness of the $R = 0$ clusters in the catalogue (Abell 1958). So a comparison between samples of different richness can give us an indication whether contamination is important. We should expect contaminations to be more significant at smaller angular and projected separations than in larger ones. Therefore, we feel that it is important to make a consistency check, applying the same technique and using the same projected separation on samples of different richness.

For the two shallow samples we study two bins in θ: $0^\circ < \theta < 10^\circ$ and $10^\circ < \theta < 25^\circ$, which are the ones used by S88 for the DR41 sample. Since the 'Deep' sample is about 3 times deeper than the DR41 and DR40, we use $0^\circ < \theta < 3.3^\circ$ and $3.3^\circ < \theta < 8.3^\circ$. The redshift correlation function $\xi_\theta(\Delta z)$ within these angular separations is shown in Figures 6.4a and 6.4b. The results are very instructive:

1.) On all angular and redshift separations, $\xi_\theta(\Delta z)$ of the DR40 sample is less than that of the DR41 sample. In fact, $\xi_\theta(\Delta z)$ of the DR41 sample is about 2 times larger than that of the DR40 sample [with only exception at $\Delta z > 0.035$ in the range $0^\circ < \theta < 10^\circ$ where the two samples have comparable $\xi_\theta(\Delta z)$]. This is consistent with the well-known richness dependent cluster clustering and inconsistent with the expectation the contaminations would have affected more the $R \geq 0$ sample.

2.) The only significant ($\geq 2\sigma$) peaks in $\xi_\theta(\Delta z)$, at the large angular separation range,

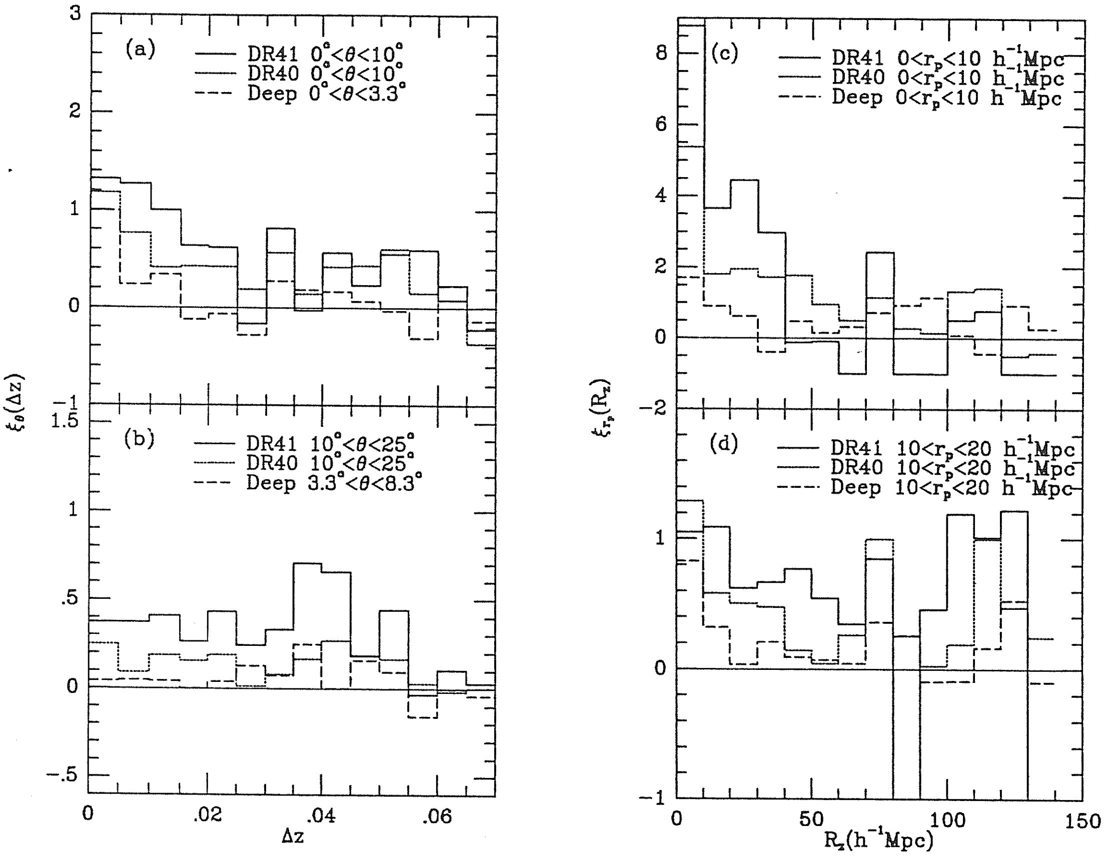

Figure 6.4 — The redshift correlation functions $\xi_\theta(\Delta z)$ [panels *a*) and *b*)] and $\xi_{r_p}(R_z)$ [panels *c*) and *d*)] of the three Abell cluster samples.

appear in the DR41 sample at $\Delta z = 0.0375$ and 0.04. These peaks are even larger than at the same Δz of the smaller angular separation range while, in general, we would expect contaminations to be more significant at the latter angular range.

3.) At the smaller angular range, $\xi_\theta(\Delta z)$ of the 'Deep' sample decreases much faster than that of the shallow samples and it is consistent with zero, within the typical Poisson error ($\sigma_\xi \approx 0.23$) for $\Delta z > 0.015$ (error bars have not been plotted on Figure 6.4 for clarity). The noticeable peaks at large Δz which show up in the two shallow samples do not appear in the 'Deep' one. Note that also for the 'Deep' sample we get that $\xi_\theta(\Delta z > 0.02)$ has similar or even higher values at the large angular separation range than at the smaller one.

Clearly all these points are contrary to the suggestion that contaminations are the main cause of the Sutherland effect.

Now we turn to the redshift correlation function $\xi_{r_p}(\Delta z)$ within a fixed projected separation range. We choose the same projected separations as in SE91. The results are presented in Figures 6.4c and 6.4d and can be summarized as following:

1.) For the DR41 sample, $\xi_{r_p}(R_z)$ is consistent with no correlation at $R_z > 40h^{-1}$Mpc for $r_p < 10\ h^{-1}$Mpc, while it does have some positive peaks at large $R_z = 50 \sim 130\ h^{-1}$Mpc for $10 < r_p < 20\ h^{-1}$Mpc most of which do not show up at the smaller r_p range (and at the same R_z).

2.) At the small projected separation range and for $R_z \geq 40\ h^{-1}$Mpc, $\xi_{r_p}(R_z)$ is generally higher in the two $R \geq 0$ samples than in the DR41 sample, which is consistent with our expectation that some contaminations may exist in the $R \geq 0$ samples.

3) At both, the small projected separation range with $R_z \leq 40\ h^{-1}$Mpc and the large one with the whole R_z range, $\xi_{r_p}(R_z)$ is systematically lower in the DR40 and 'Deep' samples than in the DR41 sample, consistent with richness-dependence clustering as proposed by BS83. We, therefore, have no evidence for significant contamination effects for $r_p \geq 10\ h^{-1}$Mpc even in the $R \geq 0$ samples.

Because of strong clustering and the small number of clusters involved, some significant peaks in the shallow samples might come from the particular way with which clusters are spatially distributed (e.g., certain orientation of supercluster chains, supercluster elongations, large voids, etc). The similarity of the shape of the redshift correlation functions of the DR40 and DR41 samples (which cover the same region of the sky), but with amplitudes about a factor 2 lower, is completely consistent with the dependence of cluster clustering on cluster richness, as found by BS83. However, for the DR40 sample some peaks in ξ_θ and ξ_{r_p} at the small angular and projected separations which are as high or higher than those of the DR41 sample, could be, at least partially, due to contamination effects.

In conclusion of this section; we have carefully examined the correlation functions $\xi_\theta(\Delta z)$ and $\xi_{r_p}(R_z)$ at two separation ranges for three redshift samples of Abell clusters. Our detailed, *consistency* check does not support that the distinctive peaks, seen in the two correlation measures, are mainly due to the contamination effects, as suggested by S88 and SE91. More precisely, we found no evidence for any significant contamination of the richness $R \geq 1$ cluster sample but we did find weak evidence, mostly from the $\xi_{r_p}(R_z)$ analysis, that the $R \geq 0$ samples (especially the DR40 sample) could be affected by contaminations. However, these effects could influence the clustering analysis of the $R \geq 0$ samples only at small projected separations ($r_p \leq 10\ h^{-1}$Mpc). Although the contaminations seem not to be the main cause of the distinctive peaks in the $\xi_{\mathcal{A}}(\mu)$, it is difficult with the present analysis to quantify the amount of contaminations in the Abell catalogue.

6.3 Comparison with simulations

In this section we will attempt to assess the probability of observing significant peaks in the redshift correlation function by analysing simulated cluster catalogues, which have similar clustering properties as the real samples and which are free, by construction, of the contamination effects.

6.3.1 Simulated cluster catalogues

The method we use to generate our simulated catalogues is similar to that of Postman et al. (1989) and it will be described in detail in §10.1. Here we shall only briefly describe the main points of our simulation method.

The simulations are performed in a cubic box with 64^3 grid cells corresponding to a volume 640 h^{-1}Mpc × 640 h^{-1}Mpc × 640 h^{-1}Mpc. Our simulated clusters are identified as high peaks of a density fluctuation field which is a Gaussian random field with a power-law power spectrum:

$$P(k) = \langle \mid \delta_k \mid^2 \rangle \propto k^n \tag{5.4}$$

A large number of points (> 70000) are randomly distributed inside the cube and each of them is assigned a density contrast $\delta_{\vec{g}} = \nu\sigma$ (where σ is the *rms* density fluctuation within the cube and $\vec{g}$ is the nearest grid point to the particle). Those particles with $\nu > \nu_{min}$ (here $\nu_{min} = 1.3$) are chosen as clusters. The amplitude and slope of the power spectrum are so adjusted that the simulated clusters have a two-point correlation function, $\xi = (r_\circ/r)^\gamma$, in the range of $10 \sim 70\ h^{-1}$Mpc with $r_\circ \geq 20\ h^{-1}$ Mpc and $\gamma = 1.8$. We generate two sets of simulated cluster catalogues (of 50 simulations each); one with $\langle r_\circ \rangle = 20\ h^{-1}$ Mpc, corresponding to the DR40 and 'Deep' sample correlation function and $\langle r_\circ \rangle = 25\ h^{-1}$ Mpc, corresponding to that of the DR41 sample.

Our final simulated cluster catalogues have the same geometrical boundaries as the real data and the individual clusters have been selected according firstly to the galactic latitude selection function and secondly applying the real-sample RSF. This procedure was stopped when the number of points was the same as the number of clusters in the real catalogues. To construct simulated cluster catalogues that resemble the DR41 or DR40 samples we set the *observer* at the centre of the simulation box while to simulate the 'Deep' sample we place the *observer* at one of the cube vertex. The RSF we use for both the DR40 and DR41 simulated samples is the smooth solid line shown in Figures 6.1 and 6.3. For the 'Deep' sample we use the RSF obtained by a random assignment of the observed redshifts perturbed by a Gaussian dispersion $\sigma_z = 0.01$. Note, however, that the redshift correlation function of the simulated catalogues depend rather weakly on the RSF choice, since the effects of the RSF are canceled by using the same RSF in the random catalogues which are used in order to obtain $\xi_{\mathcal{A}}(\mu)$.

6.3.2 Qualitative comparison of simulations with observations

Using the simulated cluster catalogues, we find that the distinctive peaks in the redshift correlation functions are quite common even at large redshift separations. As an illustration, we choose to present $\xi_\theta(\Delta z)$ of the simulated DR41 sample (qualitatively similar results are also obtained from the other samples).

In Figure 6.5, we plot the redshift correlation functions $\xi_\theta(\Delta z)$ for the first six DR41 simulated cluster catalogues (this choice is equivalent to a random one). Some features in the figure are very noticeable. Peaks and valleys are quite common even at large Δz. The amplitude of these peaks are comparable with those found in the observed sample. The peaks (or valleys) often appear coherent over some large range of redshift separations, Δz, probably because of the specific location of cluster associations in space.

In Figure 6.6, we plot $\xi_\theta(\Delta z)$ for another four simulated samples which have more similar $\xi_\theta(\Delta z)$ to that of the real data. In these simulated catalogues, $\xi_\theta(\Delta z)$ remain positive

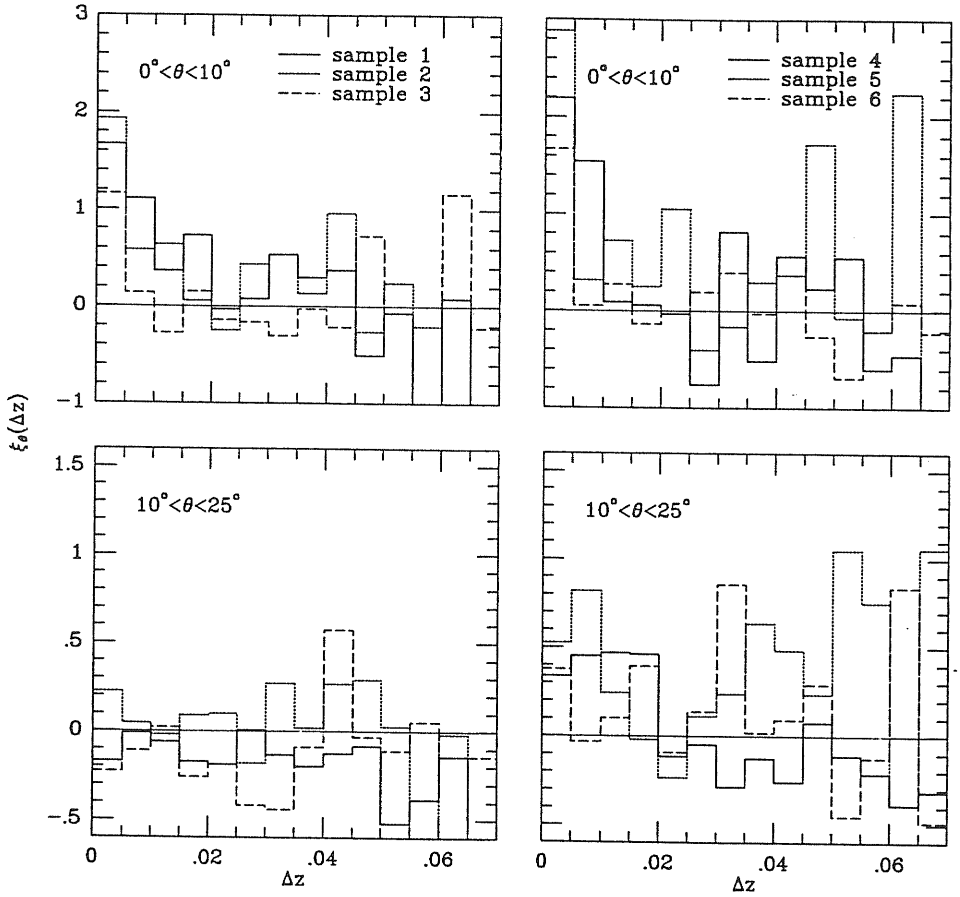

Figure 6.5 — The redshift correlation functions, $\xi_\theta(\Delta z)$, of the first six simulated DR41 cluster samples (this choice is equivalent to a random one).

on (almost) all redshift separations in the both small and large angular separations. We have checked whether this fact arises due to stronger cluster clustering in these samples, by calculating the two-point spatial correlation function $\xi(R)$ (Figure 6.7). Different symbols represent the correlation function of different samples, as indicated in the figure. The mean $\xi(R)$ over the fifty simulated samples and its standard deviation, σ, is also shown (dotted lines). We find no evidence that $\xi(R)$ of these four samples are systematically higher than the mean simulation values or than the real data values. This supports our expectations, stated in the previous section, that the distinctive peaks of the redshift correlation function in the real data are probably due to certain spatial superclustering patterns rather than being due to the contamination effects. Thus, the method of S88 to remove these peaks, which he regarded as being due to projection effects, would artificially remove signal of real clustering.

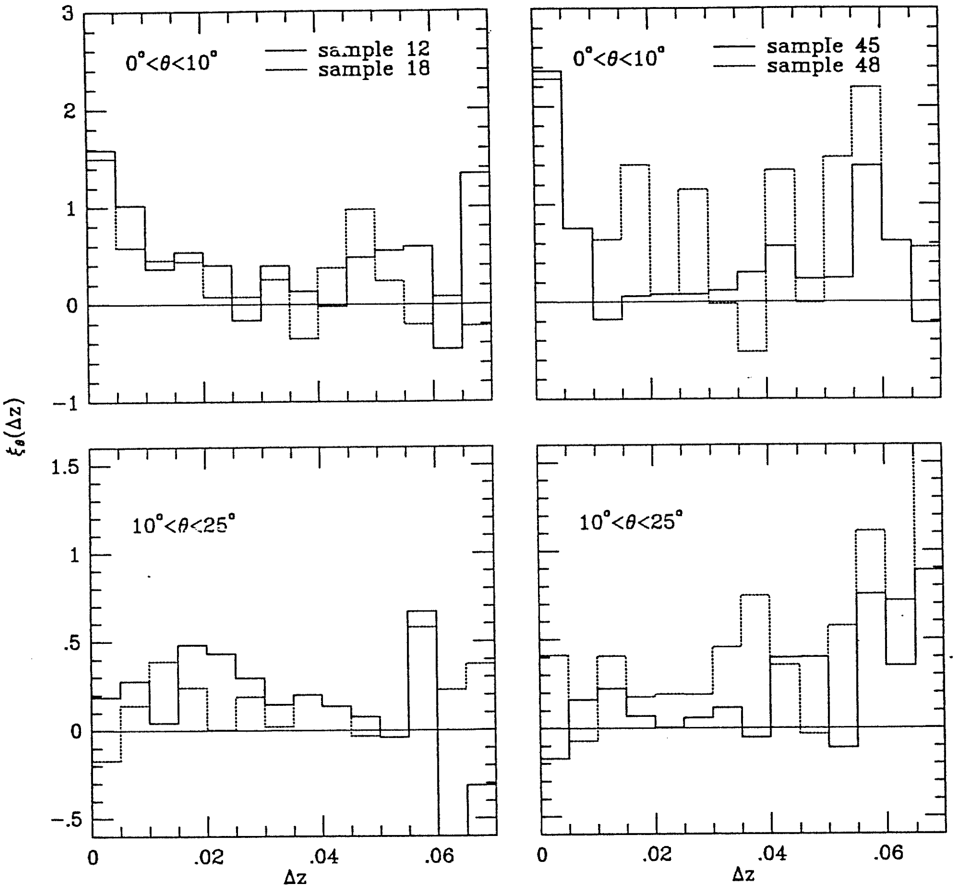

Figure 6.6 — The redshift correlation functions, $\xi_\theta(\Delta z)$, of four simulated DR41 cluster samples that resemble the features in $\xi_\theta(\Delta z)$ of the observed DR41 sample.

Another interesting feature that has been observed in the Abell cluster samples is the *redshift elongation* or *Finger-of-God* effect (Bahcall, Soneira & Burgett 1986). This manifests itself in the scatter-diagram of cluster pair separations as a systematic excess of pairs along the redshift axis R_z with respect to the orthogonal R_δ or R_α axis (declination and right ascension axes respectively), while limiting the separations along the third axis to $< 5\ h^{-1}$ Mpc. Bahcall, Soneira & Burgett (1986) attributed this effect to the existence of large ($\sim$ 2000 km s^{-1}) peculiar motions of clusters that belong in superclusters. To test this suggestion we checked whether this effect is apparent in any of our simulations (which we remind the reader are not dynamically evolved). Indeed, we did find that some of our simulations showed the same elongation effect, along the R_z axis (Figure 6.8), while some showed similar elongation effects along the orthogonal axis and others showed no such effects at all. However, the real data show a slightly crispier elongation along the R_z

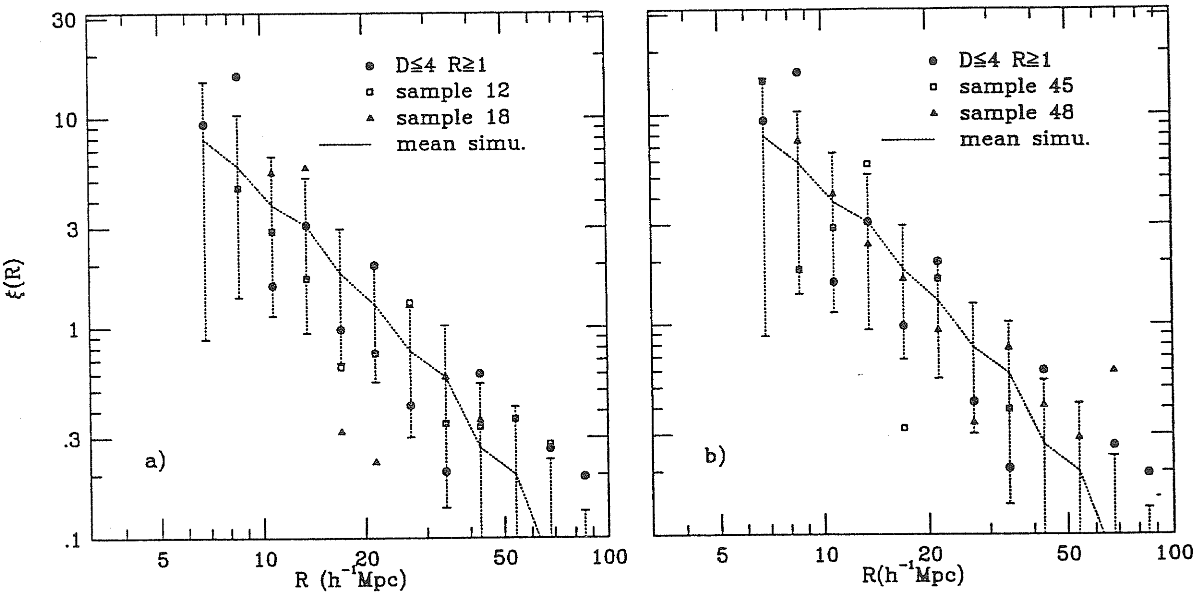

Figure 6.7 — The two-point spatial correlation functions, $\xi(R)$, of the the four simulated DR41 cluster samples of Figure 6.6 and of the DR41 sample. The mean values and the 1σ error bars from the 50 simulations are also plotted (dotted lines).

axis. Therefore, we conclude that a big part of the observed elongation effect could arise from low-order (2-p) cluster clustering coupled with the small number of clusters which often result in supercluster elongations along the line-of-sight (geometrical elongation was suggested as a possible explanation by Bahcall, Soneira & Burgett 1986). The rest of the signal could come from cluster peculiar velocities but of significantly lower amplitude < 1000 km s^{-1}. Such cluster peculiar velocities are suggested by independent estimates (e.g., Aaronson et al. 1986, Lucey & Carter 1988; Huchra et al. 1990b).

6.3.3 Quantitative comparison of simulations with observations

Now we quantitatively assess the statistical significance of our results. In Figure 6.9 and 6.10, we present the mean simulation redshift correlation functions (dotted lines) as well as those of the real samples (solid lines). In both angular separations (Figure 6.9), all $\xi_\theta(\Delta z)$ of the all three samples are consistent with the simulations within the $1 \sim 1.5\sigma$ significance level except for two peaks of the DR40 sample ($0° < \theta < 10°$ at $\Delta z = 0.0275$ and 0.0525) and for two peaks of the DR41 sample ($10° < \theta < 25°$ at $\Delta z = 0.0375$ and 0.04) which lie at $\geq 2\sigma$ level. Similar results are obtained analysing $\xi_{r_p}(R_z)$ (Figure 6.10). The

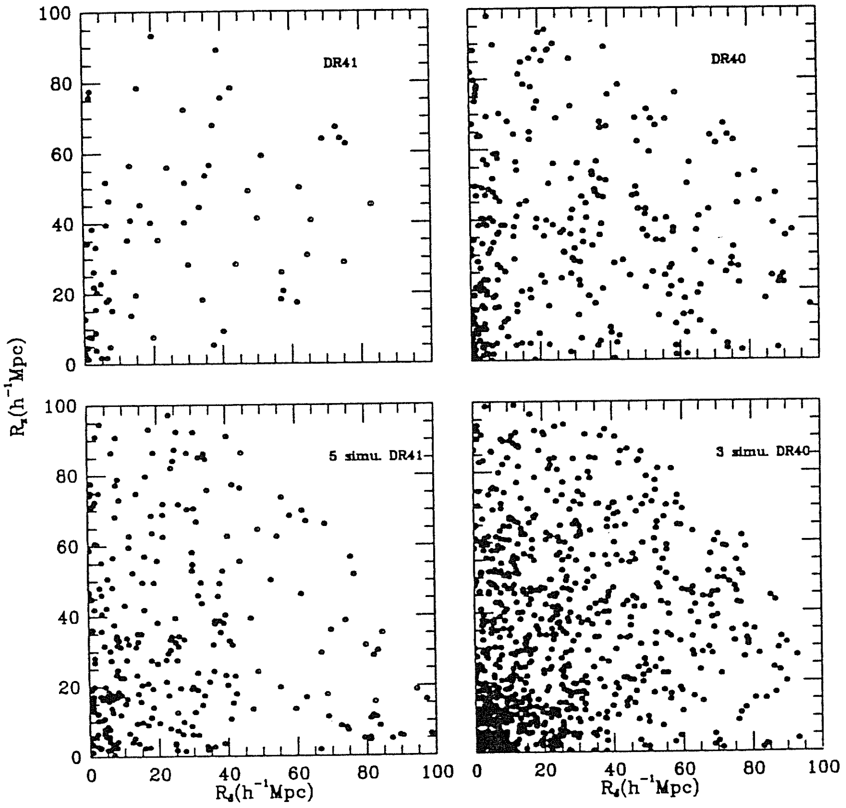

Figure 6.8 — Scatter diagrams of Abell cluster pairs (upper panels) and simulated pairs (lower panels) in the R_δ - R_z plane (in h^{-1} Mpc), with separations along the perpendicular plane < 5 h^{-1} Mpc (as in Bahcall et al. 1986). The elongation along the R_z direction is apparent in the real but also in the simulated data (although in the real case it seems crispier). The simulated catalogues used here where selected exactly because they appeared to have similar R_z - R_δ diagrams with those of the real data.

most significant deviations ($2 \sim 3\sigma$) between the observed and simulation average values of $\xi_{r_p}(R_z)$ appear at the smaller projected separation range between 30 $h^{-1} \leq R_z \leq 40$ h^{-1} Mpc only for the DR41 and DR40 samples. No such deviations are apparent in the 'Deep' sample.

To quantify these deviations we apply the χ^2-test. The χ^2 for each sample is estimated

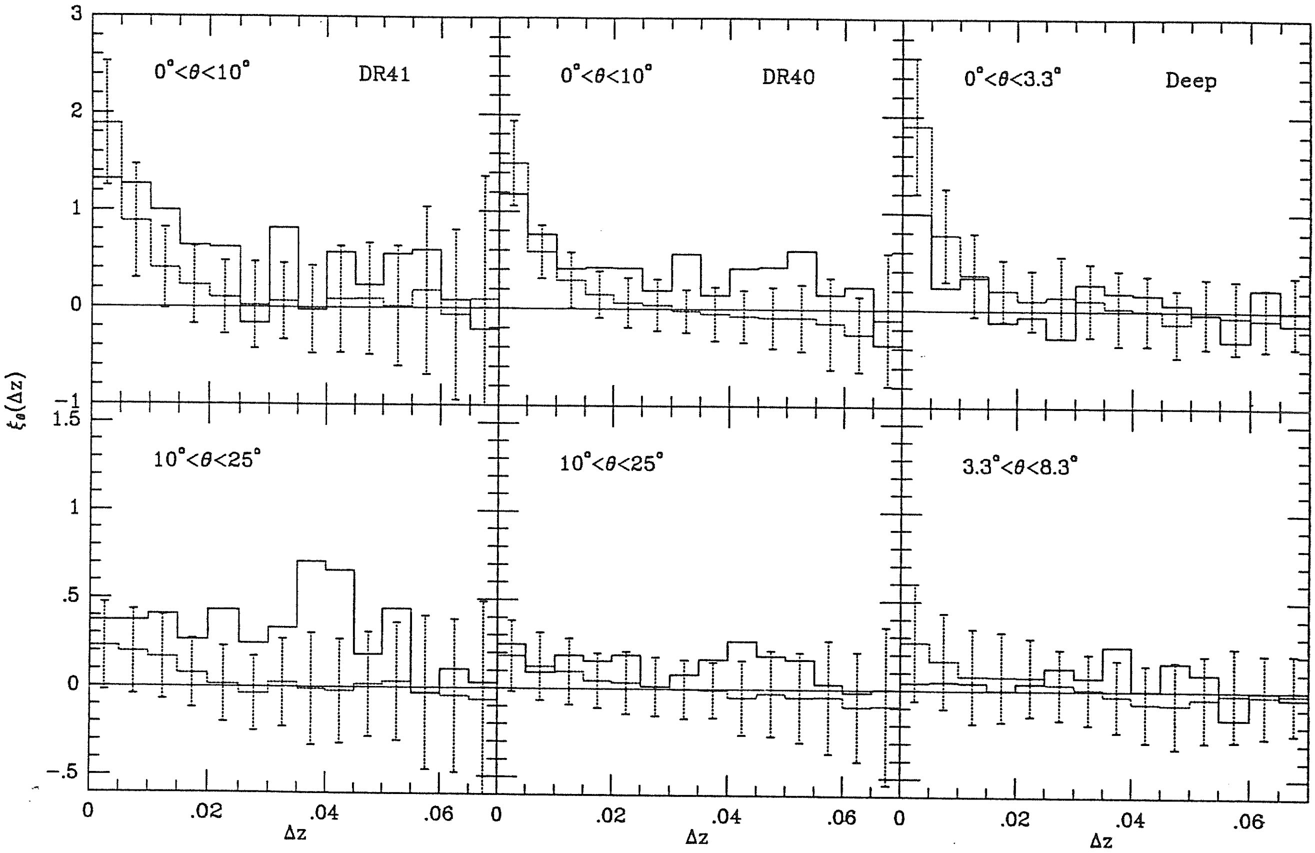

Figure 6.9 — The redshift correlation functions $\xi_\theta(\Delta z)$ of the three samples compared with the mean value of the 50 simulations. Error bars represent 1σ fluctuations.

by:

$$\chi^2 = \sum_{i=1}^{14} \frac{[\xi_{\mathcal{A}}(\mu_i) - \langle \xi^s_{\mathcal{A}}(\mu_i)\rangle]^2}{\sigma_i^2(\xi)} , \tag{6.5}$$

where $\xi_{\mathcal{A}}(\mu_i)$ is the redshift correlation function of the real sample and $\langle \xi^s_{\mathcal{A}}(\mu_i)\rangle$ is its mean value from the 50 simulations, while the summation is over 14 redshift separation intervals. The error model for $\sigma_i^2(\xi)$ is constructed by taking into account three types of errors which enter the $\xi_{\mathcal{A}}(\mu)$ estimation; the Poissonian error due to the discreteness of the cluster distribution, the fluctuations due to strong clustering and uncertainties which arise from our inaccurate knowledge of both redshift and galactic selection functions. The first two types of errors could be well represented by the standard deviation $\sigma_s(\xi)$ of the simulations. However, the third type of error is not included in σ_s because we use the same selection functions to select simulated clusters and to calculate correlation functions.

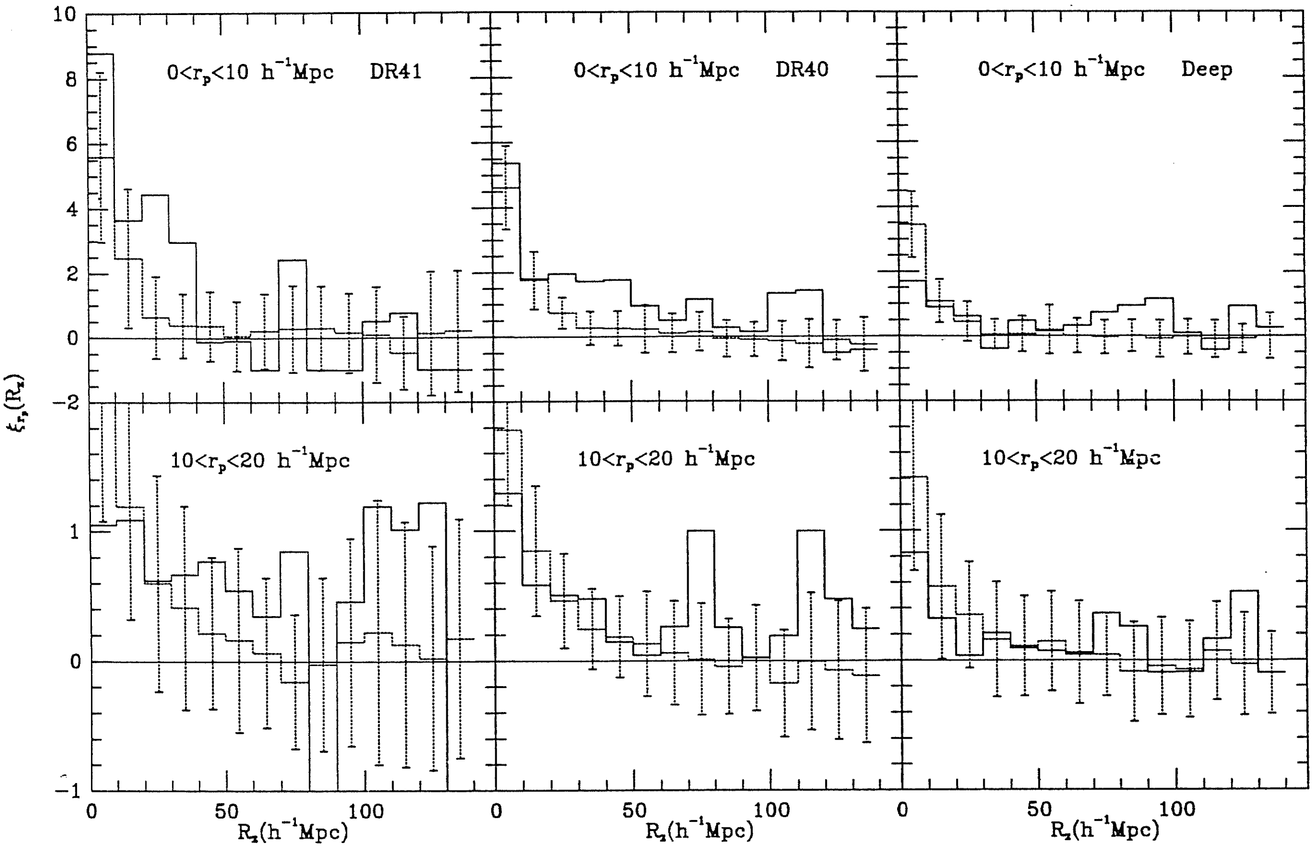

Figure 6.10 — As in Figure 6.9 but for the redshift correlation functions $\xi_{r_p}(R_z)$.

Although this kind of error is not known *a priori*, the discussion in §6.2 showed that the uncertainty in $\xi_{\mathcal{A}}$, due to such errors, could be as high as 25% - 30%. Assuming that the different types of errors are independent we take as our error model the following:

$$\sigma_i^2(\xi) = \sigma_s^2 + \eta^2 \xi_{\mathcal{A}}^2(\mu) \ . \qquad (6.6)$$

In the following discussion, η is set to 0.25. The results of the χ^2 test are listed in the second to fourth column of Table 6.1. $P(>\chi^2)$ represents the probability of obtaining larger $\xi_{\mathcal{A}}(\mu)$ peaks in the simulations than those observed in the real cluster samples, which indicates at what level our suggestion, that the high peaks of $\xi_{\mathcal{A}}$ are due to strong clustering, is accepted. The results clearly show that the observed redshift correlation functions are consistent with real clustering. The lowest two probabilities for $(\mathcal{A},\mu) = (\theta, \Delta z)$ and (r_p, R_z) are 0.17, 0.25 and 0.07, 0.32 respectively, still significantly high. The lowest probabilities, of 0.17 and 0.07, occur for the DR40 sample at the smaller angular and projected separation range respectively. This is consistent with our expectation that projection effects should affect the $R \geq 0$ samples more efficiently than the $R \geq 1$ samples. Note, however, that these effects are marginally (in the sense that even a probability of 0.07 is still large) noticeable in the DR40 sample but not at all in the other $R \geq 0$ sample ['Deep'].

Table 5.1

χ^2 tests of $\xi_\theta(\Delta z)$ and $\xi_{r_p}(R_z)$

Sample	θ [in °]	χ^2	P(> χ^2)	r_p [in h^{-1} Mpc]	χ^2	P(> χ^2)
DR41	$0 < \theta < 10$	9.17	0.82	$0 < r_p < 10$	15.9	0.32
	$10 < \theta < 25$	17.1	0.25	$10 < r_p < 20$	12.0	0.60
DR40	$0 < \theta < 10$	18.8	0.17	$0 < r_p < 10$	22.7	0.07
	$10 < \theta < 25$	6.43	0.95	$10 < r_p < 20$	10.7	0.71
'Deep'	$0 < \theta < 3.3$	7.25	0.92	$0 < r_p < 10$	16.2	0.30
	$3.3 < \theta < 8.3$	4.4	0.99	$10 < r_p < 20$	4.90	0.99

The test is rather sensitive to the existence of high peaks. For example, if in the DR41 sample we ignored the two peaks at $z \approx 0.04$ and $10° < \theta < 25°$, the P(> χ^2) would be raised from 0.25 to 0.63. These two peaks result mainly from 16 clusters in two well-known superclusters: the Hercules supercluster at $z \sim 0.035$ (Chincarini, Rood & Thompson 1981; Bahcall & Soneira, 1984) and the Corona Borealis supercluster at $z \sim 0.075$ (Bahcall & Soneira 1984; Postman, Geller & Huchra 1988). If these 16 clusters were excluded *a posteriori*, $\xi_\theta(\Delta z)$ would be lowered to 0.25, well within 1σ level. It seems, therefore, that these peaks are more probably produced by real superclustering rather than by contamination effects.

Furthermore, the fluctuations of the two-point (redshift) correlation function depend strongly on the higher order cluster clustering; the more high-order clustering, the more fluctuations in ξ (see, e.g., Peebles 1980). We have checked the three-point correlation function for the simulated clusters and found it to be $Q_{sim} \approx 0.65$ perhaps slightly weaker than the value for the Abell cluster catalogue (Jing & Zhang 1989; Tóth, Hollósi & Szalay 1989; Jing & Valdarnini 1991; Gott, Gao & Park 1991). Clearly, the probabilities $P(> \chi^2)$ in Table 6.1 would be even higher if the simulated clusters had stronger high-order clustering and therefore some significantly high peaks, seen especially in Figure 6.10 at small R_z's, could be a reflection of the stronger high-order clustering of the Abell clusters.

Therefore, our simulations show that both $\xi_{r_p}(R_z)$ and $\xi_\theta(\Delta z)$ of the observed samples are consistent with being the result of real clustering with weak evidence for some contamination effects in only one sample (DR40). This means that we do not need to invoke the contamination effects to explain *most* of the distinctive features in $\xi_{r_p}(R_z)$ and $\xi_\theta(\Delta z)$ appearing on large redshift separations.

6.4 Conclusions and implications

1.) Six different redshift selection functions (RSFs) for the DR41 sample are used to test the sensitivity of redshift correlation function to the RSF choice. We found that our inaccurate knowledge of the RSF can easily result in a $\sim 30\%$ uncertainty in the redshift correlation estimates. Any reasonable choice of the RSF, however, cannot remove all the high peaks seen in the redshift correlation functions at large redshift separations.

2.) Our careful and consistent comparison of $\xi_{\mathcal{A}}(\mu)$ between three Abell cluster samples does not support the contamination origin of these peaks, as was proposed by S88 and SE91. We find no evidence for significant contamination of the DR41 sample. However, we cannot exclude the possibility of moderate contamination effects in richness $R \geq 0$ samples. The observed properties of redshift correlation functions can be easily interpreted as the results of strong, richness-dependent clustering of *small numbers* of clusters, i.e., the peaks in $\xi_{\mathcal{A}}$ could be due to some specific superclustering pattern of clusters (e.g., geometrical elongation).

3.) Our suggestion that these peaks could originate from real clustering, was tested by numerical simulations. We constructed sets of simulated cluster catalogues which have the same sky boundaries, same selection functions, same number of clusters, and same two-point correlation functions as the real samples. Of course the simulated catalogues are free of the contamination effects and the coherent peaks (or valleys) observed in the redshift correlation function, on large Δz or R_z, are very common also in the simulations. The χ^2-test shows that we have more than $15\% \sim 30\%$ probability to obtain peaks in $\xi_{\mathcal{A}}(\mu)$, as large as the ones observed in the real cluster samples, due only to the low-order (2-p) clustering of a small number of clusters and the fact that we have only one realization of the process that forms clusters. Therefore, we do not need to invoke the contamination effects to interpret the features seen in the observed ξ_{r_p} and ξ_θ.

4.) It is important to emphasize here that previous confrontations of the observed ξ_{cc} with that predicted by theories of galaxy formation are mainly based on the result obtained from the DR41 sample (BS83). Our results support the BS83 results and therefore imply that the biassed CDM model is in gross disagreement with the observed cluster clustering, as originally thought.

5.) The elongation of cluster pairs in the redshift direction, found by Bahcall, Soneira & Burgett (1986) occurs quite often in our simulations. This suggests that the effect could be explained as being partly due to the statistical fluctuations in $\xi_{\mathcal{A}}$, without assuming the large (~ 2000 km s^{-1}) cluster peculiar velocities advocated by Bahcall et al.. In fact, even Bahcall et al. noted that such an effect may partly come from peculiar velocity of clusters but partly also from a geometrical elongation of superclusters.

---

‡The materials presented in this chapter are based on our paper: Jing, Y.P., Plionis, M. & Valdarnini, R. 1992, *The Astrophysical Journal*, **389**, 499

7

The Three-point Correlation Functions of Clusters of Galaxies

The two-point correlation function of rich clusters found by, e.g., Bahcall & Soneira (1983) is of great value in understanding the large scale structures in the Universe. However, as is well known, a full description of the distribution of rich clusters needs all N-point correlation functions. A statistical study of the three point correlation function would be necessary. Furthermore, because the three-point correlation function ζ is independent of the two-point function ξ, we would expect that ζ will put another constraint on the galaxy formation theories and therefore narrow the possible models. In this chapter, I shall present our original contributions to these related statistics.

7.1 The three-point angular correlation functions of $R \geq 1$ Abell clusters

Our study is based on the statistical catalog of $R \geq 1$ Abell clusters with high galactic latitude $\mid b^{II} \mid \geq 30°$ (Abell 1958). This sample includes 1651 clusters, of which 1055 are distributed in 2.64 sr of the northern hemisphere and the rest are in 1.62 sr of the southern hemisphere. Its survey boundaries were given in Table 1 of Abell (1958).

We estimate the angular three-point correlation function $z(\theta_{12}, \theta_{23}, \theta_{31})$ following Eq. (3.1.4b). Instead of using the variables θ_{12}, θ_{23}, and θ_{31}, we use another set of variables θ, u and v as in §4.3.2. In order to estimate $\langle DDR\rangle$ and $\langle RRR\rangle$ of Eq.(3.1.4b), we construct a random sample of twice as many points than the real sample. As usual, the selection function Eq.(6.3) is adopted in the construction of the random sample.

In order to improve the accuracy of estimating z, we used the interpolation techniques of Peebles & Groth (1975). We take the constant logarithmic intervals in θ, $\Delta\theta/\theta =$ constant, so that at small θ, and for fixed u and v, the expected counts $\langle RRR\rangle \propto \theta^4$ and $(\langle DDR\rangle - 3\langle RRR\rangle) \propto \omega(\theta)\theta^4$. We use these interpolation formulae to estimate the $\langle RRR\rangle$

and $\langle DDR \rangle$ for those intervals in which $\langle RRR \rangle$ or/and $(\langle DDR \rangle - 3\langle RRR \rangle)$ are less than 200. To good accuracy, $\omega(\theta) \propto \theta^{-0.9}$ for Abell clusters (see below).

Since computer cost is rapidly increased with the increase of θ_{31} ($\propto \theta_{31}^{4}$), we limit our estimation to $\theta_{31} \leq 10°$ triplets. Evidently, the cutoff is reasonable for our study because, as we know, the two-point angular correlation function of $R \geq 1$ Abell clusters was also well determined to a similar separation range. The determination of z starts at $\theta_{12} = 0.5°$.

Our results for the whole statistical sample of $R \geq 1$ Abell clusters are presented in Figure 7.1. In the figure, the constant intervals $\Delta \log_{10} u = 0.2$ and $\Delta \log_{10} \theta = 0.1$ are taken for the variables u and θ, respectively. For the variable v, two bins $0.5 < v \leq 1.0$ and $0 \leq v \leq 0.5$ are used. The capital letters for each bin in the figure correspond to those given in Table 1, and the shape parameters u, v of the corresponding triplets are also listed in the table. The vertical coordinate $\log_{10} z$ in the figure for every bin is shifted by a factor given in Table 7.1. The filled triangle represents the averaged value of z over the two neighboring bins, in one of which z is very small (same in the following).

We can be sure, from Figure 7.1, that the three-body correlation function exists among Abell clusters. This is expected, since there are many complex large-scale structures composed of Abell clusters (e.g., Bahcall & Soneira 1984; Tully 1987, and references therein). For quantitative analysis, a power-law form for z,

$$\log_{10} z = a + b \log_{10} \theta, \tag{7.1}$$

is assumed. The least-square fit to $z(\theta, u, v)$ (with u and v fixed) gives value b for every bin. All values of b are listed in Table 7.1, and we can see that from bin to bin, the values of b do not change much, and remain close to -2.0. Assuming all 6 b-values are statistically independent for simplicity (some coherence might exist), then we get the mean value $\bar{b}$:

$$\bar{b} = -2.10 \pm 0.21, \tag{7.2}$$

where the quoted error is the standard deviation of six b-values from the mean. The above value of $\bar{b}$ (about twice the slope of the two-point angular correlation function) reminds us that the three-point correlation of Abell clusters may also have a hierarchical form,

$$z = q(\omega_1 \omega_2 + \omega_2 \omega_3 + \omega_3 \omega_1), \tag{7.3}$$

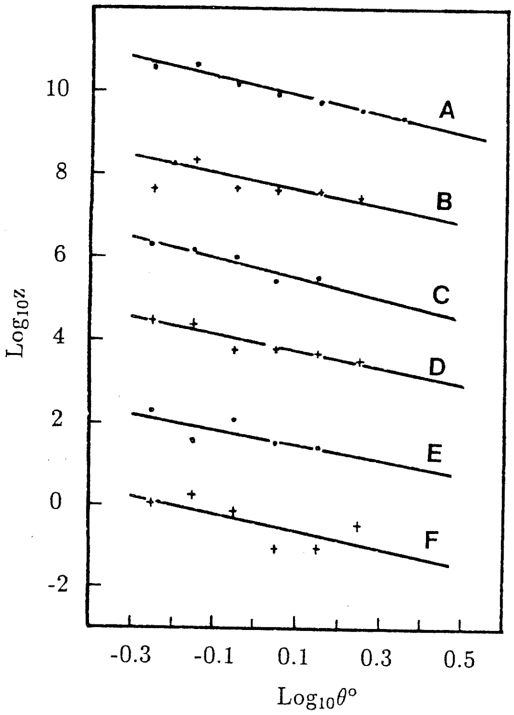

Figure 7.1 — The three-point angular correlation function z of the whole statistical sample. Upper case letters correspond to the shape range (u,v) listed in Table 7.1. Estimates have been multiplied by a power of 10, as indicated in Table 7.1. The straight lines represent the least-square power-law fits.

Table 7.1

The b-Values of the Statistical Sample

	Log u		
v	0.0–0.2	0.2–0.4	0.4–0.6
0.0–0.5	$A \times 10^{10}$ -2.26	$B \times 10^{8}$ -2.03	$C \times 10^{6}$ -2.43
0.5–1.0	$D \times 10^{4}$ -2.02	$E \times 10^{2}$ -1.80	F -2.10
Mean value	-2.10 ± 0.21		

just as for galaxies, here q is a constant.

The angular correlation functions $\omega(\theta)$ have been estimated by Bahcall & Soneira (1983) for $D = 5 + 6$ Abell clusters (including separate determinations for the northern and for the southern portions). Their samples are almost the same as those used here. However, there is some difference between two sets of samples; namely, that in the present study $D \leq 4$ clusters are included. Also, random samples can be produced in the same way in estimating z and $\omega(\theta)$. Moreover, because only triplets with $0.5^\circ \leq (\theta_{12}, \theta_{23}, \theta_{31}) \leq 10^\circ$ are included, our determination fits $\omega(\theta)$ to statistical data for the similar angle range. For all these reasons, a more accurate determination of the constant q is to be obtained by our own estimation of $\omega(\theta)$

Thus we estimate the two-point angular correlation function for the three samples discussed here. The results are plotted in Figure 7.2. The least-squares fits $\omega(\theta) \propto \theta^{-\beta}$ to these data (excluding the 0.5°–0.64° bin) show that for these samples, the power slopes β are 0.87 (for the whole sample; hereafter SW), 0.78 (for the northern sample; SN), 0.90 (for the southern sample; SS), all very close to 0.90. The single-power fits give $0.89\theta^{-0.9}$ (SW), $0.75\theta^{-0.9}$ (SN), and $1.25\theta^{-0.9}$ (SS), respectively. These expressions are to be used through Eq.(7.3) to get q.

The single power-law fits $z \propto \theta^{-1.8}$ to the statistical data of Figure 7.1 give q for each (u,v) bin, listed in Table 7.2. We can see from the table that q remains almost a constant from bin to bin, and is nearly independent of triangle shape u and v. This means that the three-point correlation function of Abell clusters can be well represented by the scaling form (7.3), just as in the case of galaxies. Also, assuming all q values for each bin are statistically independent, we get their mean value:

$$\overline{q} = 0.68 \pm 0.14. \tag{7.4}$$

The three-point correlation functions have also been estimated for the northern and the southern portions separately. The results are plotted in Figure 7.3. The straight lines in the figure represent the single power law $z \propto \theta^{-1.8}$ fits, and the corresponding q values are given in Table 7.2. It can be easily found that the scaling form of Eq.(7.3) fits the statistical data of z of the southern and northern samples well. The mean q-values are 0.57 ± 0.19 for SN and 0.87 ± 0.20 for SS, both of which are in agreement with the estimation of the statistical sample. These results support the conclusion that the z of Abell clusters has the hierarchical form, although, compared with the statistical sample, their fluctuations (especially of SN) are a little larger, which could be expected. There is a difference, although very slight, of ω and z between SN and SS. However, the cause is now unclear. It might be connected with the fact that the distribution of Abell clusters is a little more clumpy in the southern sky than in the northern sky. But it may also be

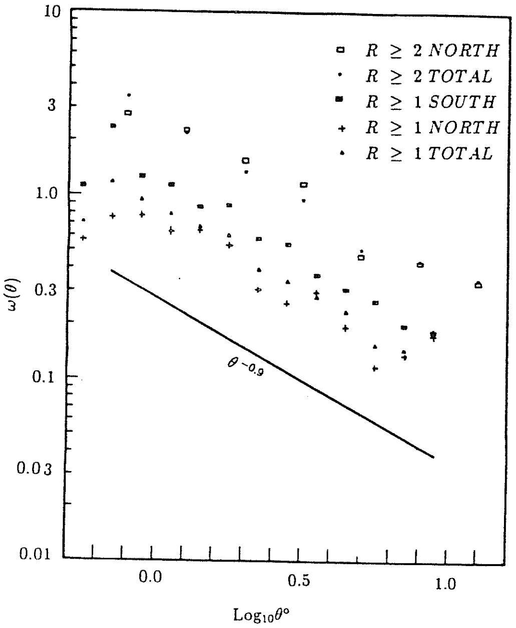

Figure 7.2 — The two-point angular correlation functions of the whole statistical sample for different zones and different richness classes.

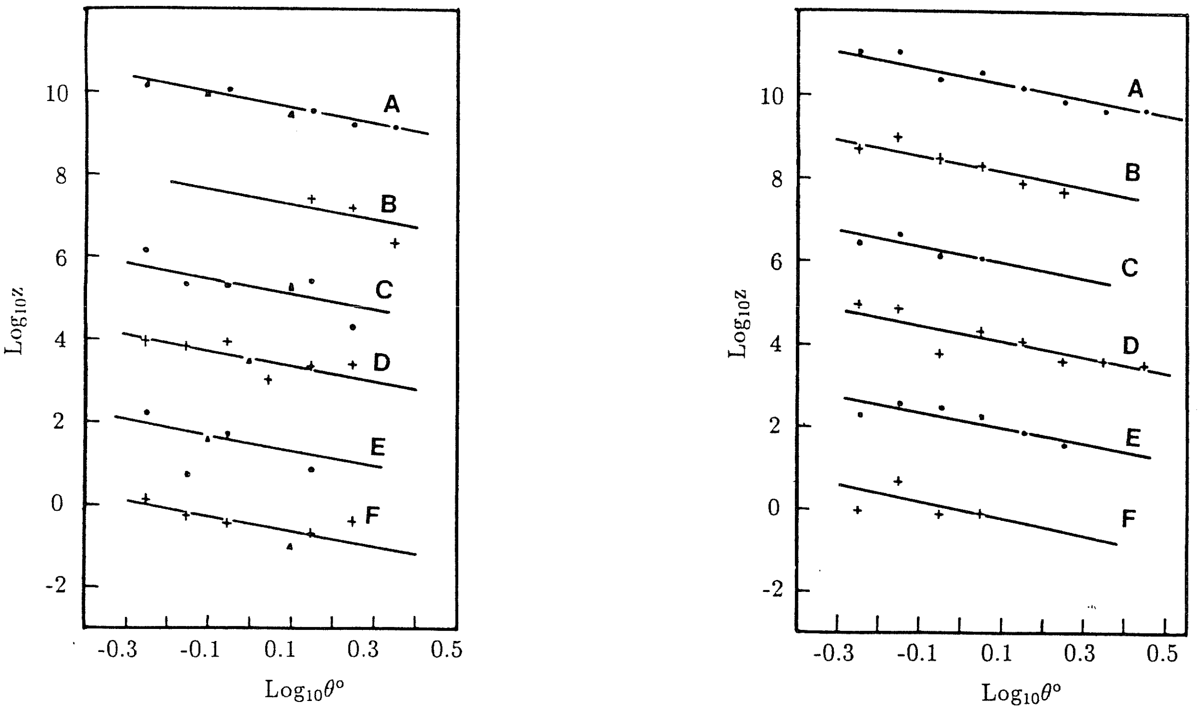

Figure 7.3 — The three-point angular correlation functions of (*a*) the northern sample and (*b*) the southern sample. Others are same as Figure 7.1, except that the lines represent single power-law $\theta^{-1.8}$ fits.

caused by observational effects, such as the strip with "bad" Palomar plates at $\delta = 72°+$, which contribute an extra modulation in the cluster distribution. However, in any case, the coincidence between the two subsamples is reasonable. And the 3-D study of §7.2 and §7.4 imply the latter might be the main cause.

7.2 The spatial three-point correlation functions of $R \geq 1$ Abell clusters — based on the estimated redshifts

We have also estimated the spatial three-point correlation functions for $R \geq 1$ Abell clusters. The samples are the same as those used in the last section. Since only 25% clusters have measured redshifts, we use the estimated redshift based on the magnitude-redshift relation (kindly made available to us by Y.Gao). The accuracy of his redshift estimates is $\sigma \log_{10} Z \approx 0.1$. We are fully aware that the accuracy is not good enough to arrive at a definite conclusion about spatial correlation functions, which has to await completion of a large redshift sample. The main purpose of doing so is only to test and, if possible, to confirm the results of the last subsection.

The redshift selection functions are obtained by examining the spatial density distributions, which are plotted in Figure 7.4 for the three samples. The smooth lines are reasonably taken as their selection functions. We have tested the sensitivity of ζ and Q to redshift selection function and found the effect is weak.

The distances to clusters are calculated and the galactic extinction effect is corrected in the same way as in §6.2. We used the method of §7.1 to estimate ζ, so we will not repeat the details.

As in the last section, we first examine the spatial two-point correlation functions which are plotted in Figure 7.5 for the samples concerned here. The least-squares fits $\xi \propto r^{\gamma}$ to the data of different samples show γ of about -1.2, considerably larger than the standard value -1.8. However, this result is expected because of the errors in estimated redshift, and is consistent with Postman et al. (1986) who used the redshift estimates of Leir & van den Bergh (1977).

The three-point correlation function of the statistical sample is presented in Figure 7.6. The meanings of symbols in the figure are clear, and are not discussed further. The

Table 7.2

THE q-VALUES FOR THREE SAMPLES

		Log u		
SAMPLE	v	0.0–0.2	0.2–0.4	0.4–0.6
All	0.0–0.5	0.760	0.674	0.903
	0.5–1.0	0.589	0.504	0.650
Mean value		0.680 ± 0.139		
South	0.0–0.5	0.956	1.071	1.081
	0.5–1.0	0.628	0.764	0.694
Mean value		0.865 ± 0.196		
North	0.0–0.5	0.597	0.437	0.495
	0.5–1.0	0.420	0.542	0.924
Mean value		0.569 ± 0.186		

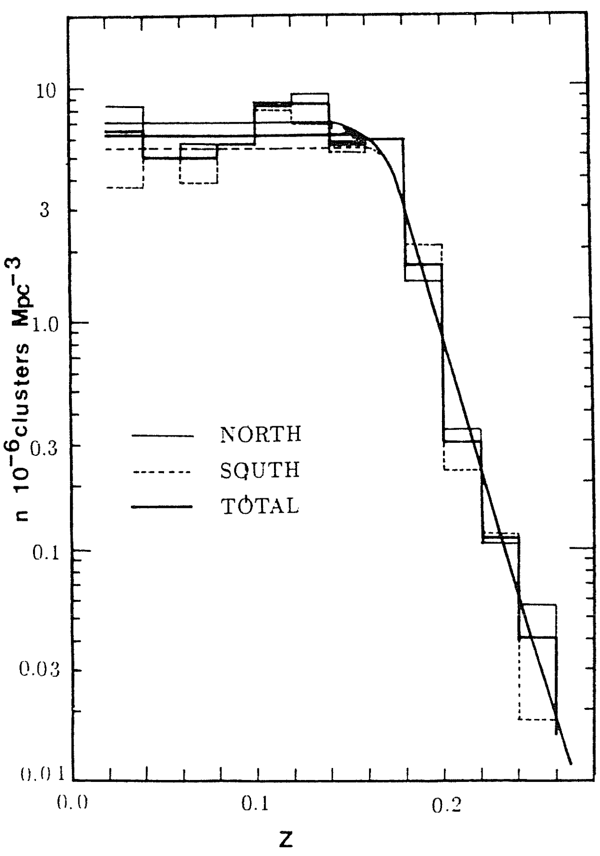

Figure 7.4 — Spatial density distributions vs. redshift of northern sample (*thin lines*), southern sample (*dashed lines*), and the total sample (*thick lines*). The solid thin, dashed, and thick lines represent their underlying mean density profiles, respectively.

least-squares fits of the power law $\zeta \propto r^{\nu}$ to the statistical data of each bin with fixed u and v give the slopes ν, which are listed in Table 7.3. The mean value of ν is

$$\overline{\nu} = -2.30 \pm 0.68, \tag{7.5}$$

if it is assumed that ν is statistically independent from bin to bin.

The slope ν would be considerably underestimated because the estimated redshifts are used. But it seems that this will not affect our discussions and conclusions much. Our main purpose is to determine whether ζ has a scaling form, and, if it does, how large the constant Q is. If the effect of the redshift estimates on ξ is modeled by $P(r)$, i.e., $\xi_{est} = \xi P(r)$, then the effect on ζ should be $\zeta_{est} = \zeta P(r)^2$ to the first order. Thus the estimated ζ_{est} is

$$\zeta_{est} \approx Q(\xi_{12}\xi_{23} + \xi_{23}\xi_{31} + \xi_{31}\xi_{12})_{est}, \tag{7.6}$$

if the hierarchical form (3.1.7) applies. Clearly, Eq.(7.5) is consistent with the hierarchical assumption.

The Q-values obtained through Eq.(7.6) are listed in Table 7.4. The values remain almost constant and have no systematic change with u and v. Its mean value is

$$\overline{Q} = 0.67 \pm 0.17. \tag{7.7}$$

We noted that the obtained Q is not sensitive to the γ of ξ adopted. Even if we take $\gamma = 1.8$, the mean value now is 0.44 ± 0.12, not too different from Eq.(7.7) (see also Table 7.4).

Our separate analyses of the northern and southern samples are consistent with the analysis of the whole sample, and I omit the figures here. The values of Q given by the power-law fits, however, are also listed in Table 4. The mean values of Q are 0.87 ± 0.29 for northern clusters and 0.68 ± 0.15 for the southern clusters, both in agreement with the estimation of the whole sample.

Now we check the consistency between the angular and spatial three-point correlation functions. Using the Limber equation (3.1.9) and the selection function of Figure 7.4, we find $q/Q = 1.1$. Evidently, the angular and spatial analyses are consistent[cf. Eqs.(7.4) & (7.7)].

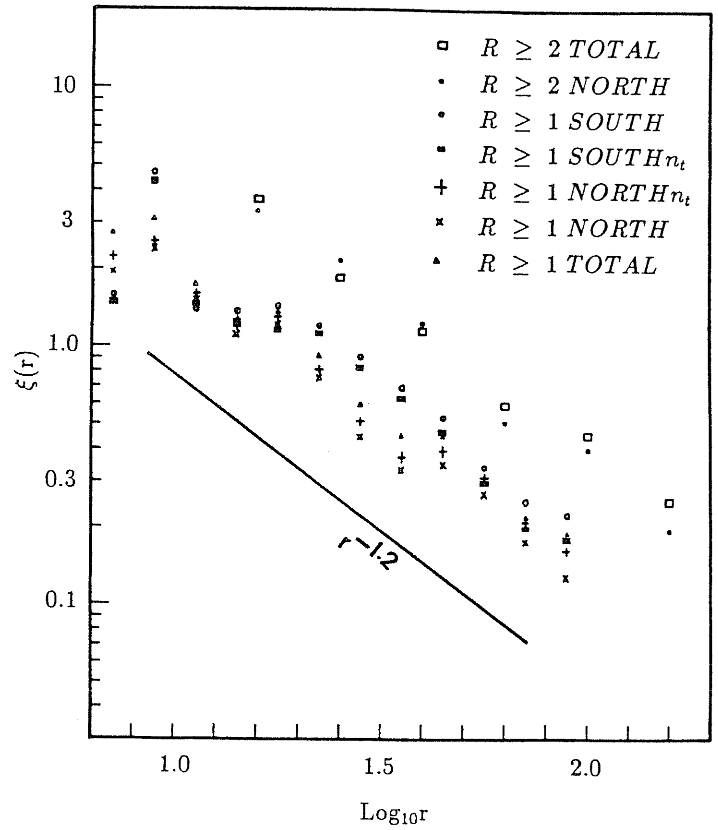

Figure 7.5 — Two-point spatial correlation functions of the statistical sample for different zones, for different redshift selection functions, and for different richness classes (as indicated on the figure).

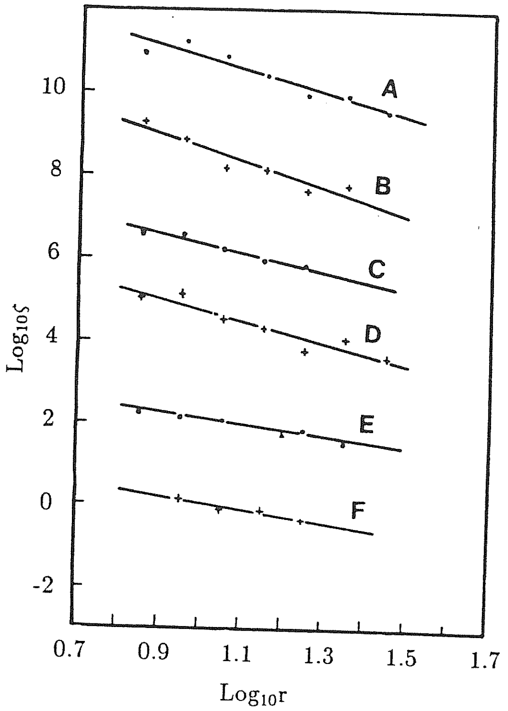

Figure 7.6 — The spatial three-point correlation function of the whole statistical sample. Others are the same as Figure 7.1.

Table 7.3

The v-Values for the Statistical Sample

v	Log u 0.0–02.	0.2–0.4	0.4–0.6
0.0–0.5	−2.73	−3.19	−2.18
0.5–1.0	−2.48	−1.39	−1.54
Mean value	−2.30 ± 0.68		

7.3 The three-point correlation functions of $R \geq 2$ clusters and Q independence on their richness

The correlation-richness dependence is very useful in constraining theories of galaxy formation. Concerning the three-point correlation functions, it is natural to ask how they depend on the richness of clusters. In order to answer such a question, we estimate the three-point correlation functions for $R \geq 2$ clusters in what follows.

In the whole statistical sample, there are 445 clusters with richness $R \geq 2$, of which

Table 7.4

THE Q-VALUES FOR THREE SAMPLES[a]

SAMPLE	v	Log u		
		0.0–02	0.2–0.4	0.4–0.6
All	0.0–0.5	0.691	0.760	0.833
		0.376	0.477	0.626
	0.5–1.0	0.723	0.398	0.564
		0.419	0.253	0.473
Mean value		0.670 ± 0.168		
		0.437 ± 0.124		
North	0.0–0.5	1.007	0.845	0.947
		0.488	0.543	0.599
	0.5–1.0	0.742	0.411	1.263
		0.440	0.275	1.256
Mean values		0.869 ± 0.285		
		0.599 ± 0.337		
South	0.0–0.5	0.834	0.642	0.659
		0.543	0.505	0.465
	0.5–1.0	0.817	0.715	0.426
		0.493	0.560	0.349
Mean value		0.682 ± 0.148		
		0.486 ± 0.075		

[a] For each (u, v) bin, two Q-values are given. Upper data are from $r^{-2.4}$ fits, and lower data are from $r^{-3.6}$ fits.

266 are distributed in the northern hemisphere. Three-point angular, as well as spatial, correlation functions are estimated for two samples: sample SN2, including all northern $R \geq 2$ clusters; and sample SW2 of all $R \geq 2$ clusters. No statistics have been done for the southern cluster subsample alone because relatively fewer clusters are included. The same techniques as used in the last two sections are applied in calculating ζ and z, except that 3 times as many random clusters than the observed ones are produced as comparison catalogs, and the larger interval separations of r and θ, $\Delta \log_{10} r = \Delta \log_{10} \theta = 0.2$ are adopted, in order to minimize the random fluctuations arising from the smaller number of clusters included and to improve the accuracy of estimation of z and ζ. The ranges of triplets are set to $0.8^\circ \leq \theta \leq \theta_{31} \leq 10^\circ$ or $15 \leq r \leq r_{31} \leq 250h^{-1}$Mpc.

The redshift selection functions are obtained by examining the density distributions, but here we omit the plot. As in the case of $R \geq 1$ clusters, the two-point correlation functions, which have already been shown in Figures 7.2 and 7.6, are estimated. The least-squares analysis techniques show that the slopes for both samples are all very close to -0.9 and -1.2 (with differences less than 10%), respectively, just as $R \geq 1$ clusters.

Figures 7.7 and 7.8 show our estimated ζ and z for the $R \geq 2$ cluster samples. It

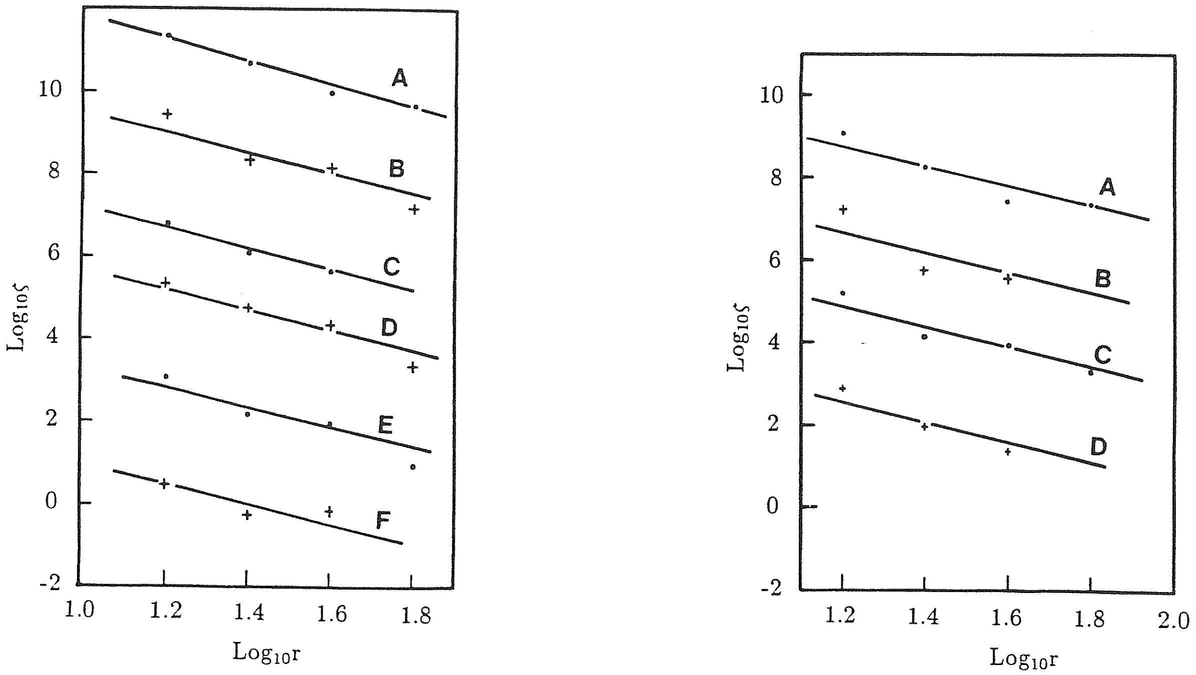

Figure 7.7 — Three-point spatial correlation functions of *a*) the northern $R \geq 2$ sample and *b*) the total $R \geq 2$ sample. The upper case letters and vertical shift factors of *a*) correspond to those in Table 7.4 and of *b*) to Table 7.5.

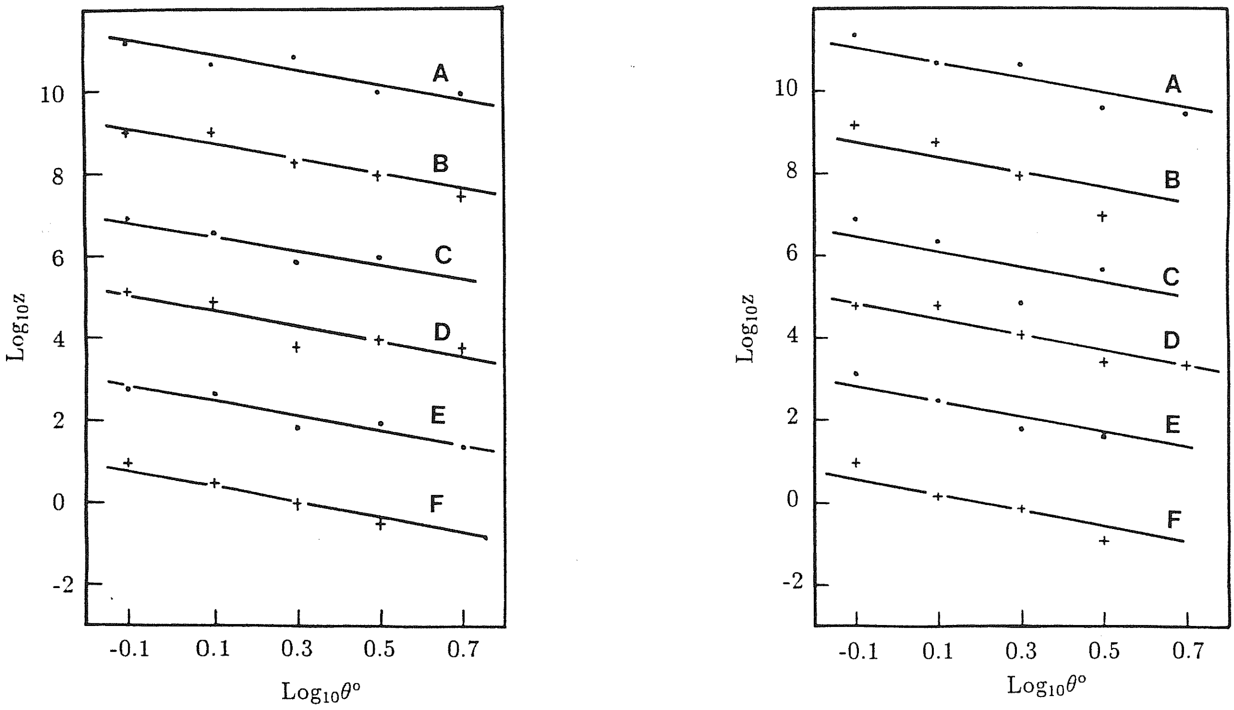

Figure 7.8 — Three-point angular correlation functions of *a*) the northern $R \geq 2$ sample and *b*) the total $R \geq 2$ sample. Others are the same as Figure 7.3.

Table 7.5

The Q-Values of $R \geq 2$ Clusters[a]

Sample	v	Log u 0.0–0.2	0.2–0.4	0.4–0.6
All	0.0–0.5	A × 10^8	B × 10^6	
		0.24	0.38	
		0.18	0.28	
	0.5–1.0	C × 10^4	D × 10^2	
		0.42	0.33	
		0.25	0.25	
Mean value		0.34 ± 0.07		
		0.24 ± 0.04		
North	0.0–0.5	0.73	0.92	0.80
		0.54	0.90	0.76
	0.5–1.0	0.85	0.65	0.57
		0.66	0.66	0.57
Mean value		0.75 ± 0.13		
		0.86 ± 0.13		

[a] See note to Table 4.

Table 7.6

The q-Values of $R \geq 2$ Clusters

Sample	v	Log u 0.0–0.2	0.2–0.4	0.4–0.6
All	0.0–0.5	0.52	0.40	0.35
	0.5–1.0	0.32	0.49	0.44
Mean value		0.42 ± 0.08		
North	0.0–0.5	0.74	0.75	0.78
	0.5–1.0	0.51	0.52	0.68
Mean value		0.66 ± 0.12		

is evident that the three-point correlation function of $R \geq 2$ clusters is much larger than that of $R \geq 1$ clusters. To give a quantitative comparison with $R \geq 1$ clusters, we use the hierarchical forms [Eqs.(3.1.7) & (3.1.8)] with $\xi \propto r^{-1.2}$ and $\omega \propto \theta^{-0.9}$ to fit the estimated results. The straight lines in the figures represent these fits. We can be sure, from the figures, that the hierarchical form are consistent with the data. The Q- and q-values thus obtained are given in Tables 7.5 and 7.6. As in the last section, we also estimate the Q taking $\xi \propto r^{-1.8}$(see Table 7.5).

If we note $q/Q = 1.1$ according to the Limber equation, we would find that our angular and spatial results are in good agreement. The Q values of the SN2 sample are very close to those of $R \geq 1$ clusters, indicating that Q is richness independent. However, the SW2 sample has a smaller Q value (about a half of $Q_{R\geq 1}$). The discrepancy is not well understood. According to our check of $\langle DDD\rangle$, $\langle DDR\rangle$, and $\langle RRR\rangle$, we find there are relatively fewer triplets in the southern sky (so the samples may not be 'fair'). However, if we note the existing sampling error and also the fact that ζ is ten times stronger than that of $R \geq 1$ clusters, we could think that Q is almost richness independent even considering the sample SW2.

7.4 An analysis of a small redshift complete sample

All the above results are based on the 2-D samples. Even in the 3-D studies, redshift is estimated by the magnitude-redshift relation. In this section, I present our recent analysis of a small sample which is almost redshift complete. The results obviously complement the previous sections.

7.4.1 The sample and the method

The data we use are from the ACO catalog of rich clusters of galaxies. In what follows, we shall treat the north and the south separately. As for the northern sample, we select those clusters with $\delta \geq -27°$, $|b^{II}| \geq 30°$, richness $R \geq 0$ and the tenth brightest magnitude $m_{10} \leq 16.4$. As a result we have 227 clusters. For 212 of them redshift is measured.

As for the southern hemisphere, the ACO catalog is complete for $\delta \leq -17°$. We select only those clusters with $m_{10} \leq 16.4$ and $R \geq 0$. The southern sample is built considering all clusters with $b^{II} < -30°$ and $\delta < -17°$. These selection criteria leave us with 103 clusters. We shall be using the estimated redshifts for 44 of them.

For those clusters without redshifts Z, we use the magnitude-redshift relation to estimate Z. For the northern sample we adopt the m_{10}-Z of Postman et al. 1986), and for the southern sample we follow Couchman et al. (1989). Again the galactic obscuration effect is corrected according to Eq.(6.3) and redshift selection function is fit to the density distributions.

In this section, we used the moment method to calculate the three-point correlation function. All necessary formulae are given in Appendix A. The method was thought to be effective in analysing small samples, when we did the work. Recently, from analysing simulations, I found the method may not be as effective as initially thought in treating small samples (see §3.1.5 for discussion). As argued in §3.1.5, however, a use of a large shell size can give a good determination of, e.g., the Q, at the expense of inability of testing the assumed function, e.g., the hierarchical form.

Table 7.7 Estimated Q-values

shell (in h^{-1}Mpc)	North	South
7—11	0.309 ± 0.073	0.718 ± 0.135
11—16	0.750 ± 0.041	0.268 ± 0.012
16—21	0.453 ± 0.051	0.184 ± 0.011
21—26	0.367 ± 0.020	0.945 ± 0.019
7—26	0.777 ± 0.003	0.702 ± 0.002
bootstrap	0.77 ± 0.35	0.70 ± 0.47

7.4.2 Results

We shall report the results obtained on the basis of (3.1.7). North and south sample results will be shown separately. In Table 7.7, we report the intervals $Q - \Delta Q, Q + \Delta Q$ obtained, for different radial shells, according to (A.11) and (A.16). The first column gives the results for the whole northern sample, and the second column for the southern sample. The limits chosen to define the shells are 7, 11, 16, 21, and 26 h^{-1}Mpc. From the table, we find that there is no systematic difference of Q between northern and southern hemispheres, in contrast with the previous 2-D analyses (see §7.1). Especially the mean values of Q of both samples coincide ($\sim$ 0.7) well for the largest bin 7 — 26 h^{-1}Mpc, which implies that the discrepancy found previously might be largely due to some "bad" Palomer plates and (or) to different project effects, but not due to the different intrinsic clustering properties.

The data of Table 7.7 are also plotted in Figure 7.9 versus r_k for Q. Error bars are the uncertainties quoted in Table 7.7. The continuous line is for the northern sample and

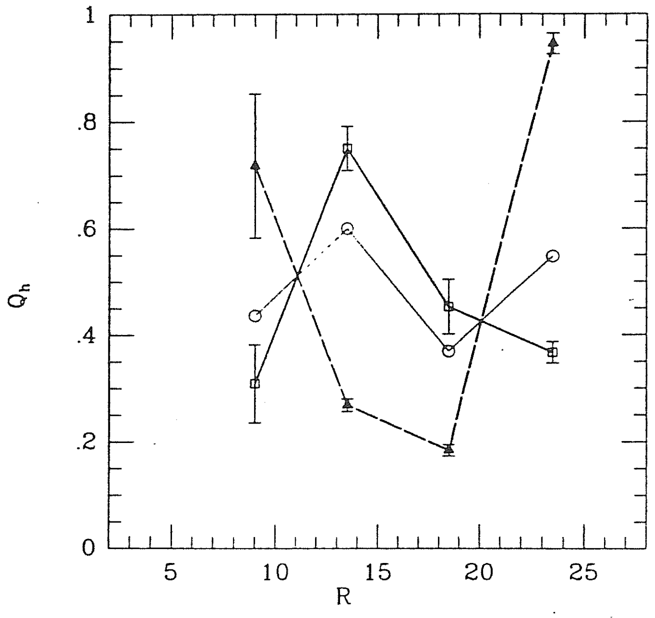

Figure 7.9 — Q for the north (continuous line) and the south (dashed line) versus radial distance. The continuous (thin) line is an average of the two samples. The plotted points correspond to $(r_k + r_{k-1})/2$. Data are taken from Table 7.7.

the dashed line for the southern one. We also plot an average of the two samples with a weight proportional to their cluster number. The averaged data seem to suggest that Q is nearly constant (0.5), consistent with the previous 2-D studies.

The errors given by (A.16) are quite formal and the actual error would be much larger. However, the *real* error of Q is not easy to obtain. By the bootstrap technique, we found the typical error is ~ 0.35 even for the single bin 7–26 h^{-1}Mpc. Such a large error may arise mainly from the small size of the samples.

In summary, this 3-D study confirms the hierarchical form (3.1.7) as a good approximation to ζ of clusters. The Q values are about 0.7, quite consistent with the previous 2-D studies. The discrepancy of Q between the northern and southern samples detected in the 2-D study (§7.1) is greatly reduced, and the results of the north and south estimates are consistent within errors.

7.5 Dependence on peak threshold in poorer clusters

As shown in §7.3, the hierarchical form of Abell clusters depends weakly on cluster richness. In this section we extend the study to poorer clusters identified by Plionis et al.(1991).

7.5.1 *Cluster samples*

The Plionis, Barrow & Frenk (1991) cluster samples were identified, using an overdensity criterion, in the 'free-of-overlap' Lick galaxy counts of $10' \times 10'$ cells (Shane & Wirtanen 1967; Seldner et al. 1977; Plionis 1988). The clusters are defined as peaks of the galaxy surface-density σ that lie above a given threshold κ, i.e., $\sigma \geq \kappa \times \langle\sigma\rangle$, where $\langle\sigma\rangle$ is the mean galaxy surface-density and the value of κ specifies the catalog. All the connected cells that fulfill the selection criteria belong to the same cluster. Their four cluster samples with $\kappa = 3.6$, 3, 2.5 and 1.8 (C36, C3, C25 and C18 samples hereafter) are used in this study. The C36 sample is the same as the cluster sample selected by Shectman (1985).

In order to minimize the Galactic extinction effect, our samples are limited to high galactic latitudes $|b| \geq 40°$. Furthermore, we checked their density gradients along b. For the NGC we find that a $cosec|b|$ law does not fit the data well. There is no significant extinction for $b > 50°$ while there is an abrupt decrease of the cluster number density in $40° < b < 50°$. Therefore, for the NGC, we estimate correlation functions only for $b \geq 50°$. For the SGC, we find that a smooth $cosec|b|$ function with the usual amplitude of 0.3 fits the data nicely for $b < -40°$. Because of the rather small number of clusters contained in high κ samples, we prefer to merge together the northern and southern parts of the C30 and C36 samples, while separate analyses for north and south are performed for C25 and C18. A summary of the samples is given in Table 7.8.

7.5.2 *Methods and Results*

We use the direct counting method to estimate the three point correlation function as in Chapter 4. The procedure is completely the same as described there, except the bins of θ, u, v are taken as follow:

$$\Theta_i < \theta \leq \Theta_{i+1} \qquad [\log(\Theta_{i+1}/\Theta_i) = 0.1,\ i = 1, \cdots, i_{max}\ ];$$

$$U_i < u \leq U_{i+1} \qquad [\log(U_{i+1}/U_i) = 0.1,\ i = 1, \cdots, 10,\ U_1 = 1];$$

$$V_i < v \leq V_{i+1} \qquad [V_{i+1} - V_i = 0.2, i = 1, \cdots, 5, V_1 = 0].$$

$\Theta_1 = 0.63°$ and $\theta_{max} = 5.0°$ are used in this section, except for the C36 sample $\Theta_1 = 0.79°$ and $\theta_{max} = 6.3°$ are used.

Table 7.8 A summary of results

		moments				*counting*			
Sample (κ)	N_{cl}	N_{bin}	Q	ΔQ	χ^2_{min}	N_{bin}	Q	ΔQ	χ^2_{min}
3.6	460	8	0.50	0.53	0.05	104	0.85	0.08	89
3.0	976	8	0.68	0.43	0.02	109	0.67	0.04	143
2.5N	1159	8	−0.11	0.57	0.01	109	0.05	0.15	17.7
2.5S	658	8	0.50	0.46	0.03	109	0.41	0.12	25.8
1.8N	2685	8	−1.10	1.20	0.04	109	−0.84	0.18	18.4
1.8S	1619	8	0.01	1.11	0.13	109	−0.43	0.18	30.4

The fitted values of Q for different samples are listed in Table 7.8 and are shown in Figure 7.10. For both northern and southern hemispheres, a negative Q is detected for the samples of the lowest density contrast ($\kappa = 1.8$), while the trend of decreasing Q with decreasing κ is obvious. Note that for the two lowest overdensity samples the Q parameter for the northern hemisphere is systematically lower than for the southern hemisphere. Indeed, since the southern galaxy density in the Lick map is less than the northern one (cf. Plionis 1988), selecting peaks with a global threshold amounts to picking up relatively higher peaks in the south. All this is consistent with the fact that the Q value is an increasing function of κ.

We have also used the moments method to study the problem. A detailed account of the method is given in Appendix A. Here we consider angular separations in the range $0.6° \leq \theta \leq 9°$. The θ values are collected in 8 bins which have the same relative amplitude $\Delta = 0.34$. The final results are listed in Table 7.8 for comparison. The central values are similar as those obtained by the direct counting method, confirming the increasing trend

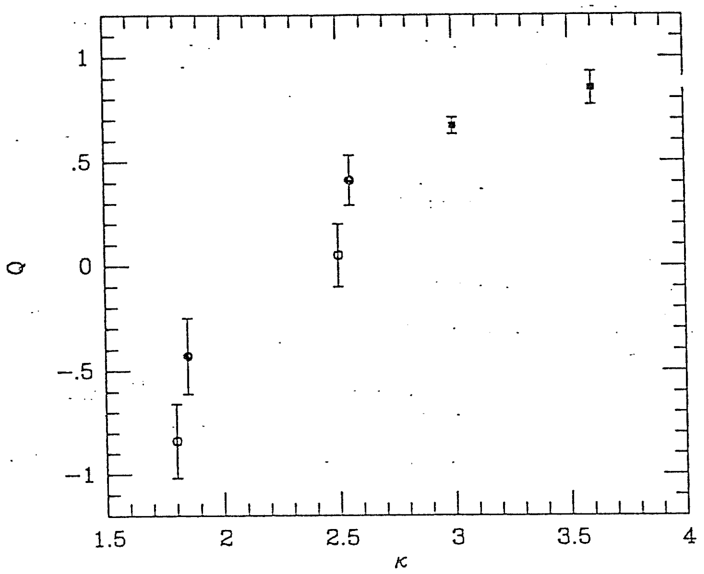

Figure 7.10 — The values of the hierarchical coefficient Q are plotted as a function of the density threshold κ. For C18 and C25, the results for northern (filled circles) and southern (open circles) are separately plotted.

of the Q with peak height. However the errors in the moments method are much larger for possible reasons given in §3.1.4.

7.6 Discussions and Conclusions

We have examined the three-point correlation functions for galaxy systems of various richness. The hierarchical expression (3.1.7) is found to be a good approximation for all cases considered here. The Q value is about 0.7 for clusters of richness $R \geq 0$, with weak richness dependence. However for the poorer clusters, the Q depends strongly on the richness and is a increasing function of the richness.

It would be interesting to compare ζ of Abell clusters with that of galaxies. As summarized in §3.2.1, the Q of galaxies is ~ 1.3 based on the Zwicky and Lick catalogues, and ~ 0.8 based on the available redshift samples and the ESO/Uppsala catalogue. These values, especially the later one, are nearly same as that obtained here for rich clusters.

The richness dependence of the Q is qualitatively in agreement with theoretical 'biasing' predictions. For example, in the Gaussian model of biased galaxy formation, Jensen &

Szalay (1986) have calculated the three-point correlation function and predicted that the equivalent Q increases with the biasing threshold (i.e., richness). Because their model is simple, a quantitative comparison between the model and the observation is not possible.

The high amplitude of ξ_{cc} of rich clusters strongly suggests that rich clusters form at the sites of high peaks (Kaiser 1984). In the high peak approximation, Matarrese et al. (1986) predict Eq.(3.2.9) for ζ_{ccc}, apparently contradictory with our results. If there were the cubic term of Eq.(3.2.9) in the observational data, it would have been manifested in our above analysis at small separations. The independent analysis of Tóth et al. (1989), which was designed especially to search for the cubic term, confirmed the lack of this term. However, the analytical prescription may be too simple; nonlinear or merge effects might be important. The recent N-body simulation of the biased CDM model (Gott et al. 1991) has reproduced the hierarchical form. And they argue that the lack of the cubic term is attributed to the merge effect of nearby high peaks.

Since conventional models fail to reproduce the ξ_{cc}, an alternative — the explosion model of galaxy formation, has been explored recently and is found to have a strong cluster-cluster correlation function (e.g., Weinberg et al. 1989). I found that in this scenario, the hierarchical form can be reproduced, nearly independent of model details (see next chapter).

‡The materials presented in this chapter are based on our three papers: Jing, Y.P. & Zhang, J.L. 1989, *The Astrophysical Journal*, **342**, 639; Jing, Y.P. & Valdarnini, R. 1991, *Astronomy and Astrophysics*, **250**, 1; Borgani, S., Jing, Y.P. & Plionis, M. 1992, *The Astrophysical Journal*, (in press).

8

Three-point correlation functions of clusters in the bubble Universe

The spatial distributions of clusters of galaxies provide us with good opportunities for testing current theories of galaxy formation. In this chapter, by assuming that the Universe is filled with bubbles and clusters form at sites where three bubbles intersect (i.e., toy models of the Ostriker explosion scenario), we demonstrate the types of three-point correlation function ζ of clusters, that are predicted, thus testing the bubble models by comparing them with that of observed cluster catalogs.

8.1 Introduction

While several possible models (such as the biasing model, the cosmic string picture) have been proposed to explain the two-point function of clusters (and other observational effects), how to naturally produce ξ still remains a great puzzle for cosmologists (e.g., Kaiser 1984; White et al. 1987b; Turok 1985; Jing & Zhang 1987; see §3.2 & §6.1). Another interesting approach to the problem has been proposed recently: galaxies are distributed on shells and clusters form at intersections of shells (Bahcall 1988b; Ostriker 1988; and Dekel 1988). This was actually predicted by the explosion theory of galaxy formation (Ostriker & Cowie 1981; Ikeuchi 1981), and is inferred from the recent observations of large bubbles in the redshift slice surveys (de Lapparent et al. 1986; hereafter LGH; Geller & Huchra 1989). In the explosion scenario, early explosions at redshift $z \sim 10$ swept their surrounding primordial gas into hot, dense shells, and galaxies form when the shells cool and fragment (Ostriker & Cowie 1981). The detailed dynamical N-body simulations (West et al. 1990) show further that clusters form preferentially at sites of shell intersections, in accordance with the observations of redshift slice surveys (LGH). Although it still remains uncertain which physical processes are responsible for the initial explosions of such high energies, there exist several physical candidate mechanisms: explosions of supermassive stars and of supernovae, electromagnetic radiation from superconducting cosmic strings, etc. (Carr et al. 1984; Ostriker & Cowie 1981; and Ostriker et al. 1987).

Weinberg, Ostriker and Dekel (1989, hereafter WOD) have made detailed numerical simulations to study spatial distributions of clusters, by identifying clusters as "knots" where three shells intersect (see also a similar discussion of Bahcall et al. 1989). In their simulations, shells have spherical geometry, with constant radius R or power law distribution of radius $P(R) \propto R^{\beta}$. They considered various effects, such as the dynamical and observational mergers of clusters, the shell mergers, etc., and included these effects in their simulation by some hand-input criteria. Armed with the mass recipe that cluster mass M_{cl} is proportional to the product of the three shell radii, i.e., $M_{cl} \propto R_1 R_2 R_3$ (based on the N-body simulations of West et al. 1990 and on reasonable theoretical arguments), they obtained the mass function of clusters. Assuming that the mass-to-light ratio is a constant for clusters, they used the luminosity function (LF) of clusters (Bahcall 1979) to constrain the possible model parameters. They also studied the two-point function of clusters and its richness dependence (Bahcall 1988a). Finally they found that if they took appropriate values for the model parameters, e.g., $\beta \sim -4$ and the filling factor (its definition given below) $f \sim 0.3$, the model can produce the right LF of clusters, the right trend of correlation-richness dependence, the right slope of ξ, but also a high correlation amplitude which could be acceptable only at the 2σ level, when distance is scaled to the mean separation of Abell clusters (however, see Bahcall et al. 1989). The overclustering problem might be relaxed only if a certain fraction of "knots" (not dependent of M_{cl}) actually succeed in producing Abell clusters and/or if there is a random component of clusters which is uniformly distributed in space having a similar mass distribution.

It would be very interesting to use the three-point function of clusters ζ to further test the bubble model. In the following sections, I shall present the predictions of ζ in various bubble models. §8.2 & §8.3 respectively study the two simplest models: 1) The radii of shells are assumed to be a constant (hereafter, constant model); and 2) Shells have a power law radius distribution, $n(R) \propto R^{\beta}$ (hereafter, power law model). The motivation to study these two cases is threefold. First, these two models perhaps could be solved analytically, like Kulsrud & Cowley (1989, hereafter KC) for the two-point correlation function. The simulation can help to test such an analysis. Secondly, the simulation can give some features such as the scales on which three clusters correlate, which would remain valid in more realistic models. Finally, due to the large difference in the shell radius distributions of the two models, we can find out how three-point correlations depend on the models.

However, the models above might be too simplified. Physically, all shells cannot have the same radius. Even in the power law models, two shells which overlap greatly and essentially sweep the same primordial gas, should be regarded as one shell, thus one of the two shells has actually lost its identity (This is the so-called anticorrelation effect of shells or shell mergers in WOD). Another important effect is cluster mergers: two primeval clusters of small separation would evolve dynamically into, or would be later observationally identified as one cluster. §8.4 studies ζ in the power law models by including these effects. In order to distinguish from the pure power law models of §8.3, we call them the modified power law models.

8.2. Equal-size shells

In this section, we study the three-point correlation functions of clusters intersected by equal-size shells. As KC and WOD showed, this model is completely fixed by two parameters: the shell radius R and the filling factor $f = (4\pi/3)n_{sh}R^3$, where n_{sh} is the spatial density of shells. KC obtained analytically the mean density n_{cl} of clusters

$$n_{cl} = \frac{9\pi}{16} f^3 R^{-3}, \tag{8.1}$$

and the cluster-cluster two-point correlation function ξ_{cl}:

$$\xi_{cl}(y) = \frac{3}{4f}\frac{1}{y} + \frac{1}{\pi^2 f^2}\frac{(1-y^2)(1+3y^2)}{y^2} + \frac{1}{3\pi^2 f^3}\frac{(1-y^2)^2}{y} \tag{8.2}$$

where $y \equiv r/2R$. Note: one can easily find a minor error (a factor 2 in the numerator of the second term) in the expression $\xi_{cl}(y)$ of KC; this has been corrected in Eq.(8.2). This expression has already been verified by the numerical experiment of WOD.

The method of our simulation is somewhat different from that of WOD. We adopt $f = 0.4$, 0.6 and 0.8 for the filling factor. We choose a spherical space of radius R_{sim} for the simulation. R_{sim} is determined by the condition that for $f = 0.4$, there are 1000 clusters produced in one realization [see Eq.(8.1)]. Considering the boundary effect of the simulation space (i.e. clusters could be formed by intersections of the inner shells and the shells whose centers just lie out of the space), we in fact first randomly place (centers of) shells in a larger sphere of radius $R_{sim} + R$, and find all the knots (clusters) where three shells intersect. Then we include all those clusters within the sphere of R_{sim} in our later calculation, thus correcting for the boundary effect. The same simulation space is used for $f = 0.6$ and $f = 0.8$ models. Certainly there would be $(0.6/0.4)^3 \times 1000 \approx 3400$ and $(0.8/0.4)^3 \times 1000 = 8000$ clusters produced in one realization of $f = 0.6$ and of $f = 0.8$. Because the computational cost is rapidly increased with N_{cl} ($\propto N_{cl}^3$) in calculating ζ, we will randomly choose 1000 clusters (hereafter, "child" sample) in each realization of the $f = 0.6$ and $f = 0.8$ models for our calculation. It is easy to prove that the "child"sample has all the same N-point correlation functions as its "parent" sample, that is, all intrinsic clustering properties are the same. This argument is similar to that of the sparse sampling of a redshift survey (Kaiser 1986; Metcalfe et al. 1989). Why we do not take a smaller simulation volume for $f = 0.6$ and $f = 0.8$ is for the "fair" sample reason. As we show below that the three-point correlation functions remain positive out to 4R (the longest side of a triangle) and as the R_{sim} which we now take is $12.8R$, reducing sample volume would probably influence the final results. This method has been verified when we checked the two-point correlation functions of the above three f cases, which reproduced the data of WOD and was completely consistent with expression (8.2). [see also §8.3]. For each model, we make ten realizations.

The procedure of estimating the three-point correlation function is the same as in Jing & Zhang (1989; see §7.1). In Figure 8.1, we illustrate the three-point correlation functions ζ of several typical (u, v) bins for the $f = 0.4$ model. Figure 8.1a shows the four cases with fixed $v = 0.05$ but different u, which covers triangles from equilateral to highly elongated atute isosceles shapes. We can find that three clusters are strongly correlated on small scales and the ζ remains positive out to $r < 2R$ and $(u + v)r \approx ur \approx 2R$. Figure 8.1b

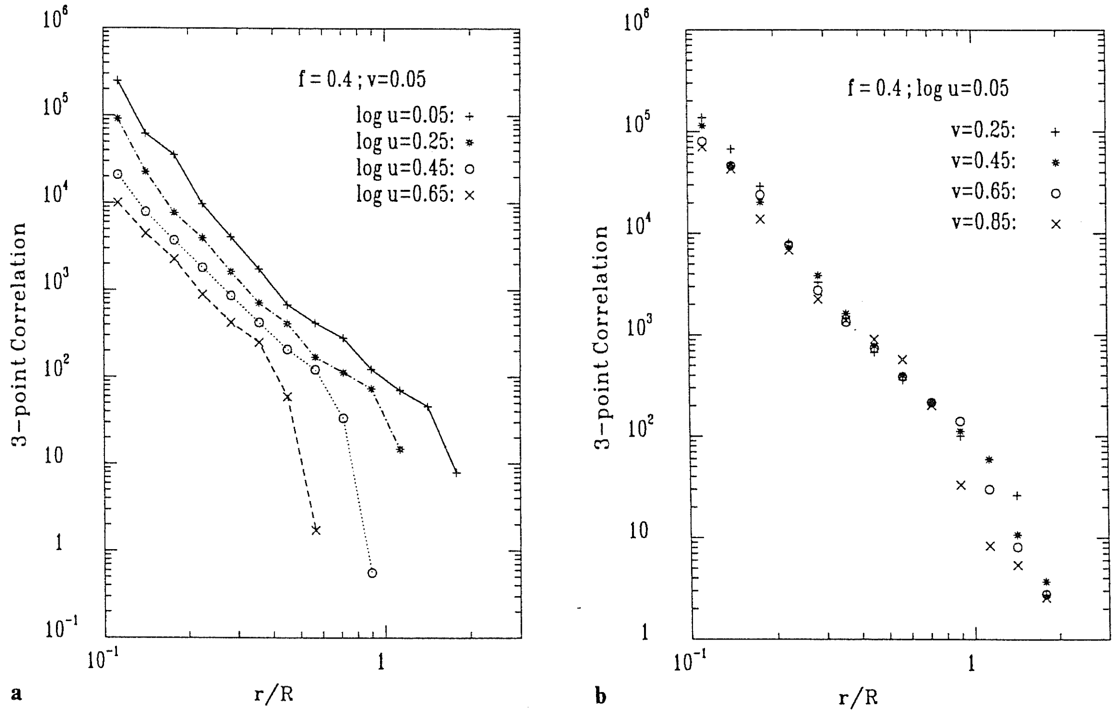

Figure 8.1 — The three-point correlation functions of the $f = 0.4$ constant model in eight typical (u, v)-bins. *a*). for fixed $v = 0.05$; *b*). for fixed $u \approx 1.1$.

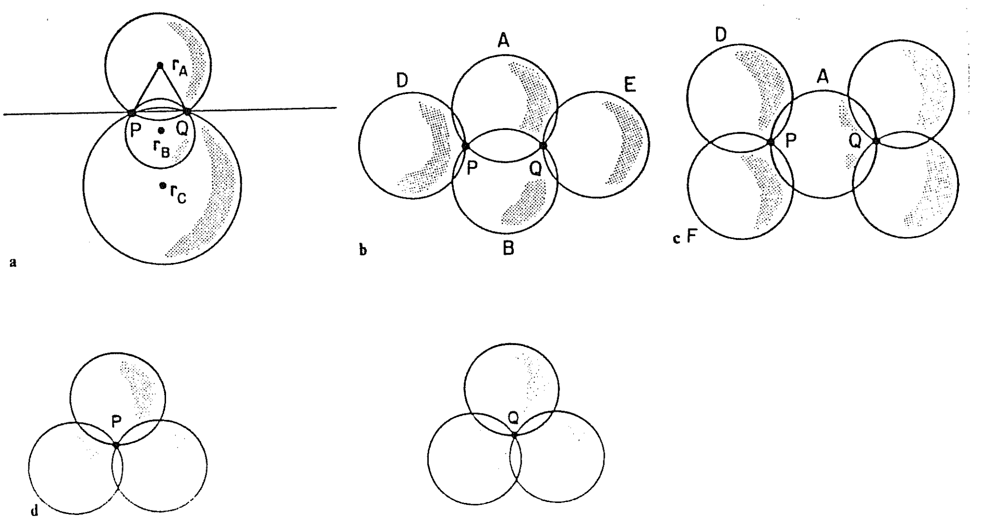

Figure 8.2 — The configurations of shells which produce two clusters. *a*). three common shells; *b*). two common shells; *c*). one common shell; *d*). All shells are different. This figure is taken from Kulsrud & Cowley (1989).

represents the other four cases with fixed $u \approx 1.1$ but different v, which includes triangles from approximate equilateral to highly oblated obtuse isosceles shapes. Again high three-point correlations are found on small scales. However, all ζ start to vanish at $r \approx ur \approx 2R$. This means that the ζ could remain positive out to $r_{31} = (u+v)r$, which is about $4R$ for $v = 0.85$. We can conclude that there are strong three-point correlations in triangles of two shorter sides r_{12}, $r_{23} \leq 2R$ and of the longest one $r_{31} \leq 4R$. We have also checked the ζ for the $f = 0.6$ and $f = 0.8$ models. The three-point clustering behaviour of these two models is very similar to that of the $f = 0.4$ model, and we omit their figures here.

This phenomenon can be easily explained by a sketch (Figure 8.2, taken from KC). It illustrates all the four configurations producing two clusters (P,Q). If a third cluster formed by three other shells (not belonging to the shells of Figure 8.2), and the first two clusters are produced by Figure 8.2d, such triplets contribute to the first term of Eq.(3.1.3). If the first two clusters are formed by either Figures 8.2a, 8.2b or 8.2c, and a third cluster is formed by the three independent shells, or if a third cluster is formed on either shell of Figure 8.2d and the first two clusters are P,Q of Figure 8.2d, such triplets contribute to the three ξ-terms of Eq.(3.1.3). It is only when a third cluster S is formed on a shell of Figures 8.2a, 8.2b or 8.2c (i.e., at least one common shell forming S, and P or/and Q) that triplets PQS would contribute to the reduced three-point correlation term of Eq.(3.1.3). It is easy to see that such triplets PQS always have two sides smaller than 2R and the longest side less than 4R.

In order for comparison with the observations, it is convenient to use the scaled three-point correlation function $Q(r,u,v)$:

$$Q(r,u,v) = \frac{\zeta(r,u,v)}{\xi(r)\xi(ur) + \xi(ur)\xi((u+v)r) + \xi((u+v)r)\xi(r)}. \tag{8.3}$$

Previous observational studies of Abell clusters show that Q is a constant between 0.5 and 1.1 (see Chapter 7). The amplitude of $Q(r,u,v)$ and its r-, u- and v- dependences then can be used to test the models.

In Figure 8.3, we show the scaled three-point correlation functions Q of Figure 8.1. Most Q fall in the range between 0.5 and 1.1. This is very encouraging. Q depends on u very weekly, and the average values of different u-bins remain almost a constant (see Figure

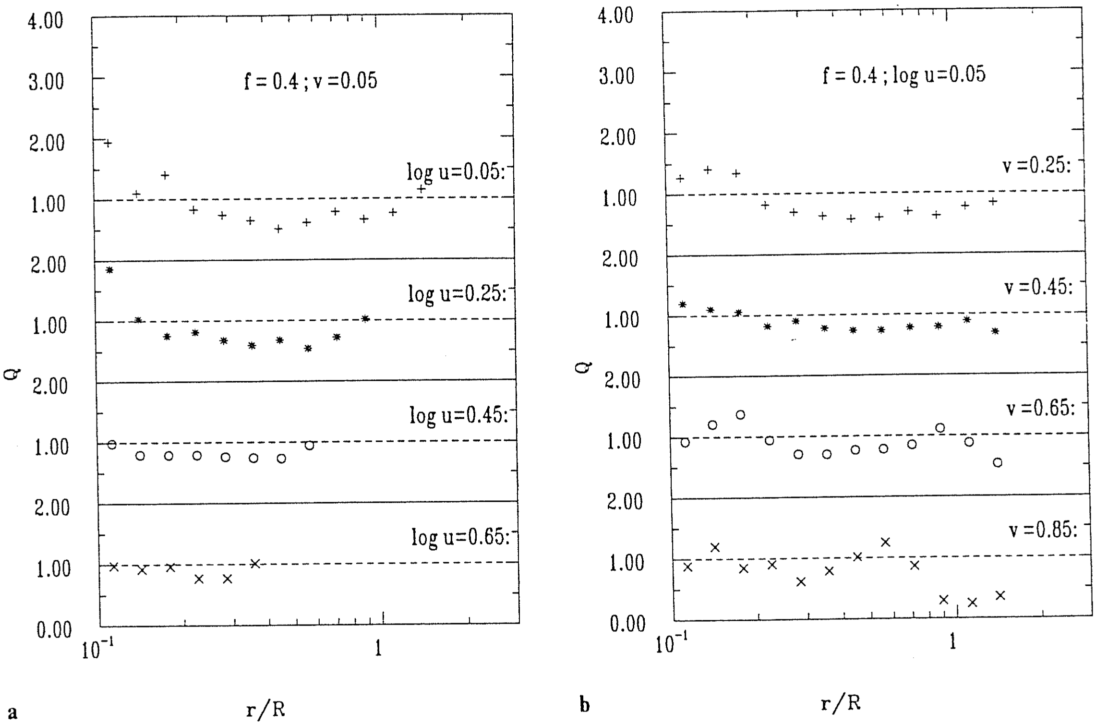

Figure 8.3 — The scaled three-point correlation functions Q of the $f = 0.4$ model. *a*) corresponds to Figure 8.1a; and *b*) corresponds to Figure 8.1b.

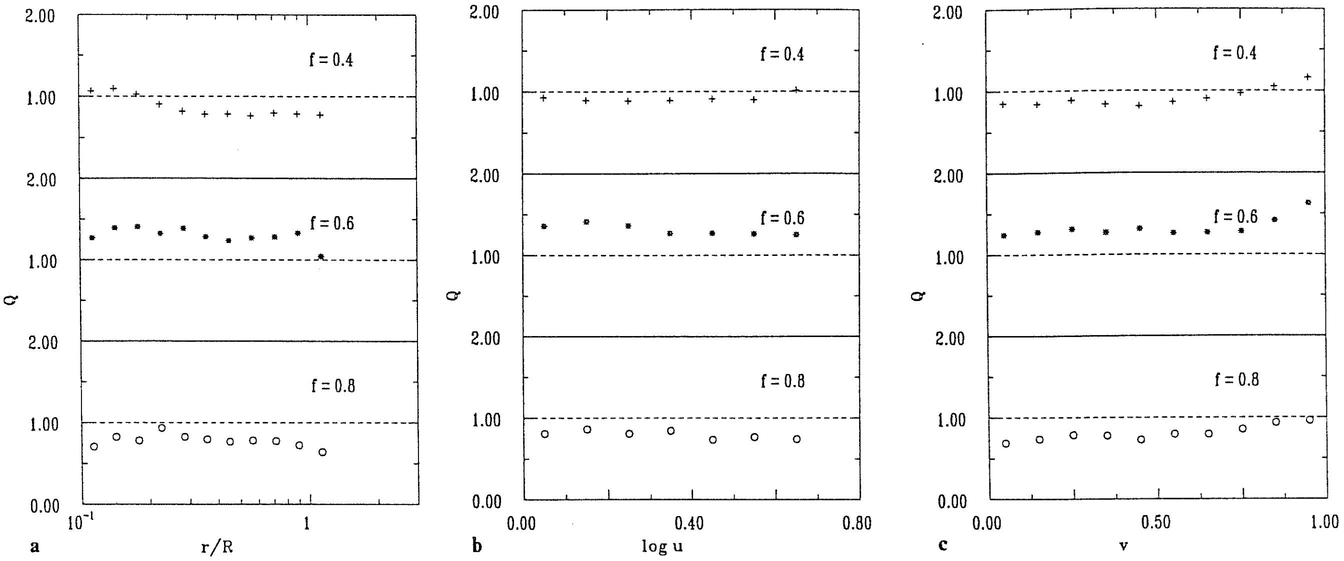

Figure 8.4 — The mean values of Q for the three constant models of different f. *a*). the average values of Q over all triplets with fixed r; *b*). the average values of Q over all triplets with fixed u; *c*). the average values of Q over all triplets with fixed v.

8.3a), although ζ for different u have very different magnitudes (Figure 8.1a). Similarly, Q also has a very week v-dependence (Figure 8.3b). For r from $0.1R$ to $2R$, the ζ changes by four magnitudes, whereas Q varies very slightly (within a factor 2).

To study the r-, u- and v-dependences of Q in more detail, we separately study each dependence following Groth & Peebles (1977). Figure 8.4a presents the arithmetic averages of $Q(r, u, v)$ over all (u, v) bins for the three different f models. Here and below we average Q over all triangles of three sides less than $2R$, for the reason that the two-point correlation function vanishes at $r > 2R$. From the figure, we find that the Q of all three models depends on r very weakly, and could be regarded as a constant with high precision ($\sim$ 15%). In Figure 8.4b, we plot the arithmetic averages of Q over (r, v)-bins. For different u, Q changes very slightly for the three models, and again could be considered as a constant for each model. Figure 8.4c shows the averages of Q over all (r, u)-bins. Although Q depends on v again very weakly, we can easily find a minor systematic variation: all models remain constant at $v \leq 0.7$, however Q rises slightly with v at the larger v.

In conclusion of this section, although the models taken here are the simplest possible ones of the explosion scenario, the results are encouraging: the observed scaling relation (3.1.7) can be easily reproduced in these models. The slight dependences of Q on r, u, and v may exist, but ζ of the models indeed could be expressed by the hierarchical form (3.1.7) with a high precision. The mean Q values are about 0.9 (for $f = 0.4$), and 0.8 ($f = 0.8$), favorably comparable to the observed value $Q_{obs} = 0.8 \pm 0.3$; while Q of the $f = 0.6$ model is about 1.3, which could be accepted within the 2σ level. It is still unclear if the slight variation of Q with f is the real feature of the model, or a statistical fluctuation in the simulations.

8.3 Power-law radius distributions

In this section, we study the models, in which the radii of shells are distributed in power laws. We assume that the mean density of shells with radius $R_1 \sim R_1 + dR_1$ is

$$n(R_1)dR_1 = n_o(R_1/R)^{\beta} dR_1, \tag{8.4}$$

where R is the maximum radius of shells. As WOD pointed out that $\beta \approx -4$ is of the most interest, and as their simulations have shown that such β could reproduce the mass function of Abell clusters well, we will adopt $\beta = -3.5$ and -4.5 here. Because the number of shells in a definite volume will diverge for $\beta \leq -4$, we must set a lower radius cutoff. The radius of shells will be limited to $R/4 \leq R_1 \leq R$.

We adopt the notations of KC. Let $n_l \equiv \int_l^\infty n(R_1)dR_1$, $a_l^2 \equiv 1/n_l \int_l^\infty n(R_1)R_1^2 dR_1$, $\overline{n} = n_l \mid_{l=0}$, $a^2 = a_l^2 \mid_{l=0}$, and the effective filling factor: $f = 4\pi/3a^3\overline{n}$. Then the cluster density is (KC)

$$n_{cl} = \frac{9\pi}{16} f^3 a^{-3}. \tag{8.5}$$

The method of simulation is similar to that of the constant models. For each β, we choose three f values: 0.2, 0.3 and 0.4. The simulation space is still a spherical volume. However, its radius R_{sim} is chosen by the condition that there are 1000 clusters [cf. Eq.(8.5)] in each realization of the $f = 0.2$ models. Now $R_{sim} = 9.2R$ for the $\beta = -4.5$ model, and $R_{sim} = 10.3R$ for $\beta = -3.5$. As only triplets of sides less 2R are considered below, this simulation space, we think, is already large enough. Again in order to correct for the boundary effects, we first randomly place (centers of) shells in the sphere of radius $R_{sim} + R$ for each $(f,\ \beta)$ model, under the condition that shells have the power law distribution (8.4). Then we find all "knots" (clusters) where three shells intersect, and include only those clusters which are in the sphere of R_{sim} in our later calculation of correlation functions. Other procedures are the same as in §8.2.

KC have analytically obtained the two-point correlation function and the mass function for the power law models. In Figure 8.5, we plotted the two-point correlation functions estimated by our simulations. Due to the domination of small shells in the shell number, ξ at small scale has behaviour very similar to the constant models, and could be represented by a power law of index about -2. At the larger scale, ξ falls more rapidly than in the constant models. The turning point appears at $r \sim 0.5R$, which could be expected because the radius of the smallest shell is $0.25R$. The analytical results of KC are plotted in the figure for comparison. We find that the data of simulations agree very well with the analytical formulae of KC. In Figure 8.6, we show the mass function of clusters obtained from our simulations. Here we adopt the mass recipe of WOD that the mass of a cluster

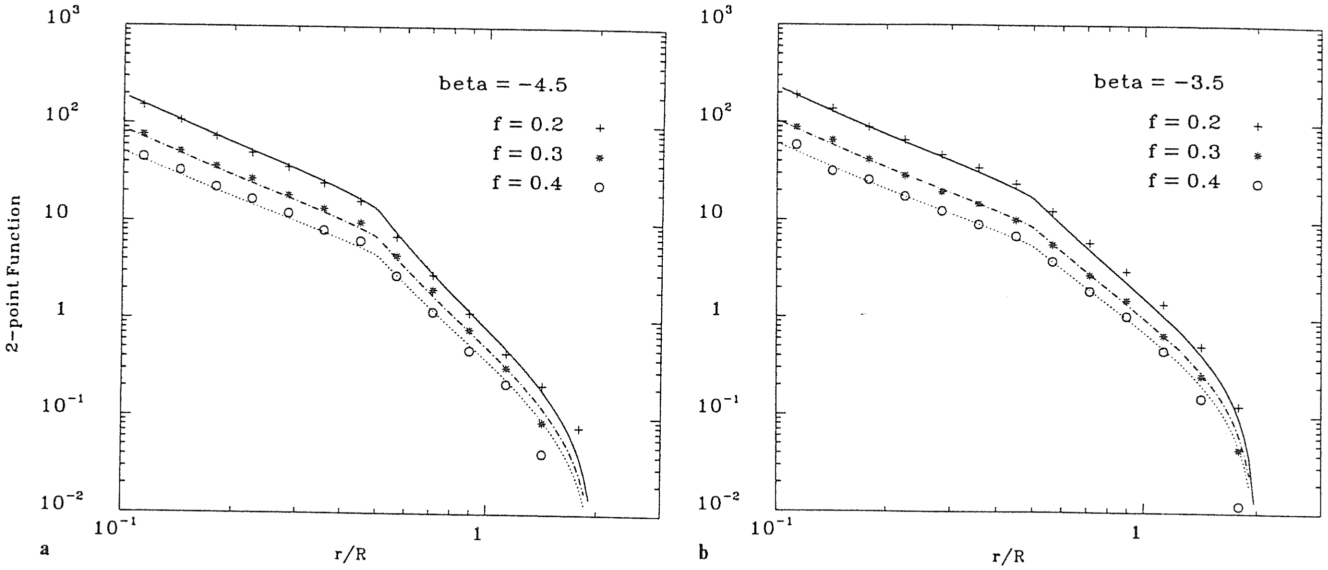

Figure 8.5 — *a*). The two-point correlation functions of the $\beta = -4.5$ power-law models with different filling factors. The symbols are the results of our simulations, and the smooth lines are the analytical results of Kulsrud & Cowley (1989). *b*). Same as a) but for $\beta = -3.5$.

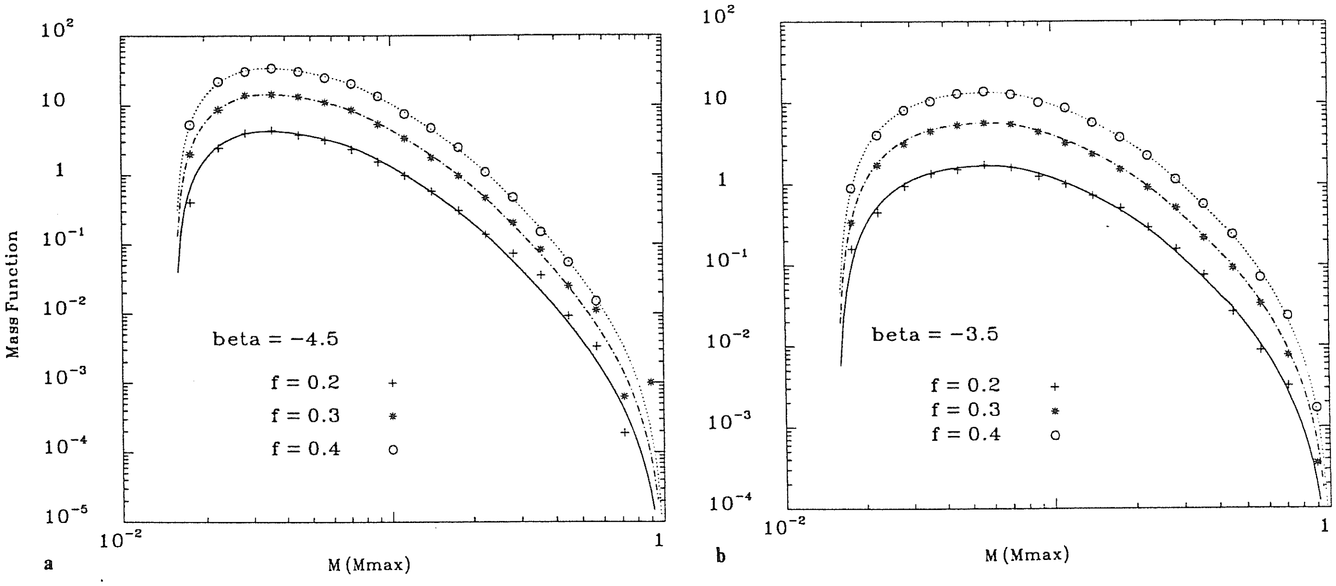

Figure 8.6 — *a*). The mass functions of the $\beta = -4.5$ power-law models with different filling factors. The symbols are the results of out simulations, and the smooth lines are the analytical results of Kulsrud & Cowley (1989). *b*). Same as a) but for $\beta = -3.5$.

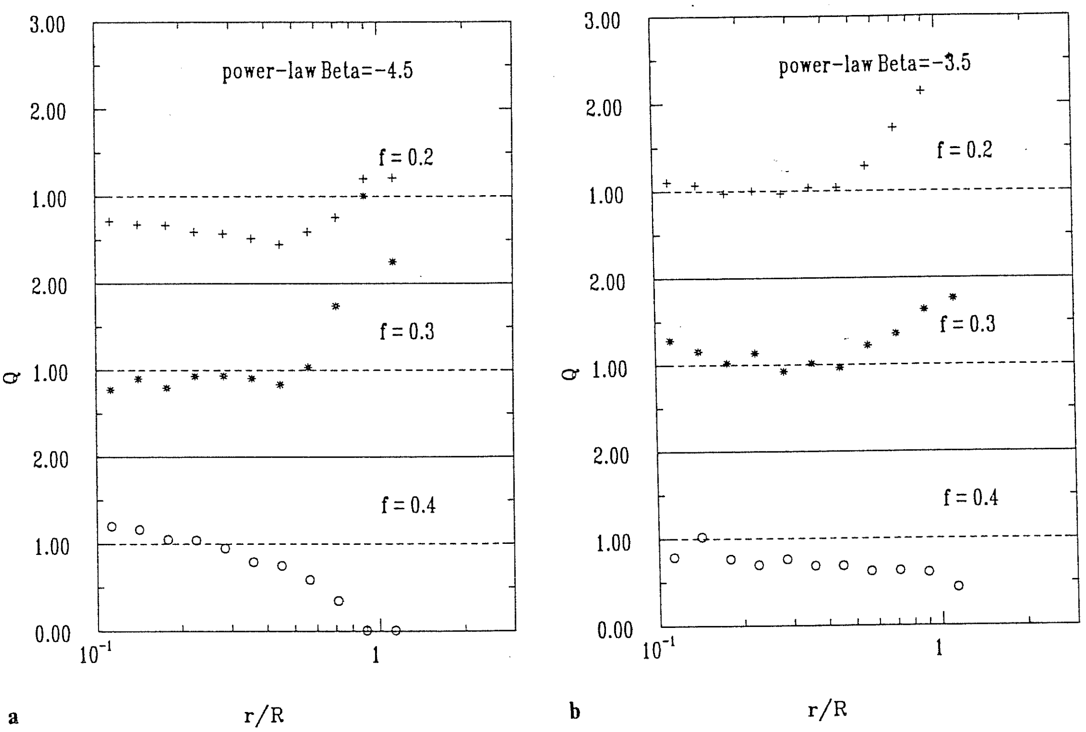

Figure 8.7 — *a*). The averages of Q over all triplets with a fixed r for the $\beta = -4.5$ power-law models with different filling factors. *b*). Same as a) but for $\beta = -3.5$.

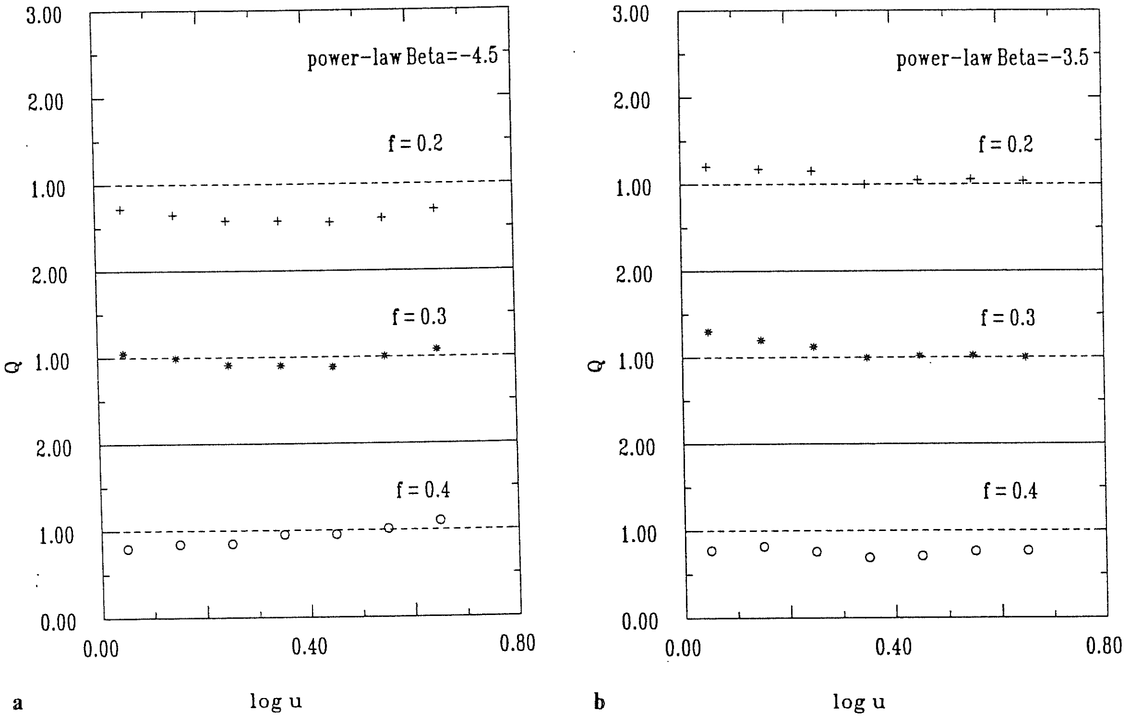

Figure 8.8 — Same as Figure 8.7 but as a function of u.

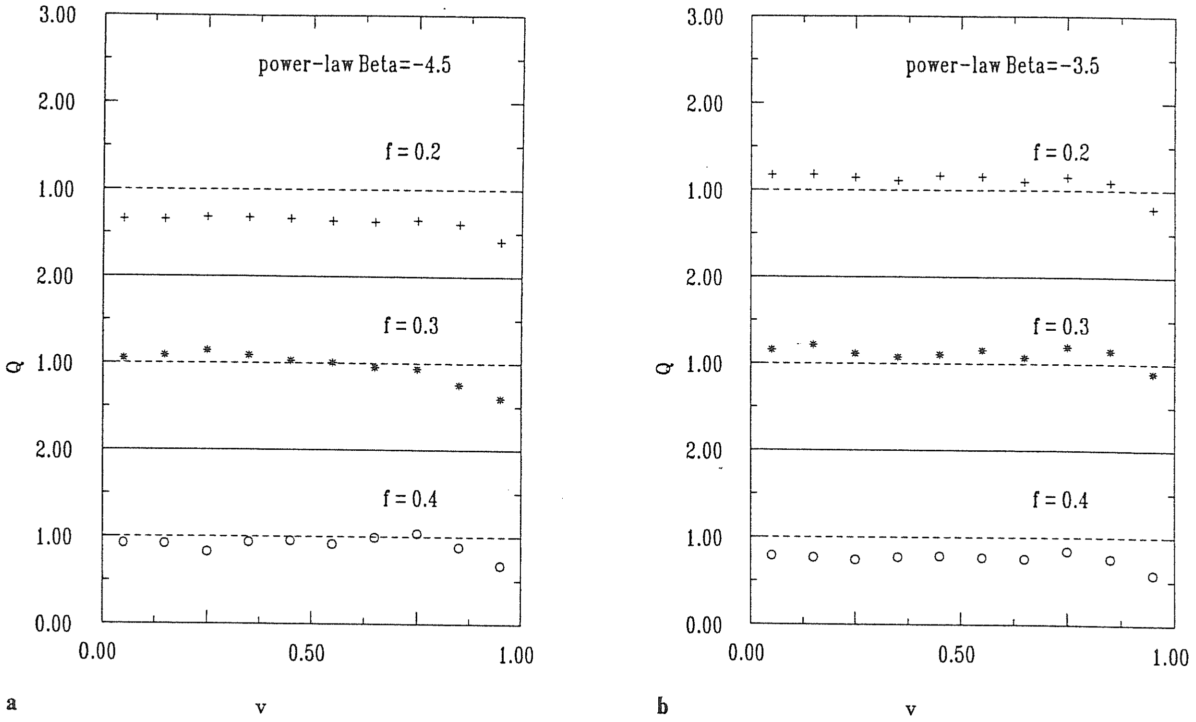

Figure 8.9 — Same as Figure 8.7 but as a function of v.

is proportional to the product of the three shell radii, that is $M = KR_1R_2R_3$ where K is a constant. In the figure, cluster masses are in units of $M_{max} = KR^3$, and the mass functions are in units of $M_{max}^{-1}R^{-3}$. The smooth lines are the analytical results of KC, which fit the simulations very well. The consistency between the analytical and the simulation results proves that the work of KC as well as our simulation methods are correct.

Now we calculate the three-point correlation functions for the models. We have not plotted ζ for several selected (u, v)-bins as in Figures 8.1 and 8.3, because they can't reveal anything new except they confirm a strong three-point correlation of triplets with two smaller sides shorter than $2R$ and the longest side shorter than $4R$. Instead we present the mean values of Q. Figure 8.7 shows the averages of Q with fixed r over all configurations. Q remains constant ~ 1 at $r \leq 0.5R$. However at larger scales, Q of the $f = 0.2$ and 0.3 models rise by a factor 1 to 2, while Q of the $f = 0.4$ models fall by a factor 0.5 to 1. Because the contributions to the small scales are dominated by small shells, a constant Q could be expected from the last section. The variations of Q at large scales may reflect a large range of shell radii.

In Figure 8.8, we present the averages of Q with fixed u over all (r, v)-bins. For all six (f, β) models, the Q depends on u very weakly. Figure 8.9 shows the dependence of Q on v. All models have a constant Q at $v \leq 0.8$, while Q falls a little at larger v. We could conclude that Q is almost independent of the shape parameters u and v. The mean values of Q are about 0.7 ($f = 0.2$), 1.0 ($f = 0.3$) and 1.0 ($f = 0.4$) for the $\beta = -4.5$ models, and 1.1 ($f = 0.2$), 1.1 ($f = 0.3$) and 0.8 ($f = 0.4$) for the $\beta = -3.5$ models, so all six models are acceptable within the 1σ level by the observations.

8.4 Modified Power Law Models

In contrast with the last section, here we eliminate all shells which are entirely inside larger shells. Because a certain fraction of small shells will lose their identity, we define the filling factor f only with the largest shells $1/2R_{max} < R < R_{max}$, as in WOD. [Note: the meaning of R_{max} is equivalent to that of R in §8.3 and R is to R_1 there.] The model is completely fixed by three parameters: f, β and R_{max}.

The model is essentially equivalent to the general power law model of WOD, except we take $R_{min} = R_{max}/4$ instead of $R_{max}/8$. Since most small shells would be eliminated due to lying inside larger shells, and since we are only interested in Abell-like clusters (not poorer clusters or groups), this difference has little influence on our discussion (also see below). So we can directly adopt some results of WOD for our simulation.

From comparison of the theoretical mass function with the observational LF of Abell clusters, WOD concluded that objects which could be identified as Abell clusters should have mass $M \geq M_*$, and

$$M_* = \begin{cases} 0.14M_{max}, & \beta = -4.5 \\ 0.23M_{max}, & \beta = -3.5 \end{cases},$$

and that the mean separation of these objects is

$$\bar{d}_* = \begin{cases} 0.29R_{max}f^{-1}, & \beta = -4.5 \\ 0.52R_{max}f^{-1}, & \beta = -3.5 \end{cases}. \tag{8.6}$$

The simulation method is similar to that used in §8.3, but the equation (8.6) is used to fix the simulation volume so as that there are about 1000 clusters of $M \geq M_*$ for $f = 0.2$ in each realization. So for $\beta = -3.5$, $R_{sim} = 15.8R_{max}$; and for $\beta = -4.5$, $R_{sim} = 9.0R_{max}$.

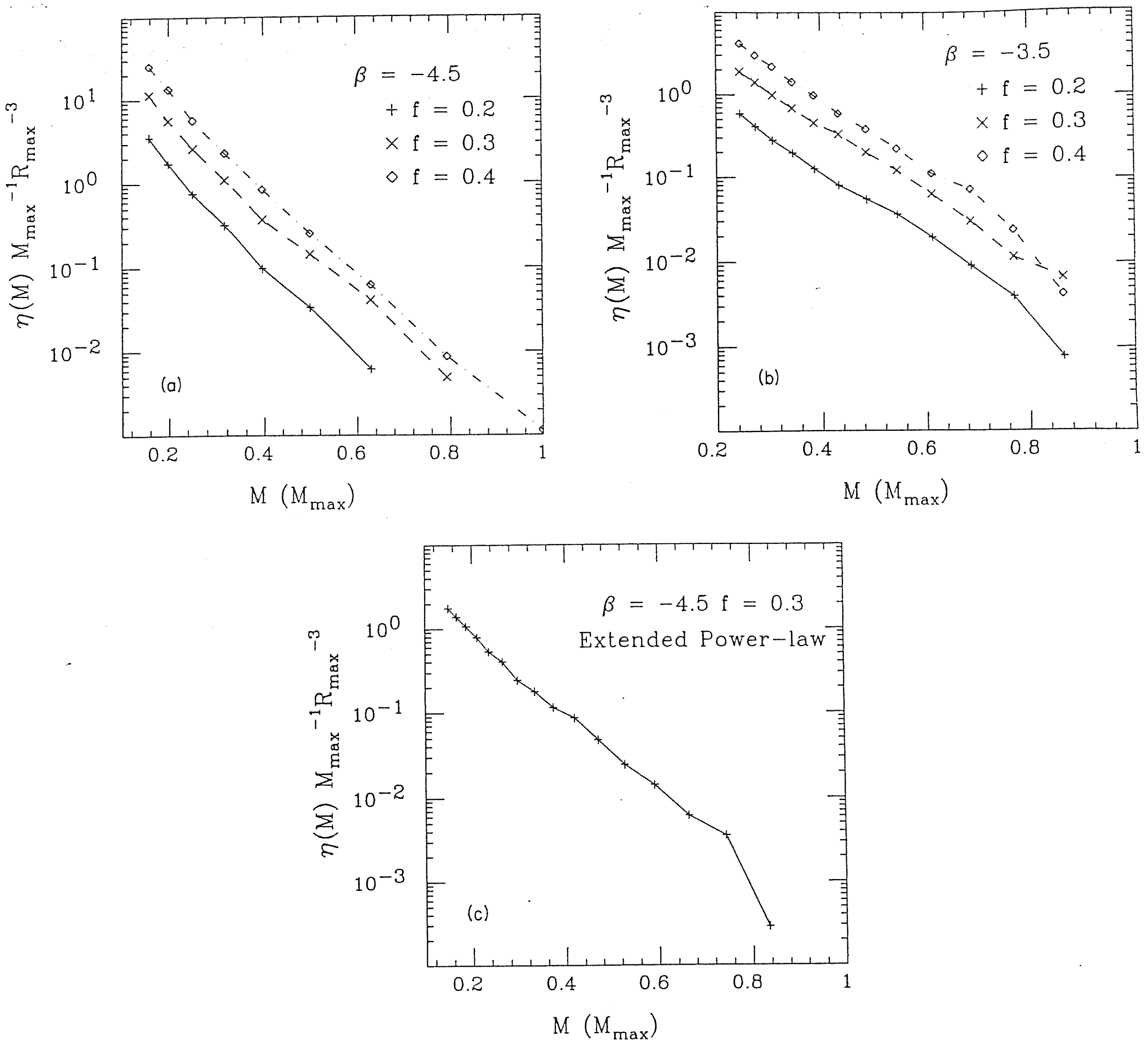

Figure 8.10 — *a*). The mass functions for the $\beta = -4.5$ modified power law models of different filling factors. *b*). Same as a) but for $\beta = -3.5$. *c*). Same as a) but for the "extended" model. These data are fairly consistent with Weinberg et al. (1989).

As a test of our simulation methods, we compare the mass function and the number density of clusters with those of WOD. In Figure 8.10, we plot the cluster mass functions of our simulations for $M \geq M_*$. Compared with Figure 3 of WOD, our results are reasonably consistent with their results. The resultant mean separation of $M \geq M_*$ clusters deviates

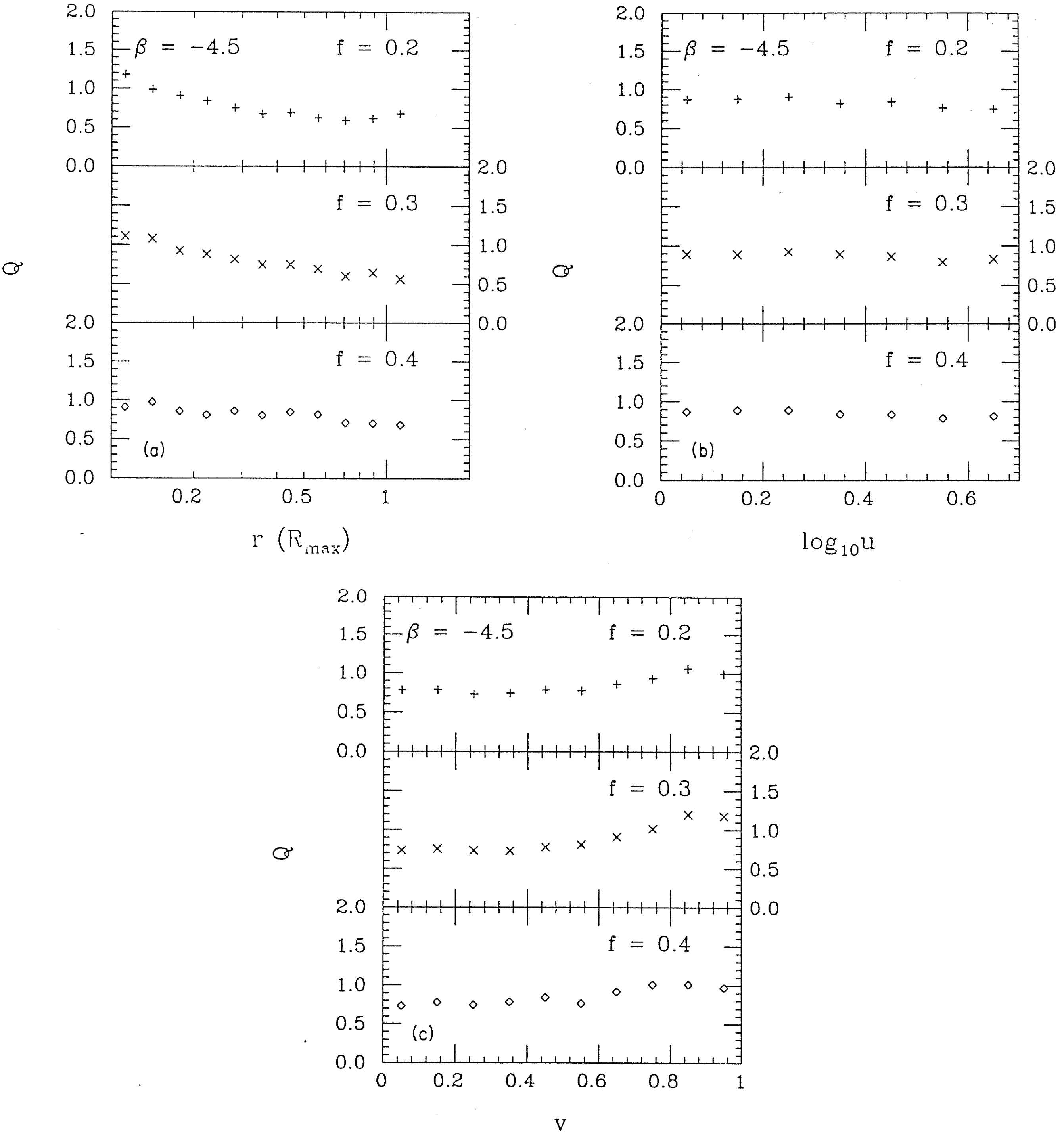

Figure 8.11 — The scaled three-point correlation function Q of the $\beta = -4.5$ models. *a*). The averages of Q over all triplets with a fixed r. *b*). The averages of Q over all triplets with a fixed u. *c*). The averages of Q over all triplets with a fixed v.

from equation (8.6) less that 3%. Since in WOD equation (8.6) was obtained from fitting the simulation data by Schechter-like function, and since there exist fluctuations in the simulation due to strong clustering, this deviation is not unexpected.

In Figures 8.11 and 8.12, we present the results of Q for the modified power law models of different indices β and different filling factors f. Figures 8.11a and 8.12a give the averaged $\overline{Q}$ as a function of r. For small filling factor $f = 0.2$, $\overline{Q}$ decreases about 50% with the increase of r about one magnitude. This dependence is weakened as f increases. For both values of β, $\overline{Q}$ of $f = 0.3 \sim 0.4$ could be well regarded as a constant with high precision ($\leq 15\%$). Comparing these results with §8.2 and §8.3, we find that $\overline{Q}$ of the modified power law models have much weaker r-dependence than the pure power law models. The variations of $\overline{Q}$ with r are only comparable to those of the constant models, which is very interesting. These results were expected, because the modifications (i.e., to remove shells which lie entirely within larger shells and to include only Abell like clusters) mainly eliminate the effects of small shells, thus narrowing the shell radius distribution.

To see the dependence on u, we plot $\overline{Q}$ as a function of u in Figures 8.11b and 8.12b. We can easily find that for all six models $\overline{Q}$ depends on u very weakly. The models of $f = 0.2$ have about 10% fluctuations around their mean values. The fluctuations of $f = 0.3 \sim 0.4$ models are much smaller. The results are very similar to those of the constant models. However, the models have a weaker u-dependence than the pure power-law models (§8.3).

The dependences of $\overline{Q}$ on v are shown in Figures 8.11c and 8.12c. For all the models, $\overline{Q}$ are approximately constants for $v \leq 0.7$ and rise $15 \sim 30\%$ for larger v. Similar behaviour was seen in the constant models. In contrast, the $\overline{Q}$ remain almost constant for $v \leq 0.8$ but fall about 30% for larger v in the pure power law models.

To summarize, the modifications considered in this section greatly improve the power law models on producing the hierarchical form (3.1.7). Compared with the constant models, the modified ones produce similar ζ but are more realistic in the physical sense and better at accounting for observational facts , such as the LF of Abell clusters, the observed bubbles in redshift slice surveys, the two-point cluster-cluster function, etc.. If we take into account the observational uncertainties (see, Jing & Zhang, 1989) and the theoretical

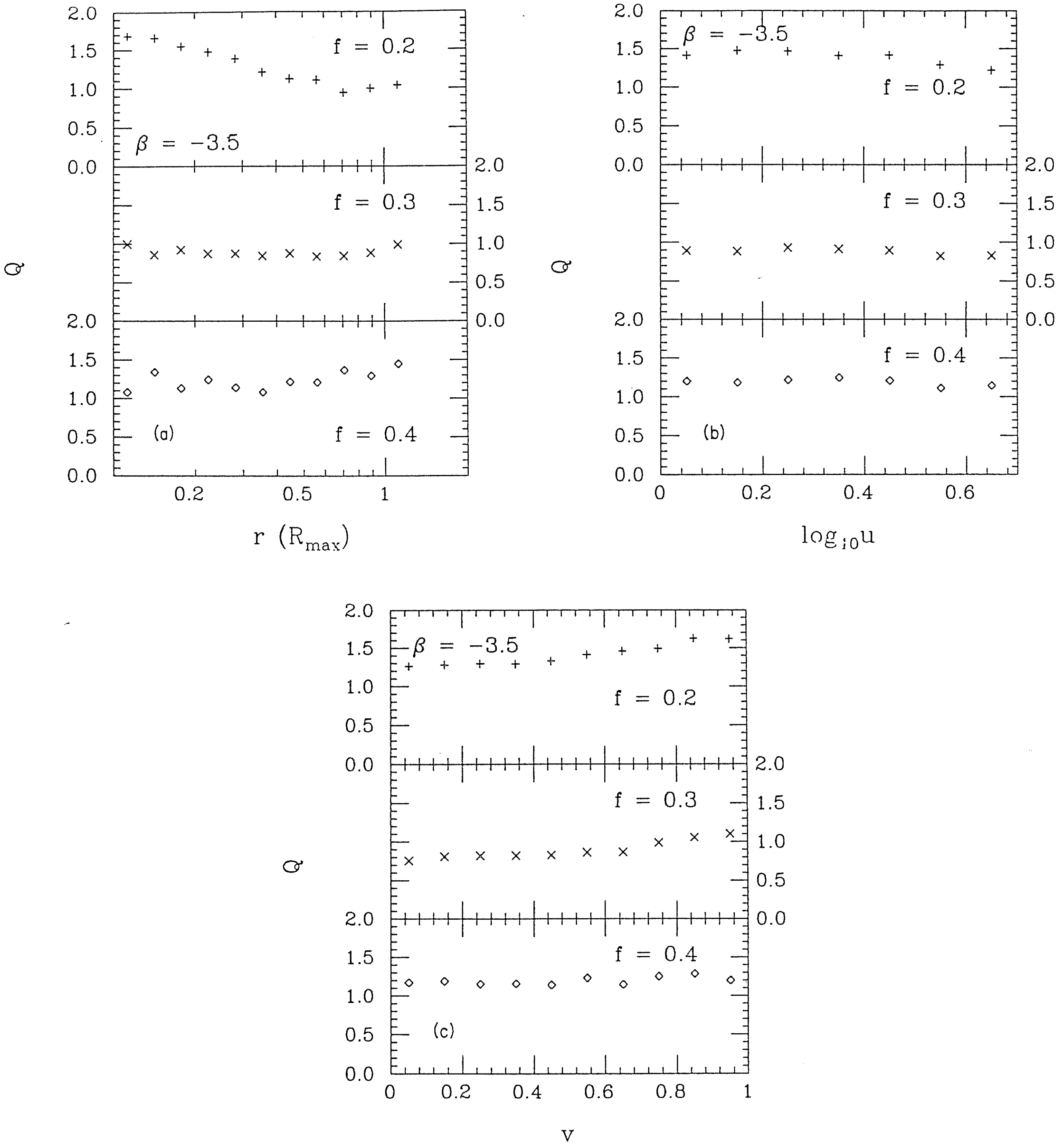

Figure 8.12 — Same as Figure 8.11 but for $\beta = -3.5$.

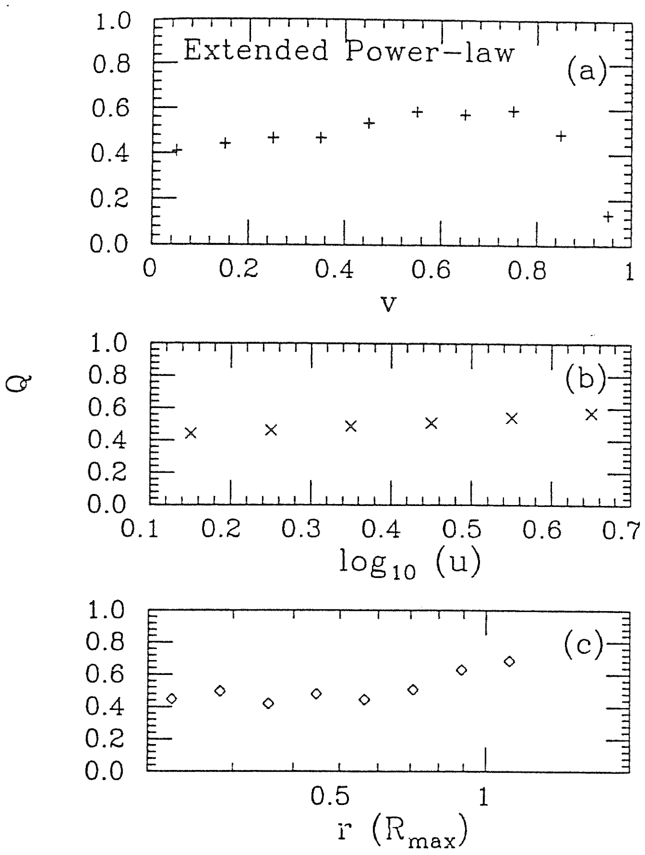

Figure 8.13 — Same as Figure 8.11 but for the "extended" model.

uncertainties, the modified models can explain well the observed hierarchical form. The mean values of Q are all about 0.85 for $\beta = -4.5$, quite consistent with the observations. For $\beta = -3.5$, only the model of $f = 0.3$ produces the right value of Q ($\sim$ 0.9); those of $f = 0.2$ and $f = 0.4$ have rather high Q values (1.3 and 1.2 respectively) though they are marginally acceptable at 1.5σ. The variations of Q with f in the $\beta = -3.5$ models bother us. At this stage, it is difficult to judge whether they are caused by the simulation fluctuations or by real features of the models. We are approaching this problem by running larger simulations.

As described in the introduction, it seems inevitable that cluster mergers and shell mergers happen in the real world. WOD show that inclusion of these effects greatly improves the model for fitting the two-point correlation function of Abell clusters. Here we will consider these effects following the techniques of WOD. We merge each group of objects which are separated by less than $R_{max}/5$ into each cluster, and the merged mass is assigned the mass of its largest component. To approximate the shell mergers, we simply follow the procedures of WOD: eliminate all seeds which lie inside larger shells. We adopt $\beta = -4.5$ and $f = 0.3$, so the model is just the "extended" model of WOD, which was regarded by them as the most successful model for fitting both the LF and the two-point function of Abell clusters. In Figure 8.10c, we plot the mass function for clusters of this model, which again accords well with that of WOD.

In Figure 8.13, we present its averaged $\overline{Q}$ as a function of one of the three variables. It is easily seen that for each variable, the mean fluctuations of Q around its mean value are less than about 15% (Here we excluded the point at $v = 0.95$). So the model could be acceptable in reproducing the observed hierarchical form. The mean value of $\overline{Q}$ is about 0.5, close to the lower observational limit.

8.5 Conclusions

We have constructed a set of numerical simulations and studied the three-point correlation functions ζ of clusters in the bubble models. The main conclusions can be summarized as the following.

1). The ζ of the constant models can be expressed well by the hierarchical form with Q about 1, consistent with the observations (except for the $f = 0.6$ model, which is at the 2σ level).

2). In the power law model, the scaled three-point correlation function $Q(r, u, v)$ depends on u and v very weakly, while it has some dependence on r. At small scales $r \leq 0.5R$, Q remains a constant about 1, however it changes a factor 1 to 2 at the larger scale.

3). The removal of small shells which lie entirely inside larger shells greatly improves the power law models in producing the observed hierarchical form. The modified models of $\beta = -4.5$ are completely consistent with the observations of ζ. While the modified model of $\beta = -3.5$ and $f = 0.3$ fits the observed ζ very well, those of $f = 0.2$

and $f = 0.4$ have rather high Q values although they could be acceptable at the 1.5σ level.

4). The "extended" model could pass the observational test of ζ, although its mean Q value is close to the lower observational limit.

5). This study has already covered a wide class of bubble models. We are aware that the models presented here are still simplified. However, it is very impressive that the three-point function of clusters, expressed in the hierarchical form, are not very sensitive to the model details. This may indicate that the bubble models meet no obstacle in passing the observational test of ζ.

‡The materials presented in this chapter are based on my two papers: Jing, Y.P. 1990, *Astronomy and Astrophysics*, **233**, 7; Jing, Y.P. 1991, *Monthly Notices of the Royal Astronomical Society*, **248**, 559.

9

Void distributions in ACO cluster catalogue

As discussed in §3.3, the void probability function (VPF) is a very useful tool for extracting information on high-order clusterings. In this chapter, we shall present the VPFs of the ACO clusters in two dimensions (2-D). Although the three-dimensional (3-D) analysis in principle is much richer than the 2-D one, several obvious practical properties lead us to do the 2-D analysis. 1). The 2-D sample is incomparably larger than the 3-D samples available, because only a small portion of clusters have the measured redshifts; 2). The 3-D samples may suffer from the problem of large peculiar velocities (Bahcall et al. 1986; cf. §5.4), redshifts not being the true distance indicators; 3). As shown by Schaeffer (1987), a universal function $\Sigma(q)$ (its definition will be given below) is approximately the same in the 2-D and 3-D statistics, provided clustering is scale-invariant, which just is the case for clusters (see below). All this makes the 2-D analysis very attractive.

9.1 Samples and Method

Table 9.1

A Summary of Samples

Sample	b^{II}	Distance	Richness	Number
DR61	$\mid b^{II} \mid \geq 40°$	≤ 6	≥ 1	1950
DR61N	$b^{II} \geq 40°$	≤ 6	≥ 1	919
DR61S	$b^{II} \leq -40°$	≤ 6	≥ 1	1031
DR51	$\lvert b^{II} \rvert \geq 40°$	≤ 5	≥ 1	829
DR62	$\lvert b^{II} \rvert \geq 40°$	≤ 6	≥ 2	523

The samples used here are from the new Abell cluster catalogue (Abell, Corwin & Olowin 1989). We restrict our analysis to the high latitude samples with $\mid b^{II} \mid \geq 40^\circ$. We first determine void probability and count probabilities for the largest sample (DR61) with richness $R \geq 1$ and distance $D \leq 6$. In order to study the scaling properties of holes, we separately estimate the VPFs for a subsample (DR51) of $D \leq 5$ and for a subsample (DR62) of $R \geq 2$. A summary of samples is given in Table 9.1.

The method used to determine the count probability $P_N(\theta)$, which is defined as the probability of finding exactly N clusters in a circle of radius θ, is similar to that of Bouchet & Lachieze-Rey (1986). We randomly place a set of points in the survey area. For each random point, we draw a set of circles around it with different radii θ, and count the number of clusters in each circle. If a circle crosses the boundary of the sample, we throw it away, thus correcting for the boundary effects. Then we can easily get the probability functions $P_N(\theta)$, and also obtain the expected counts $\langle N(\theta) \rangle = \sigma\Omega$ (where σ is the surface number density of clusters, and Ω is the solid angle of the circle) and its second moment $\langle (N - \langle N \rangle)^2 \rangle$. Thus we can simultaneously get the function Σ, which is defined as $\Sigma \equiv \ln P_0/\sigma\Omega$, and the scaling variable $q \equiv \sigma\Omega\overline{\omega(\theta)} = \langle (N - \langle N \rangle)^2 \rangle / \sigma\Omega - 1$ (see Peebles 1980), where $\overline{\omega(\theta)} \equiv \int \omega(\theta_{12}) d\Omega_1 d\Omega_2 / \Omega^2$, the average two-point angular correlation function. In the previous studies, q was usually calculated from the two-point correlation function. Our method now can by-pass this problem, and can self-consistently get Σ and q. Here 120,000 random points are taken for the DR51 and DR61 samples and 200,000 for the DR62 sample, thus minimizing the statistical uncertainty induced by the method. Since the sample lies at the high latitude, the galactic extinction effect is small and we have ignored it in our calculation. The radius θ was taken from 0.1° to the largest one, where only one void was detected, with the increment of 0.1°.

9.2 Results and Discussions

9.2.1 Count probabilities

In Figure 9.1, we present the count probabilities $P_N(\theta)$ with $N = 0 - 3$ for the DR61 sample (solid lines) as well as for a random sample (dot-dashed lines). Although the

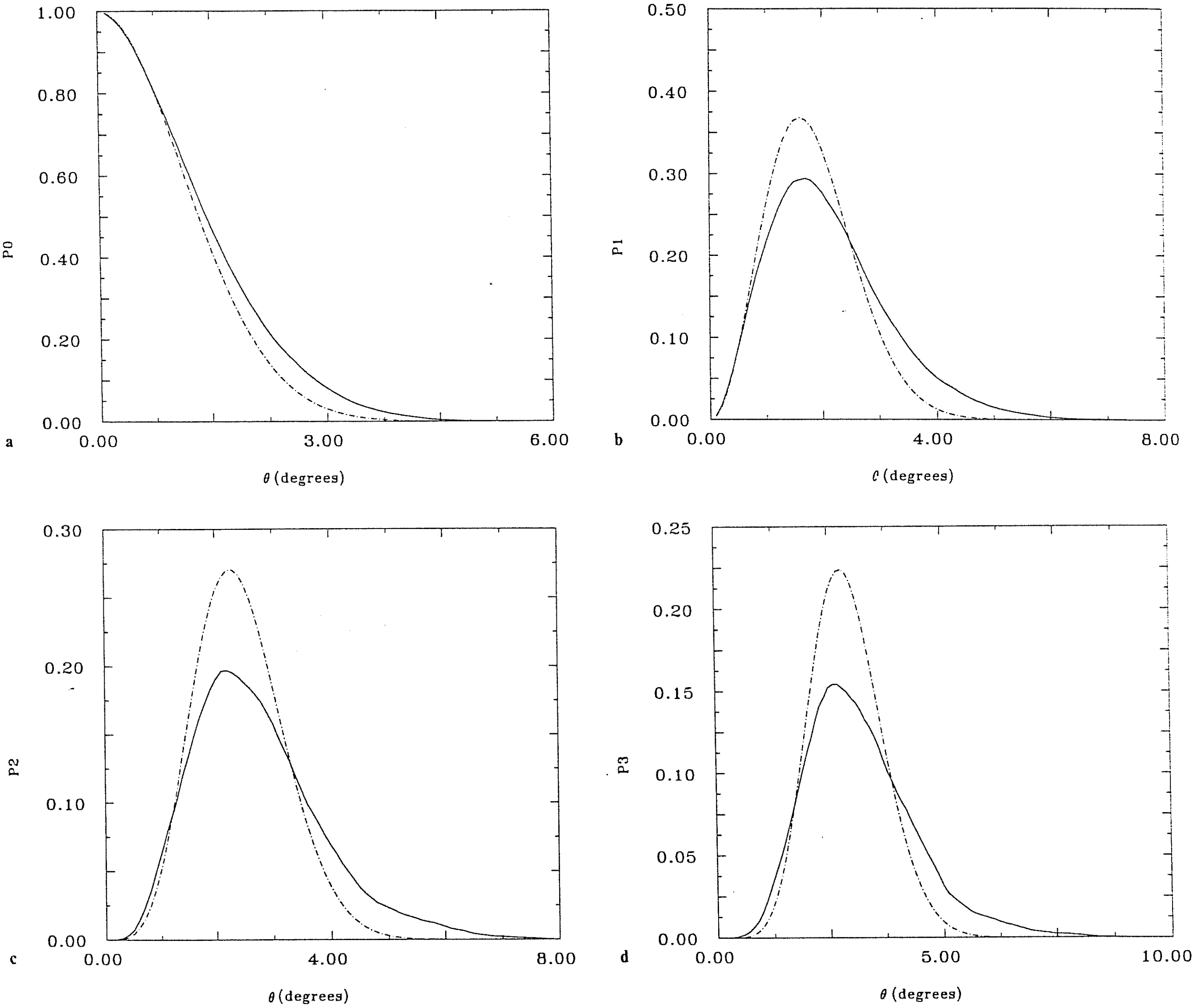

Figure 9.1 — The count probabilities $P_N(\theta)$ with $N = 0$–3 [a)–d)] for the DR61 sample (the solid lines). The dot-dashed lines represent $P_N(\theta)$ expected for a random catalogue.

general behaviour is the same in the real and random samples, we can find that clustering exists. As expected, there are always more voids in the actual distribution than in the random distribution. For $N \neq 0$, $P_N(\theta)$ flattens more in the cluster catalogue. For small and large circles (as compared with the circle where the maximum P_N shows up), $P_N(\theta)$ of the real catalogue is larger, which is consistent with the fact that superclusters and voids exist in the real sample.

9.2.2 Function $\Sigma \equiv \ln P_0/\sigma\Omega$ *and scaling*

As pointed out in §3.3, if all n-point correlation functions are scale-invariant, the $\Sigma \equiv \ln P_0/\sigma\Omega$ is only a function of the scaling variable q (White 1979; Schaeffer 1984). Sharp (1981) and Bouchet & Lachieze-Rey (1986) analysed the angular void distribution in the Zwicky and CfA catalogues and reached the conclusion that galaxy distribution has scaling invariance.

In Figure 9.2, we plot $\ln P_0/\sigma\Omega$ — q for the DR61 sample (solid line). Due to the large number of random circles placed, the statistical uncertainties introduced by the method itself are negligible. To see this, we can use the formula of Maurogordato & Lachieze-Rey (1987, hereafter ML) to estimate them. As ML claimed, such errors are significant both on small and on large sizes. We found that the errors of $\Sigma(q)$ are 0.01 at $q = 0.1$, 0.01 at $q = 1.9$, 0.02 at $q = 2.3$ and increase much faster at the larger sizes. So for the greater part of $q \leq 2.0$, in which we are mostly interested, this kind of error should be much less 0.01. However, the intrinsic fluctuations of samples cannot be avoided. To check this, we also analyse the north (DR61N) and the south (DR61S) subsamples separately, and the results are also plotted in Figure 9.2. The deviations of the north and of the south from the whole sample can be considered as the intrinsic uncertainties. As the figure shows, for q less than 1.5 (i.e., $\theta < 3.2°$ or $r < 30\,h^{-1}$Mpc), Σ of the north and of the south are fitted very well (their differences are less than 0.02), so the results in Figure 9.2 for $q < 1.5$ can be regarded as the true representation of Σ for clusters. For $q > 1.5$, fluctuations are very large because only a few of the voids are detected and the sampling errors become large. Such large intrinsic errors have already prevented us from extracting any useful information. Below we will only consider Σ for $q < 1.5$.

To check the scaling, we plot the $\Sigma(q)$ of the DR61 sample (solid line) and of the DR51 sample (dot-dashed line) separately in Figure 9.3. We can see that for $q < 1.5$, two curves are superposed with a high accuracy ($\Delta\Sigma < 0.01$). This means that the scaling relation is verified. We note that these two samples are very different in mean surface density and in mean depth. And $q = 1.5$ corresponds to $\theta = 3.2°$ or $r = 30\,h^{-1}$Mpc for the DR61 sample and $\theta = 3.6°$ or $r = 25\,h^{-1}$Mpc for the DR51 sample. So our results support the assumption that the cluster distribution is scale-invariant.

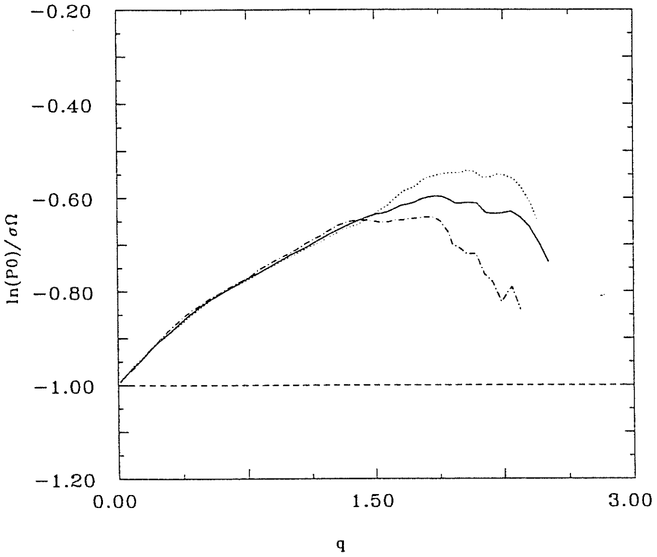

Figure 9.2 — The $\Sigma \equiv lnP_0/\sigma\Omega$ as a function of the scaling variable q. The solid line is for the DR61 sample, the dot-dashed line for the DR61N and dotted line for the DR61S.

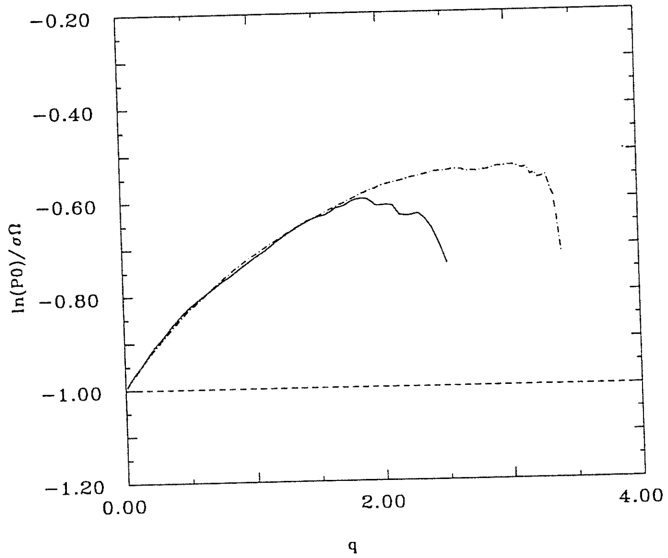

Figure 9.3 — The same as Figure 9.2. The dot-dashed line is for the DR51 sample, and the solid line for the DR61.

9.2.3 A second scaling

As Jing & Zhang (1989) emphasized in their paper, the hierarchical relation (3.1.7) holds for clusters of different richness, and Q is almost the same from galaxies to $R \geq 2$

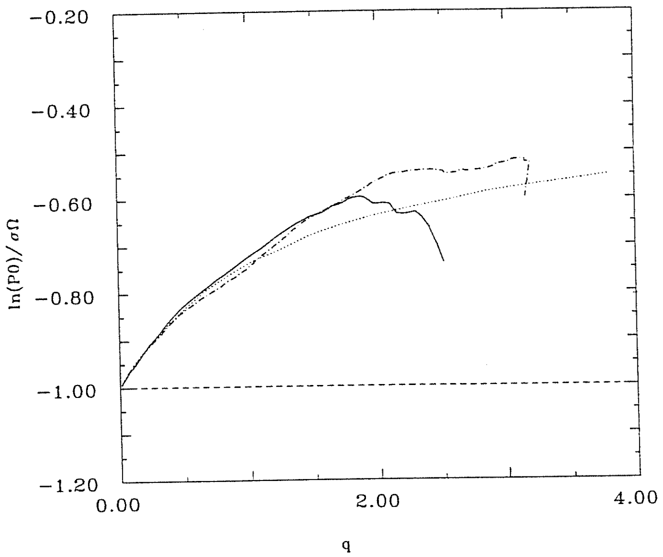

Figure 9.4 — The Same as Figure 9.2. The dot-dashed line represents the DR62 sample, the solid line is for the DR61 sample and the dotted line is for the CfA galaxy catalogue (for comparison).

clusters. The work of Maurogordato & Lachieze-Rey (1987), which dealt with the void distribution in galaxies of different luminosities, also presents a similar conclusion that the scaling relation of Σ(q) is universal and independent of luminosity. To further examine this scaling property, we estimated the Σ for $R \geq 2$ clusters (DR62 sample), and results are presented in Figure 9.4 (dot-dashed line). We again find that the two curves of $R \geq 2$ and $R \geq 1$ are superposed with great precision for $q < 1.5$ ($\Delta\Sigma < 0.02$). The mean surface density of $R \geq 1$ clusters is about 4 times higher than that of $R \geq 2$, and $q = 1.5$ corresponds to $\theta = 4.8°$ or $r = 45\,h^{-1}$Mpc for the DR62 sample. This indicates that the scaling distribution of clusters is independent of their richness.

To compare with galaxies, we also estimate $\Sigma(q)$ for the CfA survey by the same method for the self-consistency reason. From Figure 9.4, we see that the curves of galaxies and of clusters are also very similar.

9.3 Conclusions

In this chapter, we determined the count probabilities $P_N(\theta)$ for the ACO catalogue.

Examining the $\Sigma(q)$ of the DR61N and DR61S samples, we found that the errors in our measurement are very small for $q < 1.5$. By comparing the $\Sigma(q)$ of the DR61, DR51, and DR62 samples, we can conclude that the cluster distribution is scale-invariant, and this scaling property is independent of their richness. From the further comparison with the CfA sample, we tentatively conclude that the scaling relation is similar from the scale of galaxies to the scale of rich clusters. This universal scaling would be important in understanding the formation of galaxies. The results obtained here have been confirmed by the recent analysis of Cappi et al. (1991b) based on small 3-D samples.

‡The materials presented in this chapter are based on my paper: Jing, Y.P. 1990b, *Astronomy and Astrophysics*, **233**, 309.

10

A comparison of the spatial distribution of Abell clusters with that from Gaussian fluctuations

There is a considerable body of observational evidence (Kirshner et al. 1981, de Lapparent et al. 1986, Geller & Huchra 1989, Broadhurst et al. 1990) that the large scale clustering pattern of galaxies is characterized by a filamentary and sheet–like distribution over scales ranging up to $\sim 100\ h^{-1}$ Mpc, with voids of comparable size.

The intrinsic luminosity of rich galaxy clusters (Abell 1958; Abell, Corwin and Olowin 1989, hereafter ACO) allows one to study the 3–D clustering pattern out to $z \sim 0.1$, on scales much deeper than those traced by the available galaxy catalogues. Various authors (Bahcall & Soneira 1983, Klypin & Kopylov 1983, Postman et al. 1986, Batuski et al. 1989; Plionis & Borgani 1992) have reported that the two–point correlation function of rich clusters has the same slope as that of galaxies ($\gamma \sim 1.8$) but with a significantly larger clustering length. It has also been claimed that the spatial distribution of clusters is characterized by filamentary structures with lengths up to $\sim 200\ h^{-1}$ Mpc (*cf.* Batuski & Burns 1985a) and by an apparent large-scale flattening over a length-scale of $\sim 300\ h^{-1}$ Mpc (Tully 1987; Tully et al. 1992). Furthermore it has been shown recently that a coherent anisotropy, in the distribution of Abell+ACO clusters, exists over a sphere of diameter $\sim 300\ h^{-1}$ Mpc (Plionis & Valdarnini 1991; Scaramella, Vettolani and Zamorani, 1991). The existence of such structures severely challenge galaxy formation theories, in which galaxies grew through gravitational instability from a primordial density fluctuation field $\delta(\vec{x})$, with Fourier components $\delta_{\vec{k}}$ Gaussian distributed with random phases. However, *apparent large-scale structures could arise in any point distribution that is characterized by low-order clustering* and it is therefore extremely important to test the significance of the observed large-scale structures. In fact, Postman et al. (1989) have analysed the Tully sample of Abell clusters and compared the observed large-scale flattening (Tully

1987) with that expected in simulated cluster catalogues, characterized by the same low-order clustering properties as the real data. They conclude that the observed large-scale flattening of the distribution is not unexpected in the simulated catalogues and that it is probably due to a chance superposition of smaller superclusters. If, however, clusters are non–randomly distributed on scales up to $\sim 300\ h^{-1}$ Mpc, as has been recently reaffirmed by Tully et al. (1992), then the observed distribution would put strong constraints on any theoretical model of cosmic structure formation that assumes Gaussian statistics and/or the gravitational instability hypothesis. Further evidence for an excess of power on large scales has been reported recently by Saunders et al. (1991) and Efstathiou et al. (1990) in the IRAS galaxy distributions and by Maddox et al. (1990a), Picard (1991) and Collins et al. (1992) in the large digitalized photometric surveys. Clowes and Campusano (1991) found a large quasar group of size $\sim 100 - 200\ h^{-1}$ Mpc at $z \sim 1$. In light of these results and of their potential importance we have decided to re–analyse the observed clustering in the Abell & ACO cluster catalogues by using a variety of statistical techniques (percolation, statistics of shapes, minimal spanning trees, void probabilities and cluster alignments).

Some of these techniques have been found to be insensitive to different types of point distributions, while other techniques are able to distinguish. For example percolation analysis, as a discriminative technique, has been subject to criticism (Dekel & West 1985, Bhavsar & Barrow 1983), although Klypin et al. (1989) have argued for its use with specific data samples. A more promising technique is the *Minimal Spanning Tree* [MST] (Ore 1962). Barrow, Bhavsar & Sonoda (1985) have used this technique to discriminate the 2-D and 3-D galaxy distribution from randomly distributed samples as well as from numerical simulations. Using the Zwicky and CFA galaxy catalogues and the numerical simulations of Gott, Turner & Aarseth (1979) they found that this technique is able to discriminate between different galaxy distributions even when their two-point correlation functions are identical. They also noted that it picks up prominent filamentary structures. Ling (1987) and Bhavsar & Ling (1988a) have used this technique with success to investigate whether the apparent structures in the CFA catalogue are statistically significant. One, however, should be careful in applying this technique to galaxy samples since it will tend to erroneously identify virialized clusters ('fingers of God') as filaments. Another approach to the study of the large-scale structure has been the investigation of underdense regions (voids), which have been shown to exist in the distribution of galaxies (Kirshner et al. 1981; de Lapparent, Geller & Huchra 1986; Rood 1988) and clusters (cf., Bahcall & Soneira 1982a; Batuski & Burns 1985b; Tully 1986). A quantitative measure of voids is given by the void probability function, $P_\circ(V)$, the probability that a randomly placed volume V is empty. White (1979) has shown that $P_\circ(V)$ depends on the high-order correlation functions and Weinberg, Ostriker and Dekel (1989) have found that the VPFs are significantly different in different cosmogonic scenarios and therefore the VPF could be used to put strong constraints on cosmic structure formation theories. Recently, Jing (1990b) has used the VPF to analyse 2-dimensional Abell cluster samples, while Huchra et al.(1990b), Cappi, Maurogordato, Lachiéze-Rey (1991b) and Postman, Huchra & Geller (1992) have analysed several 3-D samples. Another extremely significant test of large-scale structure, which could place stringent constraints on the theories of cosmic structure formation (cf., Dekel, West & Aarseth 1984; West, Dekel & Oemler 1989), is whether clusters are aligned with their neighbours over scales of tens of Mpcs. This subject is extremely controversial with different groups presenting conflicting results (Binggeli 1982; Rhee & Katgert 1987; Flin 1987; West 1989a,b; Plionis 1992; Struble & Peebles 1985; McMillan, Kowalski & Ulmer 1989; Fong, Stevenson & Shanks 1990).

It has been clear that testing the statistical significance of the detected large-scale clustering, by comparing it with that found in a distribution of points generated with the same selection and correlation properties as those observed, can give very useful information about the primeval spectrum. Therefore, we compare here, using the above techniques, the 3–D Abell/ACO cluster distribution with an ensemble of simulated catalogues where the particle positions satisfy the same selection effects as those of the observed clusters. The simulated catalogues are generated from a Gaussian power spectrum $P(k)$ with random phases such that the particle distribution, obtained by using the Zel'dovich algorithm, has its two–point function ξ_{cc} in the same range and with the same slope as that observed. Our aim is to test whether or not the simulated catalogues, for a given ξ_{cc}, can reproduce the observed large-scale clustering, cluster filamentarity and void probability. We will also present results of cluster alignments within superclusters although we cannot test their reproducibility in the simulated catalogues since our simulations are not dynamically evolved.

10.1 Data Samples

10.1.1 Real cluster samples

a) Sample definition

We apply our analysis to two cluster samples, the Abell $R \geq 0$ sample with measured $z \leq 0.1$ and $|b| \geq 30^\circ$ which is almost a volume limited sample and the ACO $m_{10} \leq 16.4$, $b \leq -20^\circ$ sample. Although, Abell cautioned that the $R = 0$ cluster sample is not complete and therefore not suitable for statistical studies, a growing number of researchers have been using it (*e.g.*, Tully 1986, 1987; Postman et al. 1989; Huchra et al. 1990b). Recently, Postman, Huchra & Geller (1992) performed a comparative study of the density distribution and the clustering properties of the $R = 0$ and $R \geq 1$ cluster samples and found that the two samples have similar density distributions out to $z \approx 0.2$ and similar clustering properties. This then indicates that the incompleteness of the $R = 0$ sample is not severe enough to render it useless. In view of these results and in order to compare our results with those of other studies which have used similar cluster samples, we choose to include the $R = 0$ clusters in our sample. However, we will test the robustness of our results, based on the $R \geq 0$ sample, by applying the same statistical tests (discussed further below) to the $R \geq 1$ sample.

We estimate comoving distances from redshift using the standard relation (6.1) with $H_\circ = 100\ h$ km sec^{-1} Mpc^{-1} and $q_\circ = 0.2$. In the following analysis we will use a Cartesian coordinate system with:

$$x = R \sin l \cos b \qquad y = R \cos l \cos b \qquad z = R \sin b \ . \tag{10.1}$$

The subsample of the Abell catalogue that we use covers totally 4.8 steradians, 3.1 in the northern (NGC) and 1.7 in the southern galactic cap (SGC). The total number of clusters in this subsample with measured redshift ≤ 0.1 (which corresponds to a comoving distance of 284 h^{-1} Mpc for $q_\circ = 0.2$), is 206 in the northern hemisphere and 131 in the southern hemisphere. The redshifts we have used are mainly from Struble & Rood (1987) and Postman, Huchra & Geller (1992) with additions taken from Rhee & Katgert (1988) and Batuski et al. (1991). This sample is similar to that used by Tully (1987) and Postman et al. (1989) although it is more complete due to the availability of more cluster redshifts. The volume covered by this sample is $\sim 3.6 \times 10^7\ h^{-3}$ Mpc^3.

The subsample of the ACO cluster catalogue that we use is defined by $b \leq -20°$, $\delta \leq -17°$ and $m_{10} \leq 16.4$. It covers 2.2 steradians which corresponds to an approximate volume of $\sim 1.6 \times 10^7\ h^{-3}$ Mpc^3. It contains 118 clusters out of which 25 ($\sim$ 21%) have estimated redshifts from the $m_{10} - z$ relation derived in Plionis & Valdarnini (1991). The redshifts we have used are mainly from the original ACO paper but complemented with those listed in Vettolani et al. (1989), Cappi et al. (1991a) and Muriel et al. (1991), for which there is more than one redshift per cluster.

b) Selection functions

In order to compare the real data with simulations it is necessary to know and quantify the selection biases present in the cluster samples and use the same selection effects in our simulations to generate *similar* samples. The main biases we need to quantify are the redshift selection function, Galactic latitude and declination incompleteness effect.

We estimate the redshift selection function in the same way as in Postman et al. (1989), i.e., we define the function $P(z)$ to be the probability that a cluster at z would have been included in the cluster catalogue, which has the form:

$$P(z) = \begin{cases} 1 & \text{for } z \leq z_c; \\ \propto \exp(-z/z_\circ) & \text{for } z > z_c, \end{cases} \tag{10.2}$$

where z_c is the maximum redshift at which the sample exhibits a roughly constant ratio of observed to expected number of clusters (N_{obs}/N_{exp}) from a uniform distribution, and $z_\circ$ is a scaling constant. We choose z_c so that the correlation coefficient of the linear regression fit of $z(> z_c)$ vs $\log(N_{obs}/N_{exp})$ is maximized. Following this prescription we find $z_c \approx 0.081$ and 0.063 (with correlation coefficients 0.9 and 0.83) for the NGC and SGC Abell samples while for the ACO we find $z_c \approx 0.066$ with a correlation coefficient 0.9.

The Galactic latitude selection function has been estimated many times in the literature and it has always been found to be roughly consistent with a cosecant law of the form:

$$P(|b|) = \mathrm{dex}[\alpha(1 - \csc|b|)] \,, \tag{10.3}$$

with $\alpha \approx 0.3$ for the Abell sample (Bahcall & Soneira 1983; Postman et al. 1989) and $\alpha \approx 0.2$ for the ACO sample (Batuski et al. 1989).

Furthermore, no significant declination dependence has been observed in the Abell cluster sample (Postman, Huchra & Geller 1992) which we have also verified for our ACO sample.

c) Cluster space-density and 2-point correlations

In Figure 10.1a and 10.1b we present the Abell NGC and SGC cluster space-density as a function of comoving distance, evaluated in 10 equal-volume shells in the range 50 to 284 h^{-1} Mpc. The Abell cluster density out to the limit of completeness (z_c) is $\sim 1.2 \times 10^{-5}$ h^3 Mpc^{-3} and $\sim 1.7 \times 10^{-5}$ h^3 Mpc^{-3}, corresponding to a characteristic length scale of $\langle\rho\rangle^{-\frac{1}{3}} \approx 44$ h^{-1} Mpc and 39 h^{-1} Mpc, for the NGC and SGC respectively. In Figure 10.1c we present the ACO cluster space-density. Out to the limit of completeness, the ACO cluster space density ($b \leq -30°$) is $\sim 1.8 \times 10^{-5}$ h^3 Mpc^{-3} corresponding to a characteristic length-scale of $\langle\rho\rangle^{-\frac{1}{3}} \approx 38$ h^{-1} Mpc. The ACO density derived here is less by $\sim 30\%$ than that derived in Plionis & Valdarnini (1991) because we do not consider here the small region of the ACO with $b > 0°$, where the dense Shapley concentration lies (Shapley 1930; Scaramella et al. 1989; Raychaudhury 1989).

We estimate the 2-point correlation function for our samples of clusters in the standard way, i.e., using the following estimator:

$$1 + \xi(r) = \frac{N_{cc}}{\langle N_{cr}\rangle} \,, \tag{10.4}$$

where N_{cc} is the number of cluster pairs in the interval $r - \delta r/2 \leq r \leq r + \delta r/2$ and $\langle N_{cr}\rangle$ is the average, over 200 random simulations with the same boundaries, redshift and galactic latitude selection functions, of the cluster-random pairs. We have evaluated $\xi(r)$ in 16 logarithmic intervals in the range [4, 180] h^{-1} Mpc with constant logarithmic amplitude $\Delta \sim 0.1$ and the results are shown in Figure 10.2. We have estimated the

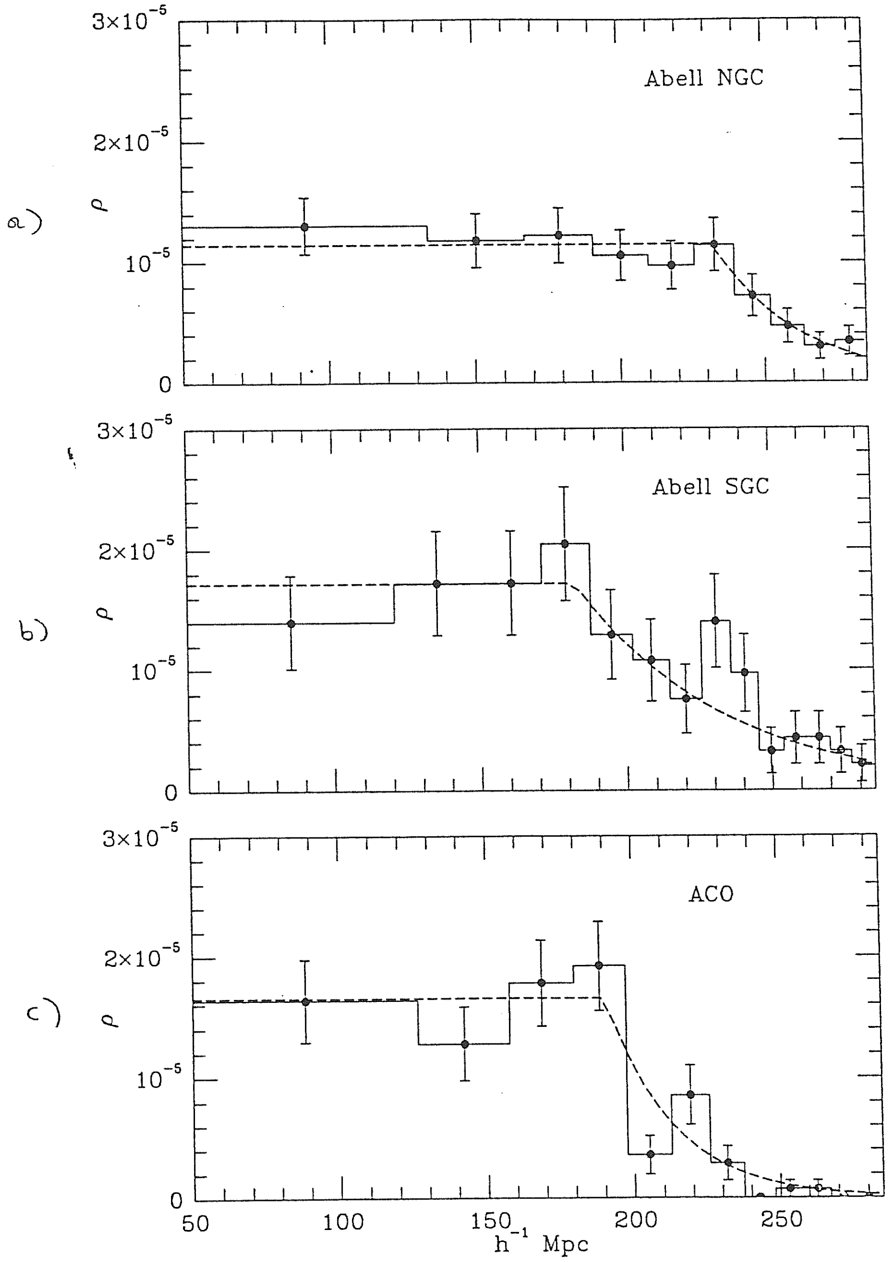

Figure 10.1 — Space density of Abell and ACO cluster samples (solid lines), estimated in equal volume shells. The error bars are Poisson fluctuations and the dashed line represents the best fit from Eq. (10.2). *a)* NGC Abell sample; *b)* SGC Abell sample; *c)* ACO sample.

variance of ξ using the bootstrap technique (Ling, Frenk & Barrow 1986) by generating 100 bootstrap resamplings for each cluster sample. The relevance of the bootstrap technique for estimating clustering errors has been recently stressed by Mo, Jing & Börner (1992) [see Chapter 4], who also showed that the bootstrap error, for the 2-p correlation function, can be analytically approximated by:

$$\sigma_{bo}^2 \approx 3 \times \sigma_{qP}^2 \,, \tag{10.5}$$

where σ_{qP}^2 is the quasi-Poisson variance. We have therefore also estimated, for comparison reasons, the quasi-Poisson errors:

$$\sigma_\xi \approx \left[\frac{1+\xi(r)}{N_{cc}}\right]^{1/2} \,. \tag{10.6}$$

In order to obtain an unbiased determination of the amplitude and slope of the 2-point correlation function we have fitted the derived values of $\xi(r)$ to the usual power-law

$$\xi(r) = \mathcal{B} r^\gamma = \left(\frac{r}{r_\circ}\right)^\gamma \tag{10.7}$$

by using a χ^2 minimization procedure, leaving both the amplitude $\mathcal{B}$ and the slope γ as free parameters to be determined by minimizing the following quantity:

$$\chi^2 = \sum_{i=1}^{16} \left[\frac{\log \xi_i(r) - \gamma \log r - \log \mathcal{B}}{w_i}\right]^2 \,, \tag{10.8}$$

where the weights w_i are defined as the noise to signal ratio, σ_i/ξ_i. To test the sensitivity of the derived γ and $\mathcal{B}$ values to the error estimate, we have used in the minimization procedure three different weights: (i) the bootstrap errors; (ii) the quasi Poisson errors and (iii) equal weights ($w_i = 1$).

The results of the above minimization are shown in Table (10.1). We find that the slope of the derived 2-p function is robust, it does not depend on the error type and it has a value $\sim 1.8 \pm 0.2$ for all samples. However the amplitudes, $\mathcal{B}$, can change quite a bit when using different error estimates. The most relevant estimate, however, of $\mathcal{B}$ is that of the

Table 10.1 — Amplitudes and slopes of the 2–point correlation function using different weighting schemes in Eq.(10.8). The fit in the NGC and SGC Abell sample is in the range 0 - 80 h^{-1} Mpc, while for the ACO sample in 0 - 50 h^{-1} Mpc. In the last two columns we present the amplitude $\mathcal{B}$ when we constrain the slope of the 2–p function to be -1.8 (the penultimate column presents results when we fit Eq.(10.8) only to those values which are larger than the quasi-Poisson error and similarly in the last column when the values are $\geq$ than the bootstrap error).

	$w = 1$	$w \propto \sigma_{qp}$	$w \propto \sigma_{bo}$	$\geq 1\sigma_{qp}$	$\geq 1\sigma_{bo}$
γ_{NGC}	-1.92 ± 0.2	-1.77 ± 0.17	-1.75 ± 0.2	-1.8	-1.8
$\mathcal{B}$	227^{+179}_{-100}	190^{+121}_{-74}	182^{+116}_{-71}	163^{+127}_{-71}	205^{+102}_{-68}
γ_{SGC}	-1.91 ± 0.18	-1.97 ± 0.2	-1.96 ± 0.22	-1.8	-1.8
$\mathcal{B}$	168^{+124}_{-71}	273^{+216}_{-120}	267^{+236}_{-125}	132^{+98}_{-56}	161^{+316}_{-106}
γ_{ACO}	-1.75 ± 0.5	-1.95 ± 0.38	-1.9 ± 0.4	-1.8	-1.8
$\mathcal{B}$	114^{+473}_{-92}	404^{+811}_{-270}	363^{+773}_{-247}	257^{+554}_{-176}	255^{+337}_{-146}

last column where we have constrained the slope γ to be -1.8 while using the bootstrap weighting in Eq.(10.8).

In Figure 10.2a and 10.2b we present the results for the 2-p correlation function of the NGC and SGC Abell samples respectively. Both seem to have a well determined power-law shape with a similar amplitude ($r_\circ \approx 18 \pm 4$ h^{-1} Mpc) although the clustering found in the SGC is of low significance since almost in all bins the bootstrap errors are larger than the actual signal (see also insert of Figure 10.2b). For the NGC Abell sample we find significant correlations out to ~ 50 h^{-1} Mpc while for the ACO sample (Figure 10.2c) we find significant 2-p correlations only out to ~ 30 h^{-1} Mpc but with a correlation length $r_\circ \approx 22 \pm 10$ h^{-1} Mpc. In the inserts of Figure 10.2 we present the noise to signal ratio defined as σ/ξ using both the bootstrap errors (solid line) and the quasi-Poisson errors

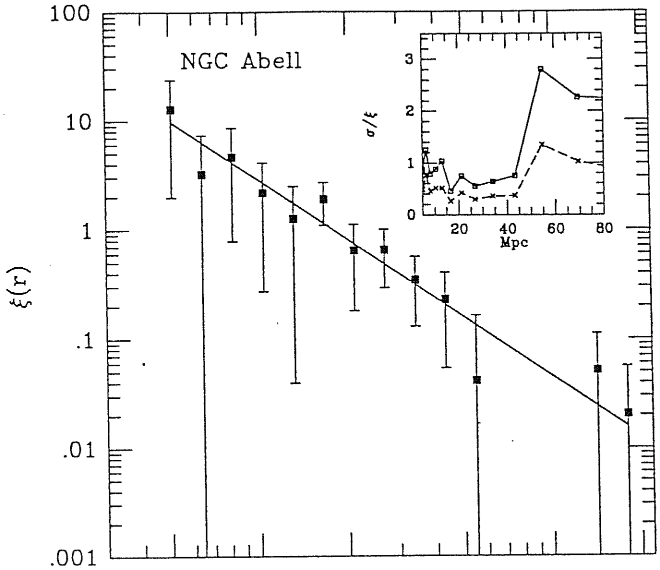
NGC Abell
100
10
1
.1
.01
.001
ξ(r)
σ/ξ
0
1
2
3
20
40
60
80
Mpc

a)

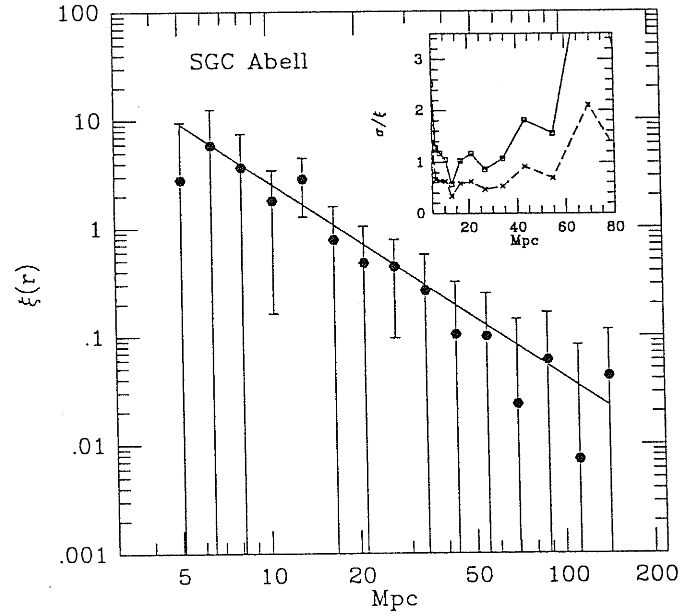
SGC Abell
100
10
1
.1
.01
.001
ξ(r)
5
10
20
50
100
200
Mpc
σ/ξ
0
1
2
3
20
40
60
80
Mpc

b)

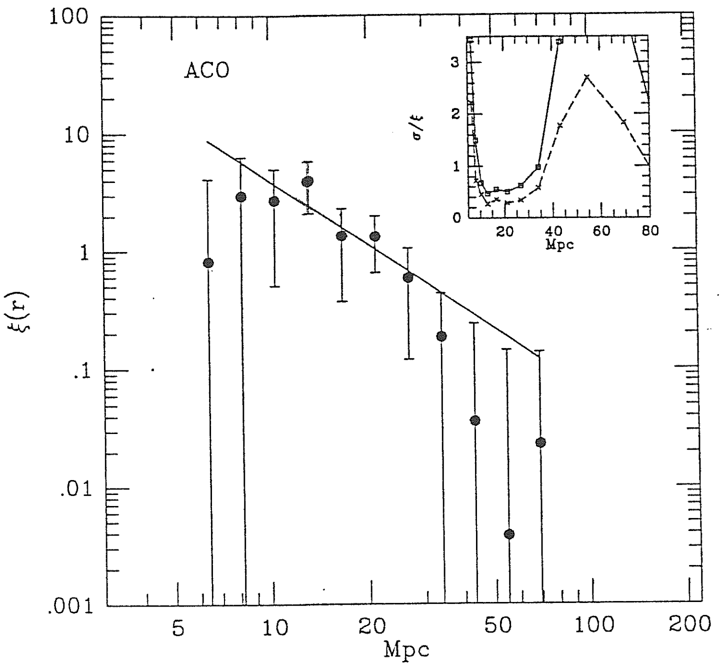

Figure 10.2 — The 2–point cluster-cluster correlation function. Error bars are estimated from 100 bootstrap resamplings. The inserts show the noise to signal ratio, σ/ξ, for the bootstrap case (solid lines) and the quasi-Poisson case (dashed lines). *a)* NGC Abell sample. The fitted line corresponds to $\gamma = -1.8$ and $r_\circ = 18\ h^{-1}$ Mpc; *b)* SGC Abell sample. The fitted line is as in a); *c)* ACO sample. The fitted line corresponds to $\gamma = -1.8$ and $r_\circ = 22\ h^{-1}$ Mpc.

(dashed line). The relative ratio of the two curves is $\sim \sqrt{3}$ as it should from Eq. (10.5) (Mo et al. 1992). Based on our analysis in Chapter 6, we believe that the cluster correlations, determined in this section, are reliable and mostly unaffected by cluster contamination effects (*cf.* Sutherland 1988).

d) Cluster 3-point correlations

Despite the relevance of the 2-point function, it is clear that it does not contain all the information about the statistics of the cluster distribution. For this reason, different authors extended the correlation analysis of the cluster distribution to the 3-point function [see Chapter 7]. Jing & Zhang (1989) and Tóth, Hollósi & Szalay (1989) realized their 3-point analysis for the Abell, ACO and Shectman (1985) cluster samples while Borgani, Jing & Plionis (1992) for poorer clusters extracted from the Lick map (Plionis, Barrow & Frenk 1991). In all the considered cases these authors found that a good fit to the spatial 3-point function is provided by the hierarchical expression (3.1.7) with values of the hierarchical coefficient in the range $0.6 < Q < 1.1$. Recently, Jing & Valdarnini (1991, JV91) analysed a redshift sample of Abell and ACO clusters. Using the bootstrap method to estimate sampling errors they found within the large error bars, the hierarchical model of Eq. (3.1.7) is in agreement with the data.

Since our present samples are more redshift complete than those of JV91, we have recalculated the hierarchical coefficient Q of the connected three–point cluster correlation function ζ. The method is the same as JV91 [see §A.1]. Using a shell with its inner and outer radii 7 and 26 h^{-1}Mpc, we find

$$Q_{NGC} \approx 0.65 \quad Q_{SGC} \approx 0.70 \quad Q_{ACO} \approx 0.30 \tag{10.9}$$

with bootstrap error of ~ 0.2, in quite good agreement with JV91.

10.1.2 Simulated cluster samples

a) Construction of catalogues

We generate our simulated cluster catalogues using a method similar to that of Postman et al. (1989). We identify the position $\vec{x}$ of points corresponding to clusters of galaxies according to the following prescription: N_p points are randomly placed in a cube of size 640 h^{-1} Mpc with $N_g^3 = 64^3$ grid points. The points are then displaced from their original positions $\vec{x}_r$ by

$$\vec{x}_i \;=\; \vec{x}_r + \sum_g W(\vec{x}_r - \vec{x}_g)\vec{D}\phi(\vec{x}_g) \,, \tag{10.10}$$

where $\vec{x}_g$ are the grid points coordinates, $W(\vec{x}_i - \vec{x}_g)$ is a TSC interpolating spline (Hockney and Eastwood 1981) and $\vec{D}\phi(\vec{x}_g)$ is a seven point difference formula, approximating the gradient of ϕ at the grid point $\vec{x}_g$. We use this high order approximation in order to suppress Poisson noise. The field $\phi(x_g)$ is defined onto the cubic grid as

$$\phi(\vec{x}_g) \;=\; \sum_{\vec{k}} \frac{\delta_{\vec{k}}}{k^2}\, e^{i\vec{k}\cdot\vec{x}_g + \phi_{\vec{k}}} \;, \tag{10.11}$$

where $\delta_{\vec{k}} = \sqrt{-2\ln r_1}\, P_k^{1/2}$, while $\phi_{\vec{k}} = 2\pi r_2$ is the random phase. Here r_1 and r_2 are two random numbers uniformly distributed between 0 and 1 and $P(k)$ is the power spectrum of the density fluctuation spectrum which we want to represent. In this way the spectrum $\delta_{\vec{k}}$ has a Gaussian distribution with random phases and $\langle \delta_{\vec{k}}^2 \rangle = P(k)$. In Eq. (10.11) the summation is over the 64^3 waves of the cube in k-space. Eqs. (10.10) and (10.11) correspond to the Zel'dovich approximation. The power spectrum $P(k)$ must be chosen so that the perturbed particle positions give a correlation function in the desired range. In accordance with Postman et al. (1989), we write $P(k)$ as

$$P(k) = A\, k^n\, \exp(-|\vec{k}|^2/\Lambda^2)\, \Theta(|\vec{k}|)\,, \tag{10.12}$$

where $\Lambda^{-1} = 0.1\ h^{-1}$ Mpc, $\Theta(|\vec{k}|) = 0$ for $|\vec{k}| > 1/80\ h^{-1}$ Mpc ($\equiv k_c$) and $\Theta(|\vec{k}|) = 1$ otherwise. The low–wavenumber cut–off k_c is such that all the wavelengths of the simulation cube with $\lambda \leq L/1.3 \approx 500\ h^{-1}$ Mpc contribute to $P(k)$; thus our simulations have more power on large scales than in Postman et al. (1989). As will be seen in §10.2 this is essential in order to draw several conclusions about the reproducibility of the real data cluster distribution in our simulations. In Eq. (10.12) A is a normalization constant and n is the spectral index. The parameters A and n must be chosen such that the two–point correlation function ξ_{cc}^{sim} , in the range $\sim 10 \sim 60\ h^{-1}$ Mpc, corresponds to the observed ξ_{cc}. Using this approach we have generated two sets of cluster catalogues, with $r_\circ = 14$ and $18\ h^{-1}$ Mpc and $\gamma \sim 1.8$. Each set corresponds to a different value of A and n and is an ensemble of 50 simulations, each one with a different random number sequence in Eq. (10.11).

For $r_\circ > 18\ h^{-1}$ Mpc the Zel'dovich approximation cannot be applied and in order to reproduce the observed ξ_{cc} one has to assign points to the peaks of the background field $\delta(\vec{x})$ according to the following prescription: each particle inside the cube is assigned a value ν such that $\delta_{\vec{g}} = \nu\sigma$, where σ is the *rms* density fluctuation within the cube and $\vec{g}$ is the nearest grid point to the particle. Here $\delta_{\vec{g}}$ is the density field smoothed with a Gaussian filter function having a filtering length $r_s = 10 h^{-1}$ Mpc. Using this approach we can reproduce a two-point correlation function with $r_\circ > 18\ h^{-1}$ Mpc and $\gamma = 1.8$, provided we choose only those particles of $\nu > 1.3$. We have, therefore, generated two more sets of simulated cluster catalogues with $r_\circ = 21$ and $r_\circ = 25\ h^{-1}$ Mpc. We shall refer to the simulations with $r_\circ = 14$ and $18\ h^{-1}$ Mpc as the Zel'dovich simulations (Z_{14} and Z_{18} respectively) and to those with $r_\circ = 21\ h^{-1}$ Mpc and $25\ h^{-1}$ Mpc as the peak ones (P_{21} and P_{25} respectively).

We note that the number of points N_p must be chosen so that, after having applied to the simulated samples the survey boundary limits and all the selection functions of the real data [Eq. (10.2) and Eq. (10.3)], we have the same number of clusters as in the real samples. For the Z simulations we choose $N_p = 13000$, while in the P case $N_p = 73000$. The latter results to about $12000 \sim 13000$ points being associated with peaks with $\delta > 1.3\sigma$. This number fluctuates because of the Gaussian distribution. For a Gaussian field with $N_g^3 = 64^3$ points there are about $0.1 N_g^3$ points with $\delta > 1.3\sigma$.

Table 10.2 — Simulation parameters: A is the normalization constant given in Eq. (10.12), n is the spectral index and N_p the particle number. $\langle r_o \rangle$ (in h^{-1} Mpc) and γ are the least square estimates of the two-point function, averaged over 50 simulations, for the *whole* simulation cube.

$A \cdot 10^6$	n	$N_p \cdot 10^4$	$\langle r_o \rangle$	$\langle \gamma \rangle$
3.3	−1.2	13	14.0	1.8
4.8	−1.0	13	18.0	1.9
1.9	−1.5	73	21.2	1.8
1.6	−1.6	73	24.9	1.8

Our final simulated cluster catalogues have the same geometrical boundaries as in the real data while the individual clusters have been selected according firstly to the galactic latitude selection function and secondly applying the real-sample redshift selection function. This procedure was stopped when the number of points was the same as the number of clusters in real catalogues. We have verified that our identification of the grid peaks with the particle subset is a faithful tracer of the peak distribution by comparing the resulting $\xi(r)$ with that obtained when doubling the particle number, N_p (*cf.* Valdarnini

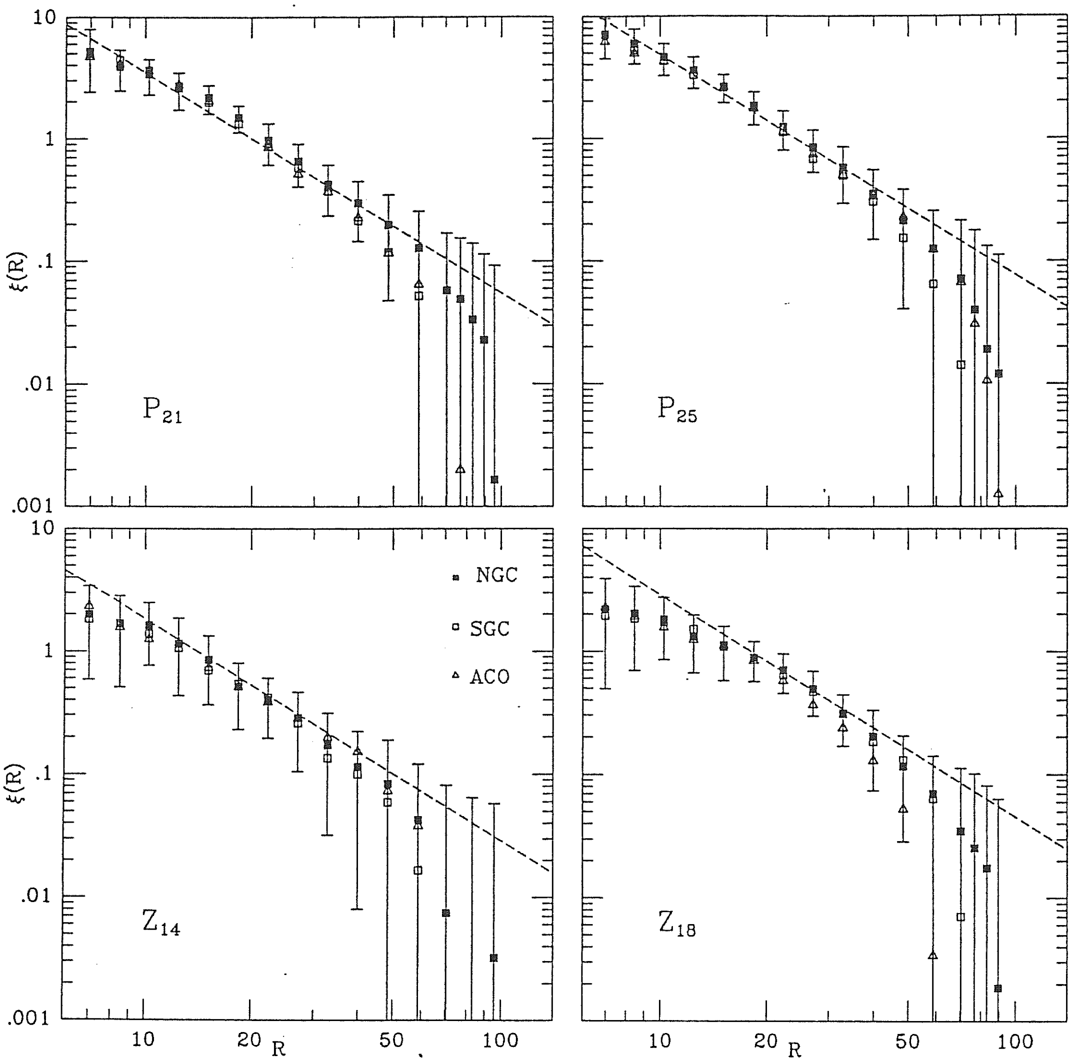

Figure 10.3 — The 2–point correlation function for the simulated cluster samples of the 4 different sets of simulations. Error bars are estimated from the ensemble fluctuations.

and Borgani 1991). The parameters A, n and N_p, together with the value of $r_\circ$ and γ, averaged over 50 simulations, are given for all four sets of simulations in Table (10.2). Note that before introducing the selection functions the cluster number density in the simulations is rather high, i.e. $\langle n \rangle \sim 5 \times 10^{-5}$. This was required in order to obtain the same number of clusters as in the real catalogues, despite the random fluctuations in the spectra and in the selection functions.

b) Simulated cluster 2 and 3-point correlations

In Figure 10.3 we present the average ξ_{cc}^{sim} (over the 50 realizations) for all of our simulated samples. As can be seen, both the slope and amplitude of the two-point function are in good agreement with our requirements. The range of scales over which the 2–point correlation function is determined, especially for the P simulation sets, is between $7 \sim 60$ h^{-1} Mpc. Note also that the two P sets of simulations have by construction non-zero higher order correlations and we have, therefore, estimated the hierarchical coefficient Q selecting from the whole cube (before applying any selection function) ~ 1600 simulated clusters (so that $\langle n \rangle$ is similar to that of the Abell catalogue) using the direct triplets-counting method. The method is the same as that in §4.3.3, except the bootstrap error of DDD is determined by the explicit formula of Mo et al. (1992). We find that the hierarchical expression of Eq. (3.1.7) is fulfilled with

$$Q_{21} \approx 0.58 \pm 0.16 \qquad Q_{25} \approx 0.65 \pm 0.09 \ , \tag{10.13}$$

where the uncertainty is the ensemble one.

In order to facilitate a comparison with the value of Q obtained from the real cluster samples (§10.1.1d) and to test the reliability of the moments method to determine the 3–point function from a small sized sample, we have applied this method to our simulated cluster catalogues using the same bin size as in the data. The results are shown in Table (10.3) and are in good agreement with those of the whole cube.

Table 10.3 — The hierarchical coefficient Q of the 3–p correlation function estimated for the real and simulated cluster catalogues.

	method	NGC Abell	SGC Abell	ACO
real samples	moments	0.65	0.3	0.7
P_{21}	moments	0.47±0.21	0.71±0.24	0.63±0.21
P_{25}	moments	0.6±0.15	0.65±0.22	0.54±0.21

10.1.3 Conclusions

We conclude that the northern and southern Abell samples have similar correlation functions with correlation length $r_\circ \approx 18 \pm 4$ h^{-1} Mpc, while the ACO sample has stronger correlations $r_\circ \approx 22 \pm 10$ h^{-1} Mpc, but with a much larger scatter. The northern Abell samples show significant correlations up to $\sim 40 - 50$ h^{-1} Mpc, while the southern Abell and ACO samples only up to ~ 30 h^{-1} Mpc. The hierarchical coefficient Q of the 3–p function is consistent, within errors, in all three cluster samples with an average value ~ 0.6. Similarly our simulated cluster catalogues all have well defined 2–point correlation functions with the same slope as that observed while the P sets of simulations have also non-zero higher order clustering and in particular their 3–point correlation function is in good agreement with that of the real cluster samples ($Q_{sim} \approx 0.6$).

Thus, *the simulated cluster catalogues are defined in the same region of the sky and reproduce not only the selection functions but also the low-order (2- and 3-point) correlation properties of the real cluster samples.*

10.2 Large-Scale Cluster-Clustering Analysis

A question that is posed often in the literature is whether the observed large-scale structures (superclusters, walls, filaments and voids) are real. This question, however, is ill-defined. What do we mean by a 'real' large-scale structure ? In any distribution of points with a low-order clustering, characterized by a 2–p function, one should expect to find some sort of large-scale structure, according to the algorithm used, independently of whether these structures are the product of dynamical interactions of their constituent members or whether they were just born correlated.

A more precise question, which we will attempt to answer, is whether there is any significant evidence to argue that the observed large-scale structure is unexpected within the context of a Gaussian background fluctuation spectrum with random phases, determined by the observed cluster 2–point correlation function (which fully specifies its clustering characteristics). We will address this question by testing, using a variety of objective analysis techniques, whether the general morphology/properties of large-scale structures found in the real cluster distribution can be reproduced in their simulated counterparts, which would then imply that the simulation construction assumptions are, at least, not in contradiction with the real world and vice-versa; if there are significant differences between the simulated and the real cluster distributions then this would imply that the construction assumptions are invalid, as far as the real world is concerned.

10.2.1 Minimal-Spanning Tree Technique

First we construct the Minimal-Spanning Trees (MST) in our observed and simulated samples. A detailed description of the MST and of its construction method is given §3.4. In Figure 10.4a and 10.4b we present the three-dimensional distribution of the Abell (NGC and SGC together) and ACO clusters, respectively, together with their MST construction (branches with more than two nodes). We are located at the center of the cube with the North Galactic pole pointing upwards and the South Galactic Pole pointing downwards. The side of the cube is 500 h^{-1} Mpc long.

In order for our structures to be 'physical' associations of clusters we use cut-off lengths such that the distance between any two clusters along the *separated* MST is not larger than the characteristic length scale ($\langle\rho\rangle^{-\frac{1}{3}}$) of the sample. The range of cut-off lengths we will use is $0.4\langle\rho\rangle^{-\frac{1}{3}} \leq l_c \leq 0.9\langle\rho\rangle^{-\frac{1}{3}}$ and in units of the mean edge-length along the MST $0.6\langle l\rangle \leq l_c \leq 1.5\langle l\rangle$. The average edge-length along the MST construction, for our real and simulated cluster samples, can be found in Table (10.4). The simulation set that best reproduces the observed $\langle l\rangle_r$, for all three cluster samples, is the P_{21} set.

Table 10.4 — Mean MST edge-length, $\langle l\rangle$, for the real and simulated cluster catalogues (in h^{-1} Mpc).

Samples	Real	Z_{14}	Z_{18}	P_{21}	P_{25}
Abell NGC	25.8	27.8±4	27 ±4	25±3.7	24±3.5
Abell SGC	24.7	26.7±4	26 ±4	24±3.7	23.2±3.5
ACO	24	26.1±4	26 ±3.8	23.4±3.6	22.2±3.4

a) $F(l)$ distribution

The frequency distribution of edges of length l along the MST, $F(l)$, was used by Barrow et al. (1985) to discriminate, with success, between cosmogonic models that have

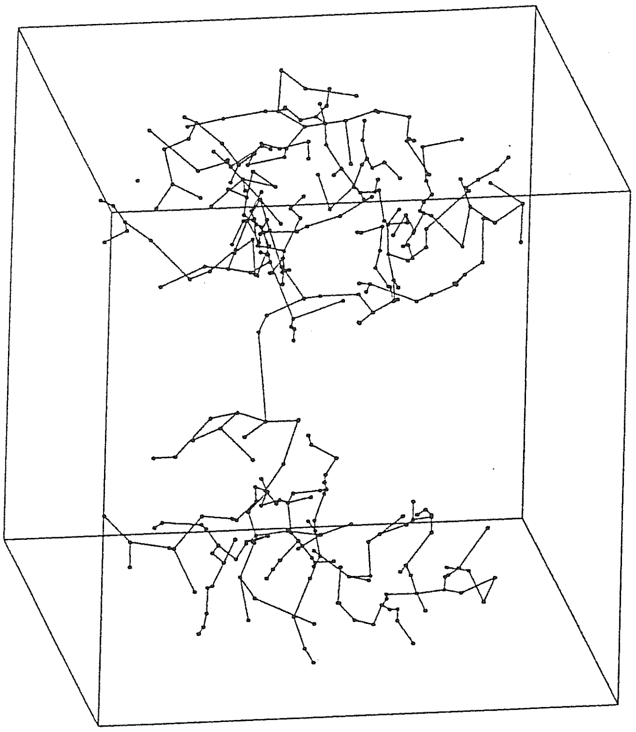

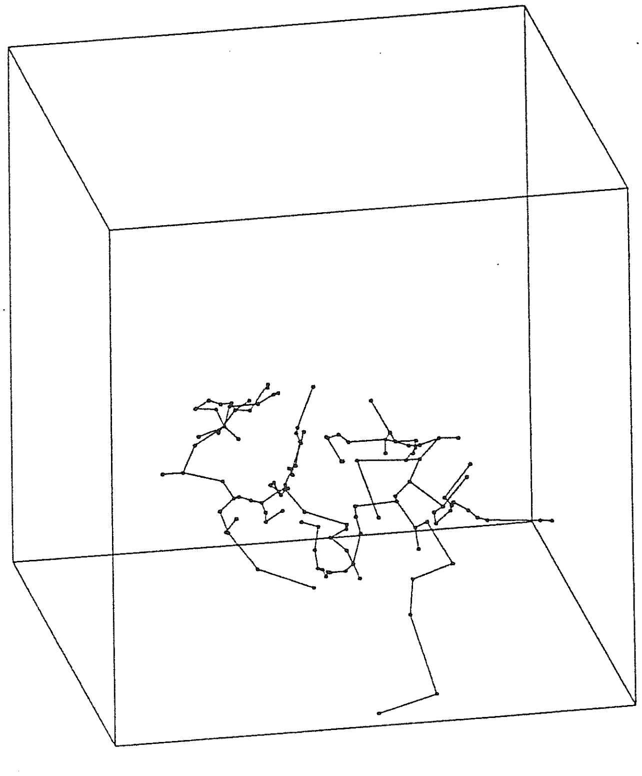

Figure 10.4 — The 3-dimensional distribution of Abell and ACO clusters together with their MST construction in Cartesian coordinates. The box size is $500^3\ h^{-3}$ Mpc^3. We are located at the center of the cube and the north galactic pole points upwards from cube centre. *a)* NGC and SGC Abell samples; *b)* ACO sample.

the same 2-point correlation function. This statistic gives a measure of the pairwise correlations within the MST construction. Plionis & Frenk (unpublished work) have found that, when a large number of points is available, this statistic is extremely sensitive to models with different exponent n of the power spectrum.

We have compared the $F(l)$ distributions of the real, the simulated and random samples (generated using the data selection functions). We have normalized the simulated MST edge-lengths to the mean of the real cluster samples, $\langle l\rangle_r$. In Figure 10.5 we present a comparison of the mean $F(l/\langle l\rangle_r)$, over all simulations (thin lines), with that of the real data (thick lines). We present the $F(l/\langle l\rangle_r)$ only for the three sets of simulations with $r_\circ \geq 18\ h^{-1}$ Mpc [since the Z_{14} $F(l/\langle l\rangle_r)$ is quite similar to that of the Z_{18}]. The NGC Abell sample shows a clear excess of small $l/\langle l\rangle_r$ in comparison with all simulations. We have also compared the observed $F(l/\langle l\rangle_r)$, to that expected from a Poisson distribution of points having the same selection functions as the real data. To quantify this comparisons we have performed a χ^2-test [Table (10.5)] which indicates that the random distribution cannot reproduce, as expected, the cluster $F(l/\langle l_r\rangle)$. The Z_{14} and Z_{18} sets of simulations perform similarly poorly for the NGC sample while for the ACO only the Z_{14} is unacceptable. The SGC sample $F(l/\langle l\rangle_r)$ could be reproduced by any set of simulations which is in agreement with the fact that its 2–point correlation function is quite noisy and of low significance.

However, the simulation that performs *best* in reproducing the observed $F(l/\langle l\rangle_r)$ (in the sense of maximizing the value of P_{χ^2}), for all three samples, is the P_{21}.

Table 10.5 — χ^2 probabilities (P_{χ^2}) that the real sample $F(l/\langle l_r\rangle)$ distribution could have been drawn from the corresponding simulated parent distribution.

Sample	Random	Z_{14}	Z_{18}	P_{21}	P_{25}
Abell NGC	0	6.9×10^{-4}	2.7×10^{-3}	0.68	0.46
Abell SGC	2×10^{-5}	0.89	0.85	0.97	0.86
ACO	0	9.8×10^{-2}	0.48	0.96	0.89

b) Filaments: branch linearity statistics

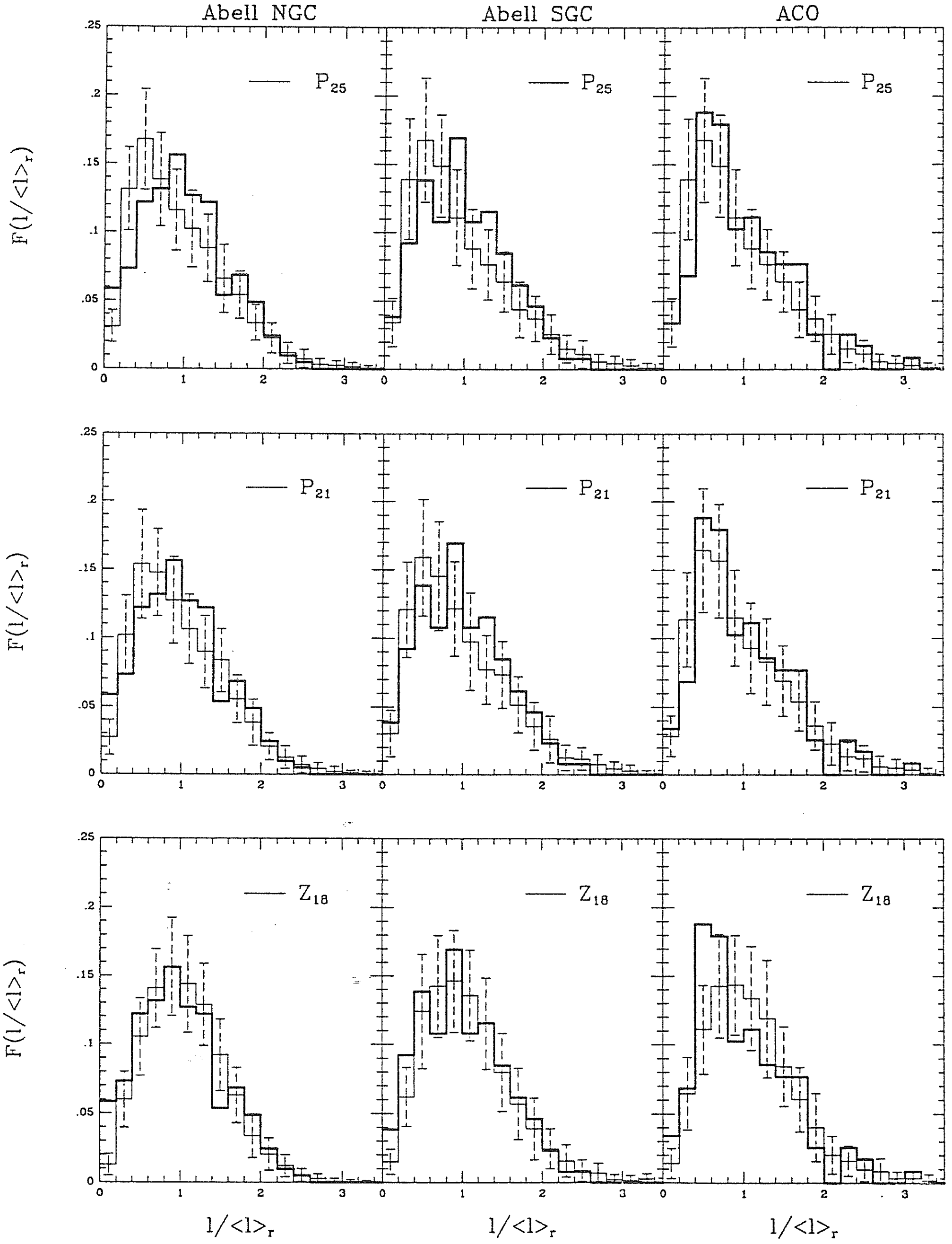

Figure 10.5 — Comparison of the $F(l/\langle l_r \rangle)$ distribution (frequency distribution of edge-lengths, normalized to the mean edge length of the real cluster MST) of our three cluster samples with the average simulation distribution (for the Z_{18}, P_{21} and P_{25} simulation sets). Error bars are estimated from the ensemble fluctuations. The simulation that best reproduces the real cluster distribution is the P_{21}, which is also confirmed from the χ^2 test [see Table (10.5)].

Once we have developed the MST for our data and simulations we *separate* the tree so that all edge-lengths with $l \geq l_c$ (where the simulation cutoff length, l_c, is in units of the mean of the real samples edge-length, $\langle l \rangle$) are removed. What remains of each MST is a set of branches that contain a variable number of clusters (we keep only those with $N \geq 3$). We now define R_L to be the ratio of the start-to-end branch-length to the total length along the branch and we will use this parameter as a descriptor of the linearity of each *individual* branch. If $R_L \approx 1$, the branch is a linear structure (filament) while if $R_L \ll 1$ the branch is an extremely curved structure (note that $R_L > 0$ from the definition of the MST). The significance of each real-cluster branch R_L measure will be assessed by comparing with the expected R_L distribution from the simulated catalogues (which, we repeat, have both the 2- and 3-point correlation functions similar to the real samples).

In Figure 10.6 we present the R_L values of the observed branches (open circles) together with the 90% (long-dashed lines) and 99% (short-dashed lines) R_L confidence level, evaluated from the R_L distribution of simulated branches, as a function of the total branch length (in h^{-1} Mpc). Although we have used the P_{21} set of simulations, note that using the P_{25} or Z_{18} sets results in qualitatively identical confidence limits. We present results for four different cutoff edge-lengths ($l_c = 0.6$, 0.8, 1.0 and 1.2 $\langle l \rangle_r$). We find that there are preferentially more linear ($R_L \sim 0.8$) real cluster branches (in all three samples), especially for $l_c \leq \langle l \rangle$ and branch-lengths ≤ 40 h^{-1} Mpc, with respect to the simulations. Furthermore, most of them lie beyond the 90% confidence limits while in some cases they lie even beyond the 99% level ($\sim 3\sigma$). For cutoff-lengths $l_c = 1.2\langle l \rangle$ we find, in the NGC Abell sample, significantly linear branches with lengths even up to ~ 150 h^{-1} Mpc. In the ACO sample and for $l_c \geq 0.8\langle l \rangle$ we find an extremely curved structure consisting of A3095, A3094, A3151, A3154 and A419. Such curved structures are also apparent in the SGC Abell sample (but not as significant).

We conclude that in our cluster samples there is significantly richer large-scale structure (filamentariness and compactness) with respect to what is found in our simulated samples which have the same 2 and 3-point correlation functions. This result holds even when comparing with the P_{25} set of simulations, which has significantly stronger clustering than is found in the real samples. This implies that our results are not due to a lack of

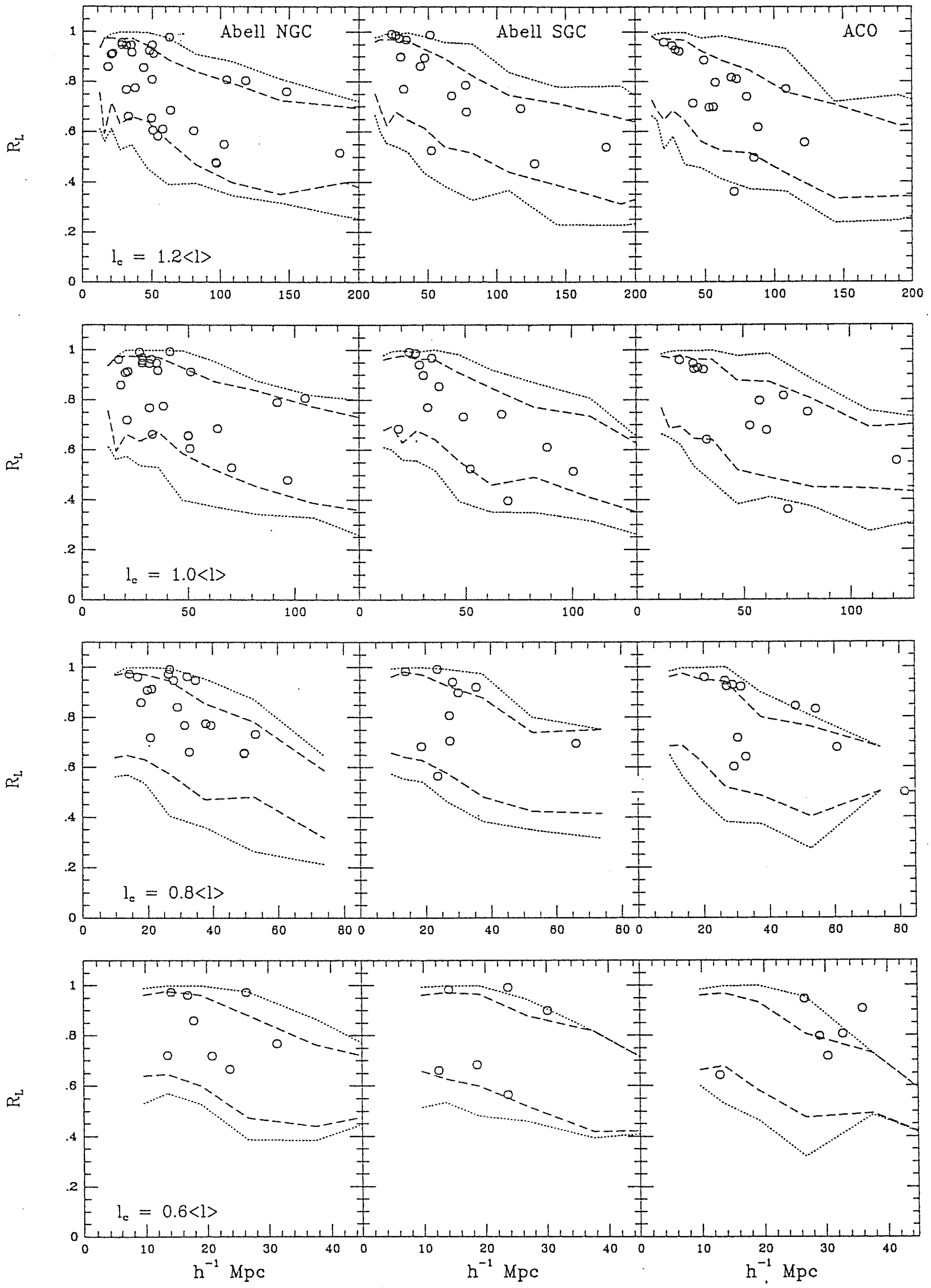

Figure 10.6 — MST branch linearities, R_L, as a function of total branch length for four different cutoff lengths, l_c. The real data values are plotted as open circles while the long-dashed and short-dashed lines correspond to the 90% and 99% confidence limits, estimated from the P_{21} simulations set. In most cases the 99% limit coincides with the outer extremes (minimum and maximum values) of the simulated branch R_L's.

clustering but could indicate that the underlying statistic used to construct the simulated cluster catalogues is different from that of the real cluster distribution.

c) Branch-length frequency distribution

We produce the frequency distribution of the branch-lengths (defined as before) and we compare them with the simulation distributions. For the case of small cutoff lengths ($l_c \leq 0.8$) we use 10 logarithmic bins in the 8–240 h^{-1} Mpc range (logarithmic bin-size of $\Delta \sim 0.15$) while for $l_c \geq 1$ we use 12 bins in the range 10–500 h^{-1} Mpc ($\Delta \sim 0.12$).

In Figure 10.7 we compare the branch-length distributions of the real samples (solid lines) and of the P_{21} set of simulations (short dashed lines). It is evident that for $l_c \leq 0.8$ there is an excess, with respect to the simulations, of relatively long branches. For larger l_c's the real and simulated sample distributions are quite alike. Qualitatively similar results are obtained when comparing with the other simulation sets. We quantify this comparison by using a χ^2-test [see Table (10.6)] which shows that there is a significant difference between real and simulated branch-length distributions only for $l_c \leq 0.8$ and mostly in the ACO sample.

Table 10.6 — χ^2 probabilities (P_{χ^2}) that the real sample branch-length frequency distributions could have been drawn from the corresponding simulated parent distributions.

	NGC			SGC			ACO		
$l_c/\langle l \rangle$	P_{25}	P_{21}	Z_{18}	P_{25}	P_{21}	Z_{18}	P_{25}	P_{21}	Z_{18}
0.6	0.003	0.18	0.076	0.41	0.42	0.15	2.7×10^{-3}	4.5×10^{-4}	6×10^{-14}
0.8	0.017	0.031	5.6×10^{-4}	0.07	0.073	0.023	1.2×10^{-3}	1.4×10^{-5}	10^{-6}
1.0	0.96	0.89	0.013	0.99	0.99	0.94	0.78	0.64	0.79
1.2	0.92	0.75	0.047	0.86	0.93	0.67	0.73	0.66	0.75

d) Alignments of clusters along the MST

Further evidence about the reality of the structures picked-up by the MST could come from studying the alignment of clusters along it. We have used new position angles, θ_i, of Abell clusters, determined from the Lick map by using a cluster finding algorithm

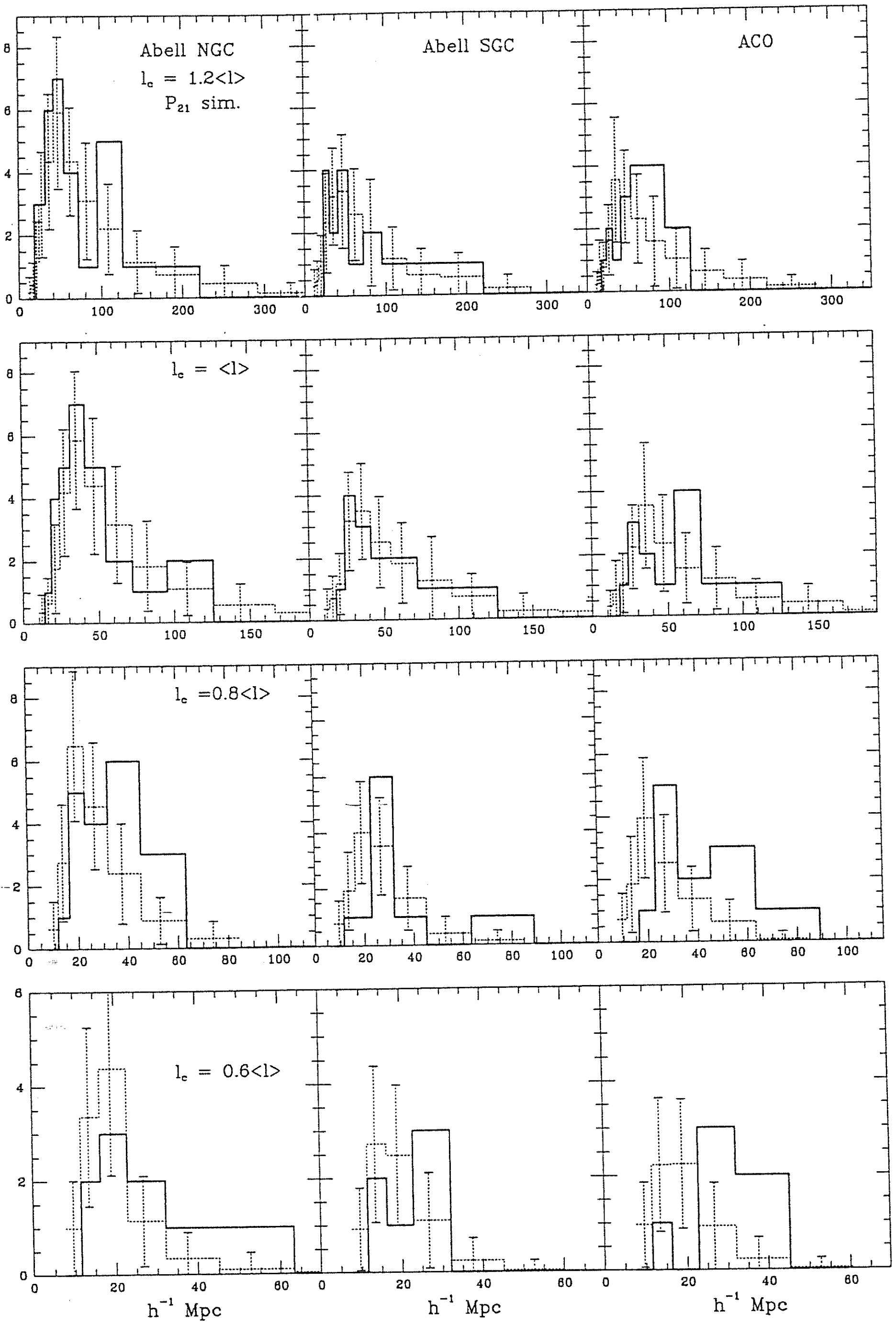

Figure 10.7 — The MST branch length frequency distribution for four different cutoff lengths, l_c. The solid lines correspond to the real cluster data while the dotted ones to the P_{21} simulation average (error bars are ensemble 1σ fluctuations). There is a clear excess of relatively long branches for $l_c \leq 0.8\langle l\rangle$ (especially for the ACO and northern Abell samples), while no such excess is observed for large values of l_c [see Table (10.6)].

based on selecting density peaks above some density threshold (for details see Plionis et al. 1991). Statistics on the position angles will be presented elsewhere (Plionis 1992) but we note here that their distribution is highly isotropic with no evidence of preferred orientation on the sky (their Fourier transform [see Eqs.(4) & (5) of Plionis et al. 1991] gives $C_1 = 0$, $S_1 = -0.3$, $C_2 = -0.8$ and $S_2 = 0.8$). Out of a total of 337 Abell clusters (NGC+SGC) we have 185 θ's ($\sim$ 55%) from the Lick map. We have complemented this sample with 32 more from West (1989b), which bring our total number of θ's to 221 ($\sim$ 66%). Armed with these position angles we search for an alignment effect (only in the two Abell samples since for the ACO we do not have available position angles) by comparing the orientation of a given cluster with the direction to its MST neighbour (note that this is not necessarily its nearest neighbour). The procedure is based on determining the acute angle, ϕ, between the cluster position angle and the great circle connecting the cluster centre to its MST neighbour. Note also that for this study we transform all our coordinates to the equatorial system (in which the position angles are defined). We have determined the quantity (Struble & Peebles 1985):

$$\delta = \sum_{i=1}^{N} \frac{\phi_i}{N} - 45 \ , \tag{10.14}$$

where N is the total number ϕ values. If these are isotropically distributed between 0° and 90° then for large N we should obtain $\delta = 0$ while a significantly negative value will indicate alignment and a positive one a anti-alignment. The significance level can be estimated from:

$$\sigma = \frac{90}{\sqrt{12N}} \ . \tag{10.15}$$

We have found that there is no significant alignment effect along the MST of the NGC sample ($\delta \approx -0.7$ and $\sigma \approx 2.2$) while, on the contrary, there is a significant alignment effect in the SGC sample ($\delta \approx -8.7$ and $\sigma \approx 2.9$). Note, however, that we have available position angles only for a subset of our samples. The alignment signal, found in the SGC sample, could be a reflection of the well known Binggeli effect (Binggeli 1982), in which clusters tend to point towards their nearest-neighbour (see also Rhee & Katgert 1987; Flin 1987). In order to see whether this is the case we have also performed a strictly nearest-neighbour alignment analysis and we found significantly less alignment in the SGC ($\delta \approx -5.2$ and $\sigma \approx 2.9$), while for the NGC again no alignment was found. Therefore there is some indication of some physical relation between the distribution of clusters along their uniquely determined MST construction.

However, the alignment effect could be artificial, due to the fact that the clusters which are near in 3-dimensions are, in many cases also near in angular space and therefore their density envelopes could be overlapping in 2D which could produce a directional bias in the determination of their position angle and thus a preferred orientation along the direction of their neighbours. We have tested whether this is the case by searching for an alignment effect of nearest-neighbours found in angular space. If there is no systematic bias in the determination of the position angles we expect to find a weaker alignment signal, since only a subset of clusters which are near in 3-dimensions are also near in angular space. We find that the alignment signal ($\delta \approx -3.6$ and $\sigma \approx 2.9$ for the SGC sample) is significantly weaker than in the 3-dimensional case, which implies that our position angles do not suffer from the above mentioned bias.

e) Conclusions

We have found that we can best reproduce the cluster $F(l/\langle l_r \rangle)$ distribution by the P_{21} simulation set, although the P_{25} is also acceptable. However, 'shape'-statistics, like the R_L or the branch-length frequency distribution reveal that the real cluster samples (especially the ACO one) have a higher 'filamentariness' and 'compactness' ($\sim 3\sigma$ events) as well as a higher frequency of long-branches (at small cutoff lengths) with respect to simulated cluster distributions that have the same low order (2- and 3-point) clustering characteristics. Furthermore, we have found, only for the SGC sample, significant alignments of clusters along the MST. Our results remain qualitatively the same when we restrict our sample only to $R \geq 1$ clusters, although at a somewhat less significance level (due to the significantly smaller number of available clusters).

10.2.2 Percolation analysis

In order to study further the possible significance of the large-scale structure in the Abell and ACO cluster samples we have used the friends-of-friends algorithm to find candidate superclusters and test their significance. Note that the superclusters, in this analysis, and the branches, of the MST analysis, are different structures; in most cases the MST branches are contained within individual superclusters. However, in order to keep a consistent definition of scale we will use the 'friendship' radius, R_p, in units of the mean MST edge-length, $\langle l \rangle_r$.

As discussed in the introduction, in any set of points that is characterized by a 2-p correlation function, one should expect to find associations of points (superclusters in our case) even of large dimensions. The existence, however, of such 'superclusters' does not necessarily imply that there is any excess power on large scales, *more than what is needed to produce the observed cluster-cluster correlation function*; such associations could be just a product of small-scale clustering coupled with random positional alignments. In this framework, in order to test the significance of the observed large-scale structure found by this technique, we have used three statistics to compare data and simulations, and we have also performed a cluster alignment analysis.

a) Fraction of clusters in superclusters

This test was performed by Postman et al. (1989) and Postman, Huchra & Geller (1992) for a similar Abell sample and found that the simulations with quite strong 2-point correlation functions ($r_\circ \sim 20 - 24\ h^{-1}$ Mpc) can reproduce the observed fraction of clusters in superclusters (which they defined as groups with ≥ 5 members).

We have repeated this analysis for our samples and in Figure 10.8 we plot the % of clusters in superclusters as a function of the radius of 'friendship' association, in units of the average MST edge-length for each real sample $\langle l \rangle_r$ (continuous line). In our case we define superclusters as groups with ≥ 2 members. The results of the simulations are plotted as individual points of varying shape for the different simulations (see figure caption). It is evident that the behaviour of this statistic for the real data does not show any great departures from the general trend found in the simulations. It is, however, consistent within $\sim 1\sigma$ only with the P_{21} set of simulations, which is in agreement with the $\xi(r)$ (§10.1.1c) and $F(l/\langle l \rangle_r)$ (§10.2.1a) analysis.

b) Multiplicity function

The superclusters have been binned in seven logarithmic multiplicity bins according

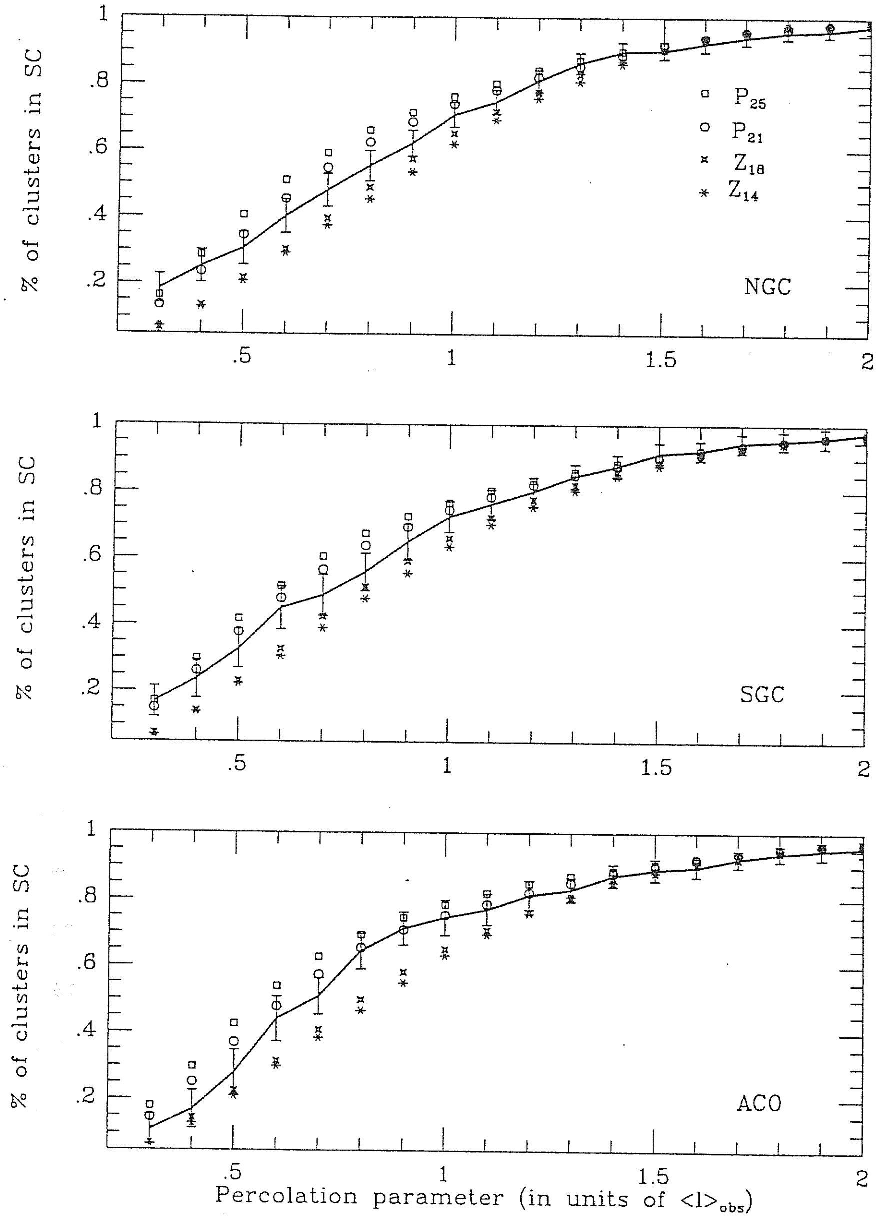

Figure 10.8 — Fraction of clusters in superclusters as a function of 'friendship' radius, R_p, which is parameterized by the mean edge length of the real cluster samples, $\langle l \rangle_r$. The continuous line represents the real cluster fraction while the corresponding values for the four simulation sets are represented by the different symbols (as indicated in the figure). The error bars, centered on the real data lines, are the P_{21} ensemble 1σ fluctuations.

to the number of member clusters that they contain. We have chosen a logarithmic binning to reduce discreteness effects and thus to accommodate the application of statistical tests (χ^2-test). We have analysed the multiplicity function (MF) at various percolation radii (ie, $R_p = 0.6$, 1 and 1.5 $\langle l \rangle_r$) and for a variety of binning parameters.

We find that for all different R_p's the NGC and SGC Abell samples show no significant difference between (all) simulation and real data MF ($P_{\chi^2} \geq 0.15$). Similar results are obtained for the ACO's sample for $R_p/\langle l \rangle_r = 0.6$ and 1. However, for $R_p/\langle l \rangle_r = 1.5$ there is a statistically significant difference when comparing the MF with that of any simulation. For the relevant case of P_{21} the probability that the ACO MF could have been drawn from a P_{21} parent MF is $P_{\chi^2} = 6 \times 10^{-3}$. Such a significance level is stable to the different binning parameters. In Figure 10.9 we compare the MF's of all our samples, at $R_p/\langle l \rangle_r = 1.5$ (solid lines), with that of the P_{21} set of simulations (dashed lines). The 'peculiarity' of the ACO MF is apparent.

We conclude that structures in the Abell samples, containing as many as 64 clusters, using a percolation radius of 1.5 $\langle l \rangle$ (Perseus-Cetus supercluster + Perseus-Pegasus chain + Pegasus-Pisces chain in Tully [1987]), appear at least once in each simulation. This result is in agreement with those of Postman et al. (1989) and Postman, Huchra & Geller (1992). However, for the ACO sample there is evidence for superclustering (as measured by the MF) in excess of what expected just from the small-scale cluster clustering in the simulations.

c) Supercluster flattening

It is usually assumed that the observed flattening of superclusters, found by friends-of-friends algorithms (using a variety of percolation radii R_p), is an indication of the physical reality of the superclusters (*cf.* West 1989b). However, this conclusion is usually based on comparing the observed flattening with that expected from a distribution of random points, which in our view can only help to understand the biases that enter in the determination of the supercluster flattening (due to small number of clusters per supercluster, for example) but it cannot directly address the question of the reality of a supercluster. The reason is, as we will see below, that in a clustered distribution, characterized by a 2-point correlation function similar to that of the real cluster distribution, the shape of 'superclusters' (found,

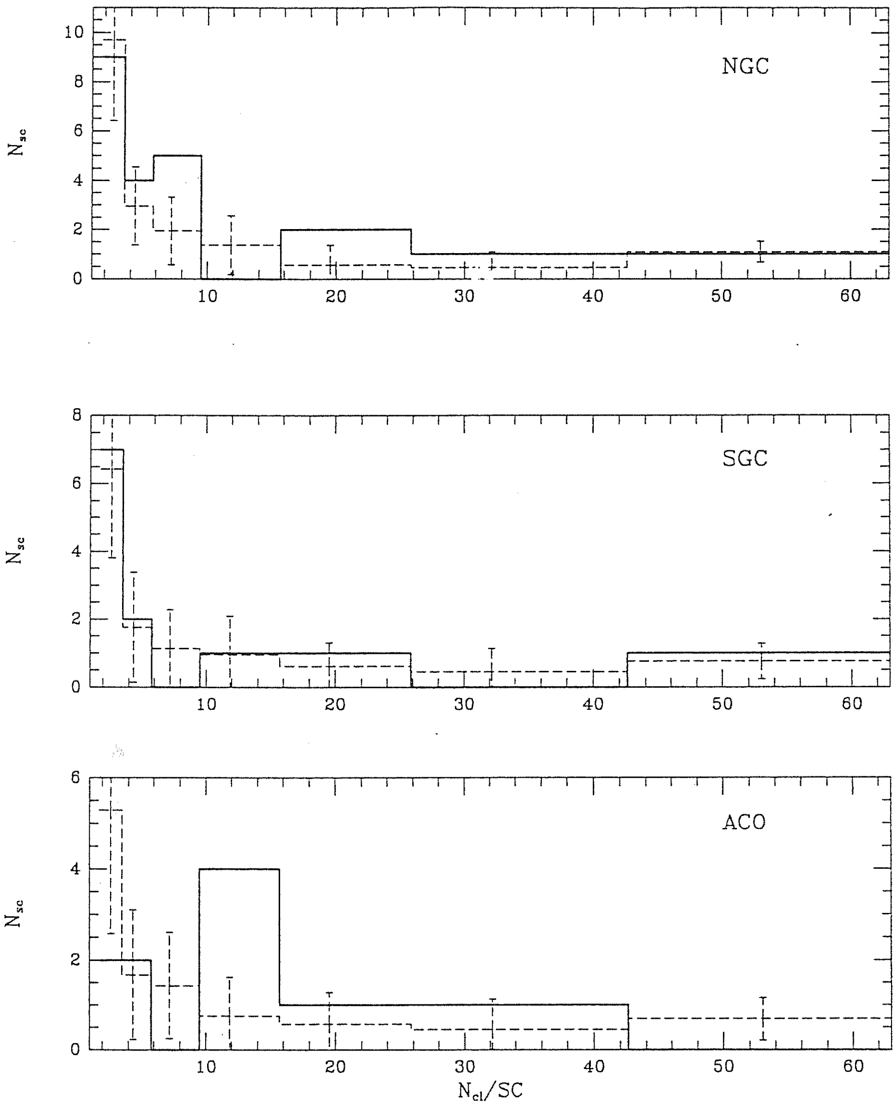

Figure 10.9 — Multiplicity function of superclusters in logarithmic binning. Solid lines represent the real cluster data while dashed lines the P_{21} simulation multiplicity functions. The error bars are the ensemble 1σ fluctuations. A significant disagreement between the simulation and the real data is apparent only in the ACO sample.

for example, by the f-of-f algorithm) is in any case non-spherical.

Furthermore when large radii R_p are used to define 'superclusters', the limited volume and the geometrical boundaries of the sample can bias the shape of the largest 'superclusters'. Therefore, in order to assess the significance of the observed superclusters, it is essential to compare the real data with simulations having the same correlation properties, survey boundaries as well as selection functions.

To illustrate this we have diagonalised the inertia tensor, **I**, for all simulation 'superclusters', found at two 'friendship' radii (i.e., $R_p = \langle l \rangle_r$ and $1.5\langle l \rangle_r$) and having at least 9 cluster-members (in order to have a relatively large number of clusters per supercluster but also a reasonable number of superclusters). The inertia tensor is defined as:

$$I_{kl} = \sum_{i=1}^{N} (x_k x_l)_i w_i \tag{10.16}$$

where $k, l = 1, 2, 3$, x_{1_i}, x_{2_i} and x_{3_i} are the Cartesian coordinates of the i^{th} cluster with respect to the centre of mass of the 'supercluster' and w_i is the weight with which each individual cluster enters the summation. Various weighting schemes can be used:

(i) $w_i = 1$, an equal weight for each contributing cluster.

(ii) $w_i = r_i^{-2}$, the inverse square distance of each cluster from the supercluster centre of mass (in order to reduce the weight of the outlining clusters; *cf.* West 1989a,b);

(iii) $w_i = N_g$, the number of galaxies in each cluster (listed in the cluster catalogue).

It is therefore clear that a unique shape of a supercluster cannot be defined. The eigenvalues of the principal axes of the inertia tensor, $a_1^2 > a_2^2 > a_3^2$, define three quantities: $\lambda_1 = 1/a_3^2$, $\lambda_2 = 1/a_2^2$ and $\lambda_3 = 1/a_1^2$ and following Bardeen et al. (1986) we define for each 'supercluster' two shape parameters:

$$e = \frac{\lambda_1 - \lambda_3}{2(\lambda_1 + \lambda_2 + \lambda_3)} \tag{10.17}$$

$$p = \frac{\lambda_1 - 2\lambda_2 + \lambda_3}{2(\lambda_1 + \lambda_2 + \lambda_3)} \ , \tag{10.18}$$

where e measures the ellipticity in the $\lambda_1 - \lambda_3$ plane and p measures the prolateness or oblateness of the fitted ellipsoid. If $0 \geq p \geq -e$ then the ellipsoid is more prolate while if $e \geq p \geq 0$ it is more oblate with limiting cases $p = -e$ (prolate spheroid) and $p = e$ (oblate spheroid).

In Figure 10.10 we present the simulation supercluster flattening distribution (for the P_{21} set), for the joint simulated ACO, NGC and SGC samples, using $R_p = 1.5\langle l \rangle_r$

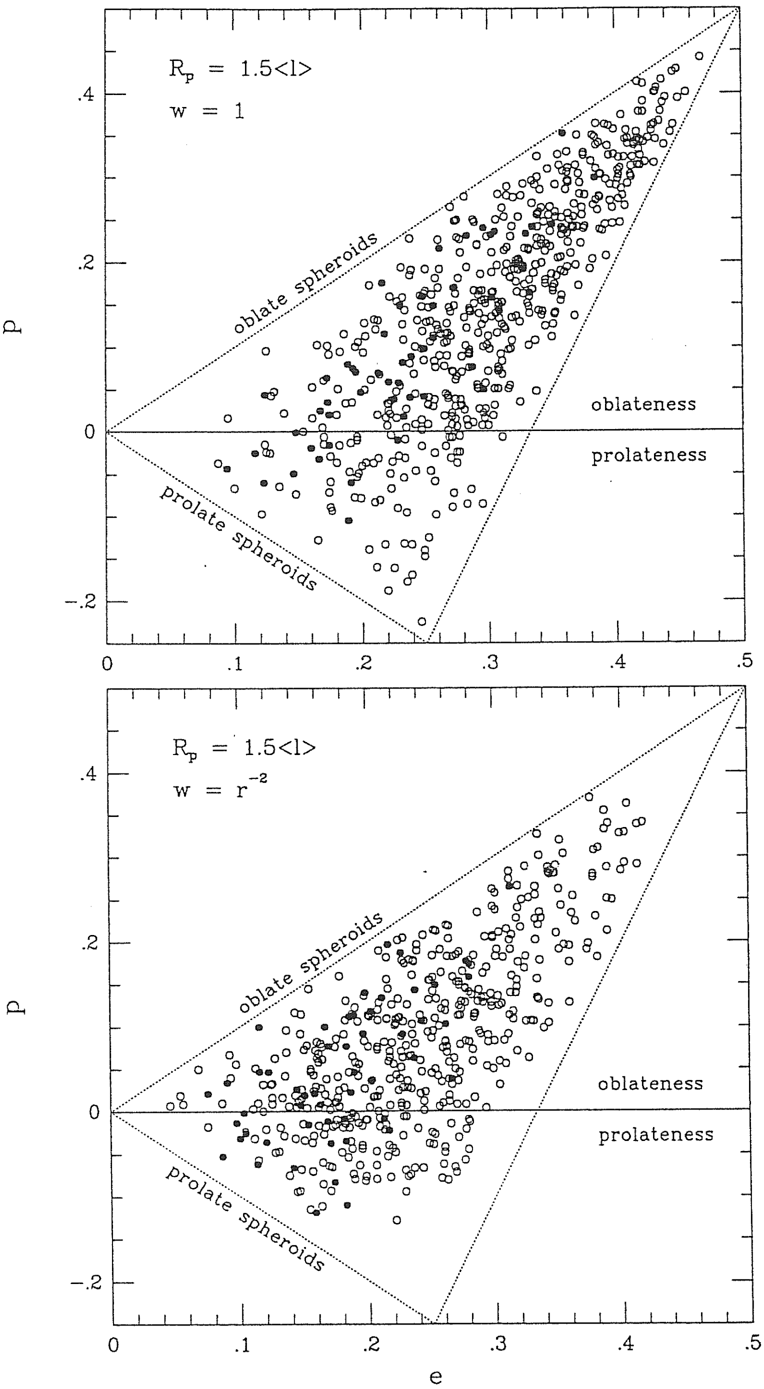

Figure 10.10 — Flattening of simulated superclusters (for the P_{21} set), found by a friends of friends algorithm with $R_p = 1.5\langle l \rangle$. Superclusters with more than 60 members are plotted as filled circles and they have a tendency to be more spherical than those containing fewer members (open circles).

(the other sets of simulations give roughly similar flattening distributions). Two different weighting schemes have been used ($w = 1$ and $w = r_i^{-2}$). It is evident that the simulation 'superclusters' are **triaxial** with a strong preference towards oblateness ($\sim$ 80% of the total number of 'superclusters' have $p \geq 0$). Note that this is the *expected* flattening of 'superclusters' found by a friends-of-friends algorithm, in a clustered distribution similar to that of the real cluster samples. Note also that there is a slight tendency for 'superclusters', containing a large number of members (filled circles in the figures) to be more spherical than those with fewer members.

To assess, therefore, whether the superclusters found in the real data are physical entities we need to compare their flattening with that found in clustered environments with the same selection functions as the real data (as in our simulations). In Figure 10.11 we present the simulated (P_{21}) supercluster flattening (based on the $w = r^{-2}$ weighting) together with that found from the real data (superclusters have ≥ 9 members) and for two values of R_p.

It is evident that the real superclusters are triaxial but in many cases have values of e and p lying beyond the extremes of the distribution of simulated values. For $R_p/\langle l \rangle = 1$ all superclusters found are more oblate than prolate (even for the $w = 1$ weighting scheme). However, for $R_p/\langle l \rangle = 1.5$ we find some extremely prolate superclusters, in all three samples, and in the case of the SGC Abell sample we obtain that the largest supercluster, with 64 members (Perseus-Cetus supercluster + Perseus-Pegasus chain + Pegasus-Pisces chain), is an accurately (when $w = r^2$) or a nearly (when $w = 1$) oblate spheroid. This is the largest supercluster found in the real samples with length of its major and intermediate axes $\sim 215\ h^{-1}$ Mpc. However, as discussed in the previous subsection, such large (and even larger) 'superclusters' appear at least once in each SGC simulation and therefore although its size is not significant, **its shape appears to be so.**

These results hold when comparing with any set of simulations and therefore they could be taken as evidence that at least some of the observed supercluster shapes cannot be produced in our simulations with the same low-order (2- and 3-point) correlation functions.

d) Alignments of clusters within superclusters

Further evidence about the significance of the above supercluster shapes could come

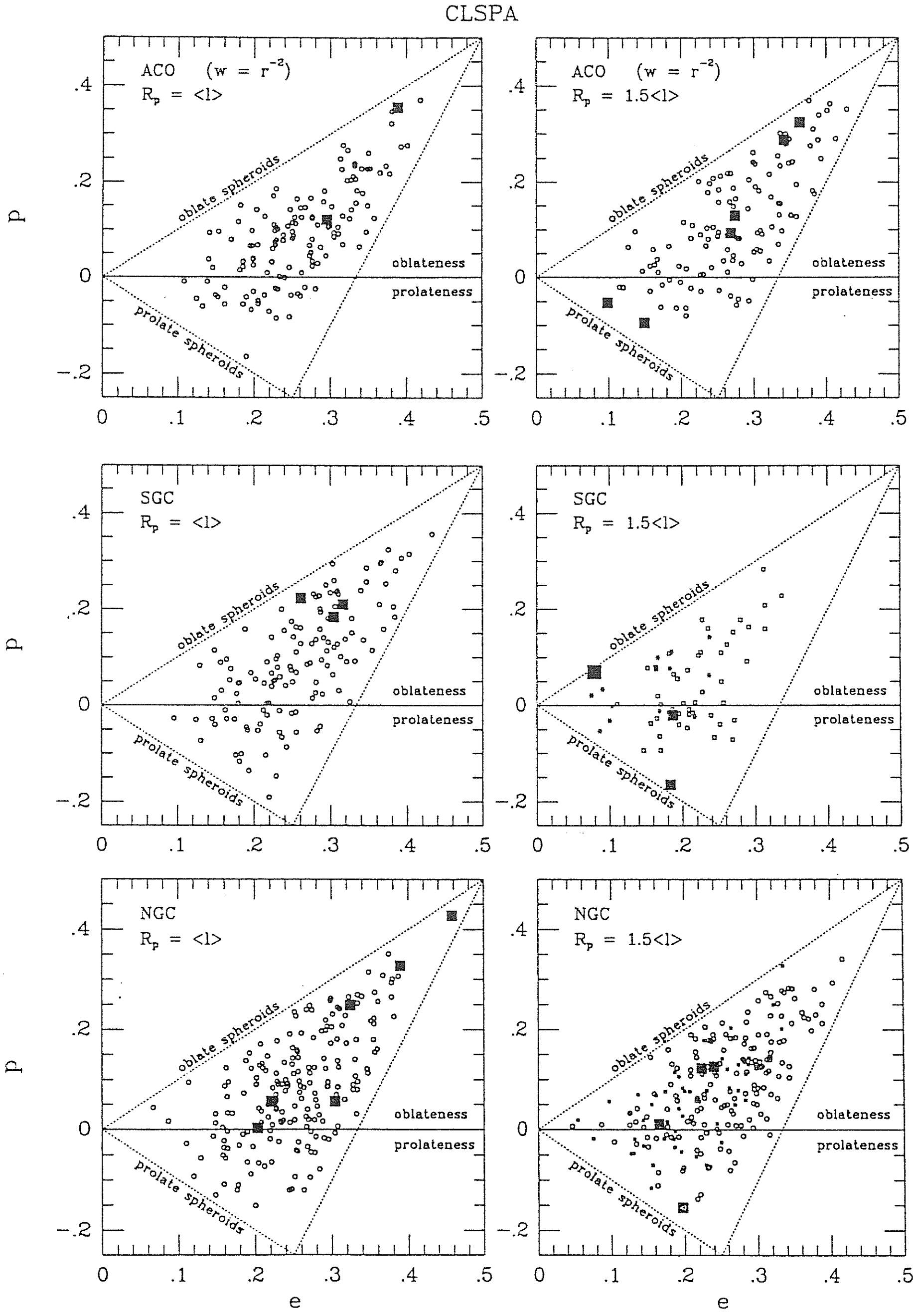

Figure 10.11 — Comparison of the shapes of the observed and simulated superclusters found at two different radii, R_p, separately for the three cluster samples (using the $w = r_i^{-2}$ weight; see text). The real data are represented by filled squares.

from a possible coherence, within each supercluster, of a cluster alignment effect (see West 1989b). In this case we search for an alignment effect by comparing the orientation of a given cluster (having a determined position angle) with the direction of all other clusters residing in the same supercluster. We determine the acute angle, ϕ, between the cluster position angle and the great circle connecting the cluster centre with that of each cluster residing in the parent supercluster.

Table 10.7 — Alignment statistics of clusters within superclusters at two different radii of 'friendship'. D_{max} is the maximum allowed separation between cluster members. N_{sep} is the total number of cluster-cluster separations considered. δ and σ are defined in the text and P_{χ^2} is the probability that the distribution of ϕ's could have been drawn from an isotropic parent one.

Sample	$R_p/\langle l \rangle$	D_{max}	N_{sep}	$\delta \pm \sigma$	δ/σ	P_{χ^2}
NGC	1	all	754	-2.1 ± 0.95	2.2	0.5
NGC	1	30 h^{-1} Mpc	350	-4.1 ± 1.4	2.9	0.038
SGC	1	all	351	-5.9 ± 1.4	4.2	0.001
SGC	1	30 h^{-1} Mpc	199	-4.8 ± 1.8	2.7	0.002
NGC	1.5	all	3109	-1.3 ± 0.46	2.8	$< 10^{-5}$
NGC	1.5	30 h^{-1} Mpc	383	-3.7 ± 1.35	2.7	0.023
SGC	1.5	all	2938	0.3 ± 0.5	-	$< 10^{-5}$
SGC	1.5	30 h^{-1} Mpc	218	-5.5 ± 1.8	3	8×10^{-4}

In Figure 10.12 we present the distribution of ϕ for all our the superclusters found using a 'friendship' radius of $\langle l \rangle$ (panel *a*) and $1.5\langle l \rangle$ (panel *b*), for the NGC Abell sample (solid lines) and for the SGC one (dashed lines). There is evidence for a slight excess towards low values of ϕ, an indication of alignments. To quantify this effect we have performed two statistical tests. Firstly we applied the χ^2 test to test the hypothesis that the observed ϕ distribution is indistinguishable from an isotropic distribution. In the last column of Table (10.7) we present the results of this test for the two different R_p values and for two different cluster separation ranges. In all cases, except for the NGC, $R_p = \langle l \rangle_r$

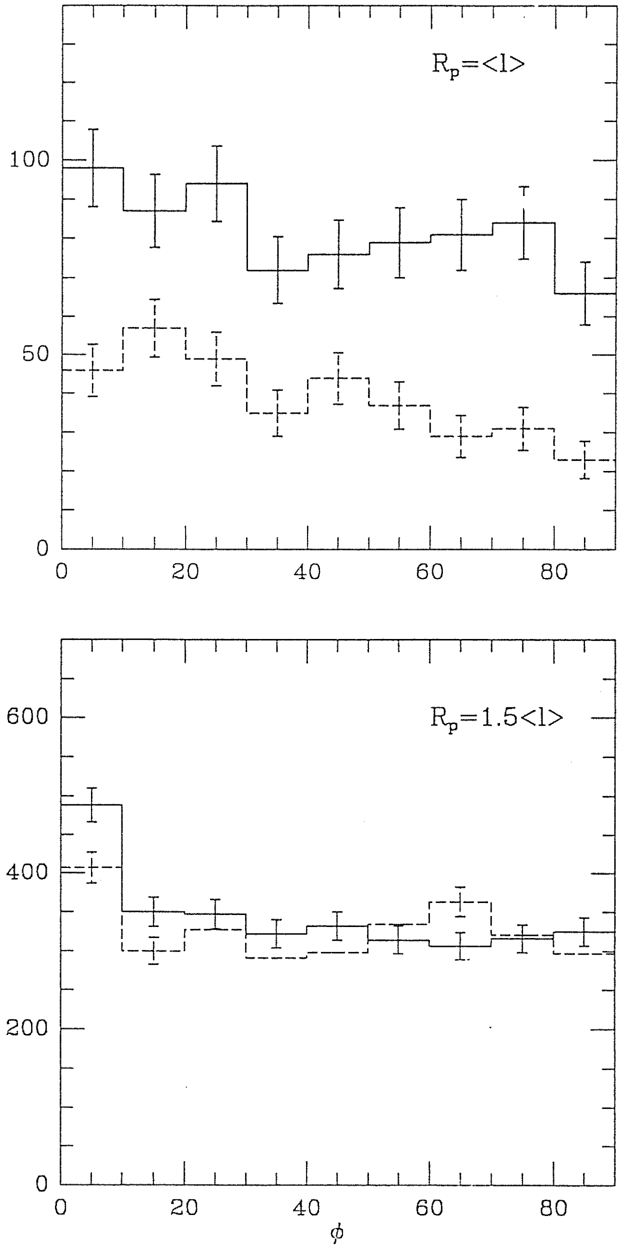

Figure 10.12 — Distribution of cluster alignment angle, ϕ, defined as the angle between the major axis of a cluster and the great circle connecting the cluster to another cluster residing in the same supercluster. Two different values of the 'friendship' radius, R_p, have been used to define the superclusters ($R_p = \langle l \rangle$ and $R_p = 1.5\langle l \rangle$; see text). The solid lines represent results based on the NGC sample while the dashed lines those based on the SGC sample. The errorbars are Poissonian.

and whole separation range, we find that the ϕ distributions are different, at a > 0.96 significance level, from an isotropic distribution.

This test, however, does not explicitly quantify the alignment effect and we have, therefore, used Eq. (10.14) and Eq. (10.15) We have estimated the average value of δ over all superclusters, with the corresponding σ which are listed in Table (10.7). It is evident that a statistically significant, but small, alignment effect is present in all samples for $R_p = \langle l \rangle$ as well as for all R_p values with $D_{min} \leq 30\ h^{-1}$ Mpc. Taking into account the fact that we possess position angles only for a subsample of our clusters, the amplitude of the alignment effect found here should be considered a lower limit to the real effect.

We have studied the alignment effect in the individual superclusters that contain ≥ 9 cluster members, as defined in the previous section. Out of the three SGC superclusters found at $R_p/\langle l \rangle = 1.5$, two show a very significant alignment with $\delta \approx -5.4$ and $\sigma \approx -1.5$ and $\delta \approx -8.4$ and $\sigma \approx -3.2$, respectively. It is interesting that both of these structures (in the Aquarius supercluster complex [Tully 1987] with a size of $80 \times 95 \times 152\ h^{-3}$ Mpc^3 and $33^2 \times 72\ h^{-3}$ Mpc^3 respectively) are more prolate than oblate and in fact one of them, the latter, is an extremely prolate structure with $p = -0.165$ (see Figure 10.11). There is also a weak alignment ($\delta \approx -4.5$, $\sigma \approx 2.1$) in the extremely oblate supercluster with 64 members (Perseus-Cetus supercluster + Perseus-Pegasus chain + Pegasus-Pisces chain of Tully [1987] with a size of $175 \times 215^2\ h^{-3}$ Mpc^3) but only when separations ≤ 30 h^{-1} Mpc are considered. In the NGC ($R_p/\langle l \rangle = 1.5$) again the only significant alignment with $\delta \approx -2.8$ and $\sigma \approx 1.1$, appears in the extremely prolate supercluster ($p = -0.154$) which contains 25 clusters with a size $66^2 \times 155\ h^{-3}$ Mpc^3 (near the Leo region [Tully 1987]). The only other supercluster that shows an alignment ($\delta \approx -5.5$, $\sigma \approx 2$), but only for separations $\leq 30\ h^{-1}$ Mpc, is in the largest supercluster found in the NGC with size $100 \times 150 \times 200\ h^{-3}$ Mpc^3 (Hercules-Corona Borealis supercluster [Tully 1987]).

Similarly for $R_p/\langle l \rangle = 1$, we find in the NGC that the two superclusters (the Hercules supercluster [*cf.* Tarenghi et al. 1979, 1980; Gregory & Thompson 1984] with a size $31 \times 39 \times 63\ h^{-3}$ Mpc^3 and part of that near the Leo region [Tully 1987] with $25 \times 35 \times 87$ h^{-3} Mpc^3) which show significant alignments, with $\delta \approx -7.6$, $\sigma \sim 2.5$ and $\delta \approx -5.6$, $\sigma \sim 2.7$ respectively, are those which have relatively higher prolateness ($p = 0.003$ and

0.056 respectively). In the SGC there is only one supercluster (part of the Pisces-Cetus supercluster [Tully 1987]) with a very significant alignment ($\delta \approx -13.5$ and $\sigma \sim 3.5$ but in this case it is significantly more oblate than prolate.

e) Conclusions

We have found that some of the superclusters in the real cluster samples, identified by a friend of friends algorithm, have shapes which in many cases fall outside what is expected from a clustered point-distribution having the same 2 and 3–point correlation function as that of the real cluster samples (more prolate or oblate). Qualitatively similar results are obtained when we restrict our sample only to $R \geq 1$ clusters, although the resulting number of superclusters is quite small.

Using a set of newly determined position angles (Plionis et al. 1991; Plionis 1992) we have also found quite a strong indication that clusters within superclusters are aligned with each other (in agreement with West 1989b). Furthermore there is some evidence for a *correlation between the shape of superclusters and the cluster-cluster alignment effect within superclusters*, with the alignment being more significant in superclusters which are nearly prolate.

10.2.3 The Void Probability Function

In this section, we use the void probability function (VPF) $P_0(V)$ to study spatial distribution of clusters in the real samples and in the simulation samples. The VPF is defined as the probability of finding no cluster in a randomly placed volume V and it is closely related to the high order correlation functions (White 1979).

a) Our method

Our method of determining VPF is similar to that of Jing (1990b). For each simulation sample or real sample, we randomly place a large set of random points (typically 5,000) in the sample volume. Around each point, we draw a set of spheres. The radii of the spheres are taken in such a way that the expected number of clusters within the spheres is N ($\equiv nV$), where $N = 1, ..., 14$. If a sphere crosses the sample boundary, we exclude it in our calculation, thus correcting for boundary effects. Because the cluster densities drop dramatically near the radial boundaries, in this section we use new radial limits for the

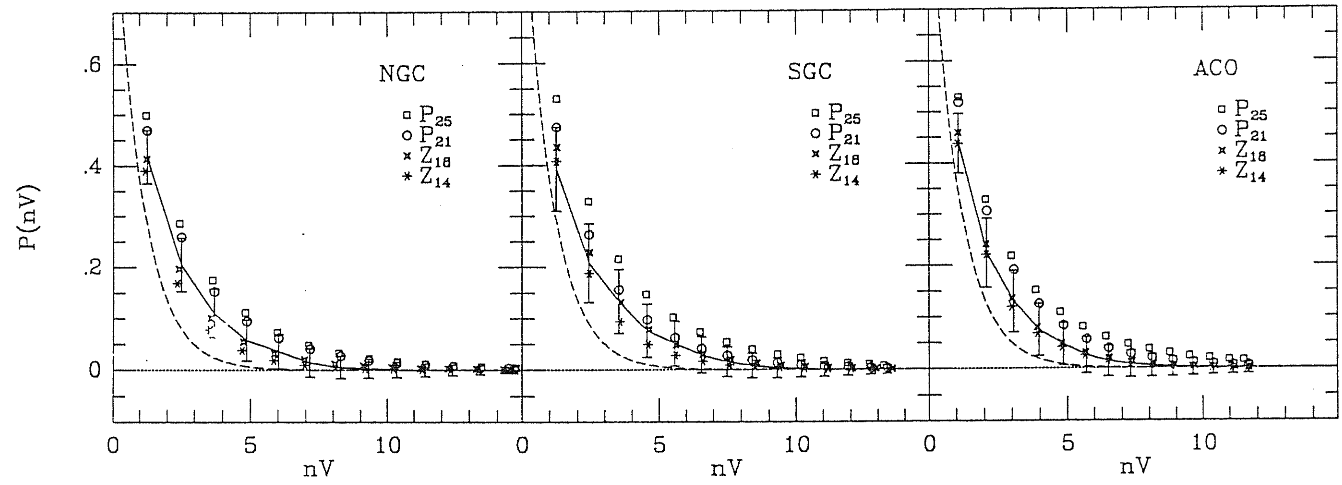

Figure 10.13 — The void probability function (see text). The real data VPF is represented by the solid lines while the simulation values by the different symbols. The dashed line represents the Poisson case, $\exp(nV)$. The error bars are the 1σ ensemble fluctuations of the P_{21} set of simulations.

real and simulated samples; 240 h^{-1}Mpc for NGC and 210 h^{-1} Mpc for SGC and ACO. Finally, we count the number of clusters in each sphere, and obtain the count probabilities.

In Figure 10.13, we plot the VPF as a function of the expected cluster number for the real data (solid lines) and simulated samples (symbols, see figure caption) as well as for the Poisson case, $\exp(-nV)$ (dashed line). The uncertainties are estimated from the fluctuations between 50 samples of the P_{21} simulation sets (similar uncertainties are obtained from the other simulation sets). For all three cluster samples the VPF of the simulation P_{25} is systematically higher than the observed VPF (at 1.5σ level), because of the large correlation length. The VPFs of the other three set of simulations are all consistent with the observed VPFs within 1σ.

b) Conclusions

We have found, using the void probability function, that both the sizes and the frequency of voids in the distribution of rich clusters are not exceptional and in agreement with that expected in any clustered distribution of points with the same 2–point correlation function, as that of the real cluster data ($r_\circ \leq 21\ h^{-1}$ Mpc).

10.3 Conclusions

We have found, using a variety of clustering techniques, that the size, the frequency of occurrence and in most cases the multiplicity function of the large-scale structures and voids, observed in the distribution of rich (Abell, ACO) clusters are not unexpected in a clustered environment characterized by the same low-order clustering as that of the real cluster distribution. In particular we found that the peak simulations with a Gaussian spectrum, random phases and $r_\circ \approx 21\ h^{-1}$ Mpc can reproduce fairly well the three-point correlation function of rich clusters ($Q \approx 0.7$), the MST $F(l/\langle l \rangle_r)$ distribution, the multiplicity function of superclusters, found by a friends-of-friends algorithm, and the fraction of clusters residing in these superclusters. These results are in agreement with Postman et al. (1989) and Postman, Huchra & Geller (1992).

However, the filamentariness and the shapes (flattening) of structures are in many cases unexpected (or at the very extremes of that expected), within the same framework. Although these results are obtained in all three cluster samples, they are particularly significant in the ACO sample. This could be attributed to the higher sensitivity of the IIIa-J emulsion plates used to construct the ACO survey, which then would imply that this catalogue samples the large-scale structure in a more detailed way than the older Abell catalogue. Another possibility is the different selection procedures used to construct the two catalogues; the original Abell catalogue is based on local density enhancements while the ACO on a global one. Yet an alternative but rather far-fetched explanation is that there is no significant selection effects but the differences between Abell and ACO samples are real properties of the cluster distribution in the regions of the sky probed by the different surveys.

Our results cannot be attributed to a deficit of clustering since even the simulation set with stronger correlations than observed ($r_\circ \approx 25\ h^{-1}$ Mpc) cannot reproduce the above features of the real cluster distribution. In fact, to test this even further we have generated *a posteriori* a set of P simulations with $r_\circ \approx 30\ h^{-1}$ Mpc and we have performed all the analysis discussed previously, finding the same results, *i.e.* significantly more 'filamentariness', 'compactness' of MST branches as well as significantly different shapes of superclusters. Therefore, decreasing the filtering length, r_s, of the Gaussian smoothed simulation field will not change our results. It is also important to stress that in our simulations, $P(k)$ has contributions from wavelengths up to $\approx 500\ h^{-1}$ Mpc. It appears, therefore, unlikely that our results on the MST branch-length statistics and on the flattening distribution would change if we would increase the box size or add more power on large scales.

Thus we suggest that a plausible explanation of these results is that the simulation construction assumptions (gaussian random-phase model) are not adequate to describe the observed large-scale structure in the universe. Other models, based on non-gaussian statistics, have been proposed (*cf.* Coles & Barrow 1987; Messina et al. 1990; Coles & Jones 1990; Moscardini et al. 1991; Matarrese et al. 1991) which keep the same low-order clustering as that of the gaussian models but provide richer large-scale structure (large bulk-motions, filaments etc.). Therefore, our results could, possibly, be explained within a non-gaussian statistics framework. In fact, a topological analysis of our cluster samples (Plionis, Valdarnini & Coles 1992) has shown that on scales where one would expect to recover the gaussian background field, the ACO sample shows a definite, although marginal, *meatball* shift.

To summarize, we have found in the distribution of Abell and ACO clusters significantly richer large-scale structure (filamentariness, shapes etc.) than what is expected in a clustered distribution of points that have the same low-order clustering (2– and 3–point functions) as that of the real data. Furthermore, we have found significant cluster alignments within superclusters, and also an apparent correlation of the cluster-alignment effect with the prolateness of superclusters.

---

‡The materials presented in this chapter are based on our paper: Plionis, M., Valdarnini, R. & Jing, Y.P. 1992, *The Astrophysical Journal*, (in press).

11

Exploring the primordial density power spectrum

As shown in Chapter 1, the power spectrum $P(k)$ of the cosmic density distribution is a very important quantity in galaxy formation theories. The $P(k)$ on large scales directly tells us information about the primordial density fluctuation, and the $P(k)$ on small scales carries information of later non-linear evolution, therefore observations of the $P(k)$ can serve to distinguish different theoretical models. In the linear gravitational instability theory, the $P(k)$ can be easily related to many important quantities, e.g., the peculiar velocity of the Local Group, the local peculiar velocity field, the flux and gravitational dipoles, large-angle anisotropy in the cosmic background radiation, etc. (see §11.1; e.g., Juszkiewicz, Vittorio, & Wyse 1990; Lahav, Kaiser, & Hoffman 1990; Vittorio, Matarrese, & Lucchin 1988). When we have measured the $P(k)$ from galaxy distribution, combining these observations we expect to be able to put constraints on the two theoretical parameters, i.e., the density parameter Ω_0 and the 'biasing' factor b. These constraints are independent of whether the Universe is dominated by cold dark matter or by hot dark matter. Furthermore, unlike the two-point correlation function, the power spectrum independently measures the clustering on different scales, therefore a measurement of $P(k)$ for different kinds of objects can better tell us the story of the 'biasing'.

In mathematics, the power spectrum $P(k)$ and the two-point correlation $\xi(r)$ are equivalent, since one is the Fourier transformation of the other (§11.1). However in the practical measurement of galaxy clustering, they are different. As Baumgart & Fry (1991) and Peacock & Nicholson (1991) reasoned, since $1 + \xi \propto 1/\overline{n}$ or $1/\overline{n}^2$ (depending on methods of normalizing random pairs) and $P(k) \propto 1/\overline{n}^2$, the $P(k)$ is much less sensitive than $\xi(r)$ in the linear regime to the mean number density $\overline{n}$ of objects which is difficult to measure accurately [cf. de Lapparent, Geller, & Huchra 1988]. Therefore, the $P(k)$ is expected to be able to more effectively explore the clustering in the linear regime where $\xi(r) < 1$.

The power spectrum $P(k)$ has been applied to several redshift surveys quite recently by several authors to measure large-scale clustering. They analysed the CfA and Perseus-Pisces redshift surveys (Baumgart & Fry 1991), the radio galaxy survey (Peacock & Nicholson 1991), the IRAS QDOT survey (Kaiser 1991), the galaxy distribution in the nearby superclusters (Gramann & Einasto 1992), the SSRS redshift sample (Park, Gott, & da Costa 1992) and the CfA slices survey (Vogeley et al. 1992).

In this chapter, we present new results of the $P(k)$ for the 2-Jy IRAS redshift survey (Strauss et al. 1992b) and for two redshift samples of Abell clusters (Huchra et al. 1990b; Postman, Huchra, & Geller 1992). The advantages of the IRAS survey for clustering studies have been stressed by Strauss et al. (1990). Instead of using volume-limited samples as in the previous studies on the optical galaxies, we use semi-volume-limited samples for IRAS galaxies, thus having a much larger number (more than 1,000 in each sample) of objects remaining for the analysis. [Peacock & Nicholson (1991) and Kaiser (1991) used non-volume-limited samples; many authors (e.g., Davis & Peebles 1983) used semi-volume-limited samples in correlation analysis.] The large sky coverage of the IRAS survey allows us to explore the power spectrum up to wavelength $\lambda \sim 100\,h^{-1}$Mpc. Our first use of Abell cluster samples, by their large spatial volumes surveyed, means that we are able to determine the $P(k)$ for wavelengths up to several hundreds h^{-1}Mpc. The main purpose of the present work is to obtain the power spectrum on a large range of spatial scales.

The arrangement of the chapter is as follows. In §11.1, we present a theoretical framework which links a number of cosmological quantities with the power spectrum. These formulae will be used in the later discussion (§11.4). In §11.2, we derive a method for estimating the power spectrum from a redshift sample. There we carefully examine the effects arising from the 'alias' which however have never been considered in the previous studies. Then we apply the method to the IRAS sample and the Abell samples in §11.3. A detailed comparison of the observed power spectrum with other observations is given in §11.4.

11.1 Expressions of cosmological quantities in terms of the power spectrum

Many cosmological observational quantities can be expressed in terms of the power spectrum. In this section, we shall derive some of these expressions. Most of these formulae are not new and can be found in one form or another in literature. However, no single reference contains all the formulae. The aim of this section is to provide a unified formulation which is to be used in §11.4.

First let's recall the definition of the power spectrum $P(k)$. Let $\rho(\vec{r})$ be the cosmic density field. Its mean density is denoted by $\overline{\rho}$. The density field then can be represented by a dimensionless field $\delta(\vec{r})$ (which is usually referred as to the density contrast):

$$\delta(\vec{r}) = \frac{\rho(\vec{r}) - \overline{\rho}}{\overline{\rho}}. \tag{11.1.1}$$

Based on the cosmological principle, we expect $\rho(\vec{r})$ to be periodic in some large rectangular volume V_μ. Its Fourier transformation then is defined by

$$\delta(\vec{k}) = \frac{1}{V_\mu} \int_{V_\mu} \delta(\vec{r}) e^{i\vec{r}\cdot\vec{k}} d\vec{r}, \tag{11.1.2}$$

and the power spectrum $P(k)$ is simply related to $\delta(\vec{k})$ by

$$P(k) \equiv \langle \mid \delta(\vec{k}) \mid^2 \rangle , \tag{11.1.3}$$

where $\langle \cdots \rangle$ means the ensemble average.

11.1.1 The two-point correlation function $\xi(r)$

The two-point correlation function $\xi(r)$ has been widely used to measure the large scale clustering in the Universe (Peebles 1980; §3.1). Here we shall express $\xi(r)$ in terms of the power spectrum $P(k)$. As we see below, $\xi(r)$ simply is the Fourier transform of $P(k)$. Since

$$\begin{aligned} \langle \delta(\vec{k}_1) \delta^*(\vec{k}_2) \rangle &= \frac{1}{V_\mu^2} \int_{V_\mu} \langle \delta(\vec{r}_1) \delta(\vec{r}_2) \rangle e^{i\vec{r}_1\cdot\vec{k}_1 - i\vec{r}_2\cdot\vec{k}_2} d\vec{r}_1 d\vec{r}_2 \\ &= \frac{1}{V_\mu^2} \int_{V_\mu} \xi(\mid \vec{r}_{12} \mid) e^{i\vec{r}_{12}\cdot\vec{k}_1 + i\vec{r}_2\cdot(\vec{k}_1 - \vec{k}_2)} d\vec{r}_{12} d\vec{r}_2, \end{aligned} \tag{11.1.4}$$

where $\vec{r}_{12} = \vec{r}_1 - \vec{r}_2$. Noting

$$\frac{1}{V_\mu} \int_{V_\mu} e^{i\vec{r}\cdot(\vec{k}_1 - \vec{k}_2)} d\vec{r} = \delta_{\vec{k}_1, \vec{k}_2}, \tag{11.1.5}$$

we have

$$\langle \delta(\vec{k}_1)\delta^*(\vec{k}_2)\rangle = \frac{\delta_{\vec{k}_1,\vec{k}_2}}{V_\mu}\int_{V_\mu} \xi(r)e^{i\vec{k}_1\cdot\vec{r}}d\vec{r}. \tag{11.1.6}$$

Obviously we have the following relations

$$\langle \delta(\vec{k}_1)\delta^*(\vec{k}_2)\rangle = P(k_1)\delta_{\vec{k}_1,\vec{k}_2}, \tag{11.1.7}$$

$$P(k) = \frac{1}{V_\mu}\int_{V_\mu} \xi(r)e^{i\vec{k}\cdot\vec{r}}d\vec{r}, \tag{11.1.8}$$

and

$$\xi(r) = \sum_{\vec{k}} P(k)e^{-i\vec{k}\cdot\vec{r}}. \tag{11.1.9}$$

Eqs.(11.1.8) and (11.1.9) show that the power spectrum and the two-point correlation function form a Fourier transform pair.

In the continuous limit of $\vec{k}$, using the relation

$$\frac{V_\mu}{(2\pi)^3}\int d\vec{k} \rightarrow \sum_{\vec{k}}, \tag{11.1.10}$$

we express $\xi(r)$ [Eq.(11.1.9)] in integral form:

$$\xi(r) = \frac{V_\mu}{(2\pi)^3}\int P(k)e^{-i\vec{k}\cdot\vec{r}}d\vec{k}. \tag{11.1.11}$$

Since

$$\int f(k)e^{-i\vec{k}\cdot\vec{r}}d\vec{k} = 4\pi\int \frac{\sin kr}{kr} f(k)k^2 dk, \tag{11.1.12}$$

we have

$$\xi(r) = \int \Delta^2(k)\frac{\sin kr}{kr}\frac{dk}{k}, \tag{11.1.13}$$

where the variance $\Delta^2(k)$ is defined as

$$\begin{aligned}\Delta^2(k) &\equiv \frac{V_\mu}{(2\pi)^3}4\pi k^3 P(k) \\ &= \frac{2k^3}{\pi}\int \frac{\sin kr}{kr}\xi(r)r^2 dr.\end{aligned} \tag{11.1.14}$$

Using the $\Delta^2(k)$ to represent the power spectrum has the advantage that the $\Delta^2(k)$ is independent of V_μ and physically measures clustering strength.

For a power-law two-point correlation: $\xi(r) = (r_0/r)^\gamma$, the integral in Eq.(11.1.14) can be worked out. It is:

$$\begin{aligned}\Delta^2(k) &= \frac{2k^3}{\pi}\int \frac{\sin kr}{kr}(\frac{r_0}{r})^\gamma r^2\,dr \\ &= \frac{2}{\pi}(r_0 k)^\gamma \Gamma(2-\gamma)\sin\frac{(2-\gamma)\pi}{2}.\end{aligned} \tag{11.1.15}$$

11.1.2 The second moment of correlation function $J_3(x)$

Although current inflation theories can predict the shape of the $P(k)$, it is generally thought that they are unable to give its amplitude. In most previous theoretical studies, the amplitude is normalized to fit one observable quantity which can be predicted from the linear gravitational instability theory. One such quantity is the second moment of correlation function $J(x)$ at $x \approx 10 \sim 20\,h^{-1}$Mpc. The $J(x)$ is defined as

$$J_3(x) \equiv \int_0^x \xi(r) r^2\,dr. \tag{11.1.16}$$

Inserting the expression (11.1.13) into the above equation, we get

$$J_3(x) = \int \Delta^2(k)[\sin kx - kx\cos kx]\frac{dk}{k^4}. \tag{11.1.17}$$

From their spatial correlation analysis of the CfA redshift survey, Davis & Peebles (1983) find

$$J_3(10\,h^{-1}\text{Mpc}) = 270(\,h^{-1}\text{Mpc})^3 \tag{11.1.18}$$

for galaxy distribution in redshift space.

11.1.3 The mean square mass fluctuation σ_c^2

Another commonly used normalization is the mean square mass fluctuation σ_c^2 in a sphere of radius $R = 8\,h^{-1}$Mpc. The σ_c^2 has also been proven to be a very powerful measure of large-scale clustering where correlation function ξ is weak (Efstathiou et al. 1990; Saunders et al. 1990). If we measure the mass with a window function $W(\vec{r})$, the expected mass should be:

$$\overline{M} = \int \langle\rho(\vec{r})\rangle W(\vec{r})d\vec{r} = \bar{\rho}V_W, \tag{11.1.19}$$

where $V_W = \int W(\vec{r})d\vec{r}$. The mean square mass is then

$$\langle M^2 \rangle = \int \langle \rho(\vec{r}_1)\rho(\vec{r}_2)\rangle W(\vec{r}_1)W(\vec{r}_2)d\vec{r}_1 d\vec{r}_2, \tag{11.1.20}$$

and the mean square mass fluctuation is

$$\begin{aligned} \sigma_c^2(\overline{M}) &\equiv \frac{\langle M^2 \rangle - \overline{M}^2}{\overline{M}^2} \\ &= \frac{V_\mu}{(2\pi)^3}\frac{1}{V_W^2}\int P(k)W(\vec{r}_1)W(\vec{r}_2)e^{-i\vec{k}\cdot(\vec{r}_1-\vec{r}_2)}d\vec{r}_1 d\vec{r}_2 d\vec{k} \qquad (11.1.21) \\ &= \int \frac{1}{4\pi k^3}\Delta^2(k) \mid W(\vec{k}) \mid^2 d\vec{k}, \end{aligned}$$

where $W(\vec{k}) = \int W(\vec{r})e^{i\vec{k}\cdot\vec{r}}d\vec{r}/V_W$.

Clearly the variance σ_c^2 depends on the window function through $\mid W(\vec{k}) \mid^2$. Here we present $W(\vec{k})$ for three typical cases which are simple to apply to galaxy catalogues.

I. For *the top-hat window function:*

$$W(r) = \begin{cases} 1, & r \le R; \\ 0, & \text{otherwise,} \end{cases} \tag{11.1.22a}$$

we have

$$W(\vec{k}) = \frac{3}{y^3}(\sin y - y\cos y), \tag{11.1.22b}$$

where $y = kR$. From their spatial correlation analysis of the CfA redshift survey, Davis & Peebles (1983) find

$$\sigma_c^2(8\,h^{-1}\mathrm{Mpc}) = 1 \tag{11.1.23}$$

for the galaxy distribution in redshift space.

II. For *the cube-hat window function:*

$$W(\vec{r}) = \begin{cases} 1, & -l/2 \le (x,y,z) \le l/2; \\ 0, & \text{otherwise,} \end{cases} \tag{11.1.24a}$$

we have

$$W(\vec{k}) = \frac{\sin(\frac{l}{2}k_x)\sin(\frac{l}{2}k_y)\sin(\frac{l}{2}k_z)}{(\frac{l}{2}k_x)(\frac{l}{2}k_y)(\frac{l}{2}k_z)}. \tag{11.1.24b}$$

Figure 3.4 shows the variance measured by Efstathiou et al. (1990) using this window for the QDOT IRAS survey.

III. For *the Gaussian window function:*

$$W(r) = \exp(-\frac{r^2}{2R^2}), \tag{11.1.25a}$$

we have

$$W(\vec{k}) = \exp(-\frac{k^2R^2}{2}). \tag{11.1.25b}$$

Saunders et al. (1990) use this window function to determine the variance in the QDOT IRAS survey and they find $\sigma_c^2(R) = 0.436 \pm 0.091\,, 0.184 \pm 0.050\,,$ and 0.0669 ± 0.019 for $R = 5\,, 10\,,$ and $20\,h^{-1}$Mpc.

11.1.4 The rms bulk peculiar velocity

Instead of measuring the mass fluctuation as in Eq.(11.1.21), we now measure the peculiar velocity. From linear perturbation theory, we have (Peebles 1980):

$$\vec{v}_{\vec{k}} = -if(\Omega)H_0\frac{\vec{k}}{k^2}\delta(\vec{k}), \tag{11.1.26}$$

where $f(\Omega) \approx \Omega^{0.6}$. The mean square bulk velocity with a window function $W(\vec{r})$ is then:

$$\begin{aligned}\overline{v^2} =& \langle(\frac{\int \vec{v}(\vec{r})W(\vec{r})d\vec{r}}{\int W(\vec{r})d\vec{r}})^2\rangle \\ =& \frac{1}{V_W^2}\int\sum_{\vec{k}_1,\vec{k}_2}\langle\vec{v}(\vec{k}_1)\cdot\vec{v}(\vec{k}_2)\rangle e^{-i\vec{r}_2\cdot\vec{k}_2 - i\vec{r}_1\cdot\vec{k}_1}W(\vec{r}_1)W(\vec{r}_2)d\vec{r}_1d\vec{r}_2 \\ =& [f(\Omega)H_0]^2\int\frac{1}{4\pi k^5}\Delta^2(k)\mid W(\vec{k})\mid^2 d\vec{k}\,.\end{aligned} \tag{11.1.27}$$

11.1.5 The peculiar velocity of the Local Group

One application of Eq.(11.1.27) is the peculiar velocity of the Local Group (LG). Until 1992, the only undoubted detection of the Cosmic Background Radiation (CBR) anisotropy is the dipole anisotropy which is generally interpreted as arising from the peculiar motion of the earth through the CBR. Correcting for the motions of the earth relative to the Sun and of the Sun relative to the center of mass of the Local Group (LG), one can deduce a velocity $\vec{V}_{LG}$ for the LG relative to the CBR. The COBE DMR experiment (Smoot et al. 1991) gives $\vec{V}_{LG} = 622 \pm 20\,\mathrm{kms}^{-1}$ with its direction towards $b^{II} = 30° \pm 2°$, and

$l^{II} = 277° \pm 2°$. A sphere of radius $\sim 7\,h^{-1}$Mpc around the Group participates in the same peculiar motion (e.g., Faber & Burstein 1988; Peebles 1986), thus we expect that the linear perturbation theory [Eq.(11.1.27)] can specify the peculiar velocity of the LG using the window function Eq.(11.1.22b) of $R \approx 5\,h^{-1}$Mpc (see further discussion at the end of §11.1.7). However, one must keep cautious when using the observation to test theoretical models, since the observation only concerns the peculiar velocity of *one particular* sphere in the Universe (i.e., our nearby region), but Eq.(11.1.27) gives a *rms* value $V(R)$. Our LG may not have a 'typical' peculiar velocity, therefore we need the probability distribution function (PDF) to quantify the problem. For a Gaussian field of density distribution, the PDF of the peculiar velocity $\vec{v}$ is very simple: it is a 3-variate, zero-mean Gaussian function with the covariance matrix

$$\sigma_{ij} = \frac{V^2(R)}{3}\delta_{ij} \equiv \sigma\delta_{ij}, \tag{11.1.28}$$

that is,

$$P(\vec{v})d\vec{v} = \frac{d\vec{v}}{(2\pi\sigma^2)^{3/2}} \exp -\frac{v^2}{2\sigma^2}. \tag{11.1.29}$$

11.1.6 The local bulk motions

The discussion in the last subsection can be straightforwardly applied to the Local bulk motions (Lynden-bell et al. 1988). The most recent reanalysis gives bulk motions $388 \pm 67\,\mathrm{kms}^{-1}$ toward $L = 177°$, $B = -15°$ and $327 \pm 82\,\mathrm{kms}^{-1}$ toward $L = 194°$, $B = 5°$ for the spheres of radii $40\,h^{-1}$Mpc and $60\,h^{-1}$Mpc around the LG (Bertschinger et al. 1990). Because the surveyed regions are centered on the LG, it's probably more proper to study the conditional probability distribution functions, that is, the PDFs of bulk velocity $\vec{v}_2$ for a sphere of radius r_2 given its central sphere r_1 $(< r_2)$ having velocity $= \vec{V}_{LG}$. Let us denote the variables for the central sphere by subscript 1 and for the outer one by subscript 2. Defining $C_{ij} \equiv \langle \vec{v}_i \cdot \vec{v}_j \rangle / 3$ $(i, j = 1, 2)$, in analogy with the derivation for Eq.(11.1.27), we can easily get

$$C_{ij} = \frac{[f(\Omega)H_0]^2}{3} \int \frac{1}{4\pi k^5}\Delta^2(k)W_i(\vec{k})W_j(\vec{k})d\vec{k}. \tag{11.1.30}$$

For a Gaussian density field, the conditional PDF for $\vec{v}_2$ given $\vec{v}_1$ is:

$$P(\vec{v}_2|\vec{v}_1) = \frac{1}{(2\pi\sigma^2)^{3/2}} \exp -\frac{(\vec{v}_2 - \alpha\vec{v}_1)^2}{2\sigma^2}, \tag{11.1.31}$$

where

$$\alpha = C_{12}/C_{11} \tag{11.1.32a}$$

and

$$\sigma^2 = C_{22}(1 - \frac{C_{12}^2}{C_{11}C_{22}}). \tag{11.1.32b}$$

From Eq.(11.1.31), we can construct many physical quantities which can be compared with observations. Here we give some. One quantity is the *rms* value of $\vec{v}_2$ which reads:

$$\begin{aligned} \langle \vec{v}_2^2 \rangle^{1/2} =& \int P(\vec{v}_2|\vec{v}_1)\vec{v}_2^2\, d\vec{v}_2 \\ =&[3\sigma^2 + \alpha^2 v_1^2]^{1/2}\,. \end{aligned} \tag{11.1.33}$$

Another quantity is the probability of v_2 less than V_2:

$$\begin{aligned} P(v_2 < V_2|v_1) =& \int_{v_2<V_2} P(\vec{v}_2|\vec{v}_1)d\vec{v}_2 \\ =&\frac{1}{\sqrt{2\pi}}\frac{\sigma}{\alpha v_1}\{\exp[-\frac{(V_2+\alpha v_1)^2}{2\sigma^2}] - \exp-[\frac{(V_2-\alpha v_1)^2}{2\sigma^2}]\} \\ &+ \frac{1}{\sqrt{2\pi\sigma^2}}\int_{-V_2-\alpha v_1}^{V_2-\alpha v_1} \exp-(\frac{x^2}{2\sigma^2})dx. \end{aligned} \tag{11.1.34}$$

This equation can help to set the theoretical upper limits and/or lower limits to v_2 at a given confidence level.

Because $\vec{v}_2$ is a vector, it is important to study statistics relevant to direction. One statistic is the PDF of the misalignment angle θ between $\vec{v}_2$ and $\vec{v}_1$ [$\mu \equiv \cos\theta = \hat{\vec{v}}_1 \cdot \hat{\vec{v}}_2$]:

$$\begin{aligned} P(\mu) =&2\pi \int P(\vec{v}_2|\vec{v}_1)v_2^2 dv_2 \\ =&\exp(-\frac{y_1^2}{2})\{\frac{y_2}{\sqrt{2\pi}} + [1+y_2^2]\exp(\frac{y_2^2}{2})\frac{1}{\sqrt{2\pi}}\int_{-y_2}^{\infty}\exp(-\frac{x^2}{2})dx\}, \end{aligned} \tag{11.1.35}$$

where $y_1 = \alpha v_1/\sigma$ and $y_2 = \alpha\mu v_1/\sigma$.

In the limit of large y_1, $P(\mu)$ peaks at $\mu \sim 1$ ($\theta \sim 0$) and the angle θ distribution is approximately

$$P(\theta)d\theta = P(\mu)d\mu \approx y_1^2\theta\exp(-\frac{y_1^2\theta^2}{2})d\theta\,. \tag{11.1.36}$$

Therefore $\sqrt{\pi/2}/y_1$ measures the expected misalignment angle. On the other hand, in the limit of $y_1 \to 0$, then $P(\mu) = 1/2$, i.e., the vectors $\vec{v}_1$ and $\vec{v}_2$ are randomly orientated as expected. From the Eq.(11.1.35), we can easily give upper and lower limits on θ at some confidence level. The *rms* value of θ can be obtained by numerical integration.

11.1.7 Acceleration vector

The acceleration of a position $\vec{r}_0$ contributed by matter distributed on a shell with inner radius r_a and outer radius r_b around $\vec{r}_0$ is

$$\vec{g}(\vec{r}_0) = \frac{3}{4\pi}\int_{r_a}^{r_b} \delta(\vec{r}_0 + \vec{r})\frac{\vec{r}}{r^3}d\vec{r}. \tag{11.1.37}$$

In the linear instability theory, this acceleration produces a peculiar velocity at the position $\vec{r}_0$:

$$\vec{U} = \frac{1}{3}f(\Omega)H_0\vec{g}. \tag{11.1.38}$$

The above equation allows us to relate the peculiar velocity of the LG to the acceleration, and to express $\vec{g}$ in velocity units.

There exist many statistical studies which try to derive the acceleration $\vec{g}$ of the LG from redshift surveys of galaxies and clusters. Strauss & Davis (1989) and Yahil (1989) analysed their 2-Jy IRAS redshift survey and found that the acceleration of the LG starts to converge at distance $\sim 50\,h^{-1}$Mpc, i.e., the origin of the acceleration is quite local. Furthermore, they found that the angle between their inferred $\vec{U}$ and $\vec{V}_{LG}$ is in the range 6 to 25 degrees. Rowan-Robinson et al. (1990) studied the QDOT IRAS survey. While they obtained a similar misalignment angle, they found that the acceleration keeps rising about 30% at distance from $50\,h^{-1}$Mpc to $100\,h^{-1}$Mpc, then begins to converge. The pseudoconvergence shown in the 2-Jy IRAS sample probably is due to its limited size. The recent analyses of redshift samples of ACO clusters (Plionis & Valdarnini 1991; Scaramella et al. 1991) show an even larger convergence radius (about $150\,h^{-1}$Mpc), and they find about 20% rise in $\vec{g}$ beyond $100\,h^{-1}$Mpc. Since the cluster samples have depth $\sim 300\,h^{-1}$Mpc, probably the convergence detected is a real one.

In analogy with the local bulk motions, one needs the conditional PDF of the acceleration to test theoretical models or to make theoretical predictions. Since galaxies and clusters probably are 'biased' tracers of the matter distribution, here for simplicity we adopt the linear 'biasing' assumption and denote the biasing factor by b. All the derivations of Eqs.(11.1.31 – 11.1.35) can be applied to studying $\vec{U}$, except $\vec{v}_2$ and C_{ij} should be substituted by $\vec{U}$ and C^U_{ij}. If we are studying the acceleration attributed by a shell with radii r_a and r_b to its center LG, then we have

$$C^U_{ij} = \frac{[f(\Omega)H_0]^2 b^{i+j-2}}{3} \int \frac{1}{4\pi k^3} \Delta^2(k) W^U_i(\vec{k}) W^U_j(\vec{k}) d\vec{k}, \tag{11.1.39}$$

where

$$W^U_1(\vec{k}) = \frac{\sin(kr_1)}{kr_1} \tag{11.1.40a}$$

and

$$W^U_2(\vec{k}) = \frac{\sin(kr_a)}{kr_a} - \frac{\sin(kr_b)}{kr_b}. \tag{11.1.40b}$$

Note that C^U_{11} and C_{11} are approximately the same, since the bulk motion of a sphere r_1 is essentially from the gravitational pull of matter outside r_1.

The misalignment angle test could not be a powerful test. As shown by Villumsen & Davis (1986) based on their N-body experiment, the nonlinear effect can result in a typical misalignment angle 25° between the real peculiar velocity of a region like our LG and the one predicted from the linear instability theory. Since the observed misalignment angle θ between $\vec{U}$ and $\vec{V}_{LG}$ is typically 25°, it is difficult to estimate how much is from the linear theory [Eq.(11.1.35)]. In contrast, Villumsen and Davis show that the nonlinear evolution only slightly affects the amplitude of the LG peculiar velocity. Therefore in §11.4 we will only consider tests relevant to the amplitudes of $\vec{V}_{LG}$, $\vec{v}_2$ and $\vec{U}$.

11.1.8 Large-angle CBR anisotropy: the Sachs-Wolfe effect

It is well known that the CBR anisotropy $\Delta T/T$ on angle scales $\theta \gg 1°$, after excluding the dipole component [the substantial part of which is thought to be induced by the motion of the earth relative to the CBR (§11.1.5)], is dominated by the potential fluctuation on the last-scattering surface, usually called the Sachs-Wolfe effect. [Here we have assumed that the primordial perturbation is adiabatic. For an isocurvature perturbation, see Efstathiou & Bond (1986)]. Since length scales corresponding to the angular scales exceed the horizon size at the recombination era t_R, the $\Delta T/T$ is insensitive to the microphysical processes operating at t_R and can be used to probe the primeval density fluctuation. In a flat universe and under the synchronous gauge, the Sachs-Wolfe effect can be expressed by:

$$\frac{\Delta T}{T}(\vec{\Omega}) = \frac{1}{3}\Phi(\vec{x}) \,, \tag{11.1.41}$$

where Φ is the Newtonian potential (time-independent) at the position $\vec{x} = (2H_0^{-1}, \vec{\Omega})$ on the last-scattering surface. Using the relation (Peebles, 1980)

$$\Phi_{\vec{k}} = -\frac{4\pi G\rho_0}{k^2}\delta_{\vec{k}} \,, \tag{11.1.42}$$

we get

$$\frac{\Delta T}{T}(\vec{\Omega}) = -\frac{H_0^2}{2}\sum_{\vec{k}} \frac{\delta_{\vec{k}}}{k^2} e^{-i\vec{k}\cdot\vec{x}} \,. \tag{11.1.43}$$

The temperature correlation function is then:

$$\begin{aligned} C(\theta) &\equiv \langle \frac{\Delta T}{T}(\vec{\Omega}_1)\frac{\Delta T}{T}(\vec{\Omega}_2)\rangle \\ &= \frac{H_0^2}{4}\int \frac{\Delta^2(k)}{k^5}\frac{\sin(2xk\sin\frac{\theta}{2})}{2xk\sin\frac{\theta}{2}}dk \,, \end{aligned} \tag{11.1.44}$$

where $\cos\theta = \vec{\Omega}_1 \cdot \vec{\Omega}_2$. Expanding $C(\theta)$ in Legendre functions:

$$C(\theta) = \sum_l C_l P_l(\cos\theta), \tag{11.1.45}$$

we obtain the coefficients

$$C_l = \frac{H_0^4(2l+1)}{4}\int \frac{\Delta^2(k)}{k^5} j_l^2(kx) dk \,, \tag{11.1.46}$$

where $j_l(x)$ is the spherical Bessel function of order l. For a power law spectrum $\Delta^2(k) = \Delta_0 k^{n+3}$, we have

$$C_l = H_0^4(2l+1)\Delta_0\pi 2^{n-6}x^{1-n}\frac{\Gamma(3-n)\Gamma(l-\frac{1}{2}+\frac{n}{2})}{\Gamma^2(2-\frac{n}{2})\Gamma(\frac{5}{2}+l-\frac{n}{2})} \tag{11.1.47}$$

if $n < 3$ (otherwise the integral diverges at large wavenumber).

Quite recently the COBE DMR successfully detected $\Delta T/T$ on angular scales $\geq 7°$ (Smoot et al. 1992). Their data support the hypothesis that the primordial density power spectrum is a Harrison-Zel'dovich one ($n = 1$) for wavelengths $\lambda \geq 500\,h^{-1}$Mpc, and they give a quadrupole $Q = C_2^{1/2} = (6 \pm 1.5) \times 10^{-6}$. For $n = 1$ case, the density fluctuation can be characterized by the variable ϵ:

$$\epsilon^2 \equiv \frac{V_\mu}{(2\pi)^3} 4\pi k^3 |\Phi_k|^2 = \frac{9}{4} \frac{H_0^4}{k^4} \Delta^2(k) = \frac{9}{4} H_0^4 \Delta_0 \,, \tag{11.1.48}$$

that is, the potential variance per logarithmic k, which is a constant for $n = 1$ and $\Omega = 1$. In this case, from Eq.(11.1.47), we can find:

$$Q = \sqrt{\frac{5}{108}}\,\epsilon. \tag{11.1.49}$$

The COBE observation tells us that $\epsilon = (2.7 \pm 0.7) \times 10^{-5}$ for wavelengths greater than $500\,h^{-1}$Mpc. This provides an ideal quantity to normalize the primordial power spectrum in any theoretical studies. In contrast, the normalizations like Eqs.(11.1.18) and (11.1.23) have a lot of uncertainties (e.g., uncertainties in the measures themselves; redshift distortion; biasing in the galaxy distribution; etc.).

11.2 How to measure the power spectrum from galaxy distributions

In this section, we shall develop a method of obtaining the power spectrum from a sample of extragalactic objects. Since there are only a finite number of objects in each sample, we need to correct the 'discreteness' effect arising from the Poisson shot noise. To show this, let's consider an ideal dataset of discrete objects $\{i\}$. The number density distribution can be written as $n(\vec{r}) = \sum_i \delta(\vec{r} - \vec{r}_i)$ and we assume that the distribution is periodic in a large rectangular volume V_μ. In analogy with the continuous case, the Fourier transform of $n(\vec{r})$ is defined as:

$$\delta^d(\vec{k}) = \frac{1}{V_\mu \overline{n}} \int_{V_\mu} n(\vec{r}) e^{i\vec{r}\cdot\vec{k}} d\vec{r} - \delta_{\vec{k},\vec{0}} \,, \tag{11.2.1}$$

where $\overline{n}$ is the global mean number density. Following Peebles (1980), we divide the volume V_μ into infinitesimal elements $\{dV_i\}$ with n_i objects inside dV_i. Then the above equation can be written as:

$$\delta^d(\vec{k}) = \frac{1}{N} \sum_i n_i e^{i\vec{r}_i\cdot\vec{k}} - \delta_{\vec{k},\vec{0}} \,, \tag{11.2.2}$$

where N is $\overline{n}V_\mu$ the number of objects in V_μ. Since dV_i is taken so small that n_i is either 0 or 1, we have $n_i = n_i^2 = n_i^3 = \cdots$. Then we can find the ensemble average of $\delta^d(\vec{k}_1)\delta^{d*}(\vec{k}_2)$ which reads:

$$\begin{aligned}\langle\delta^d(\vec{k}_1)\delta^{d*}(\vec{k}_2)\rangle =& \frac{1}{N^2}\sum_{i,j}\langle n_i n_j\rangle e^{i\vec{r}_i\cdot\vec{k}_1 - i\vec{r}_j\cdot\vec{k}_2} - \delta_{\vec{k}_1,\vec{0}}\delta_{\vec{k}_2,\vec{0}} \\ =& \frac{1}{N^2}\sum_{i\neq j}\langle n_i n_j\rangle e^{i\vec{r}_i\cdot\vec{k}_1 - i\vec{r}_j\cdot\vec{k}_2} \\ &+ \frac{1}{N^2}\sum_{i}\langle n_i\rangle e^{i\vec{r}_i\cdot(\vec{k}_1-\vec{k}_2)} - \delta_{\vec{k}_1,\vec{0}}\delta_{\vec{k}_2,\vec{0}} \\ =& \langle\delta(\vec{k}_1)\delta^*(\vec{k}_2)\rangle + \frac{1}{N}\delta_{\vec{k}_1,\vec{k}_2}\,.\end{aligned} \tag{11.2.3}$$

Finally we get the desired result:

$$P(k) = \langle|\ \delta^d(\vec{k})\ |^2\rangle - \frac{1}{N}\,. \tag{11.2.4}$$

The meaning of the above equation is quite clear: the discreteness (or shot noise) effect is to give an additional term $1/N$ to the power spectrum. To correct for the discreteness effect means to subtract the constant $1/N$ from the power spectrum calculated from Eq.(11.2.1).

However in observational cosmology, one can not be so fortunate that he has a catalogue uniformly surveyed in a cubic volume. For examples, the galactic obscuration prevents optical telescopes from observing extragalactic objects along the galactic plane; even at higher galactic latitudes, some fraction of objects is missing because the galactic extinction makes the objects look fainter. Magnitude-limit or flux-limit as a main selection criterion for defining a sample makes the sample include more objects at a smaller distance than at a larger one. Of course one could, from such an observed sample, select a subsample with a cubic volume uniformly surveyed, but he would lose a substantial fraction of objects thus weakening the quality of the statistics. In order to keep the sample as large as possible, one needs to treat these effects carefully. These effects can be modeled by one function $S(\vec{r})$ which will be called the 'selection function' later on. The definition of $S(\vec{r})$ is very simple: due to some selection criteria, only a fraction $S(\vec{r})$ of objects at position $\vec{r}$ has been included in the sample. Therefore if the underlying density distribution is $n(\vec{r})$, the density distribution $n^s(\vec{r})$ in the surveyed sample is:

$$n^s(\vec{r}) = S(\vec{r})n(\vec{r})\,. \tag{11.2.5}$$

Now we take the Fourier transform as if there were no selection effects:

$$\begin{aligned}\delta^s(\vec{k}) =& \frac{1}{N}\int n^s(\vec{r})e^{i\vec{r}\cdot\vec{k}}d\vec{r} - \delta_{\vec{k},\vec{0}}\\ =& \frac{1}{N}\sum_i n_i^s e^{i\vec{r}_i\cdot\vec{k}} - \delta_{\vec{k},\vec{0}}\,,\end{aligned} \tag{11.2.6}$$

where N is the number of objects in the sample and we calculate:

$$\begin{aligned}\langle\delta^s(\vec{k}_1)\delta^{s*}(\vec{k}_2)\rangle =& \frac{1}{N^2}\sum_{i\neq j}\langle n_i^s n_j^s\rangle e^{i\vec{r}_i\cdot\vec{k}_1 - i\vec{r}_j\cdot\vec{k}_2} + \frac{1}{N^2}\sum_i\langle n_i\rangle e^{i\vec{r}_i\cdot(\vec{k}_1-\vec{k}_2)}\\ &-\frac{1}{N}\sum_i\langle n_i\rangle e^{i\vec{r}_i\cdot\vec{k}_1}\delta_{\vec{k}_2,\vec{0}} - \frac{1}{N}\sum_i\langle n_i\rangle e^{-i\vec{r}_i\cdot\vec{k}_2}\delta_{\vec{k}_1,\vec{0}} + \delta_{\vec{k}_1,\vec{0}}\delta_{\vec{k}_2,\vec{0}}\\ =& S(\vec{k}_1)S(-\vec{k}_2) + \sum_{\vec{k}_3} S(\vec{k}_3+\vec{k}_1)P(\vec{k}_3)S(-\vec{k}_2-\vec{k}_3)\\ &+\frac{1}{N}S(\vec{k}_1-\vec{k}_2) - S(\vec{k}_1)\delta_{\vec{k}_2,\vec{0}} - S(-\vec{k}_2)\delta_{\vec{k}_1,\vec{0}} + \delta_{\vec{k}_1,\vec{0}}\delta_{\vec{k}_2,\vec{0}}\,,\end{aligned} \tag{11.2.7}$$

where $S(\vec{k})$ is defined as:

$$S(\vec{k}) = \frac{1}{\int S(\vec{r})d\vec{r}}\int S(\vec{r})e^{i\vec{r}\cdot\vec{k}}d\vec{r}. \tag{11.2.8}$$

Taking $\vec{k}_1 = \vec{k}_2 = \vec{k}$, we get

$$\langle\mid\delta^s(\vec{k})\mid^2\rangle = \mid S(\vec{k})\mid^2 + \sum_{\vec{k}_1}\mid S(\vec{k}-\vec{k}_1)\mid^2 P(\vec{k}_1) + \frac{1}{N}. \tag{11.2.9}$$

Since the function $S(\vec{r})$ is broad in space, its Fourier transform peaks at $\vec{k}\approx 0$. Except for small wavenumbers (or large wavelength $\sim$ the sample size), we have

$$P(k) = \frac{\langle\mid\delta^s(\vec{k})\mid^2\rangle - \mid S(\vec{k})\mid^2 - \frac{1}{N}}{\sum_{\vec{k}}\mid S(\vec{k})\mid^2}. \tag{11.2.10}$$

Therefore the selection effect is easy to correct for.

We can also form another Fourier quantity $\delta_1^s(\vec{k})$ to treat the selection effect. Instead of subtracting $\delta_{\vec{k},\vec{0}}$ in Eq.(11.2.6), we form $\delta_1^s(\vec{k})$ by subtracting $S(\vec{k})$, i.e.,

$$\delta_1^s(\vec{k}) = \frac{1}{N}\int n^s(\vec{r})e^{i\vec{r}\cdot\vec{k}}d\vec{r} - S(\vec{k})\,. \tag{11.2.11}$$

It is easy to find:

$$\langle \delta_1^s(\vec{k}_1)\delta_1^{o*}(\vec{k}_2)\rangle = \sum_{\vec{k}_3} S(\vec{k}_3+\vec{k}_1)P(\vec{k}_3)S(-\vec{k}_2-\vec{k}_3) + \frac{1}{N}S(\vec{k}_1-\vec{k}_2)\,, \tag{11.2.12}$$

therefore

$$P(k) = \frac{\langle \mid \delta_1^s(\vec{k}) \mid^2\rangle - \frac{1}{N}}{\sum_{\vec{k}} \mid S(\vec{k}) \mid^2}\,. \tag{11.2.13}$$

Although it is possible to use the direct summation of Eq.(11.2.6) or Eq.(11.2.11) to estimate the power spectrum for a sample of ~ one thousand objects (like available redshift surveys of galaxies), it is generally thought that it is convenient to use the FFT to make the Fourier transform. In fact, all the previous statistical studies of the power spectrum are based on the FFT. Moreover, it would be impossible to use the direct summation to study the power spectrum in a N-body simulation because of the large a number of objects employed. However using the FFT, we need first to collect density values $\rho(\vec{r}_g)$ on grids (which is usually called 'mass assignment'). The mass assignment in fact is equivalent to convolving the density field by one chosen function $W(r)$ and sampling the convolved density on a finite number of grids, therefore the FFT of $\rho(\vec{r}_g)$ generally is not equal to the FT of $\rho(\vec{r})$. This point, however, has never been considered seriously in the previous works. Now let's show this effect. The FFT can be written as:

$$\delta^f(\vec{k}) = \frac{1}{N}\sum_g n^f(\vec{r}_g)e^{i\vec{r}_g\cdot\vec{k}} - \delta_{\vec{k},\vec{0}}\,, \tag{11.2.14}$$

where $n^f(\vec{r}_g)$ is the convolved density value on the $\vec{g}$th grid $\vec{r}_g = \vec{g}H$ ($\vec{g}$ is an integer vector; H is the grid spacing):

$$n^f(\vec{r}_g) = \int n^s(\vec{r})W(\vec{r}-\vec{r}_g)d\vec{r}\,. \tag{11.2.15}$$

Following Hockney and Eastwood (1981), the FFT of Eq.(11.2.14) can be expressed in a more compact way by using the so-called 'Sampling Function'. The sampling function $\Pi(\vec{r})$ is defined as a sum of Dirac-δ functions spaced at unit length in all three spatial directions, i.e., $\Pi(\vec{r}) = \sum_{\{\vec{n}\}}\delta(\vec{r}-\vec{n})$ where $\vec{n}$ is an integer vector. Defining

$$n'^f(\vec{r}) = \Pi(\frac{\vec{r}}{H})\int n^s(\vec{r}_1)W(\vec{r}_1-\vec{r})d\vec{r}_1 \tag{11.2.16}$$

and constructing

$$\delta'^f(\vec{k}) = \frac{1}{N}\int n'^f(\vec{r})e^{i\vec{r}\cdot\vec{k}}d\vec{r} - \delta_{\vec{k},\vec{0}}\,, \tag{11.2.17}$$

one can easily show

$$\delta'^f(\vec{k}) = \delta^f(\vec{k}). \tag{11.2.18}$$

Now one can express $\delta^f(\vec{k})$ as:

$$\delta^f(\vec{k}) = \frac{1}{N}\int_{V_\mu} \Pi(\frac{\vec{r}}{H})\sum_i n_i^s W(\vec{r}_i - \vec{r})e^{i\vec{r}\cdot\vec{k}}d\vec{r} - \delta_{\vec{k},\vec{0}}. \tag{11.2.19}$$

The ensemble average of $\delta^f(\vec{k}_1)\delta^{f*}(\vec{k}_2)$ then reads:

$$\begin{aligned}\langle\delta^f(\vec{k}_1)\delta^{f*}(\vec{k}_2)\rangle =& \frac{1}{N^2}\int \Pi(\frac{\vec{r}_1}{H})\Pi(\frac{\vec{r}_2}{H})\sum_{i\neq j}\langle n_i^s n_j^s\rangle W(r_{i1})W(r_{j2})e^{i\vec{r}_1\cdot\vec{k}_1 - i\vec{r}_2\cdot\vec{k}_2}d\vec{r}_1 d\vec{r}_2 \\ &+ \frac{1}{N^2}\int \Pi(\frac{\vec{r}_1}{H})\Pi(\frac{\vec{r}_2}{H})\sum_i\langle n_i^s\rangle W(r_{i1})W(r_{i2})e^{i\vec{r}_1\cdot\vec{k}_1 - i\vec{r}_2\cdot\vec{k}_2}d\vec{r}_1 d\vec{r}_2 \\ &- \frac{1}{N}\int \Pi(\frac{\vec{r}_1}{H})\sum_i\langle n_i^s\rangle W(r_{i1})e^{i\vec{r}_1\cdot\vec{k}_1}\delta_{\vec{k}_2,\vec{0}}d\vec{r}_1 \\ &- \frac{1}{N}\int \Pi(\frac{\vec{r}_2}{H})\sum_i\langle n_i^s\rangle W(r_{i2})e^{-i\vec{r}_2\cdot\vec{k}_2}\delta_{\vec{k}_1,\vec{0}}d\vec{r}_2 \\ &+ \delta_{\vec{k}_1,\vec{0}}\delta_{\vec{k}_2,\vec{0}}\,,\end{aligned} \tag{11.2.20}$$

where $r_{ij} = |\vec{r}_i - \vec{r}_j|$. The FT of $\Pi(\vec{r}/H)$ is

$$\Pi(\vec{k}) = \frac{1}{V_\mu}\int_{V_\mu}\Pi(\frac{\vec{r}}{H})e^{i\vec{r}\cdot\vec{k}}d\vec{r} = \sum_{\vec{n}}\delta_{\vec{l},\vec{n}L}\,, \tag{11.2.21}$$

where L is the number of grids on each side of V_μ, and $\vec{l} = \vec{k}LH/2\pi$ and $\vec{n}$ are integer vectors. For $\vec{k}_1 \neq 0$ and $\vec{k}_2 \neq 0$, one can find:

$$\begin{aligned}\langle\delta^f(\vec{k}_1)\delta^{f*}(\vec{k}_2)\rangle = \sum_{\vec{n}_1,\vec{n}_2}& \big[S(\vec{k}_1')S(-\vec{k}_2')W(\vec{k}_1')W(-\vec{k}_2') \\ &+ W(\vec{k}_1')W(-\vec{k}_2')\sum_{\vec{k}_3'}S(\vec{k}_1' + \vec{k}_3')P(\vec{k}_3')S(-\vec{k}_2' - \vec{k}_3') \\ &+ \frac{1}{N}S(\vec{k}_1' - \vec{k}_2')W(\vec{k}_1')W(-\vec{k}_2')\big]\,,\end{aligned} \tag{11.2.22}$$

where $\vec{k}_i' = \vec{k}_i + \vec{n}_i 2\pi/H$ and $W(\vec{k})$ has the same definition as in Eq.(11.1.21). For the NGP ($p = 1$), CIC ($p = 2$) and TSC ($p = 3$) mass-assignment schemes, the $W(k)$ can be expressed by (Hockney & Eastwood 1981):

$$W(\vec{k}) = \left[\frac{\sin(\frac{H}{2}k_x)\sin(\frac{H}{2}k_y)\sin(\frac{H}{2}k_z)}{(\frac{H}{2}k_x)(\frac{H}{2}k_y)(\frac{H}{2}k_z)}\right]^p. \tag{11.2.23}$$

Because $S(\vec{k})$ peaks at $\vec{k} \approx 0$ and the selection effect is only important at small k, we obtain from Eq.(11.2.22) for $\vec{k}_1 = \vec{k}_2 = \vec{k}$:

$$\langle|\delta^f(\vec{k})|^2\rangle = S^2(\vec{k}) + \sum_{\vec{k}_3} S^2(\vec{k}_3) \sum_{\vec{n}} W^2(\vec{k} + \frac{\vec{n}2\pi}{H}) P(\vec{k} + \frac{\vec{n}2\pi}{H}) + \frac{1}{N} \sum_{\vec{n}} W^2(\vec{k} + \frac{\vec{n}2\pi}{H}) \tag{11.2.24}$$

The meaning of each term on the *rhs* of the above equation is clear. The first term and the factor of $\sum_{\vec{k}} S^2(\vec{k})$ come from the selection effect as in Eq.(11.2.9). The density convolution in the FFT introduces the $W^2(\vec{k})$ factor in both the power spectrum and the shot noise ($1/N$). The finite sampling of the convolved density field results in the summation of the 'alias' power spectrums (i.e., the sums over $\vec{n}$). The 'alias' effect is well-known in Fourier theory, but has never been taken seriously in the power spectrum analysis of large-scale clustering in observational cosmology. The effect is significant near the Nyquist wavenumber. As long as we have selected the assignment function, the shot-noise effect [the last term on the *rhs* of Eq.(11.2.24)] is easy to correct. In contrast, the second term is a little more trouble to treat, since our aim is to extract $P(k)$. Fortunately in the cosmological clustering studies, $P(k)$ is a decreasing function beyond the Nyquist wavenumber k_N. Since $W(\vec{k})$ always is a decreasing function, therefore for $|k_i| < k_N$ ($i = 1, 2, 3$) the summation in the second term is between $P(k)W^2(\vec{k})$ and $P(k)\sum_{\vec{n}} W^2(\vec{k} + \frac{\vec{n}2\pi}{H})$. As the final result, we have

$$P(\vec{k}) = \frac{\langle|\delta^f(\vec{k})|^2\rangle - |S(\vec{k})|^2 - D^2(\vec{k})}{C_1 C_2(\vec{k})}, \tag{11.2.25}$$

where

$$D^2(\vec{k}) = \frac{1}{N} \sum_{\vec{n}} W^2(\vec{k} + \frac{\vec{n}2\pi}{H}), \tag{11.2.26}$$

$$C_1 = \sum_{\vec{k}} S^2(\vec{k}) = \frac{\int_{V_\mu} S^2(\vec{r}) d\vec{r} \int_{V_\mu} d\vec{r}}{[\int_{V_\mu} S(\vec{r}) d\vec{r}]^2}, \tag{11.2.27}$$

and

$$W^2(\vec{k}) < C_2(\vec{k}) < \sum_{\vec{n}} W^2(\vec{k} + \frac{\vec{n}2\pi}{H}). \tag{11.2.28}$$

If we construct $\delta_1^f(\vec{k})$ as in Eq.(11.2.11), then we shall have

$$P(\vec{k}) = \frac{\langle | \delta_1^f(\vec{k}) |^2 \rangle - D^2(\vec{k})}{C_1 C_2(\vec{k})}, \tag{11.2.25a}$$

The inequality (11.2.28) of course is not a satisfactory formula for practical applications. The author is looking for an empirical formula for $C_2(\vec{k})$ in case of a power-law $P(k)$.

The $D^2(\vec{k})$ can be worked out for the NGP-CIC-TSC schemes which reads:

$$D^2(\vec{k}) = \frac{1}{N} C_3(\vec{k}) = \begin{cases} \frac{1}{N}, & \text{for NGP;} \\ \frac{1}{N}\Pi_{i=1,3}[1 - \frac{2}{3}\sin^2(\frac{H}{2}k_i)], & \text{for CIC;} \\ \frac{1}{N}\Pi_{i=1,3}[1 - \sin^2(\frac{H}{2}k_i) + \frac{2}{15}\sin^4(\frac{H}{2}k_i)], & \text{for TSC.} \end{cases} \tag{11.2.29a}$$

One can easily find out that the $D^2(\vec{k})$ of the CIC and TSC schemes is approximately isotropic when $k \leq k_N$, i.e.,

$$D^2(\vec{k}) \approx \begin{cases} \frac{1}{N}[1 - \frac{2}{3}\sin^2(\frac{H}{2}k)], & \text{for CIC;} \\ \frac{1}{N}[1 - \sin^2(\frac{H}{2}k) + \frac{2}{15}\sin^4(\frac{H}{2}k)], & \text{for TSC.} \end{cases} \tag{11.2.29b}$$

We have tested the equation (11.2.29) by calculating $D^2(\vec{k}) = \langle | \delta^f(\vec{k}) |^2 \rangle$ for 10 random samples. Each random sample consists of 10^5 points randomly distributed in a unit cube. The results are shown in Figure 11.1 for different mass assignment schemes by different symbols. In Figure 11.1a, we show the estimated $D^2(k)N$. The error bars are the fluctuation between the ten samples. The solid, dotted and dashed lines are the prediction of Eq.(11.2.29b) for the NGP, CIC and TSC schemes. Clearly the equation (11.2.29b) fits the simulated data very well. In Figure 11.1b, we show $D^2(\vec{k})N/C_3(\vec{k})$ estimated from the simulation. Its value is expected to be 1 from Eq.(11.2.29a). Clearly the simulation supports the equation (11.2.29).

11.3 Application to IRAS galaxies and Abell clusters

11.3.1 Observed samples

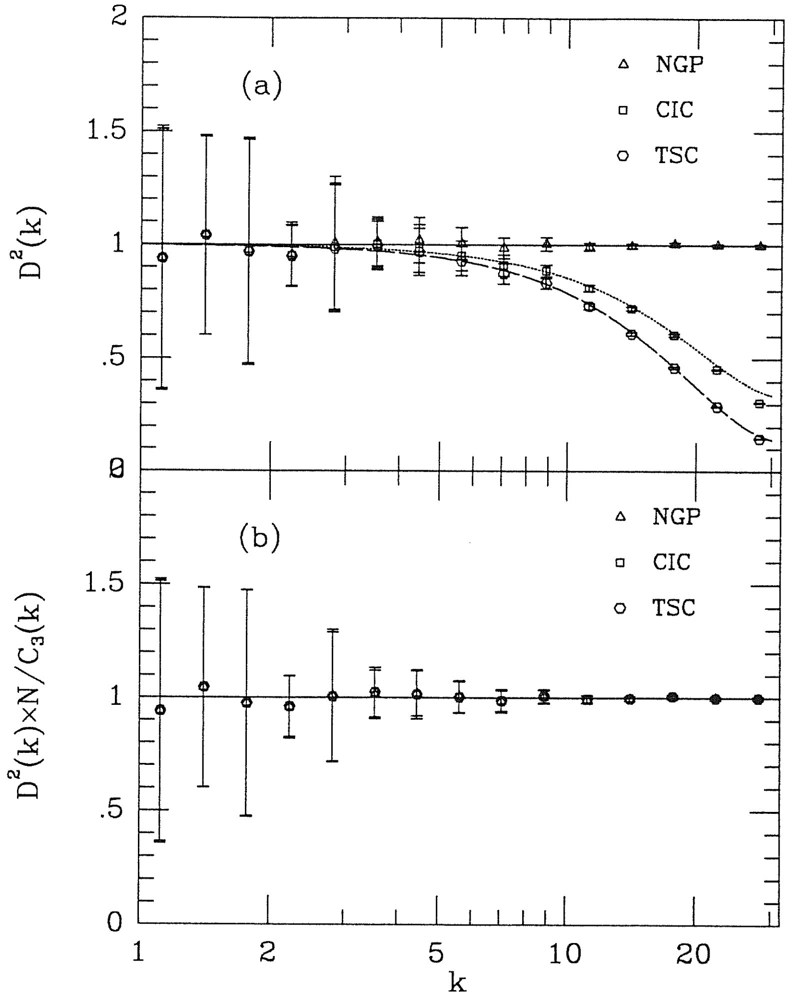

Figure 11.1 — The simulation test of the 'alias' effect on the discreteness after smoothing. *a*). The function $D^2(k)N$ plotted as a function of wavenumber k. The mean values estimated from ten random samples are represented by the symbols as indicated in the figure. Error bars are the scatters between the ten samples. Our analytical prediction is the solid line for the NGP, the dotted line for the CIC [Eq.(11.2.29b)] and the dashed line for the TSC [Eq.(11.2.29b)]; *b*). Similar to a), but the function $D^2(\vec{k})N/C_3(\vec{k})$. The analytical prediction is 1 for all mass assignment schemes.

One set of samples used here is from the 2-Jy IRAS redshift survey (kindly provided by Michael Strauss). A detailed description of the survey can be found in Strauss et al. (1990). Here we only describe how we take subsamples for our purpose. We take semi-volume-limited samples, in order to have a large fraction of galaxies kept while making the selection function reasonably broad [the later is important when obtaining Eq. (11.2.25)]. Each sample thus is characterized by two parameters V_1 and V_2: the first one limits the sample to include only those galaxies which would be bright (at 60 μm) enough to be included in the parent survey if they were put at the distance V_1; the second one simply sets an outer boundary for the sample. In this study we set $V_2 = 2V_1$. A total of three samples are selected in this way with $V_2 = 50$, 70.7 and 100 h^{-1}Mpc. They contain 1122, 1283 and 1288 galaxies respectively, and will be called 'IRAS50', 'IRAS70' and 'IRAS100' in the following discussion. The radial selection function of Yahil et al. (1991) is used in this study.

To explore the power spectrum on wavelengths of $\sim$ hundreds h^{-1}Mpc, we use redshift samples of Abell clusters. The advantages of using cluster samples to study large-scale clustering have been emphasized by a number of authors (e.g., Bahcall 1988; Postman et al. 1992). We take two samples for our analysis from the two largest redshift surveys of Abell clusters (Huchra et al. 1990a; Postman et al. 1992). The first sample (called 'MR1650') includes 257 clusters of richness $R \geq 0$ in the region $\delta \geq -27.5°$ and $|b| \geq 30°$ with the tenth brightest magnitude $m_{10} \leq 16.5$ and redshift $z \leq 0.1$. The second sample (called 'Deep') contains 131 clusters of $R \geq 0$ in the region $58° \leq \delta \leq 78°$ and $10^h \leq \alpha \leq 15^h$ with distance class $D \leq 6$ and $0.06 \leq z \leq 0.24$. The galactic latitude selection function Eq.(6.3) is used in this study (Bahcall & Soneira 1983; Postman et al. 1992).

We determine radial selection functions for the cluster samples by plotting their density distributions against redshift. In Figure 11.2, we present the comoving number density as a function of redshift. The density is calculated in shells of width Δz_s at redshift intervals of Δz_i. For the MR1650 sample, $\Delta z_s = 0.01$ and $\Delta z_i = 0.005$; for the Deep sample, $\Delta z_s = 0.02$ and $\Delta z_i = 0.01$. The 50% overlapping in the shell bins is to smooth out fluctuations arising from small-scale clustering. Because the tenth brightest members of Abell clusters have a narrow range of absolute magnitude (e.g., Postman et al. 1985)

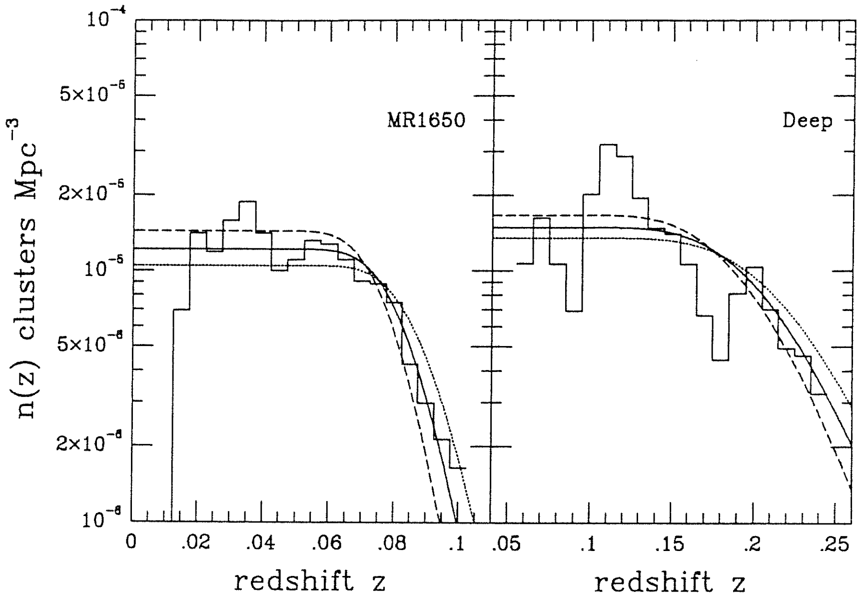

Figure 10.2 — The spatial density distribution of Abell clusters as a function of redshift. Bins are 50% overlapping. The solid lines are the radial selection functions used in the paper. The dotted and dashed lines are trial functions which are used to test robustness of final results to the radial selection functions. The left panel is for the MR1650 sample, and the right one for the Deep sample.

and the samples used here are m_{10}-limited, we expect the mean number density to be a constant at small redshift and fall rapidly at large redshift. The smooth solid lines in Figure 11.2 should reasonably represent the redshift selection functions of the two samples. Some peaks and valleys in the density distributions relative to the selection functions could come mostly from strong superclustering. For example, the huge void shown in the pie-diagram of Huchra et al. (1990a, Figure 5b in their paper) results in the low density of the Deep sample at $z \sim 0.16$, while the wall around the void produces the high peaks at $z \sim 0.12$ and $z \sim 0.19$. Since the MR1650 sample has a larger sky coverage and a larger sample size than the Deep sample, its density distribution is much smoother. In order to test how our results are sensitive to the selection functions, we repeat our analyses using two other functions which are shown in the figure by dotted and dashed lines. We found that the power spectra are quite insensitive to these changes.

In this Chapter, comoving coordinates are used with distances to objects (IRAS galaxies and Abell clusters) calculated from redshift using Eq.(6.1).

11.3.2 Simulations

In order to test the estimation procedures given in §11.2, we apply them to simulations. The simulation samples are the ensembles Z14 and P21 of Plionis, Valdarnini & Jing (1992) [Chapter 10]. These samples are generated by the Zel'dovich approximation in $640^3(h^{-1}\mathrm{Mpc})^3$ cubes, and the P21 set selects only high density peaks. For the simulation algorithms, see the last chapter. Here we only summarize those relevant to our following analysis.

Each ensemble contains 50 samples and each sample has about 13,000 objects. The simulations have power-law two-point correlation functions $\xi(r) \approx (r_0/r)^{1.8}$ in the range of r between 7 and 70 h^{-1}Mpc. The P21 set has $r_0 \approx 21\,h^{-1}$Mpc and the Z14 has $r_0 \approx 14\,h^{-1}$Mpc. Since the Zel'dovich approximation gives a non-vanishing three-point correlation ζ (see, e.g., Peebles 1980; Lucchin, Matarrese, & Vittorio 1988; Coles & Frenk 1991), we have examined ζ for the simulations. The ζ of the simulated objects is approximately hierarchical with the coefficient Q about 0.6, similar to the observations (e.g., Peebles 1980; Jing, Mo, & Börner 1991 for spiral galaxies; Jing & Valdarnini 1991 for $R \geq 0$ clusters). Thus, the P21 set has clustering properties similar to the $R \geq 0$ clusters, as far as low-order clustering is concerned. In order to compare with the IRAS samples, we scale the Z14 box by a factor 3.2, i.e., the box size is $\sim 200\,h^{-1}$Mpc and the clustering length r_0 becomes $\sim 4.4\,h^{-1}$Mpc (similar to the r_0 of IRAS galaxies). Finally, we select our simulated IRAS samples from the scaled Z14 ensemble and our simulated cluster samples from the P21 ensemble, by applying the boundaries and selection effects of §11.3.1 to the simulations, thus mimicking the observed samples. The simulated samples have the same number of objects as the observed ones.

Therefore, these simulated samples have the same boundaries, selection effects and similar low-order clustering properties as the observed ones.

11.3.3 Results

We present the results in terms of the variance. Ten equal logarithmic intervals of $\log_{10} k_i - \log_{10} k_{i-1} = \Delta \log_{10} k = 0.15$ $(i = 1, 2, \cdots, 10)$ were taken for k starting at $k_0 = 2\pi / V_u^{1/3}$. In this chapter, we used the NGP scheme and 64^3 grids for the FFT. We used Eq.(11.2.25a) with $C_2(\vec{k}) = W^2(\vec{k})$ as our working formula. [Since the results presented in this section had been obtained before the author carefully checked the 'alias' effect (§11.2), like all the previous studies, $C_2(\vec{k}) = W^2(\vec{k})$ was used at that time. As shown in §11.2, the $C_2(\vec{k})$ is still uncertain and taking $C_2(\vec{k}) = W^2(\vec{k})$ in the NGP case may overestimate the $\Delta^2(\vec{k})$ up to a factor 2 at $k = k_N$ but much less at the smaller k. Since the results presented below are mainly at $k \ll k_N$, we expect that the uncertainty arising from the $C_2(\vec{k})$ is tiny. To assure this statement, we tried another extreme limit $C_2(\vec{k}) = 1$, and we found that the final result is still represented by Eq.(11.3.1) only with the constants 1.3 and 2.7 replaced by 1.2 and 2.8. The correct reproduction of $\xi(r)$ from the estimated $P(k)$ (§11.4) further shows that the uncertainty induced by the $C_2(\vec{k})$ must be small.]

a) Simulation tests and sampling error

We first show our simulation tests in Figure 11.3. As examples, we have chosen the samples which are selected according to the selection functions of DR1650 and of IRAS70. (The results of the simulated Deep samples are qualitatively similar to those of DR1650; and the results of the other two simulated IRAS samples are similar to those of IRAS70.) The filled symbols represent the mean variances of the simulated samples of each ensemble, and the error bars are the 1σ scatter between the 50 samples. For comparison, we have also analysed the simulations before subjecting them to any observed selection effects (i.e., uniformly surveyed in cubic volumes), and we show them in the figure by open symbols (no error bars are given, since they are smaller than those plotted). The good agreement of the variances between the samples before and after introducing the selection effect means that the procedures given in §11.2 are very successful.

The derivation of Eq. (11.2.25) is based on the assumption that the sample is fair, or more precisely the correlation ξ_{c-s} between clustering and selection function is weak. Of course, the simulated samples satisfy this condition. As for the observed samples, since

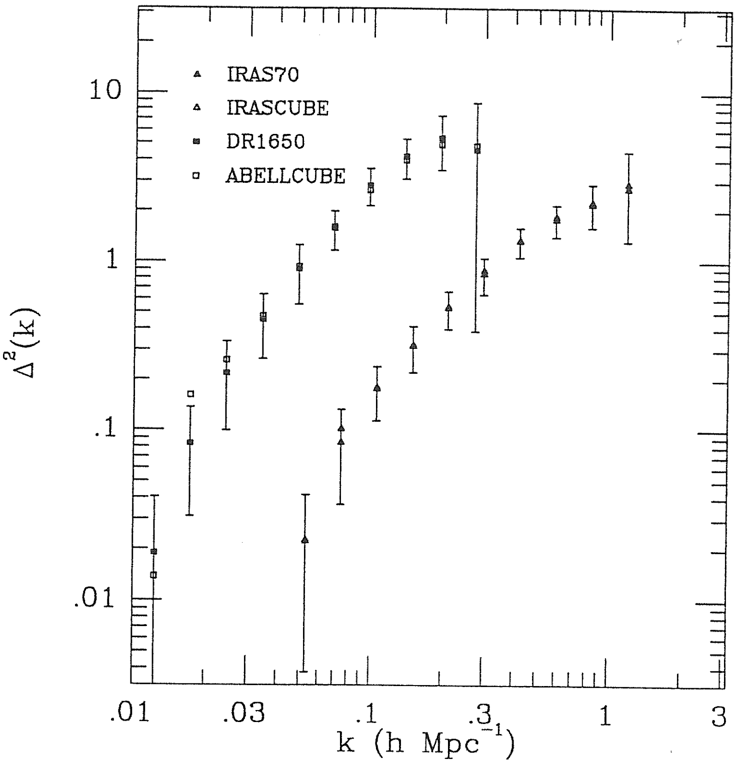

Figure 10.3 — The variances of the simulations as a function of wavenumber. The filled squares and the filled triangles are for the simulated samples of DR1650 and of IRAS70 respectively; the open squares and the open triangles are for the simulations of Abell clusters and of IRAS galaxies without any selection effect. The error bars are the 1σ scatters between the 50 simulated samples with the selection effects.

the selection function used for the IRAS samples is derived by the clustering-independent techniques (Yahil et al. 1991), and the volume-limiting at $r < V_1$ has minimized the effect of the local supercluster, the ξ_{c-s} should be reasonably weak. As shown by Plionis & Valdarnini (1991) and Scaramella, Vettolani & Zamorani (1991), the dipole anisotropy in the cluster distribution converges at $r \sim 150\,h^{-1}$Mpc, implying that the DR1650 is nearly fair. Therefore, we expect that Eq. (11.2.25) can be applied to the observed samples.

Some accidental correlation ξ_{c-s} may remain between clustering and selection functions. To show this, let us consider the IRAS samples. The Local Supercluster gives a positive ξ_{c-s}, and the Local Void and other distant superclusters would give a negative

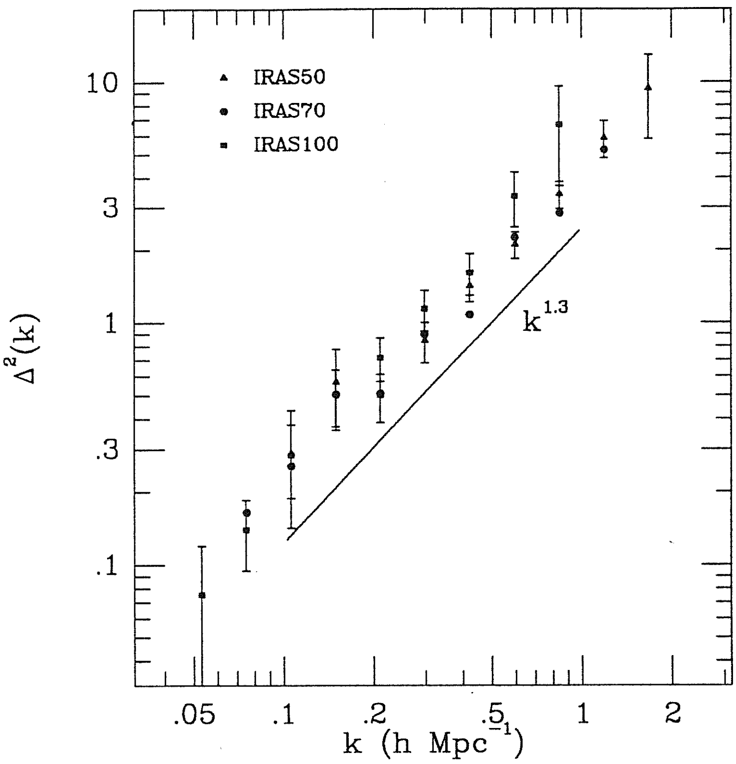

Figure 10.4 — The variances of three IRAS samples as a function of wavenumber. One symbol represents the results of one sample as indicated in the figure. The solid line is a power law $\propto k^{1.3}$.

contribution to ξ_{c-s} [see the comprehensive discussion of Strauss et al. (1992a) on the IRAS galaxy distribution]. The overall ξ_{c-s} may not be strong, but must fluctuate and would introduce uncertainty in the statistics. Since the available samples at best have just approached 'fairness', clustering fluctuations must exist between samples. Furthermore, a finite number of objects in each sample would further introduce uncertainty in our statistics. These stochastic uncertainties are difficult to distinguish in practice, and will together be called 'sampling error' for short. In this work, we estimate the sampling error by analysing a set of 50 simulated samples.

b) Results from the observed samples

Figure 11.4 shows the variance as a function of wavenumber k for the three IRAS samples. We have neglected the values of the first bin (i.e., $i = 1$), since their sampling

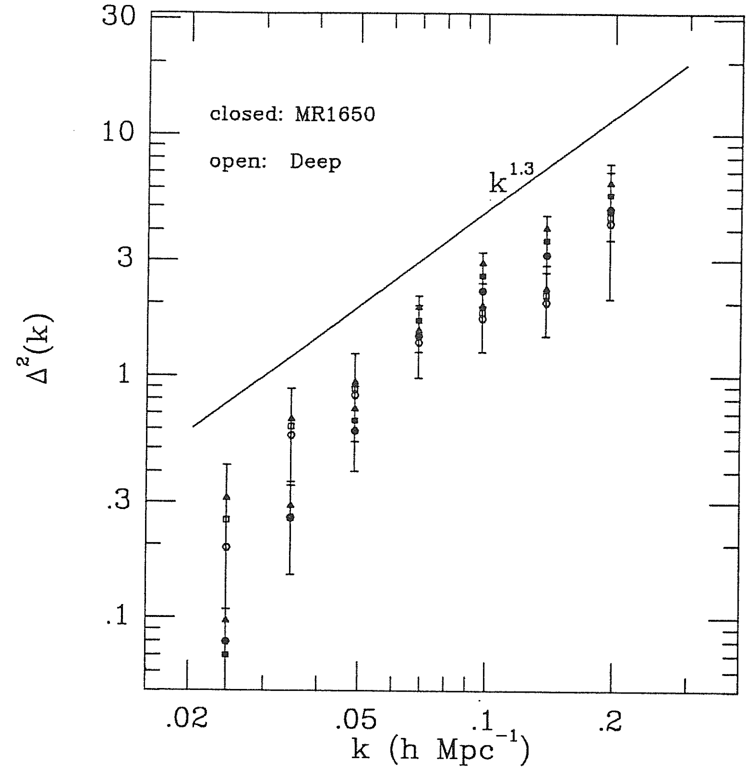

Figure 11.5 — The variances of Abell cluster samples as a function of wavenumber. The closed symbols are for the MR1650 sample, and the open ones for the Deep. The squares represent the results when the solid lines in Figure 11.2 are used as the radial selection functions, and the triangles and hexagons represent those when the dotted and dashed lines are used. The solid line is a power law $\propto k^{1.3}$.

errors, as shown by our simulation, exceed 50%. Different symbols are used for different samples as indicated in the figure. The error bars plotted are the sampling errors estimated from the simulations. For clarity and also because of the slight overlapping (1/3 objects in common) of IRAS100 and IRAS50 samples, we have only plotted sampling errors for these two samples. Within the sampling errors, the results of the three samples are in good agreement. Although we note a systematically higher variance $\Delta^2(k)$ in the IRAS100 sample at $k \geq 0.2\,h\,\mathrm{Mpc}^{-1}$, typically 20% fluctuations between samples in the simulations render this difference not statistically significant. For all three samples, the $\Delta^2(k)$ are well described by a power law $\Delta^2(k) \propto k^{1.3}$.

In Figure 11.5, we plot our estimated variance $\Delta^2(k)$ of Abell clusters. Again, we only plot those k bins with sampling errors less than $\sim 50\%$. The closed symbols are for the DR1650 sample, and the open ones for the Deep sample. The squares represent the results calculated when the solid lines in Figure 11.2 are used as the radial selection functions. The error bars have the same meaning as in Figure 11.4, and are plotted only for the results represented by the squares. Within the error bars, the variances of the two samples accord reasonably well. We have noted that the $\Delta^2(k)$ values of the Deep sample at $k \sim 0.03\,h\,\mathrm{Mpc}^{-1}$ ($\lambda \sim 200\,h^{-1}\mathrm{Mpc}$) are higher than those of the DR1650 (though within the sampling errors), which could reflect the fact that the Deep sample is dominated by the large void of this size [see §11.3.1 and Figure 5b of Huchra et al. (1990)]. At $k > 0.06\,h\,\mathrm{Mpc}^{-1}$, the variances $\Delta^2(k)$ of both samples are approximately a power law $\Delta^2(k) \propto k^\gamma$ with $\gamma \sim 1.3$; at the smaller wavenumbers, the $\Delta^2(k)$ of the DR6150 falls more rapidly with decreasing k [the 'break' is near $k \sim 0.05\,h\,\mathrm{Mpc}^{-1}$ or $\lambda \sim 130\,h^{-1}\mathrm{Mpc}$], while that of the Deep retains a power law form. The lack of an obvious break in the Deep is probably due to the large void in the sample.

The results for Abell clusters only change slightly when one reasonably alters the radial selection functions. To show this, in Figure 11.5 we also give the variances $\Delta^2(k)$ which are calculated using different functions. The triangles in the figure represent the results when the dotted lines of Figure 11.2 are used, and the hexagons represent those when the dashed ones are used. One can see from the figure that the results are quite robust. We have done similar analyses for $R > 0$ clusters only. For both samples, we have found no significant difference in the power spectrum between $R > 0$ and $R \geq 0$ clusters, in accordance with the correlation function analysis of Postman et al.(1992) on these samples.

In Figure 11.6, we show the variances $\Delta^2(k)$ averaged for the three IRAS samples and for the two Abell samples. The averages and error bars are estimated with weights proportional to the number of objects in each sample. The $\Delta^2(k)$ of clusters has been scaled down vertically by a factor of 10 in the figure. The error bars are comparable with the typical sampling errors of simulated samples. It is interesting to note that in the overlap k region explored by galaxy and cluster samples, their variances $\Delta^2(k)$ have the

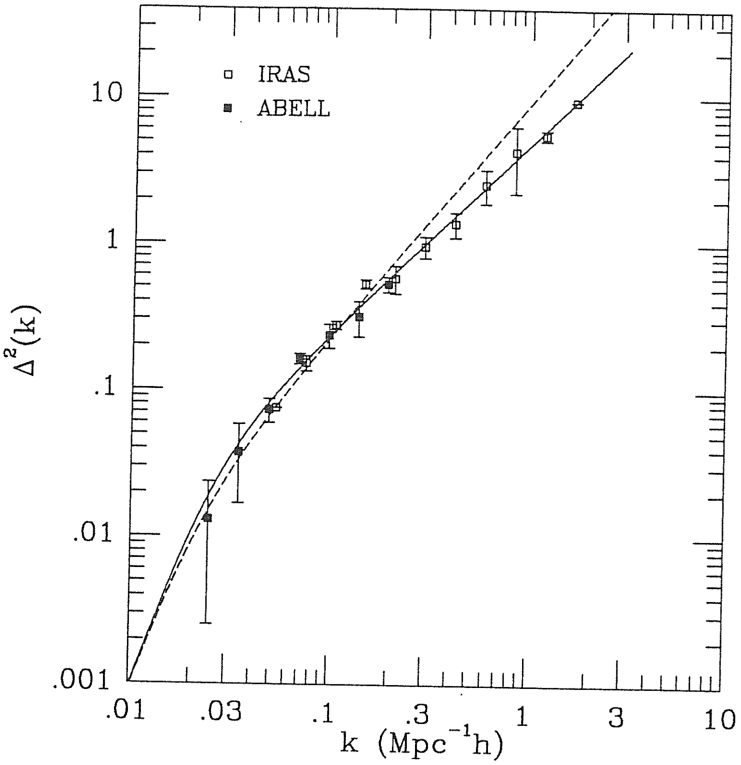

Figure 11.6 — The averaged variances of the three IRAS samples and of the two cluster samples. The values of clusters have been scaled down vertically by a factor of 10. The solid line represents Eq. (11.3.1) in the text. The dashed line is the power spectrum obtained by Peacock (1991) from his fitting to the APM angular two-point correlation function.

same shapes but different amplitudes, supporting the 'linear' biasing mechanism as the origin of rich clusters (e.g., Kaiser 1984). Based on this fact, we are able to combine the two datasets together and study the power spectrum over a wide range of scales. Adopting a similar formula as in Peacock (1991), we find that the data in Figure 11.6 is well fit by

$$\Delta^2(k) = \frac{(k/0.3)^{1.3}}{[1+(k/0.025)^{-2.7}]}, \tag{11.3.1}$$

where k is in $h\,\mathrm{Mpc}^{-1}$. Note the formula is consistent with the idea of a scale-invariant power spectrum ($\Delta^2(k) \propto k^4$ for small k).

11.4. Comparison with other observations

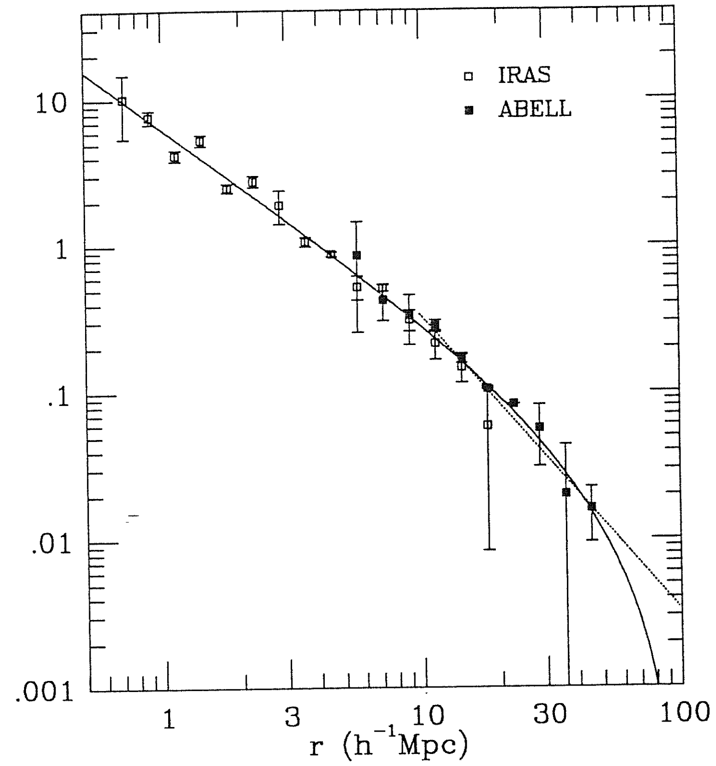

Figure 11.7 — The two-point correlation function of the three IRAS samples and of the two cluster samples. The values of clusters have been scaled down vertically by a factor of 10. The solid line represents the prediction from the variance of Eq. (11.3.1). The dotted line is the power law $(18/r)^2$ scaled down by a factor of 10.

First we would like to stress that all the analysis in §11.3 for the observed samples has been done in redshift space, and the power spectrum obtained above therefore only represents that in redshift space. Peculiar velocities (e.g., Kaiser 1987) distort the spatial distribution of galaxies in redshift space. The 'Finger-of-God' effect smears clustering on small scales, and coherent peculiar velocities on large scales, on the other hand, amplify clustering by a constant factor, i.e.,

$$\Delta^2(\text{Red. Spa.}) = [1 + \frac{2}{3}\frac{\Omega^{0.6}}{b} + \frac{1}{5}\frac{\Omega^{1.2}}{b^2}]\Delta^2(\text{Real Spa.}), \qquad (11.4.1)$$

where b is the biasing factor of galaxies. Both effects make the variance $\Delta^2(k)$ (if $\propto k^\gamma$) in redshift space have a much flatter slope (smaller γ) than that in real space.

Given the variance $\Delta^2(k)$, we can predict the correlation function $\xi(r)$ in redshift space by Eq.(11.1.13). In Figure 11.7, the solid line is the $\xi(r)$ predicted from the variance of Eq.(11.3.1). We also directly analysed the two-point correlation function for each sample by counting pairs, and we averaged the results as we did for the $P(k)$. The final results are shown in the figure, with the $\xi(r)$ of clusters scaled down again by a factor of 10. It is encouraging that the predicted $\xi(r)$ agrees very well with the estimated one, further showing that the method given in §11.2 is correct. Using the selection functions (the solid) given in Figure 11.2, we found no meaningful residual correlation on $r > 50\,h^{-1}$Mpc, which might mean that the selection functions are the proper ones. Our estimated $\xi(r)$ are consistent with Strauss et al. (1992a) on the IRAS survey and with Postman et al. (1992) on the Abell samples.

In Figure 11.6, we also plot the power spectrum (scaled down by a factor 1.5) obtained by Peacock (1991) from his fitting to the angular two-point correlation function $\omega(\theta)$ of the APM survey (Maddox et al. 1990a). It is very encouraging that his spectrum overlaps ours on large scales. The difference shown on small scales could be attributed to the redshift distortion. Therefore our result is consistent with the $\omega(\theta)$ of the APM survey. In principle, from this comparison we can extract the biasing factor of optical galaxies relative to IRAS ones, but uncertainties in the clustering evolution and in the conversion of $\xi(r)$ to $\omega(\theta)$ prohibit us getting a meaningful value.

The DR1650 sample strongly suggests a 'break' at $k \sim 0.05\,h\,\mathrm{Mpc}^{-1}$ in the power spectrum. The averaged results of the two cluster samples also show this tendency. It might be wise not to put too much confidence in the 'break' from this *single* study. However, independent studies of the APM survey and the radio galaxy survey have revealed the 'break' on similar scales (Peacock 1991). The cross-correlation analysis of IRAS galaxies, Abell clusters and radio galaxies (Mo et al. 1992) also suggests a similar bend scale. Combining all these results, we can be much more assured of the existence of this 'break'. Because of the great importance of the 'break', large redshift surveys with wide sky coverage and depth of $z \sim 0.2$ are needed to set it more conclusively.

The existence of the 'break' at $k \sim 0.05\,h\,\mathrm{Mpc}^{-1}$ is also needed to interpret the two-point correlation function $\xi_{cc}(r)$ of rich clusters. The dotted line showed in Figure 11.7 is a power law $(18\,h^{-1}\mathrm{Mpc}/r)^2$ scaled down by a factor 10. Clearly it is a good approximation to the numerical integration [Eq.(11.1.13)] as well as to the observational data on the range of $r = 10$ to $50\,h^{-1}$Mpc. If there were no such 'break', the correlation function would be a power law $\propto r^{-1.3}$ which can hardly be consistent with the observations. Because of the 'break', $\xi_{cc}(r)$ falls off very rapidly at $r \sim 50\,h^{-1}$Mpc. It's perhaps the reason why $\xi_{cc}(r)$ has not clearly been detected on $r > 50\,h^{-1}$Mpc. We also note the predicted correlation function [Eq.(11.1.13)] has a shape similar to the $\xi_{cc}(r)$ of clusters automatically selected from the APM and COSMOS surveys (Dalton et al. 1992; Nichol et al. 1992).

The above discussions have shown that Eq.(11.3.1) is consistent with all the available two-point correlation functions of galaxies, clusters, radio galaxies etc., only if appropriate biasing factors are used for these objects. These comparisons are relatively direct because they are done in coordinate space. Now we are going to compare the derived power spectrum with the CBR anisotropy, peculiar velocities and acceleration dipoles, therefore we make the following assumptions:

1. The universe is flat;
2. All the structures and peculiar velocities are induced by the gravitational instability, so Eq.(11.1.26) applies;
3. The primeval density fluctuation is adiabatic and of Gaussian type;
4. The 'linear' biasing mechanism is adequate on the scales of interest.

First we would like to point out that the scale-invariance of Eq.(11.3.1) at large wavelengths is supported by the recent COBE observation of structure in the CBR (Smoot et al. 1992). The Sachs-Wolfe effect (§11.1.8) predicts a quadrupole $Q = 1.1 \times 10^{-5}$ in the CBR if the matter distribution has the power spectrum of Eq.(11.3.1). However as pointed out previously, Eq.(11.3.1) only represents the IRAS galaxy distribution in redshift space. Both the redshift distortion Eq.(11.4.1) and possible biasing of IRAS galaxies have amplified the spectrum Eq.(11.3.1) relative to the matter distribution. Taking these factors into account, we find that the variance of Eq.(11.3.1) with a biasing factor $b_I = 1.5$ for IRAS galaxies can correctly produce the COBE quadrupole $Q = 6 \times 10^{-6}$. The biasing value is quite reasonable.

With the variance normalized to fit the COBE result, we can predict peculiar velocities and dipoles. Using $R = 5\,h^{-1}$Mpc for the LG, we find the predicted *rms* value of the peculiar velocity [Eq.(11.1.27)] is about $500\,\mathrm{kms}^{-1}$, comparable with the observed value $600\,\mathrm{kms}^{-1}$. The difference $100\,\mathrm{kms}^{-1}$ is not unexpected, since an individual velocity generally deviates from its *rms* value and since the PDF [Eq.(11.1.29)] is rather broad (see §11.1.5). In Figure 11.8a, we use a solid line to show the predicted *rms* value for our local bulk motion velocity [Eq.(11.1.33)]. The dashed lines gives the upper and lower limits at 95% confidence level [Eq.(11.1.34)]. The filled squares are the observational results derived by Bertschinger et al.(1990). In Figure 11.8b, we show the predicted acceleration dipoles (§11.1.7) with a comparison with the observational data from the QDOT survey (Rowan-Robinson et al. 1990). The lines in the figure have the same meaning as in Figure 11.8a, and the biasing factor $b_I = 1.5$ is used for IRAS galaxies. Clearly the local peculiar velocities and the acceleration dipoles are very consistent with the observed power spectrum.

Another point we noted is the slope of the $\Delta^2(k)$ around the scale of rich clusters (i.e., around $k \sim 0.3\,h\,\mathrm{Mpc}^{-1}$) which is about 1.3. The shape of $\Delta^2(k)$ on this scale should be little altered by peculiar motions. It is interesting to note that this slope is in perfect agreement with the measurements from the cluster x-ray temperature function (Henry & Arnaud, 1991) and the cluster x-ray luminosity function (Henry et al. 1992).

Now let's summarize our main results of this chapter.

1. We have carefully examined the method of the power spectrum analysis, and found that the 'alias' effect is important especially in the high-order assignment schemes. This effect has never been considered in the previous works on estimating the power spectrum either in observed samples or in N-body simulations.
2. We have measured the power spectra of IRAS galaxies and of Abell clusters by analysing the 2-Jy redshift survey and two redshift samples of Abell clusters. In terms of the variance $\Delta^2(k)$, we find that the $\Delta^2(k)$ of IRAS galaxies obeys a power law $\Delta^2(k) \propto k^{1.3}$ up to the largest possible wavelength $\lambda = 2\pi/k \sim 100\,h^{-1}$Mpc which the survey is able to explore. The $\Delta^2(k)$ of Abell clusters has the same slope as that of IRAS galaxies for $\lambda < 100\,h^{-1}$Mpc but has an amplitude about 10 times higher, which supports the linear biasing mechanism as the origin of rich clusters. At larger

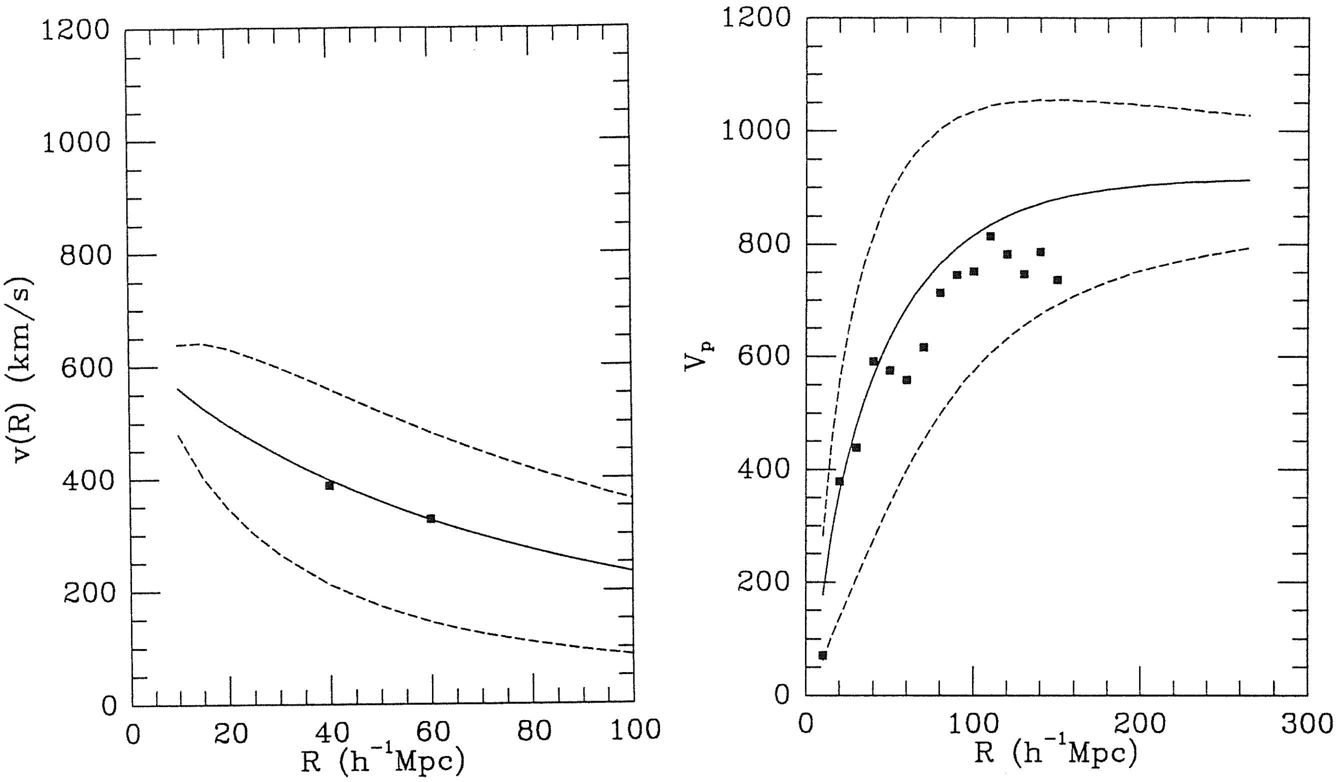

Figure 11.8 — *a*). The peculiar velocity of a sphere of radius R. The solid line is the mean value predicted from the variance Eq.(11.3.1). The dashed lines are theoretical predictions at the 95% confidence level. The squares are the observed values of Bertschinger et al. (1990); *b*). Similar to a), but for the peculiar velocity induced by a sphere of radius R. The observed values are from Rowan-Robinson et al. (1990) and a biasing factor $b_I = 1.5$ is assumed for IRAS galaxies.

wavelengths, the variance of Abell clusters falls more rapidly than the power law. Under the 'linear' biasing assumption, the $\Delta^2(k)$ of IRAS galaxies is well expressed by Eq.(11.3.1). The fitting formula is taken to be scale-invariant at large wavelength, which is supported by the recent COBE DMR observation as well as inflation theories.

3. The observed variance is consistent with all the available two-point correlation functions of galaxies, clusters and radio galaxies. In a flat universe with primordial adiabatic Gaussian fluctuations, the above variance with a biasing factor 1.5 for IRAS galaxies can reproduce the temperature quadrupole $Q = 6 \times 10^{-6}$ observed in the

COBE experiment by the Sachs-Wolfe effect and can account for the peculiar velocity of the LG, the local bulk motions and the acceleration dipoles. These good agreements on one hand support the gravitational instability theory of galaxy formation, and on the other hand suggest that the functional form $\Delta^2(k)$ of Eq.(11.3.1) does approximately describe the truth.

4. Compared with the standard CDM or HDM models, the above results suggest one economical modification in these flat models, i.e., the transfer function. Altering the constitution of the Universe amounts to modifying the transfer function. A hybrid model with both CDM and HDM might solve problems in the standard CDM or/and HDM models. The author is working in this direction.
5. We have not considered open cosmological models in this chapter. It appears that a cosmological constant dominated flat CDM model can also account for all observations listed above.

‡Part of the materials presented in this chapter is based on our paper: Jing, Y.P. & Valdarnini, R. 1992, *The Astrophysical Journal*, (accepted).

An outlook

In the future, many problems considered here will be further clarified with the advent of a new generation of observational catalogues. Several large deep machine-scanned surveys, such as the APM, COSMOS and POSS II surveys, are near completion. Several subsamples of bright galaxies extracted from these surveys are under further observations, in order to obtain morphology classification and galaxy redshifts. There also are great international efforts on completion of large redshift surveys of Zwicky, UGC and ESO/Uppsala galaxies. Fermilab/Chicago/Princeton are going to launch a new project to construct a digitalized survey of $\sim 10^2$ million galaxies brighter than $m_J \approx 22$ in $\sim \pi$ steradians of the northern sky. Morphology classification and redshift will be observed for a subsample of ~ 1 million galaxies of $m_J \leq 19$. Cluster catalogues are being constructed by applying objective finding algorithms to the deep digital sky surveys and the ROSAT x-ray survey will result in a catalogue of x-ray bright clusters. With these surveys, nearly all topics presented here are expected to be addressed much more accurately in the next decade.

According to most popular models of galaxy formation, the anisotropy $\Delta T/T$ on small angular scales $\theta < 1^\circ$ is near the current detection sensitivities of several telescopes if the COBE result is right. Detection or much smaller upper limits of $\Delta T/T$ on $\theta < 1^\circ$ would tell us much about the early Universe. There are other observations, such as surveys of the Ly-α forest, of quasars, etc., which will also help us understand the large scale structures.

With the increase of computational capability, the model research is also prospective. Large N-body simulations with good resolutions are being run. Several hydrodynamical codes have been included in the pure gravitational N-body codes. Physical processes of galaxy formation, such as the 'biasing mechanism', are expected to be better understood with such simulations. Comparisons between theories and observations will thus be made more properly. Our knowledge of the origin and evolution of the LSS will be greatly enhanced by the model studies.

Although the standard CDM, HDM and baryon dominated models do not appear to work perfectly, the analysis in Chapter 11 shows that all observations are consistent within the gravitational instability frame and Big-bang cosmology. Several modifications suggested in §1.5 may improve theoretical confrontations with the observations. Via N-body simulation, we have recently studied the large scale structures observed in the CDM ($\Omega_{CDM} \approx 0.7$) plus HDM ($\Omega_{HDM} \approx 0.3$) dominated universe (Jing, Mo & Börner, in preparation). All other model parameters are similar to those of the standard CDM model. From the results obtained up to now, we found that the model is in good agreement with observations, including the two-point correlation of galaxies, two-point correlation function of rich clusters, count-in-cell statistics of the QDOT survey, and the COBE quadrupole. I hope that these results will be presented when I defend the thesis.

Observational and model studies are endless and I have to end the thesis now.

Appendix

In this Appendix, we shall discuss the moment method to calculate the 3–point correlation function. Three-dimensional and two-dimensional cases are discussed separately. Some specific parameters, if appear, are used in §7.4 and §7.5, since the appendix is specially designed to understand the contents there.

A. Three-dimensional case

Let us consider a fair sample made of $\mathcal{N}$ objects distributed in a given volume $\mathcal{V}$. Around each object we center spheres of radii r_k. Let δr_k be the thickness of the shell between the $(k-1)$-th and the k-th sphere and N_{jk} be the number of neighbours of the j-th object in the shell. We shall then take the average of N_{jk}, made over the $\mathcal{N}$ possible j's, $N_k = \langle N_{jk} \rangle_j$.

Afterwards, we generate an artificial sample of $\bar{\mathcal{N}} >> \mathcal{N}$ objects, distributed in the same volume $\mathcal{V}$ with the same selection effects as the original sample.

Then let $\bar{N}_k = (\mathcal{N}/\bar{\mathcal{N}})\langle \bar{N}_{kj} \rangle_j$. Here $\bar{N}_{jk}$ is the number of *random* neighbours of the j-th object in the shell k [let us draw attention to the normalization factor $(\mathcal{N}/\bar{\mathcal{N}})$].

The 2–point function $\xi(r_k) = \xi_k$ can then be defined according to

$$N_k = \bar{N}_k[1 + K(\delta_k)\xi_k] \qquad (A.1)$$

where $\delta_k = \delta r_k / r_k$.

Here, assuming

$$\xi(r) \ = \ (r_{cc}/r)^\gamma, \qquad (A.2)$$

we have

$$K(\delta) \ = \ K_{\gamma,\delta} \ = \ \frac{3}{\gamma_3}\frac{1-(1-\delta)^{\gamma_3}}{1-(1-\delta)^3} \qquad (A.3)$$

where

$$\gamma_i = i - \gamma. \qquad (A.4)$$

Among the central moments

$$S_k^{(m)} = \langle (N_{kj} - N_k)^m \rangle_j \tag{A.5}$$

providing information on the $(m+1)$–point function, we shall consider, in particular,

$$S_k^{(2)} = \langle N_{kj}^2 \rangle_j - N_k^2 . \tag{A.6}$$

Let us then consider the joint expected numbers of objects in δV_1 and δV_2 at distances r_{01} and r_{02} from real objects

$$\langle \delta N_1 \delta N_2 \rangle = \delta \bar{N}_1 \delta \bar{N}_2 (1 + \xi_1 + \xi_2 + \xi_{12} + \zeta_{012}), \tag{A.7}$$

which depends on the connected 3-point function ζ. [In (A.7) and hereafter $\xi_i = \xi(r_{0i})$ while $\delta \bar{N}_1$ and $\delta \bar{N}_2$ are the (normalized) numbers of random objects in δV_1 and δV_2.]

We shall consider here two alternative expressions for ζ_{012} :

$$\zeta_{012} = Q(\xi_1 \xi_2 + \xi_1 \xi_{12} + \xi_2 \xi_{12}) \ , \tag{hm}$$

$$\zeta_{012} = \tilde{Q}(\xi_1 \xi_2 + \xi_1 \xi_{12} + \xi_2 \xi_{12} + \xi_1 \xi_2 \xi_{12}) \ , \tag{ks}$$

Here *hm* stands for *hierarchical model* and *ks* for *Kirkwood superposition.* The former expression does not actually follow from the requirement of hierarchical clustering (bottom–up scenarios), but is fully coherent with it. The latter expression, first introduced by Kirkwood in the study of gases, expresses a limiting case in the framework of *biased* theories of galaxy formation; it should then also be $\tilde{Q} = 1$.

Let us then integrate (A.7) over $\mathbf{r}_1$ and $\mathbf{r}_2$ in the k-th shell. The result is to be corrected to subtract the effect of the *overlapped* physical objects. This leads to the relation

$$S_k^{(2)} - N_k = \bar{N}_k^2 \{ J_{\gamma,\delta_k} \xi_k + [(Q-1) K_{\gamma,\delta_k}^2 + 2Q \tilde{K}_{\gamma,\delta_k}] \xi_k^2 \} \tag{A.8}$$

holding for *hm*. Here

$$\begin{aligned} J_{\gamma,\delta} =& \frac{1}{8(1-\delta+\delta^2/3)^2} \frac{1}{\gamma_3 \gamma_4} \left\{ \frac{2^{\gamma_6} - 2(2-\delta)^{\gamma_6} + [2(1-\delta)]^{\gamma_6}}{\delta^2 \gamma_6} \right. \\ & \left. - \frac{8\delta^{\gamma_2}}{\gamma_2} (1 - \delta + \delta^2 \gamma_6) + 2(2-\delta)^{\gamma_4} \gamma_2 \right\} . \end{aligned} \tag{A.9}$$

and

$$\begin{aligned}\tilde{K}(\gamma,\delta) =& \frac{1}{\gamma_2\gamma_3}\frac{1}{2\left(1-\delta+\frac{\delta^2}{3}\right)^2}\int_0^1 dx(1-x\delta)^{\gamma_1} \\ &\times\left[2^{\gamma_3}\frac{\left(1-\frac{x}{2}\delta\right)^{\gamma_3}-\left(1-\frac{x+1}{2}\delta\right)^{\gamma_3}}{\delta}-\frac{2^{\gamma_4}}{\gamma_4}\frac{\left(1-\frac{x}{2}\delta\right)^{\gamma_4}-(1-x+12\delta)^{\gamma_4}}{\delta}+\right. \\ &+2^{\gamma_3}\left(1-\frac{x+1}{2}\delta\right)^{\gamma_3}-\delta^{\gamma_2}\left((1-x)^{\gamma_3}+x^{\gamma_3}\right) \\ &\left.+\delta^{\gamma_3}\left((1-x)^{\gamma_3}+\frac{x^{\gamma_4}-(1-x)^{\gamma_4}}{\gamma_4}\right)\right].\end{aligned} \qquad (A.10)$$

Then, according to (A.6) and (A.8),

$$Q = \frac{1}{c_1(\delta,\gamma)}\left[\frac{S_k^{(2)}-N_k}{(N_k-\bar{N}_k)^2}-c_2(\delta,\gamma)\frac{\bar{N}_k}{N_k-\bar{N}_k}+1\right] \qquad (A.11)$$

where

$$\begin{aligned}c_1(\delta,\gamma) &= 1+\frac{2\tilde{K}_{\gamma,\delta_k}}{K^2_{\gamma,\delta_k}} \\ c_2(\delta,\gamma) &= \frac{J_{\gamma,\delta}}{K_{\gamma,\delta_k}}\end{aligned} \qquad (A.12)$$

For ks, (A.11) ought to be modified into

$$\tilde{Q} = \frac{1}{c_1(\delta,\gamma)+c_3(\delta,\gamma)\frac{N_k-\bar{N}_k}{\bar{N}_k}}\left[\frac{S_k^{(2)}-N_k}{(N_k-\bar{N}_k)^2}-c_2(\delta,\gamma)\frac{\bar{N}_k}{N_k-\bar{N}_k}+1\right] \qquad (A.13)$$

with

$$c_3(\delta,\gamma) = H_{\gamma,\delta}/K^3_{\gamma,\delta} \qquad (A.14)$$

where

$$\begin{aligned}H\gamma,\delta \;=&\; \frac{1}{V^2\xi^3}\int_{R-\delta R}^{R}\xi_1\xi_2\xi_{12}dV_1dV_2 = \\ =& \frac{1}{\gamma_2}\frac{1}{2\delta^2\left(1-\delta+\frac{\delta^2}{3}\right)^2}\int_{1-\delta}^{1}dx_1x_1^{\gamma_1}\int_{1-\delta}^{1}dx_2x_2^{\gamma_1}\left[(x_1+x_2)^{\gamma_2}-|x_1-x_2|^{\gamma_2}\right] .\end{aligned} \qquad (A.15)$$

(some of the above relations are taken from Pons et al. 1990).

The division of the distance axis r into intervals (*bins*) δr_k is to be performed in a suitable distance interval r_{min}, r_{max}. In the case of *pointlike* objects (galaxies, QSO's, etc.) we can take $r_{min} = 0$. This is not convenient for more complicated systems, with an intrinsical characteristic size l, as clusters of galaxies are. It is then wise to take r_{min} at least a few times greater than l. A reasonable choice for r_{max}, instead, is $\sim r_{cc}$. Above $\sim 2\,r_{cc}$ the power law (A.2) can no longer be assumed to hold. Therefore, in our case, we have taken $r_{min} = 7\,h^{-1}$Mpc and $r_{max} = 26\,h^{-1}$Mpc.

A further point is the division of the interval $\Delta r = r_{max} - r_{min}$ into δr_k's. If no dividing is performed and $\delta r = \Delta r$, there is no direct possibility of checking the expressions *hm* and/or *ks*. If one shares Δr in a few δr_k, different (but non independent) estimates of Q ($\tilde{Q}$) follow from each bin. Their agreement is an indication of the validity of the expression used for the 3-point function.

Each bin collects the information concerning triplets set on the vertices of triangles with 2 sides having length between $r_k - \delta r_k$ and r_k and a third side between 0 and $2\,r_k$. For small δr_k, each bin tends to report information coming from nearly isosceles triangles, with two sides $\sim r_k$. It is clear that this selection leaves apart the contribution of a number of possible triplets, whose geometry does not fulfill the above requirements.

Any division scheme is however to be carefully performed in order that at least a few triplets remain in each bin. Too small δ_k cause empty bins or bins where all objects have 0 or 1 partners. Negative Q estimates then appear. They have no physical meaning, being caused by the artificial suppression of existing triplets (2 partners for some object). In any case the minimal variation of Q arising formally adding an extra partner to each object in a shell is to be checked. Such variation

$$\Delta Q_k \;=\; [\mathcal{N}_k c_1(\delta,\gamma)(N_k - \bar{N}_k)^2]^{-1} \qquad (A.16)$$

($\mathcal{N}_k$: total number of objects in the k-th shell) can be large; ΔQ_k then allows us to evaluate the usefulness of a given δr_k. Furthermore, in possible averaging procedures, the estimate of Q coming from a given shell should be given a weight inversely proportional to the corresponding ΔQ_k.

B. Two-dimensional case

For a two-dimensional distribution of objects, let $N_i(\theta)$ be the number of objects at angular separation between $\theta - \Delta\theta/2$ and $\theta + \Delta\theta/2$ from the i-th object. We define for the object distribution the moment of order k, at the angular scale θ, as

$$\langle N^k \rangle_\theta = \sum_N N^k(\theta)\, P_N(\theta) \,. \qquad (A.17)$$

In this expression, $P_N(\theta)$ represents the probability of finding N objects in the ring of radius θ and width $\Delta\theta$. Notice that the determination of this quantity is of key importance since it specifies completely the clustering properties of the system through the moments of all orders (*e.g.*, Fry 1986).

In fact, it is possible to show that the k^{th} order moment is related to the $(k+1)$-point correlation function according to

$$\begin{aligned} \langle N^k \rangle_\theta =& (\text{discreteness terms of order } m < k) \\ &+ n^k \int_{\Omega_1} d\Omega_1 ... \int_{\Omega_k} d\Omega_k [1 + w^{(k+1)}_{dis,01...k}] \end{aligned} \qquad (A.18)$$

(*e.g.*, Peebles 1980; Sharp, Bonometto & Lucchin 1984). Here, the quantity $w^{(k)}_{dis,01...k}$ represents the *disconnected* correlation function between $k+1$ points, while n is the mean density of objects in the sample. In Eq.(A.18) all the integration domains are angular rings of radius θ and constant relative width Δ.

If the 2-point function, $w(\theta)$, is modeled as a simple power-law, then Eq.(A.4) simplifies into

$$\langle N \rangle_\theta = \bar{N}_\theta \left[1 + w(\theta)\right] . \qquad (A.19)$$

In the above equation $\bar{N}_\theta (\equiv nA)$ is the expected number of clusters in the angular shell of area A. However, in order to account for boundary effects and systematic density gradients, which are always present in real data samples, we prefer to normalize Eq.(A.19) so that $\bar{N}_\theta$ is the average first-order moment over 20 random samples that contain the same number of points and have the same angular selection function as the real sample.

In the case of the 3-point correlation, Eq.(A.18) gives

$$\begin{aligned} \langle N^2 \rangle_\theta =& \langle N \rangle_\theta + n^2 \int_0^{2\pi} d\varphi_1 \int_0^{2\pi} d\varphi_2 \int_{(1-\Delta/2)\theta}^{(1+\Delta/2)\theta} d\theta_{01} \sin\theta_{01} \int_{(1-\Delta/2)\theta}^{(1+\Delta/2)\theta} d\theta_{02} \sin\theta_{02} \\ & \times \left[1 + w_{01} + w_{02} + w_{12} + z_{012}\right] . \end{aligned} \qquad (A.20)$$

In this expression z_{012} is the *connected* 3-point correlation function, which in the following is assumed to have the *hierarchical* form:

$$z_{012} \; = \; Q\left[w_{01}w_{02} + w_{01}w_{12} + w_{02}w_{12}\right] \qquad (A.21)$$

(*e.g.*, Groth & Peebles 1977; Sharp, Bonometto & Lucchin 1984; Jing & Zhang 1989; Tóth et al. 1989). Notice that assuming the simple power-law expression, $w(\theta) = B\theta^{1-\gamma}$ causes some integrals in Eq.(A.20) to diverge for $\gamma = 2$, the value which is always very near to the observed one (Plionis & Borgani 1992). Such a divergence is essentially due to the unphysical divergence of the 2-point function at $\theta \to 0$. However, due to the finite size of objects, we expect that a small-scale cutoff should be superimposed in the background field and, consequently, $w(\theta)$ should flatten at small separations. For this reason, it is appropriate to introduce the *smoothed* correlation function

$$w(\theta) \; = \; B(\theta^q + \theta_c^q)^{(1-\gamma)/q}\,, \qquad (A.22)$$

where the parameter q specifies the smoothing model, while we take $\theta_c = 30\,arcmin$ for the smoothing scale. Let us observe that, as far as the 2-point function analysis is concerned, we always have $\theta \gg \theta_c$ for the separations we are dealing with, and, consequently, the pure power-law expression of $w(\theta)$ holds.

According to Eqs.(A.20) and (A.21), we estimate the Q parameter over the considered range of angular separations by minimizing the quantity

$$\chi^2 \; = \; \sum_{i=1}^{N_{bin}} \left\{ \frac{\langle N^2\rangle_\theta - \langle N\rangle_\theta - \bar{N}_\theta^2\left[1 + (2+K_\theta)\,w(\theta) + Q\,(1+2K_\theta)\,w^2(\theta)\right]}{\sigma} \right\}^2, \qquad (A.23)$$

where the sum extends over the N_{bin} angular bins. In the above expression we weight each bin by means of the error model

$$\sigma^2 \; = \; \sigma^2_{\langle N^2 - N\rangle} + \bar{N}^4(2+K_\theta)^2\sigma_w^2\,. \qquad (A.24)$$

Since the quantities $\langle N^2\rangle$ and $\langle N\rangle$ are not independent, we prefer to estimate from the bootstrap resamplings the quantity $\sigma^2_{\langle N^2 - N\rangle}$ instead of the variances of the second- and first-order moments. The errors in the 2-point function, σ_w^2, are estimated from the uncertainties in the amplitude B, once $\gamma = 2$ is assumed (cf. Plionis & Borgani 1992). Since the first-order moment for the random distribution is estimated after averaging over 20 realizations, no significant uncertainties are associated with $\bar{N}$.

In Eqs.(A.23) and (A.24) we introduced the quantity

$$K_\theta \; = \; (2\pi\Delta)^{-1} \int_0^{2\pi} d\varphi \int_{1-\Delta/2}^{1+\Delta/2} dy\, y \left([2y^2(1 - cos\,\varphi)]^{q/2} + (\theta_c/\theta)^q \right)^{\frac{1-\gamma}{q}} , \qquad (A.25)$$

that turns out to be independent of θ in the limit $\theta_c \to 0$. We have verified that reasonable choices of θ_c and q (i.e., $\theta_c <<$ scales of interests and $q \sim 1$) leave the determination of Q essentially unaffected.

References

Aaronson, M., Bothun, G., Mould, H., Huchra, J., Schommer, R., & Cornell, M. 1986, ApJ, 302, 536

Abell, G.O. 1958, ApJS, 3, 211

Abell, G.O., Corwin, H.G., & Olowin, R.P. 1989, ApJS, 70, 1

Adler, R.J. 1980, The Geometry of Random Fields, Willy, New York

Bahcall, N.A. 1979, ApJ, 232, 689

Bahcall, N.A. 1988a, ARA&A, 26, 631

Bahcall, N.A. 1988b, in IAU Symposium 130, Evolution of Large-Scale Structures in the Universe. eds. J. Audouze, M.-C.Pelletan, & A. Szalay (Kluwer Academic Publishers), p229

Bahcall, N.A., Henriksen, M.J., & Smith, T.Ed. 1989, ApJ, 346, L45

Bahcall, N.A. & Soneira, R.M. 1982a, ApJ, 258, L17

Bahcall, N.A., & Soneira, R.M. 1983, ApJ, 270, 20 (BS83)

Bahcall, N.A., & Soneira, R.M. 1984, ApJ, 277, 27

Bahcall, N.A., Soneira, R.M., & Burgett, W. 1986, ApJ, 311, 28

Bahcall, N.A. and West, M.J. 1992, ApJ, (in press)

Bardeen, J.M., Bond, J.R., Kaiser, N., & Szalay, A.S. 1986, ApJ, 304, 15

Barrow, J.D., Bhavsar, S.P., & Sonoda, D.H. 1984, MNRAS, 210, 19P

Barrow, J.D., Bhavsar, S.P., & Sonoda, D.H. 1985, MNRAS, 216, 17

Batuski, D.J., Bahcall, N.A., Olowin, R.P, & Burns, J.O. 1989, ApJ, 341, 599

Batuski, D.J. & Burns, J.O. 1985a, AJ, 90, 1413

Batuski, D.J. & Burns, J.O. 1985b, ApJ, 299, 5

Batuski, D.J., Burns, J.O., Newberry, M.V., Hill, J.M., Deeg, H.J., Laubscher, B.E. & Elston, R.J. 1991, AJ, 101, 1983

Batuski, D.J., Melott, A.L., & Burns, J.O. 1987, ApJ, 322,48

Baumgart, D.J. & Fry, J.N. 1991, ApJ, 375, 25

Bean, A.J., Efstathiou, G., Ellis, R.S., Peterson, B.A., & Shanks, T. 1983, MNRAS, 205, 605

Bertschinger, E., Dekel, A., Faber, S.M., Dressler, A. & Burstein, D. 1990, ApJ, 364, 370

Bhavsar, S.P. 1978, ApJ, 222, 412

Bhavsar, S.P. 1980, ApJ, 237, 671

Bhavsar, S.P. & Barrow, J.D. 1983, MNRAS, 205, 61p

Bhavsar, S.P., & Ling, E.N. 1988a, ApJ, 331, L63

Bhavsar, S.P., & Ling, E.N. 1988b, PASP, 100, 1314

Binggeli, B. 1982, A&A, 107, 338

Binggeli, B., Sandage, A., & Tammann, G.A. 1988, ARA&A, 26, 509

Binggeli, B., Tareghi, M., & Sandage, A. 1990, A&A, 228, 42

Börner, G. & Mo, H.J. 1989a, A&A, 223, 25

Börner, G. & Mo, H.J. 1989b, A&A, 224, 1

Börner, G. & Mo, H.J. 1990, A&A, 227, 324

Börner, G., Mo, H.J., Zhou, Y.Y. 1989, A&A, 221, 191

Bond, J.R., Efstathiou, G., Lubin, P.M., & Meinhold, P.R. 1991, Phys. Rev. Letters, 66, 2179

Borgani, S. 1990, MS thesis, SISSA, Trieste.

Borgani, S., Jing, Y.P., & Plionis, M. 1992, ApJ, (in press)

Bothum, G.D., Beers, T.C., Mould, J.R., & Huchra, J.P. 1986, ApJ, 308, 510

Bouchet, F.R., & Lachieze-Rey, M. 1986, ApJ, 302, L37

Broadhurst, T.J., Ellis, R.S., Koo, D.C. & Szalay, A.S. 1990, Nat, 343, 726

Brown, E.M. & Groth, E.J. 1989, ApJ, 338, 605

Calzetti, D., Giavalisco, M., & Ruffini, R. 1988, A&A, 198, 1

Cappi, A., Focardi, P., Gregorini, L. & Vettolani, G. 1991a, A&AS, 88, 349

Cappi, A., Maurogordato, S., & Lachiéze-Rey, M. 1991b, A&A, 243, 28

Carr, B. J., Bond, J. R., & Arnett, W. D. 1984, ApJ, 277, 445

Chincarini, G., Rood, H.J., & Thompson, L.A. 1981, ApJ, 249, L47

Clowes, R.G. & Campusano, E. 1991, MNRAS, 249, 218

Coles, P. 1988, MNRAS, 234, 509

Coles, P. & Barrow, J.D. 1987, MNRAS, 228, 407

Coles, P. & Frenk, C.S. 1991, MNRAS, 253, 727

Coles, P. & Jones, B.J.T. 1990, MNRAS, 248, 1

Coles, P. & Plionis, M. 1991, MNRAS, 250, 75

Collins, C.A., Heydon-Dumbleton N.H., & MacGillicray, H.T. 1989, MNRAS, 236, 7p

Collins, C.A., Nichol, R.C., & Lumsden, S.L. 1992, MNRAS, 254, 295

Couchman, H.M.P., McGill, C., & Olowin, R.P. 1989, MNRAS, 239, 513

da Costa, L.N., Pellegrini, P.S., Davis, M., Meiksin, A., Sargent, W.L.W., & Tonry, J.L. 1991, ApJS, 75, 935

Dalton, G.B., Efstathiou, G., Maddox, S.J., & Sutherland, W.J. 1992, ApJ, 390, L1

Davis, M., Efstathiou, G., Frenk, C. S., & White, S. D. M. 1985, ApJ, 292, 371

Davis, M., & Geller, M.J. 1976, ApJ, 208, 13

Davis, M., Geller, M.J., & Huchra, J. 1978, ApJ, 221, 1

Davis, M. & Djorgovski, S. 1985, ApJ, 299, 15

Davis, M., Meiksin, A., Stauss, M.A., da Costa, L.N., & Yahil, A. 1988, ApJ, 333, L9

Davis, M., & Peebles, P.J.E. 1983, ApJ, 267, 465

Dekel, A. 1988, in IAU Symposium 130, Evolution of Large-Scale Structures in the Universe. eds. J. Audouze, M.-C.Pelletan and A. Szalay (Kluwer Academic Publishers), 598

Dekel, A., Blumenthal, G.R., Primack, J.P., & Olivier, S. 1989, ApJ, 338, L5

Dekel, A. & Rees, M.J. 1987, Nat, 326, 455

Dekel, A., & Silk, J. 1986, ApJ, 303, 39

Dekel, A., & West, M.J. 1985, ApJ, 288, 411

Dekel, A., West, M.J., & Aarseth, S.J. 1984, ApJ 279, 1

de Lapparent, V., Geller, M.J., & Huchra, J.P. 1986, ApJ, 302, L1 (LGH)

de Lapparent, V., Geller, M.J., & Huchra, J.P. 1988, ApJ, 332, 44

Dressler, A., Fader, S.M., Burstein, D., Davies, R.L., Lynden-Bell, D., Terlevich, R.S. & Wegner, G. 1987, ApJ, 313, L37

Eder, J.A., Schombert, J.M., Dekel, A., & Oemler, Jr.,A. 1989, ApJ, 340, 29

Efstathiou, G. 1988, In Large-Scale Motions in the Universe, eds. V.C. Rubin and G.V. Coyne, Princeton Univ. Press, p299

Efstathiou, G. & Bond, J.R. 1986, MNRAS, 218, 103

Efstathiou, G., Ellis, R.S., & Peterson, B.A. 1988, MNRAS, 232, 431

Efstathiou, G., & Jedrzejewski, R.I. 1984, Adv. Space Res., 3, 379

Efstathiou, G., Kaiser, N., Saunders, W., Lawrence, A., Rowan-Robinson, Ellis, R.S., & Frenk, C.S. 1990, MNRAS, 247, 10p

Efstathiou, G., & Silk, J. 1983, Fundamentals of Cosmic Physics, 9, 1

Einasto, J., Klypin, A., & Saar, E. 1986, MNRAS, 219, 457

Einasto, J., Klypin, A., Saar, E. & Shandarin, S.F. 1984, MNRAS, 206, 529

Faber, S.M. & Burstein, D. 1988, In Large-Scale Motions in the Universe, eds. V.C. Rubin and G.V. Coyne, Princeton Univ. Press, p115

Fall, S. M., & Tremain, S. 1977, ApJ, 216, 682

Flin, P. 1987, MNRAS, 228, 941

Fong, R., Stevenson, P.R.F. & Shanks, T. 1990, MNRAS, 242, 146

Frenk, C.S., White, S.D.M., Davis, M. & Efstathiou, G. 1988, ApJ, 327, 507

Fry, J.N. 1984, ApJ, 277, L5

Fry, J.N. 1986, ApJ, 306, 358

Fry, J.N., Giovanelli, R., Haynes, M.P., Melott, A.L., and Scherrer, R.J. 1989, ApJ, 340, 11

Fry, J.N., & Melott, A.L. 1985, ApJ, 292, 395

Gao, Y., & Jing, Y.P. 1989, MNRAS, 236, 559

Geller, M.J. & Huchra, J.P. 1983, ApJS, 52, 61

Geller, M.J., & Huchra, J.P. 1988, In Large-Scale Motions in the Universe, eds. V.C. Rubin and G.V. Coyne, Princeton Univ. Press, p3

Geller, M.J. & Huchra, J.H. 1989, Sci, 246, 897

Giovanelli, R., Haynes, M.P., & Chincarini,G.L. 1986, ApJ, 300, 77

Gott, J.R., Gao, B., & Park, C. 1991, ApJ, 383, 90

Gott, J.R., Melott, A.L., & Dickinson, M. 1986, ApJ, 306, 341

Gott, J.R., Miller, J., Thuan, T.X., Schneider, S.E., Weinberg, D.H., Gammie, C., Polk, K., Vogeley, M., Jeffrey, S., Bhavsar, S.P., Melott, A.L., Giovanelli, R., Haynes, M.P., Tully, R.B., & Hamilton, A.J.S. 1989, ApJ, 340, 625

Gott, J.R. , Turner, E.L., & Aarseth, S.J. 1979, ApJ, 234, 13

Gramann, M. & Einasto, J. 1992, MNRAS, 254, 453

Gregory, S.A. & Thompson, L.A. 1984, ApJ, 286, 422

Groth, E.J., & Peebles, P.J.E. 1977, ApJ, 217, 385

Hamilton, A.J.S., Gott, J.R., & Weinberg, D. 1986, ApJ, 309, 1

Hauser, H.G., & Peebles, P.J.E. 1973, ApJ, 185, 757

Haynes, M.P., & Giovanelli, R. 1986, ApJ, 306, L55

Henry, J.P. & Arnaud, K.A. 1991, ApJ, 372, 410

Henry, J.P., Gioia, I.M., Maccacaro, T., Morris, S.L., Stocke, J.T., & Wolter, A. 1992, ApJ, 386, 408

Hockney, R.W. & Eastwood, J.W. 1981, Computer simulations using particles. Mc Graw-Hill

Hoessel, J.G., Gunn, J.E., & Thuan, T.X. 1980, ApJ, 241, 486

Holtzman, J.A. 1989, ApJS, 71, 1

Huchra, J., Davis, M., Latham, D. & Tonry, J. 1983, ApJS, 52, 89

Huchra, J.P., & Geller, M.J. 1982, ApJ, 257, 423

Huchra, J.P., Geller, M.J., de Lapparent, V. & Corwin, H.G. 1990a, ApJS, 72, 433

Huchra, J.P., Henry, J.P., Postman, M., & Geller, M.J. 1990b, ApJ, 365, 66

Ikeuchi, S. 1981, PASJ, 33, 211

IRAS Point Source Catalog, Version 2 1988. Joint IRAS Working Group, GPO, Washington, DC

Jensen, L.G., & Szalay, A.S. 1986, ApJ, 305, L5

Jing, Y.P. 1990a, A&A, 233, 7

Jing, Y.P. 1990b, A&A, 233, 309

Jing, Y.P. 1991, MNRAS, 248, 559

Jing, Y.P., Mo, H.J., & Börner, G. 1991, A&A, 252, 449

Jing, Y.P., Plionis, M., & Valdarnini, R. 1992, ApJ, 389, 499

Jing, Y.P., & Valdarnini, R. 1991, A&A, 250, 1

Jing, Y.P., & Valdarnini, R. 1992, ApJ, (in press)

Jing, Y.P., & Zhang, J.L. 1987, Ap&SS, 138, 105

Jing, Y.P., & Zhang, J.L. 1988, A&A, 190, L21

Jing, Y.P., & Zhang, J.L. 1989, ApJ, 342, 639

Joeveer, M., Einasto, J., & Tago, E. 1978, MNRAS, 185, 357

Juszkiewicz, R., Vittorio, N., & Wyse, R. 1990, ApJ, 349, 408

Kaiser, N. 1984, ApJ, 284, L9

Kaiser, N. 1986, MNRAS, 219, 785

Kaiser, N. 1987, MNRAS, 227, 1

Kaiser, N. 1991, Talk presented at the Texas/ESO-CERN conference, Brighton

Kashlinsky, A. 1987, ApJ, 317, 19

Kirshner, R., Oemler, A., Schecther, R. & Shectman, S. 1981, ApJ, 248, L57

Klypin, A.A., Einasto, J., Einasto, M. & Saar, E. 1989, MNRAS, 237, 929

Klypin, A.A., & Kopylov, A.I. 1983, SvA, 9, L41

Kopylov, A.I., Kuznetsov, D. Yu., Fetisova, T.S., & Shvartsman, V.F. 1987, in Proc. Semm. Large Scale Structure of the Universe, 1986, 39. Stavropol, USSR Spec. Astrophys. Obs.

Kulsrud, R. M., & Cowley, S. C. 1989, ApJ, 346, 546 (KC)

Lahav, O., Edge, A.C., Fabian, A.C., & Putney, A. 1989, MNRAS, 238, 881

Lahav, O., Kaiser, N., & Hoffman, Y. 1990, ApJ, 352, 448

Lahav,O., Rowan-Robinson,M., & Lynden-Bell,D. 1988, MNRAS, 234, 677 (LRL)

Lauberts, A. 1982, The ESO-Uppsala Survey of the ESO(B) Atlas, European Southern Observatory

Leir, A.A., & van den Bergh, S. 1977, ApJS, 34, 381

Lilje, P.B., & Efstathiou, G. 1988, MNRAS, 231, 635

Ling, E.N. 1987, PhD thesis, Sussex Univ.

Ling, E.N., Frenk, C.S., & Barrow, J.D. 1986, MNRAS, 223, 21p

Lucchin, F. & Matarrese, S. 1985, Phys. Rev. D32, 1316

Lucchin, F., Matarrese, S., & Vittorio, N. 1988, ApJ, 330, L21

Lucey, J.R. 1983, MNRAS, 204, 33

Lucey, J.R., & Carter, D. 1988, MNRAS, 235, 1177

Lumsden, S.L., Nichol, R.C., Collins, C.A. and Guzzo, L. 1992, MNRAS, (in press)

Lynden-Bell, D., Faber, S.M., Burstein, D., Davies, R.L., Dressler, A., Terlevich, R.J., & Wegner, G. 1988, ApJ, 326, 19

Maddox, S.J., Efstathiou, G., Sutherland, W.J., & Loveday, J. 1990a, MNRAS, 242, 43p

Maddox, S.J., Sutherland, W.J., Efstathiou, G., & Loveday, J. 1990b, MNRAS, 243, 692

Maia, M.A.G., & da Costa, L.N. 1990, ApJ, 349, 477

Maia, M.A.G., da Costa, L.N., & Latham, D.D. 1989, ApJS, 69, 809

Matarrese, S., Lucchin, F., & Bonometto, S.A. 1986, ApJ, 310, L21

Matarrese, S., Lucchin, F., Messina, A., & Moscardini, L. 1991, MNRAS, 253, 35

Mattig, W. 1958, Astr. Nach., 284, 109

Maurogordato, S., & Lachieze-Rey, M. 1987, ApJ, 320, 13 (ML)

McMillan, S.L.W., Kowalski, M.P. & Ulmer, M.P. 1989, ApJS, 70, 723

Melott, A.L. 1990, Phys. Report, 193, 1

Melott, A.L., & Fry, J.N. 1986, ApJ, 305, 1

Messina, A., Moscardini, L., Lucchin, F. & Matarrese, S. 1990, MNRAS, 245, 244.

Metcalfe, N., Fong, R., Shanks, T., & Kilkenny, D. 1989, MNRAS, 236, 207

Mo, H.J. & Börner, G. 1990, A&A, 238, 3

Mo, H.J., Jing, Y.P., & Börner, G. 1992, ApJ, 392, 452

Mo, H.J., Peacock, J.A. & Xia, X.Y. 1992, MNRAS, (in press)

Moore, B., Frenk, C.S., Weinberg, D.H., Saunders, W., Lawrence, A., Ellis, R.S., Kaiser, N., Efstathiou, G., Rowan-Robinson, M. 1992, MNRAS, 256, 477

Moscardini, L., Matarrese, S., Lucchin, F. & Messina, A. 1991, MNRAS, 248, 424

Muriel, H., Nicotra, M., Lambas, D.G. 1991, AJ, 101, 1997

Nichol, R.C., Collins, C.A., Guzzo, L., & Lumsden, S.L. 1992, MNRAS, 255, 21p

Nilson, P. 1973, Uppsala General Catalogue of Galaxies, Uppsala.

Olivier, S., Blumenthal, G.R., Dekel, A., Primack, J.R., & Stanhill, D. 1990, ApJ, 356, 1

Ore, O. 1962, Amer. Math. Soc. Colloq. Publ., 38

Ostriker, J.P., & Cowie, L.L. 1981, ApJ, 243, L127

Ostriker, J. P., Thompson, C., & Witten, E. 1986, Phys. Letters B180, 231

Ostriker, J.P. 1988, in IAU Symposium 130, Evolution of Large-Scale Structures in the Universe. eds. J. Audouze, M.-C.Pelletan and A. Szalay (Kluwer Academic Publishers), 321

Park, C., Gott, J.R., & Da Costa, L.N. 1992, ApJ, (in press)

Parry, W.E. 1977, Phys. Letters, A60, 265

Peacock, J.A. 1991, MNRAS, 253, 1p

Peacock, J.A. & Nicholson, D. 1991, MNRAS, 253, 307

Peebles, P.J.E. 1975, ApJ, 196, 647

Peebles, P.J.E. 1979, AJ, 84, 730

Peebles, P.J.E. 1980, The large-scale structure of the Universe, Princeton Princeton University Press

Peebles, P.J.E. 1981, in Annals New York Academy of Science, 157

Peebles, P.J.E. 1988, ApJ, 332, 17

Peebles, P.J.E., & Groth, E.J. 1975, ApJ, 195, 1

Picard, A. 1991, ApJ, 368, L7

Pietronero, L. 1987, Physica, 144A, 257

Politzer, D., & Wise, M.B. 1984, ApJ, 285, L1

Pons, B., Iovino, M.J., & Bonometto, S.A. 1991, AJ, 102, 495

Postman, M., Geller, M.J., & Huchra, J.P. 1986, AJ, 91, 1267

Postman, M., Geller, M.J. & Huchra, J.P. 1988, AJ, 95, 267

Postman, M., Huchra, P., & Geller, M. 1992, ApJ, 384, 404

Postman, M., Huchra, J.P., Geller, M.J., & Henry, J.P. 1985, AJ, 90, 1400

Postman, M., Spergel, D.N., Satin, B., & Juszkiewicz, R. 1989, ApJ, 346, 588

Plionis, M. 1988, MNRAS, 234, 401

Plionis, M. 1992, in preparation

Plionis, M., Barrow, J.D., & Frenk, C.S. 1991, MNRAS, 249, 662

Plionis, M., & Borgani, S. 1991, MNRAS, 251, 575

Plionis, M. & Valdarnini, R. 1991, MNRAS, 249, 46

Plionis, M., Valdarnini, R. & Coles, P. 1992, MNRAS, (in press)

Plionis, M., Valdarnini, R. & Jing, Y.P. 1992, ApJ, (in press)

Ramella, M., Geller, M.J., & Huchra, J.P. 1989, ApJ, 344, 57

Ramella, M., Geller, M.J., & Huchra, J.P. 1990, ApJ, 353, 51

Raychaudhury, S. 1989, Nat, 342, 251

Readhead, A.C.S., Lawrence, C.R., Myers, S.T., Sargent, W.L.W., Hardeback, H.E., & Moffet, A.T. 1989, ApJ, 346, 566

Rhee, G.F.R. & Katgert, P. 1987, A&A, 183, 217

Rhee, G.F.R. & Katgert, P. 1988, A&AS 72, 243

Rood, H.J. 1988, ARA&A, 26, 245

Rowan-Robinson, M., Lawrence, A., Saunders, W., Crawford, J., Ellis, R., Frenk, C.S., Parry, I., Xiaoyang, X., Allington-Smith, J., Efstathiou, G., & Kaiser, N. 1990, MNRAS, 247, 1

Salzer, J.J., Hanson, M.M., & Gavazzi, G. 1990, ApJ, 353, 39

Santiago, B.X., & da Costa, L.N. 1990, ApJ, 362, 386

Saunders, W., Rowan-Robinson, M., Lawrence, A., Efstathiou, G., Kaiser, N., Ellis, R.S., & Frenk, C.S. 1990, MNRAS, 242, 318

Saunders, W. et al. 1991, Nat, 349, 32

Scaramella, R., Baiesi-Pillastrini, G., Chincarini, G., Vettolani, G. & Zamorani, G. 1989, Nat, 338, 562

Scaramella, R., Vettolani, G., & Zamorani, G. 1991, ApJ, 376, L1

Schaeffer, R. 1984, A&A, 134, L15

Schaeffer, R. 1987, A&A, 180, L5

Seldner, M., & Peebles, P.J.E. 1977, ApJ, 215, 703

Seldner, M., Siebers, B., Groth, E.J., & Peebles, P.J.E. 1977, AJ, 82, 249

Shane, C.D. & Wirtanen, C.A. 1967, Pub. Lick. Obs., 22, 1

Shapley, H. 1930, Harvard Obs. Bull., 874, 9

Sharp, N. A. 1981, MNRAS, 195, 857

Sharp, N.A., Bonometto, S.A., & Lucchin, F. 1984, A&A, 130, 79

Shectman, S.A. 1985, ApJS, 57, 77

Smoot, G.F., Bennett, C.L., Kogut, A., Aymon, J., Backus, C., De Amici, G., Galuk, K., Jackson, P.D., Keegstra, P., Rokke, L., Tenorio, L., Torres, S., Gulkis, S., Hauser, M.G., Janssen, M.A., Mather, J.C., Weiss, R., Wilkinson, D.T., Wright, E.L., Boggess, N.W., Cheng, E.S., Keisall, T., Lubin, P., Meyer, S., Moselley, S.H., Murdock, T.L., Shafer, R.A., & Silverberg, R.F. 1991, ApJ, 371, L1

Smoot, G.F., Bennett, C.L., Kogut, A., Wright, E.L., Aymon, J., Boggess, N.W., Cheng, E.S., De Amici, G., Gulkis, S., Hauser, M.G., Hinshaw, G., Lineweaver, C., Loewenstein, K., Jackson, P.D., Janssen, M.A., Kaita, E., Kelsall, T., Keegstra, P., Lubin, P., Mather, J.C., Meyer, S., Moselley, S.H., Murdock, T.L., Rokke, L., Silverberg, R.F. Tenorio, L., Weiss, R., & Wilkinson, D.T. 1992, ApJ, (in press)

Soneira, R.M., & Peebles, P.J.E. 1978, AJ, 83, 845

Strauss, M.A. & Davis, M. 1988, In Large-Scale Motions in the Universe, eds. V.C. Rubin and G.V. Coyne, Princeton Univ. Press, p255

Strauss, M. A., Davis, M., Yahil, A. and Huchra, J.P. 1990, ApJ, 361, 49

Strauss, M.A., Davis, M., Yahil, A., & Huchra, J.P. 1992a, ApJ, 385, 421

Strauss, M.A., Davis, M., Yahil, A., & Huchra, J.P. 1992b, ApJS, (in press)

Struble, M.F. & Peebles, P.J.E. 1985, AJ, 90, 582

Struble, M.F. & Rood, H.J. 1987, ApJS 63, 543

Struble, M.F., & Rood, H.J. 1991a, ApJS, 77, 363

Struble, M.F., & Rood, H.J. 1991b, ApJ, 374, 395

Sutherland, W. 1988, MNRAS, 234, 159 (S88)

Sutherland, W., & Efstathiou, G. 1991, MNRAS, 248, 159 (SE91)

Szalay, A.S. 1988, ApJ, 333, 21

Szalay, A.S., Hollósi, J., & Tóth, G. 1989, ApJ, 339, L5

Tarenghi, G.A., Chincarini, G., Rood, H.G. & Thompson, L.A. 1980, ApJ, 235, 724

Tarenghi, G.A., Tifft, W.G., Chincarini, G., Rood, H.G. & Thompson, L.A. 1979, ApJ, 234, 793

Thuan, T.X., Alimi, J.M., Gott, J.R., & Schneider, S.E. 1991, ApJ, 370, 25

Thuan, T.X., Gott, J.R., & Schneider, S.E. 1987, ApJ, 315, L93

Thuan, T.X., & Seitzer, P.O. 1979, ApJ, 231, 327

Tóth, G., Hollósi, J., & Szalay, A.S. 1989, ApJ, 344, 65

Tully, B. 1986, ApJ, 303, 25

Tully, B. 1987, ApJ, 323, 1

Tully, B., Scaramella, R., Vettolani, G. & Zamorani, G. 1992, ApJ, (in press)

Turok, N. 1985, Phys. Rev. Letters, 55, 1700

Uson, J.M. & Wilkinson, D.J. 1984, ApJ, 277, L1

Valdarnini, R. & Borgani, S. 1991, MNRAS, 251, 575

Valdarnini, R., Borgani, S. & Provenzale, A. 1992, ApJ, 394, 422

Vettolani, G., Cappi, A., Chincarini, G., Focardi, P, Garilli, B., Gregorini, L. & Maccagni, D. 1989, A&AS, 79, 147

Villumsen, J.V. & Davis, M. 1986, ApJ, 308, 499

Vittorio, N., Matarrese, S., & Lucchin, F. 1988, ApJ, 328

Vittorio, N., Meinhold, P., Muciaccia, P.F., Lubin, P., & Silk, J. 1991 ApJ, 372, L1

Vogeley, M.S., Park, C., Geller, M.J., Huchra, J.P. 1992, ApJ, 391, L5

Weinberg, D.H. 1988, PASP, 100, 1373

Weinberg, D. H., Ostriker, J. P., & Dekel, A. 1989, ApJ, 336, 9 (WOD)

Weinberg, S. 1972, Gravitation and Cosmology, New York John Wiley

West, M.J. 1989a, ApJ, 344, 535

West, M.J. 1989b, ApJ, 347, 610

West, M.J., Dekel, A. & Oemler, A.Jr. 1989, ApJ, 336, 46

West, M.J., & Van den Bergh, S. 1991, ApJ, 373, 1

West, M.J., Weinberg, D. H., & Dekel, A. 1990, ApJ, 353, 329

White, S. D. M. 1979, MNRAS, 186, 145

White, S.D.M., Davis, M., Efstathiou, G., & Frenk, C.S. 1987a, Nat, 330, 351

White, S.D.M., Frenk, C.S., Davis, M., & Efstathiou, G. 1987b, ApJ, 313, 505

Whitmore, B. 1989, STScI preprint, 410

Yahil, A. 1988, In Large-Scale Motions in the Universe, eds. V.C. Rubin and G.V. Coyne, Princeton Univ. Press, p219

Yahil, A., Strauss, M.A., Davis, M., & Huchra, J.P. 1991, ApJ, 372, 380

Xia, X.Y., Deng, Z.G., & Zhou, Y.Y. 1987, in Observational Cosmology, IAU Symp. 124, eds. A. Hewitt, G. Burbidge, & L.Z. Fang, Reidel.

Zwicky, F., Herzog, E., Wild, P., Karpovicz, M., & Kowal, C. 1961-68 Catalogue of Galaxies and Clusters of Galaxies, Vols 1-6, California Institute of Technology, Pasadena